A unified modelling framework for vibratory pile driving methods

Tsetas, A.

DOI
10.4233/uuid:c9cb4a2a-abeb-4de5-b0b0-5bebd3416407

Publication date
2023

Document Version
Final published version

Citation (APA)
Tsetas, A. (2023). *A unified modelling framework for vibratory pile driving methods*. [Dissertation (TU Delft), Delft University of Technology]. https://doi.org/10.4233/uuid:c9cb4a2a-abeb-4de5-b0b0-5bebd3416407

Important note
To cite this publication, please use the final published version (if applicable).
Please check the document version above.

A unified modelling framework for vibratory pile driving methods

A unified modelling framework for vibratory pile driving methods

Dissertation

for the purpose of obtaining the degree of doctor
at Delft University of Technology,
by the authority of the Rector Magnificus Prof. dr. ir. T.H.J.J. van der Hagen,
chair of the Board for Doctorates,
to be defended publicly on
Thursday 6 July 2023 at 12:30 o'clock

by

Athanasios TSETAS

Master of Science in Civil Engineering,
Aristotle University of Thessaloniki, Greece
born in Drama, Greece.

This dissertation has been approved by the promotors.

Composition of the doctoral committee:

Rector Magnificus,	chairperson
Prof. dr. A. V. Metrikine,	Delft University of Technology, promotor
Dr. ir. A. Tsouvalas	Delft University of Technology, copromotor

Independent members:

Prof. dr. P. G. Steeneken	Delft University of Technology
Prof. dr. L. Cheng	The Hong Kong Polytechnic University, China
Prof. dr. G. Degrande	Katholieke Universiteit Leuven, Belgium
Prof. dr. N. Kessissoglou	The University of New South Wales, Australia
Prof. dr. E. Pavlovskaia	University of Aberdeen, Scotland
Prof. dr. P. J. Vardon	Delft University of Technology, reserve member

This work is part of the GDP research project (GROW joint research programme), which is (partly) financed by the *Topsector Energiesubsidie van het Ministerie van Economische Zaken* under grant number TEHE117100.

Keywords: pile driving, monopile installation, vibratory driving, Gentle Driving of Piles, vibrations of shells, soil dynamics, Thin-Layer Method, Green's functions, Harmonic Balance Method, friction fatigue, friction redirection

Printed by: Uitgeverij U2pi - The Hague, the Netherlands

Cover design: Elissavet Markozani

ISBN 978-94-6366-716-6

An electronic version of this dissertation is available at `https://repository.tudelft.nl/`.

τὸ τῆς ἀνάγκης ἔστ᾽ ἀδήριτον σθένος
the might of necessity is unconquerable
Aeschylus, *Prometheus Bound*

Contents

Summary

The ambitious goals towards the decarbonization of the global energy sector have amplified the demand for renewable energy resources. Amongst the renewables, offshore wind possesses a pivotal role in this endeavour, showcasing remarkable growth in recent years. However, this rapid expansion has been accompanied by a series of technical challenges. Foundation installation comprises one of the most critical phases in the construction of an offshore wind farm and engineering advancements in this topic are vital to accommodate this developmental pace. Bottom-fixed foundations are primarily used to support offshore wind turbines and amongst the available concepts, the monopile is the foremost one. The installation of these substructures is most commonly performed via impact hammering. Notwithstanding the robustness and efficacy of this technique, major environmental concerns have been raised due to the significant levels of underwater noise pollution during driving. In view of this alarming issue, alternative and sustainable pile installation techniques have been progressively drawing attention during the last decade and an increasing number of research projects focus on their investigation and development.

At present, the offshore wind industry is increasingly adopting vibratory pile driving. The previous method has been successfully employed in onshore projects for decades, albeit its wider use in the offshore environment is hindered due to the incompleteness of available field observations. To boost the improvement of vibratory installation methods, a new technology has been recently proposed by the Delft University of Technology, namely the Gentle Driving of Piles (GDP). The preceding method aims to enhance the installation performance of vibratory driving for tubular (mono)piles and to reduce the associated noise emissions, via the simultaneous application of low-frequency/axial and high-frequency/torsional vibrations. Naturally, the shift to these technologies is accompanied by emerging research questions pertaining to pile installation, vibro-acoustic and post-installation performances. In this thesis, the development of an engineering-oriented modelling framework for axial vibratory driving and GDP is the primary objective, thereby focusing on the topic of sustainable monopile installation.

In the first chapters of the thesis, the theoretical background pertaining to the dynamic pile and soil behaviours is presented, accompanied by the respective numerical developments. In particular, the dynamic pile behaviour is discussed on the basis of cylindrical shells, according to Love's first approximation theories. The soil medium is described as a linear elastic layered half-space in terms of Green's functions in the frequency-space domain. For the purpose of numerical modelling, the developments introduced in this thesis are briefly: (i) the Semi-analytical Finite Element (SAFE) method for thin/thick cylindrical shells, (ii) the Thin-Layer Method (TLM) coupled with Perfectly Matched Layers (PMLs) for layered soil half-spaces and (iii) a sequential Harmonic Balance Method (HBM) for nonlinear dynamical systems with quasi-periodicity. The preceding schemes are characterized by remarkable versatility and computational performance while being applicable to a wide set of engineering problems. For that purpose, the relevant treatments are retained as

generic and accessible as possible, with a view to benefit a diverse readership.

The experimental work follows and comprises one of the major highlights of this thesis, namely the GDP field campaign. The campaign scope encompassed both installation and post-installation lateral loading tests. Focusing on the installation aspect, a purpose-built GDP shaker was designed in order to demonstrate the efficacy of the GDP method and a medium-scale field tests campaign was executed at the Maasvlakte II site in Rotterdam. Following the successful proof of concept, a primary objective of the field tests was the comparison of GDP with two conventional techniques, namely impact hammering and axial vibratory driving. Furthermore, an extensive dataset of pile and soil measurements was collected and utilized for comparison and numerical model development purposes, thereby serving a multitude of objectives in the research line of GDP. Both pile and soil response records provided favourable results for GDP, encouraging its further development and upscaling. In summary, the field campaign provided a preliminary demonstration of the GDP technology and the comparison of axial vibratory driving and GDP showcased the beneficial effect of torsion.

As regards vibratory pile installation, a comprehensive understanding of the physical mechanisms involved and their incorporation into effective engineering-oriented models are still elusive for axial vibro-driving. To that end, the numerical developments of this thesis (i.e. SAFE and TLM+PMLs) are integrated into a computationally efficient model, that aims to bridge the gap between the available medium- and high-fidelity approaches. The present approach alleviates physical drawbacks possessed by the former, without engendering the practical and computational limitations of the latter. The pile-soil interaction is governed by a history-dependent frictional interface and a visco-elasto-plastic tip model, whereas the non-linear problem is solved by a novel HB-based scheme. The main component of the soil reaction is found to correspond to the shaft friction, whereas its hereditary character is based on a memory mechanism based on loading cycles accumulation; the latter effect is commonly termed friction fatigue. Finally, drivability predictions are compared against field data from the vibro-driven pile of the campaign, indicating the prediction potential of the present model.

The preceding modelling framework is utilized as a basis and further developed, with a view to analysing pile installation via GDP. By means of this numerical tool, the interpretation of field observations is greatly facilitated and the driving mechanism of GDP is comprehended. Based on the numerical results, the redirection of the friction force vector manifests itself as the major mechanism of GDP, that greatly enhances installation performance. In particular, the high-frequency torsion expends the majority of shaft friction in the circumferential direction and the soil reaction along the penetration axis diminishes substantially, thereby enabling faster installation and reduced axial driving loads. Conclusively, a numerical investigation is conducted to assess the induced ground motion by axial vibro-driving and GDP, with the latter leading to reduced environmental disturbance and energy redistribution from SV-P to SH waves.

Pile drivability predictions are essential to assess the capability of a driving device to install a pile to the target penetration depth and to anticipate and prevent occurrences of high operational risk, e.g. early pile refusal or pile running. The role of pile installation cannot be overemphasized in offshore wind farm construction, as the installation process itself affects greatly both vibro-acoustic and post-installation performances. By means

of the present framework, a path towards integrated design of the preceding aspects is enabled. In this thesis, an endeavour to bridge the gap between medium- and high-fidelity approaches is presented, in order to shift the paradigm of standard engineering-oriented frameworks and better the engineering aspects of sustainable monopile installation.

Samenvatting

De ambitieuze doelstellingen om de wereldwijde energiesector koolstofvrij te maken, hebben de vraag naar hernieuwbare energiebronnen doen toenemen. Onder de hernieuwbare energiebronnen speelt offshore-windenergie een centrale rol in dit streven, met een opmerkelijke groei in de afgelopen jaren. Deze snelle groei gaat echter gepaard met een reeks technische uitdagingen. De installatie van funderingen is een van de meest kritieke fasen in de bouw van een offshore windmolenpark en technische vooruitgang op dit gebied is van vitaal belang om dit ontwikkelingstempo aan te kunnen. Voor de ondersteuning van offshore-windturbines wordt voornamelijk gebruik gemaakt van bodemfunderingen en van de beschikbare concepten is de monopile de belangrijkste. De installatie van deze substructuren gebeurt meestal door middel van hamerslagen. Ondanks de robuustheid en doeltreffendheid van deze techniek is er grote bezorgdheid over het milieu ontstaan door de aanzienlijke geluidsoverlast onder water tijdens het slaan. In het licht van dit alarmerende probleem hebben alternatieve en duurzame paalinstallatietechnieken de laatste tien jaar geleidelijk de aandacht getrokken en een toenemend aantal onderzoeksprojecten is gericht op het onderzoek en de ontwikkeling ervan.

Momenteel wordt in de offshore windindustrie steeds meer gebruik gemaakt van trilpalen. De vorige methode wordt al tientallen jaren met succes toegepast in onshore-projecten, maar een ruimere toepassing in de offshore-omgeving wordt belemmerd door de onvolledigheid van de beschikbare veldwaarnemingen. Om de trilinstallatiemethoden te verbeteren, heeft de Technische Universiteit Delft onlangs een nieuwe technologie voorgesteld, namelijk Gentle Driving of Piles (GDP). De voorgaande methode heeft tot doel de installatieprestaties van het trillen van buisvormige (mono)palen te verbeteren en de bijbehorende geluidsemissies te verminderen, via de gelijktijdige toepassing van laagfrequente/axiale en hoogfrequente/torsietrillingen. Uiteraard gaat de verschuiving naar deze technologieën gepaard met opkomende onderzoeksvragen met betrekking tot het installeren van palen, vibro-akoestische en post-installatie prestaties. In dit proefschrift is de ontwikkeling van een engineering-georiënteerd modelleringskader voor axiaal trillen en BBP de primaire doelstelling, waarbij het onderwerp duurzame monopaal installatie centraal staat.

In de eerste hoofdstukken van het proefschrift wordt de theoretische achtergrond met betrekking tot dynamisch paal- en grondgedrag gepresenteerd, vergezeld van de respectievelijke numerieke ontwikkelingen. In het bijzonder wordt het dynamische paalgedrag besproken op basis van cilindrische schalen, volgens de eerste benaderingstheorieën van Love. Het grondmedium wordt beschreven als een lineair elastische gelaagde halve ruimte in termen van groene functies in het frequentie-ruimtedomein. Ten behoeve van de numerieke modellering worden in dit proefschrift kort de volgende ontwikkelingen geïntroduceerd: (i) de Semi-analytische Eindige Elementen Methode (SAFE) voor dunne/dikke cilindrische schalen, (ii) de Dunne-Lagen Methode (TLM) gekoppeld aan Perfectly Matched Layers (PMLs) voor gelaagde bodemhelften en (iii) een sequentiële Harmonic Balance Method (HBM) voor niet-lineaire dynamische systemen met quasi-periodiciteit. De voorgaande

schema's worden gekenmerkt door een opmerkelijke veelzijdigheid en rekenprestaties, en zijn tegelijkertijd toepasbaar op een brede reeks engineeringproblemen. Daartoe worden de relevante behandelingen zo algemeen en toegankelijk mogelijk gehouden, met het oog op een divers lezerspubliek.

Het experimentele werk volgt en omvat een van de belangrijkste hoogtepunten van dit proefschrift, namelijk de GDP-veldcampagne. Deze campagne omvatte zowel installatie- als post-installatieproeven met zijdelingse belasting. Om de doeltreffendheid van de GDP-methode aan te tonen werd een speciaal voor dit doel gebouwde GDP-schudder ontworpen en werd een middelgrote veldtestcampagne uitgevoerd op de locatie Maasvlakte II in Rotterdam. Na de succesvolle proof of concept was een primaire doelstelling van de veldproeven de vergelijking van GDP met twee conventionele technieken, namelijk impacthameren en axiaal trillen. Bovendien werd een uitgebreide dataset van paal- en bodemmetingen verzameld en gebruikt voor vergelijkingen en de ontwikkeling van numerieke modellen. Zowel de metingen van de heipalen als die van de bodemrespons leverden gunstige resultaten op voor GDP, wat de verdere ontwikkeling en opschaling ervan bevordert. Kortom, de veldcampagne gaf een eerste demonstratie van de GDP-technologie en de vergelijking tussen axiaal trillen en GDP toonde het gunstige effect van torsie aan.

Wat de installatie van trilpalen betreft, is een volledig begrip van de betrokken fysische mechanismen en de verwerking daarvan in effectieve engineeringgerichte modellen nog steeds ver te zoeken voor axiaal trillen. Daartoe worden de numerieke ontwikkelingen van dit proefschrift (d.w.z. SAFE en TLM+PMLs) geïntegreerd in een rekenkundig efficiënt model, dat de kloof tussen de beschikbare medium- en high-fidelity benaderingen moet overbruggen. De huidige benadering vermindert de fysische nadelen van de eerste, zonder de praktische en rekenkundige beperkingen van de tweede. De paal-bodem interactie wordt beheerst door een historisch afhankelijke wrijvingsinterface en een visco-elastisch tipmodel, terwijl het niet-lineaire probleem wordt opgelost door een nieuw HB-gebaseerd schema. De belangrijkste component van de bodemreactie blijkt overeen te komen met de schacht-wrijving, terwijl het erfelijke karakter ervan berust op een geheugenmechanisme gebaseerd op de accumulatie van belastingscycli; dit laatste effect wordt gewoonlijk wrijvingsmoeheid genoemd. Ten slotte worden de voorspellingen van de berijdbaarheid vergeleken met veldgegevens van de trilpaal van de campagne, wat het voorspellingspotentieel van het huidige model aantoont.

Het voorgaande modelkader wordt als basis gebruikt en verder ontwikkeld, met het oog op de analyse van de installatie van palen via het BBP. Met behulp van dit numerieke instrument wordt de interpretatie van veldwaarnemingen sterk vergemakkelijkt en wordt het aandrijfmechanisme van GDP begrepen. Uit de numerieke resultaten blijkt dat de heroriëntatie van de wrijvingskrachtvector het belangrijkste mechanisme van GDP is, dat de installatieprestaties sterk verbetert. Met name de hoogfrequente torsie verdrijft het grootste deel van de wrijving van de as in de omtrekrichting en de bodemreactie langs de penetratieas vermindert aanzienlijk, waardoor een snellere installatie en minder axiale aandrijfbelastingen mogelijk zijn. Er wordt een numeriek onderzoek uitgevoerd naar de geïnduceerde bodembeweging door axiale vibro-aandrijving en GDP, waarbij de laatste leidt tot minder verstoring van de omgeving en herverdeling van energie van SV-P naar SH-golven.

Voorspellingen van de heibaarheid zijn essentieel om het vermogen van een heimachine

te beoordelen om een paal tot op de beoogde indringdiepte te installeren en om te anticiperen op voorvallen met een hoog operationeel risico, zoals vroegtijdige paalweigering of paalloop. De rol van de hei-installatie kan niet genoeg worden benadrukt bij de bouw van offshore windparken, aangezien het installatieproces zelf een grote invloed heeft op zowel de vibro-akoestische als de post-installatieprestaties. Door middel van het huidige raamwerk wordt een weg naar een geïntegreerd ontwerp van de voorgaande aspecten mogelijk gemaakt. In dit proefschrift wordt een poging gedaan om de kloof tussen een medium- en high-fidelity benadering te overbruggen, om het paradigma van standaard engineering-georiënteerde kaders te verschuiven en de engineering-aspecten van duurzame monopile installatie te verbeteren.

Preface

This dissertation signifies the culmination of a remarkable journey for me. The doctoral research is a multi-faceted process and each individual experiences it in a dissimilar manner. In my view, the doctoral journey is a transformation process that an individual goes through in the pursuit of knowledge. Within the following pages, roughly spanning 200, the reader may delve into the intricacies pertaining to the topic of monopile installation, thus I deem it appropriate to omit any associated discussion in the ensuing. The following paragraphs are devoted to an indispensable element in the transformation process of a PhD, namely the people that this experience is shared with. Reminiscing any part of my PhD trajectory, it becomes evident to me that the people involved made it memorable, unique and most certainly impossible without their contribution. Therefore, the following part of this preface is dedicated to them, as a minor token of sincere appreciation and gratitude.

First, I would like to thank my PhD supervisors, with whom I have had the honor and privilege of working over the past four years. Apostolos, as my supervisor and mentor throughout my PhD journey, your guidance and support have been truly invaluable. Your unwavering motivation and encouragement have propelled me forward, while at the same time you provided me with absolute freedom and autonomy to shape my work. I am deeply grateful for your faith in me, starting from the very first day we embarked on this academic endeavour together. Andrei, you have been an endless source of inspiration for me, both as an academic and as an individual. Your intellectual prowess never ceases to astound me, while the more I have come to know you, the more I admire your remarkable character. The flourishing of our amazing research group, of which I am honoured to be a part, is the most tangible testament of your qualities. In summary, I am genuinely proud to have been a PhD student of both of you.

I would like to extend my heartfelt thanks to the individuals who comprised the GDP team, making the field campaign an incredible success. My sincere appreciation goes out to Ahmed, Faraz, Federico, Kees, Maxim, Rob and Sergio for their invaluable contributions. Their expertise, diligence, and collaborative spirit were instrumental in making this experimental campaign possible, and for that, I am immensely grateful. Sergio, we have spent a considerable amount of time working together following the completion of the GDP experiments. It is through this collaboration that I got to know you better and truly enjoyed our time spent together.

The contribution of my research group has been paramount in making my PhD journey immensely enjoyable and memorable. Our cherished coffee breaks, engaging group seminars, early-Monday Bright minds meetings, lively PSOR drinks, EM symposia, great conference trips and delightful Christmas dinners will remain etched in my mind, as they fostered a genuine group atmosphere that I will always treasure and reminisce. It is the remarkable individuals within this group who made these experiences truly special and unforgettable. Among these amazing people, special thanks go to my roommates Timo and Vagelis, for our enjoyable office atmosphere and mostly for tolerating my charming

presence the last four years.

My wonderful friends have played a significant role in the attainment of this milestone. I am immensely grateful to Annie, Giorgos, Ioanna, Konstantina, Thomas and Vagelis, whose presence in my life during my time in Delft has been truly invaluable. Your friendship is the first generous thing that life in Delft offered me and without you, this journey would have not been the same. My dear friends, Christos, Tasos and Thanasis, you have been my beloved company all these years, despite living in different countries and not being able to spend as much time together as we used to in the past. Every reunion with you invigorates me greatly and feels like coming home. You have a special place in my heart and I am certain that without you, I would not have made it this far. Lastly, Angeliki, you have been my guardian angel during these years and supported me in literally every aspect of my life. Being there in my best and worst moments, I cannot thank you enough for doing so with genuine care. Thank you wholeheartedly for being my friend. I look forward to cherishing many more significant moments with all of you in the future.

To my parents, Fotis and Varvara, and my little sister Kelly, thank you for your love and unconditional support all these years. As you know, I may not be the most expressive person, but I am deeply thankful for your understanding and support during my PhD and your unwavering encouragement throughout my life. In conclusion, there is a special person, who entered into my life in the beginning of this journey and became so much more over time. Elissavet, you have an innate understanding of me like no one else. To say that this achievement would not be possible without you is an understatement. I am not a talkative person, yet with you I can seamlessly discuss from the ideas of Plato and Nietzsche to wave propagation; this is happiness to me. Thank you for being in my life.

Finally, I would like to conclude these acknowledgements with two people, who have shaped my life. My grandfather, Alekos, passed away in the second month of my PhD; not a single person in this world would have been happier than him for this achievement. My grandmother, Kyriaki, is a person of great subtlety and exemplary character; there is no other individual who evokes such profound admiration and gratitude within me. I can say confidently that each step forward I have taken throughout my life would have been impossible without you. It is beyond doubt that this thesis is dedicated to you.

Athanasios Tsetas
Delft, July 2023

1

Introduction

1.1. Global energy outlook and renewables

The global endeavour towards the decarbonisation of the energy sector has been intensified in the past decades. A series of major international agreements between countries was initiated at the United Nations Conference on Environment and Development (UNCED), also known as the 'Earth Summit' in 1992 [1]. The United Nations Framework Convention on Climate Change (UNFCCC) was signed by the conference parties, aiming to stabilize the concentration of greenhouse gases in the atmosphere to preclude anthropogenic interference with the climate [2]. As a follow-up of UNFCCC, the Kyoto protocol was established in 1997; industrialized countries and economies in transition committed to adopt policies and measures to reduce greenhouse gases emissions [3]. The Kyoto Protocol was succeeded by the Paris agreement, an international treaty of 196 countries on climate change with the utmost goal to limit global warming and to achieve a climate-neutral world by the mid-century [4]. This series of international pledges was concluded with the Sustainable Development Goals (SDGs) established by the UN in 2015, not solely restricted to climate and energy-related actions, albeit interlinked [5].

In this framework of worldwide mobilization towards these common goals, it is essential to assess the current state and the future outlook of the energy sector. Global energy demand has been ceaselessly rising the previous decades and the future projections indicate that this trend will persevere [6]. Overall, investments and policies to meet the future energy demand and achieve the aforementioned sustainability targets are falling short [7, 8].

Presently, a consensus has been reached that renewable energy resources comprise a key feature to achieve the set climate objectives [9]. The share of renewables among the various energy sources has been growing tremendously over the past two decades [10, 8], with solar and wind energy being the front-runners in the energy transition. In accordance with the European Green Deal, Europe is leading the energy transition paradigm with the aim of becoming the first climate-neutral continent by 2050 [11]. Notwithstanding the notable increase in the deployment of renewables and the prodigious efforts towards decarbonisation, the data analysis indicates that we are falling behind with the necessary

investments to achieve the set climate targets [7, 8]. A short-term acceleration of the energy transition via a carbon tax has been proposed by a number of studies [12, 13, 7]. However, there is widespread consensus that investment in technological innovation constitutes the most efficient approach to reduce the cost of renewables and to mitigate the risk of policy volatility [14, 15, 9].

1.2. Engineering advancements in offshore wind energy – monopile installation

In the wind energy sector, the majority of newly installed capacity has been traditionally onshore [16]. In contrast to its onshore counterpart, that has been utilized for power generation for millennia, offshore wind energy is a recent technology with the first offshore wind farm installed in 1991 at Vindeby, Denmark [17]. However, the share of installed wind capacity that corresponds to offshore wind farms has increased rapidly during the last decade [16], aided by the vast experience of the oil and gas industry in offshore operations [18]. This notable increase of offshore wind projects compared to onshore projects is due to a multitude of advantages, e.g. the availability of vast areas for large offshore wind farms, the higher and steadier wind speeds encountered at the offshore environment and the elimination of visual and auditory nuisance [19, 20]. On the other hand, onshore wind remains the most economical solution among the renewables; the levelized cost of electricity (LCoE) is lower for onshore than offshore wind [21], yet the difference is declining [22]. Specifically, the costs of offshore foundations and installation are significantly higher than the respective costs for an onshore wind project.

Figure 1.1: Various concepts of offshore wind substructures based on water depth - after Smith et al. [23].

Presently, 15-24% of the investment for an offshore wind farm relates to the design, production and installation of substructures (see Fig. 1.1) [24]. In Europe, over 80% of the existing offshore wind turbines are hitherto founded on so-called monopile foundations [25, 26]. The design simplicity and robustness, the mass-fabrication aptness and the ease of installation constitute the major advantages of monopiles compared to other foundation concepts [27, 28, 15, 25, 26]. Accordingly, these foundations are growing in unprecedented sizes in the past years, as they are being employed in ever deeper waters and larger distances to the shore [26, 29]. Inevitably, the latter rapid development is accompanied by significant engineering challenges in the installation process.

During the installation phase, the monopile is driven into the seabed up to an adequate embedment depth that fulfils the various design criteria, e.g. lateral bearing capacity. The installation process, commonly known in the field of civil engineering as pile driving, is chiefly performed by means of an impact hammer [30, 31]. During impact pile driving, a hammer device is mounted on the pile head (see Fig. 1.2a) and upon the application of hundreds (or even thousands) hammer blows the pile penetrates into the seabed for tens of meters. This installation method, albeit robust and well-established, has raised concerns about its environmental impact [31]. Specifically, the stress waves excited in the monopile by the hammer impacts result in radial expansion of the pile surface; these waves propagate in supersonic speeds and the resultant sound waves radiate in the seawater in the form of Mach cones [32]. This topic has been extensively researched in the last decade and recent studies indicate that the noise emissions related to impact pile driving can lead to temporary habitat loss for aquatic species, as well as potential auditory damage to marine mammals [33, 34].

In response to these alarming concerns, regulatory bodies pose various criteria based on noise emissions for new offshore wind projects [35]. To comply with the various regulations, offshore wind industry is adopting a range of actions from noise mitigation strategies to alternative monopile installation methods. Noise mitigation strategies aim to reduce the noise levels caused by pile installation via the use of various barrier mechanisms, e.g. air bubble curtains [36–38], isolation casings [39] and resonator-based barriers [40]. However, the adoption of such noise mitigation measures can increase the installation costs appreciably and moves the energy sector further away from the ultimate goal of reducing the offshore wind energy LCoE [41].

In view of these constraints, alternative and environmentally friendly methods are investigated for monopile installation. The community of impact pile driving has proposed new alternatives to the traditional impact hammer approach, such as HiLo driving [42] and BLUE Piling [43]. The concept of piling with high (blow) frequency at low (impact) energy, the so-called HiLo driving was conceived in order to lower the noise emissions by reducing the amplitude of the impact. On the other hand, BLUE Piling technology utilizes a large water column to force the pile into the seabed; the resultant pulse from the BLUE Hammer is longer in duration and the energy content of the force input is shifted to lower frequencies compared to standard hammers. In essence, the aforementioned technologies operate on the same principles of impact piling, attempting to lower the input amplitude and/or to shift the energy content of the input force to lower frequencies.

Vibratory technology presents an interesting alternative to impact piling (see Fig. 1.2b), as it has been widely used in the onshore environment since the 1930s [44]. In principle,

(a) Hydrohammer S-90

(b) CV-25

Figure 1.2: (a) Impact hammer and (b) axial vibratory device mounted on the top of tubular piles from the GDP field campaign.

vibratory pile driving is considered to achieve quiet and fast installation via the application of low-amplitude (compared to impact) axial vibrations at the pile head [45, 46]. However, the widespread employment of the vibratory method in monopile installation is hindered by a number of factors, including the limited availability and inconclusiveness of field observations. Major knowledge gaps are also associated with the dynamic soil behaviour during vibratory driving [47] and the installation effects on the operational performance of the pile [48].

To boost the development of vibratory methods, a new technology – the Gentle Driving of Piles (GDP) – has been recently proposed in the Netherlands as the core of a joint industry project led by the Delft University of Technology (TU Delft) [49]. GDP targets enhanced piling performance and reduced noise emissions through the simultaneous application of low-frequency/axial and high-frequency/torsional vibrations. The major hypothesis of the method is that the introduction of torsion will enhance both installation and acoustic performances by reducing the axial driving loads, since it does not induce radial expansion in the pile. To that end, an experimental campaign has been executed at Maasvlakte II in the Port of Rotterdam (Fig. 1.3) and a series of numerical works has been undertaken to support the development of the GDP method [49–54].

1.3. State-of-the-art in pile installation modelling

Customarily, the operation of pile driving was based on simple empirical formulae until the 1960s, when Smith [55] developed the first pile driving model, in particular for impact piling. This model was based on a pile described as a thin rod and discretized into a series of lumped masses and springs, according to the central finite difference method of $\mathcal{O}(2)$. The soil reaction was represented by a rheological model comprised by an elastic-perfectly plastic element in parallel with a non-linear dashpot. Moreover, the parameters of this

Figure 1.3: The test site of the GDP field campaign at Maasvlakte II in the Port of Rotterdam.

soil reaction analogue were not related to standard soil properties, but comprised a set of empirical values initially proposed by Smith based on past field experience. Research efforts to improve Smith's model were undertaken promptly, given the significance of the approach for engineering practice. Early works in this direction focused on the experimental identification of the proposed soil parameters in Smith's model [56–60]. The aforementioned studies, albeit valuable, still were limited in the sense that the model parameters were mostly correlation coefficients that neglected the physics of pile driving that were yet to be understood.

The next frontier in the development of pile driving models addressed that aspect, with the aid of contributions originating in the area of earthquake engineering. Specifically, a multitude of pioneering works related to vibrations of foundations and soil-structure interaction were initiated in the 1960s with application to earthquake engineering and seismology [61–78]. From this class of studies, elements of pile-soil interaction modelling were incorporated into Smith's model, i.e. replacing Smith's empirical parameters with values that were derived by an approximate analytical treatment of pile-soil interaction problems [79, 66, 67]. A large collection of drivability models ensued upon this development, the so-called rational pile driving models [80–84]. A limited number of studies focused on the development of analytical models for the impact hammer, in order to facilitate further parametric studies and provide an efficient alternative to numerical modelling of the hammer component [85, 86]. Among recent studies, a more elaborate model that accounts explicitly for the non-linear soil stiffness has been presented by Salgado et al. [87] and has been employed for the derivation of pile driving formulas in sandy and clayey soil layers. In that approach, the near-field soil was modelled as a shear band at the pile-soil interface, connected with a thin disk characterized by a hyperbolic stress-strain relationship in series with an approximate far-field boundary condition.

In parallel to the above developments, the geotechnical community focused on the improvement of a critical parameter that all rheological soil models shared, namely the static resistance to driving (SRD), by utilizing the inflow of new data records [88–91]. Recent

advances in the assessment of the axial static capacity of piles based on extensive field tests have been valuable for that purpose [92, 93]. Even though these methods were not developed as SRD models, Byrne et al. [94] attempted to incorporate these CPT-based approaches in 1-D wave equation analyses. A modification factor was introduced in these CPT-based approaches and improved the respective predictions, which were found to be in good agreement with pile penetration records. However, the applicability of the SRD models in large-diameter monopiles remains questionable, as these approaches are largely empirical and their calibration has been performed based on databases of piles with diameters smaller than 2 m. In an extensive study by Byrne et al. [95], both the existing SRD models and the modified CPT-based approaches were proved not to provide reliable predictions of the blow counts.

The preceding works are dedicated to impact pile driving and employ 1-D models that are widely used in engineering practice. Naturally, vibratory driving approaches have adopted components of the impact piling models, as the latter preceded the developments in vibratory driving modelling. Even though the number of studies about vibratory driving is appreciably smaller compared to the respective ones about impact piling, there is substantial diversity in the models employed. As was stated above, the 1-D wave equation analysis was one of the first approaches employed in the analysis of vibratory pile driving, including both the original and modified versions of Smith's soil model [96–99]. In a recent study, Mazza and Holeyman [47] employed a 1-D model (ALLwave-VDP [100]) to back-analyse field data of vibratory driving. The authors concluded that inflow of additional data sets from field tests is necessary to improve the available models, as most of the empirical parameters in these approaches have been calibrated by impact pile driving databases and their values were found unsuitable for vibratory driving analysis.

Next to the 1-D wave equation analysis, a class of single-degree-of-freedom (SDoF) models was developed for vibratory driving and found wide acceptance in the community. In essence, these models were based on the assumption that the pile behaves as a rigid body during the vibratory installation process [44, 101–104]. The latest developments in these approaches have focused on the study of the input excitation [105] and the introduction of CPT-based soil reaction accounting for 'friction fatigue' [106]. An improvement to these engineering-oriented models was realized by 1-D radial models [107–109]. In the latter approach, a rigid pile is considered in contact with a series of concentric rigid cylinders representing the discretized soil medium; the transmitted forces between the adjacent cylinders and the pile followed a hypoplastic constitutive law [110, 111]. As can be understood, such a modelling approach precludes the possibility to address the soil layering explicitly, thus an averaging process of the soil properties over the depth is necessary (similarly to the SDoF models).

As computational methods advanced, the number of studies employing high-fidelity models for pile installation increased. Starting with impact pile driving, Smith and Chow [112] developed a finite element (FE) model for the analysis of pile installation in clayey soil. This study was among the first that aimed at enabling the use of standard soil properties in pile drivability analysis. One of the first main concerns in studies employing high-fidelity models was the development of large soil deformations in the immediate vicinity of the pile. In view of this challenge, the updated Lagrangian formulation of the finite element method (FEM) became the method of choice [113, 114]. In the latter studies, the developments in

soil constitutive modelling at the time were also utilized (i.e. bounding surface plasticity) [115, 116].

In the analysis of pushed-in piles, an updated Lagrangian FE model was used to study the installation process in clayey soil [117, 118]. The contact kinematics at the pile-soil interface permitted the formation of normal gap between the two bodies, while the tangential contact was described by Coulomb's friction law [119]. In the preceding studies, significant mesh distortion was encountered and the authors remarked that the use of an arbitrary Lagrangian-Eulerian (ALE) scheme is considered an effective remedy for this problem. An ALE formulation allows the decoupling of mesh and material points, although this process is amenable to numerical errors from the remeshing and mapping of state variables [120]. A numerical method, that falls into the category of ALE schemes, has been applied to the problem of pile jacking, namely the Material Point Method (MPM) [121, 120, 122]. The latter originates in the Particle-in-Cell (PiC) method, which was developed at the Los Alamos National Laboratory (LANL) for problems in fluid dynamics involving highly distorted flows [123–125]. Recently, the MPM has been also utilized to simulate cone penetration tests (CPTs) in dry sand [126].

During the last decade, an appreciable number of studies have focused on the problem of vibratory pile installation and the development of relevant computational schemes. As stated previously, the large deformations developed during pile installation lead to significant numerical issues, thus various approaches have been employed to tackle this challenge. Machaček et al. [127] used an updated Lagrangian formulation in a comparative study of three different soil models, namely two hypoplastic models [128, 129] and SANISAND [130–132], against lab-scale vibratory driving tests and element tests. A total Lagrangian formulation has been employed in numerical studies focusing on the comparison of pile penetration with lab-scale experiments [133, 134], as well as in investigating the influence of the relative acceleration between the solid and the water phases in saturated sands [135]. Conclusively, Staubach et al. [136] developed a hydromechanically Coupled-Eulerian-Lagrangian (CEL) method, which was applied to the back-analysis of vibratory pile tests in saturated sand; good agreement was found between the CEL and the total Lagrangian formulations.

1.4. Research scope

As can be understood from the preceding review, a multitude of approaches is available for pile drivability analysis. Notwithstanding that certain connections are apparent between the various frameworks, the different types of installation (e.g. impact, vibratory, jacking) are fundamentally driven by dissimilar physical mechanisms. The latter is strongly reflected in the medium-fidelity approaches - hereafter also termed as engineering-oriented - where the pile and soil reaction modelling may vary to a great degree for different driving methods. In the following, the scope of this thesis is focused on the aspect of engineering-oriented modelling for pile driving via vibratory and GDP methods, with a view to further support sustainable monopile installation.

Vibratory driving predictions are essential to assess the capability of a driving device to install a pile in a certain soil profile to the target penetration depth, as well as to anticipate and prevent occurrences that engender great risk for the operation or even the overall project, e.g. early pile refusal or pile running. However, it is noted that reliable drivability

predictions for offshore monopiles are not solely valuable per se, but they provide valuable input for other design stages. In particular, two major aspects of offshore monopiles rely heavily on the installation process, i.e. the underwater noise emissions during installation and the lateral response of the structure during operation. Both aspects are studied during the design phase and their output depends on the proper analysis of the installation process (either in an integrated or a two-step approach). Therefore, drivability of offshore monopiles may greatly affect various design stages and its significance cannot be overemphasized.

As regards medium-fidelity approaches, their main drawback lies in their (semi-)empirical character, leading to insufficient description of the physical process (and by extension inaccuracy). Customarily, medium-fidelity models possess a simplistic pile description (e.g. 1-D rod) and almost exclusively disregard pile-soil interaction, by employing local, frequency-independent soil reaction analogues (due to simplicity and ease of implementation). The existing approaches have already been found inadequate for impact piling of large-diameter monopiles [95], whereas for vibratory driving an established approach cannot even be distinguished. In particular, comprehensive understanding of the physical mechanisms involved and their incorporation into effective engineering-oriented models are still elusive for vibro-driving. In view of the above, an endeavour to bridge the gap between medium- and high-fidelity approaches is undertaken, to shift the paradigm of standard engineering-oriented approaches and better the engineering aspects of monopile installation.

In this thesis, the research objectives are accomplished via the execution of an experimental campaign and the development of numerical models for pile installation analysis. The former serves to better understand pile installation via vibratory and GDP techniques with the aid of the collected data, which in turn will be utilized for model calibration and validation purposes. The numerical developments introduced in this thesis are briefly: i) the Semi-analytical Finite Element (SAFE) method for thin/thick cylindrical shells, ii) the Thin-Layer Method (TLM) coupled with Perfectly Matched Layers (PMLs) for layered soil half-spaces and iii) the Harmonic Balance Method (HBM) for non-linear dynamical systems. These approaches - characterized by remarkable versatility and computational performance - pertain to semi-analytical and numerical methods applicable to a wide set of engineering problems. For that purpose, the relevant sections are retained as generic and accessible as possible, in order to benefit the readership from diverse communities to the greatest degree.

Conclusively, the first and primary aim of this thesis is the development of a methodology for the analysis of vibratory pile installation, that encompasses the mathematical formulation, the process of parameter calibration based on *in-situ* measurements and the implementation of a high-performance numerical scheme for engineering purposes. As a continuation of this objective, the potential extension of this numerical framework is pursued to analyse the installation process via GDP and decipher its main driving mechanisms; the latter task is considered the ultimate aim of this thesis.

1.5. Thesis outline

Following the present introduction chapter, the vibrations of thin-walled cylindrical structures are studied in Chapter 2, with a view to large-diameter monopiles. The first approximation theory for thin shells is outlined, as the optimal choice for the analysis of these tubular structures. Wave propagation and dispersion characteristics of thin-walled cyl-

indrical structures are briefly discussed on the basis of different theories. Subsequently, a Semi-analytical Finite Element (SAFE) model is developed, with the aim of facilitating the study of thin (and thick) cylindrical shell vibrations in this thesis.

The focus of Chapter 3 lies on the study of two physical mechanisms present in pile installation and their significance for large-diameter monopiles, namely dispersion of elastic waves and non-local soil reaction. The former mechanism is addressed by description of the pile as a thin cylindrical shell, whereas the latter is achieved by introducing non-local kernel functions to the standard local reaction analogues. The results of this study showcase that physically sound pile description is pivotal for accurate drivability predictions, since wave dispersion becomes more prominent with increasing pile diameter and larger impact hammers. As regards the soil reaction, the adopted formulation is neither rigorously based on a 3-D soil medium, nor possesses temporal non-locality (i.e. frequency dependence), thus the direct treatment of the 3-D soil continuum is considered the optimal next step.

To realize the preceding objective, a discourse on wave propagation in linear elastic layered media is presented in Chapter 4. A framework that can seamlessly treat arbitrarily layered soil media is indispensable with regard to pile installation analysis. In view of this challenge, the Thin-Layer Method (TLM) is utilized to eradicate the formidable complications introduced by soil layering. Specifically, explicit expressions of Green's functions for ring sources are obtained by means of a normal modes approach in the context of the TLM. Furthermore, a more recent formulation of the previous method, i.e. coupled with Perfectly Matched Layers (PMLs), is employed for the approximate representation of the underlying half-space. With these developments, the theoretical background that pertains to the ensuing chapters has been presented along with the respective numerical approaches.

Chapter 5 focuses on the pile installation tests of the GDP field campaign and elucidates on the motivation for this research work, namely the demand for sustainable methods of offshore monopile installation. To contribute towards the latter objective, a new vibratory installation technique has been recently proposed by TU Delft, namely the 'Gentle Driving of Piles' (GDP) method. The founding principles of the method and the purpose-built GDP shaker are first presented. Furthermore, the geotechnical characterisation of the test site is outlined, with the main body of the chapter discussing the installation tests of vibro-driven and GDP piles. The comparison between piling data associated with classical vibratory driving and GDP showcases the beneficial effect of torsion and the potential of the proposed installation technology.

In Chapter 6, the numerical developments of the preceding chapters are integrated into a vibratory pile driving model, that aims to bridge the gap between the available medium- and high-fidelity modelling approaches. A numerical framework is proposed that significantly reduces the simplifications and empirical components of the former and alleviates the practical and computational impediments of the latter. The pile-soil coupling is realized through a history-dependent frictional interface and a visco-elasto-plastic tip reaction model, both characterized by standard *in-situ* geotechnical tests (SCPT-based). For the numerical solution, a hybrid time-frequency scheme is presented based on sequential application of the Harmonic Balance Method (HBM). Finally, installation data from the GDP campaign are compared with model predictions - showcasing its predictive capabilities - and further investigation into certain aspects of the vibratory installation process is performed.

To further support and interpret the field observations from the GDP campaign, numer-

ical modelling work is imperative in order to comprehend the main driving mechanisms. For that purpose, the developed vibratory pile installation model is augmented in Chapter 7 to formulate a GDP framework. Numerical simulations lead to deciphering the mechanics of the GDP method, the main novel contribution of this chapter. Specifically, the redirection of the friction force vector emerges as the major driving mechanism of GDP, as it enhances installation performance by greatly reducing the soil reaction along the penetration axis. Conclusively, a case study is performed to compare the axial vibratory and GDP methods in terms of induced soil motion, showcasing abatement of environmental disturbance for GDP by elicitation of SH waves and reduction of the SV-P wavefield.

Conclusively, Chapter 8 summarises the major findings of this thesis, accompanied by recommendations for further research.

2

Vibration of thin cylindrical shells

Customarily, pile drivability models adopt simplified approaches that consider the pile foundation either as a 1-D thin rod or even as a rigid body (mostly in vibratory driving). The validity of such modelling choices depends naturally on the pile geometry and the frequency range of the structural response. For slender small-diameter piles, that have been the industry standard in offshore engineering applications in the past, the thin rod approximation constitutes indeed an appropriate engineering model for drivability purposes. However, the growth of offshore wind in the past two decades has prompted the re-assessment of current design approaches with the advent of large-diameter monopiles. These large tubular structures fairly raise a concern about the capability of standard 1-D models to sufficiently capture their response during installation. With a view to thin-walled cylindrical structures (e.g. tubular monopiles), a thin shell theory is considered the optimal choice for a physically accurate and computationally efficient pile model.

In this chapter, the interest lies in the vibrations of thin-walled cylindrical structures. As a point of departure, the first approximation theory for thin cylindrical shells is discussed, based on Love's postulates that form the theoretical basis for the shell governing equations. The propagation of harmonic waves in a thin cylindrical shell is studied in a brief, yet concise manner, with a focus on wave dispersion in comparison with other associated structural theories. Subsequently, the focus is placed on free vibrations of finite shells - inherently connected to wave propagation - and the mathematical process to obtain the shell normal modes is outlined. Conclusively, a Semi-analytical Finite Element (SAFE) model is presented and validated, with the aim of facilitating the numerical modelling of thin/thick cylindrical shells.

2.1. Love's first approximation shell theories

A three-dimensional solid that is bounded by two closely-spaced curved surfaces is defined as a shell [137]. The engineering theories used to describe these bodies, in lieu of three-dimensional elasticity, are categorized into thin and thick shell theories [138]. This distinction is based on the thickness of the shell compared to its other characteristic dimensions.

The dynamic behaviour of thin shells is decomposed into extensional and bending parts, whereas the effects of shear deformation and rotary inertia are neglected [139]. The theoretical framework for the study of thin shells under small displacements is founded on Love's postulates [140]. The shell theories derived in accordance with these four assumptions are defined as Love's first approximation theories. In the ensuing, the vibrations of cylindrical shells will be studied based on Love's first approximation theories, with a view to the shell structures of our interest, i.e. tubular (mono)piles.

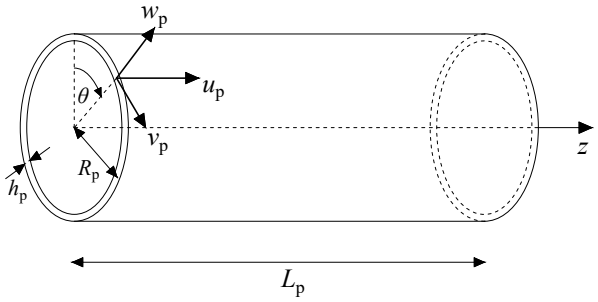

Figure 2.1: Geometry and coordinate system of a cylindrical shell.

A uniform thin cylindrical shell is considered, with finite length L_p, mid-surface radius R_p, and wall thickness h_p, as shown in Fig. 2.1. The shell is comprised of linear isotropic elastic material with Young's modulus E_p, Poisson's ratio ν_p and mass density ρ_p. The displacement components of any material point on the shell satisfy the Kirchhoff hypothesis [141] (one of the four Love's postulates) for any first approximation shell theory and are defined as [139]:

$$u_{z,\mathrm{p}}(r,\theta,z,t) = u_\mathrm{p}(\theta,z,t) + \left(r - R_\mathrm{p}\right)\beta_z(\theta,z,t) \tag{2.1a}$$

$$u_{\theta,\mathrm{p}}(r,\theta,z,t) = v_\mathrm{p}(\theta,z,t) + \left(r - R_\mathrm{p}\right)\beta_\theta(\theta,z,t) \tag{2.1b}$$

$$u_{r,\mathrm{p}}(r,\theta,z,t) = w_\mathrm{p}(\theta,z,t) \tag{2.1c}$$

where u_p, v_p, w_p are the mid-surface displacement components ($r = R_\mathrm{p}$) with the shell occupying radially the domain $R_\mathrm{p} - h_\mathrm{p}/2 \leq r \leq R_\mathrm{p} + h_\mathrm{p}/2$. The rotations of the normal to the mid-surface about the θ and z axes are denoted by β_z and β_θ, respectively, and read [139]:

$$\beta_z = -\frac{\partial w_\mathrm{p}}{\partial z} \tag{2.2a}$$

$$\beta_\theta = \frac{1}{R_\mathrm{p}}\left(v_\mathrm{p} - \frac{\partial w_\mathrm{p}}{\partial \theta}\right) \tag{2.2b}$$

As can be seen in Eq. (2.2), the shell rotations are fully determined by the mid-surface displacement components. In the case of thick shells, these two rotations are unknown as

well, thus the equations of motion increase in number (from three to five) and the governing equations become much more complicated [142, 143].

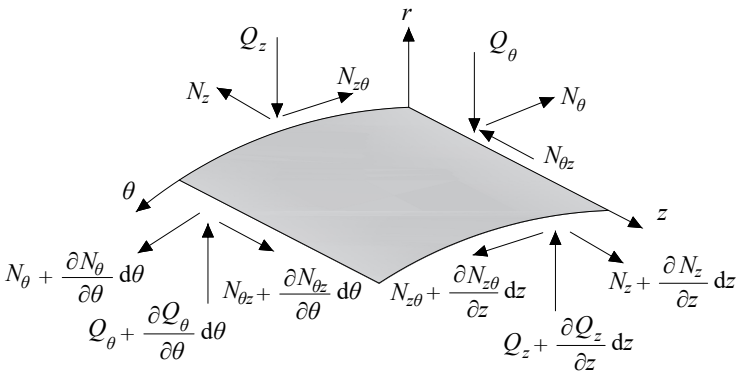

Figure 2.2: Force resultants in a thin cylindrical shell element.

Even amongst the first approximation theories a multitude of discrepancies can be found in their governing equations, due to different assumptions and/or the point at which these assumptions are introduced in the derivation process. The equations of motion in force/moment resultant form are common for all first approximation shell theories and read [144]:

$$\frac{\partial N_z}{\partial z} + \frac{1}{R_\mathrm{p}} \frac{\partial N_{\theta z}}{\partial \theta} + p_{z,\mathrm{p}} = \rho_\mathrm{p} h_\mathrm{p} \frac{\partial^2 u_\mathrm{p}}{\partial t^2} \tag{2.3a}$$

$$\frac{\partial N_{z\theta}}{\partial z} + \frac{1}{R_\mathrm{p}} \frac{\partial N_\theta}{\partial \theta} + \frac{Q_\theta}{R_\mathrm{p}} + p_{\theta,\mathrm{p}} = \rho_\mathrm{p} h_\mathrm{p} \frac{\partial^2 v_\mathrm{p}}{\partial t^2} \tag{2.3b}$$

$$\frac{\partial Q_z}{\partial z} + \frac{1}{R_\mathrm{p}} \frac{\partial Q_\theta}{\partial \theta} - \frac{N_\theta}{R_\mathrm{p}} + p_{r,\mathrm{p}} = \rho_\mathrm{p} h_\mathrm{p} \frac{\partial^2 w_\mathrm{p}}{\partial t^2} \tag{2.3c}$$

where N_z, N_θ, $N_{z\theta}$ and $N_{\theta z}$ are the in-plane force resultants, Q_z and Q_θ are the transverse shear force resultants and $p_{z,\mathrm{p}}$, $p_{\theta,\mathrm{p}}$ and $p_{r,\mathrm{p}}$ are the external surface loads. In Fig. 2.2, the force resultants are shown acting on a differential shell element. Equations (2.3a) to (2.3c) describe the dynamic force equilibria for a thin cylindrical shell, which are supplemented

by three dynamic moment equilibria as follows [144]:

$$\frac{\partial M_z}{\partial z} + \frac{1}{R_\mathrm{p}}\frac{\partial M_{\theta z}}{\partial \theta} - Q_z = 0 \tag{2.4a}$$

$$\frac{\partial M_{z\theta}}{\partial z} + \frac{1}{R_\mathrm{p}}\frac{\partial M_\theta}{\partial \theta} - Q_\theta = 0 \tag{2.4b}$$

$$N_{z\theta} - N_{\theta z} - \frac{M_{\theta z}}{R_\mathrm{p}} = 0 \tag{2.4c}$$

where M_z, $M_{\theta z}$, $M_{z\theta}$ and M_θ denote the moment resultants (see Fig. 2.3). In principle, Eqs. (2.4a) and (2.4b) are substituted in Eqs. (2.3b) and (2.3c), while Eq. (2.4c) is identically satisfied by virtue of the symmetry of the stress tensor, i.e. $\tau_{z\theta,\mathrm{p}} = \tau_{\theta z,\mathrm{p}}$. Therefore, the number of equations of motion that govern the vibrations of thin cylindrical shells may be ultimately reduced to three. Equations (2.3a) to (2.4c) are widely accepted as the equations of motion for thin cylindrical shells [139] and have been derived either by direct formulation of force/moment resultant equilibria (Newtonian approach) [145] or by application of Hamilton's principle (variational approach) [137]. Finally, it is remarked that neither $N_{z\theta} = N_{\theta z}$ nor $M_{z\theta} = M_{\theta z}$ is implied by the symmetry of the stress tensor invoked above; the equivalence of these force and moment resultants may or may not hold depending on the shell theory under consideration.

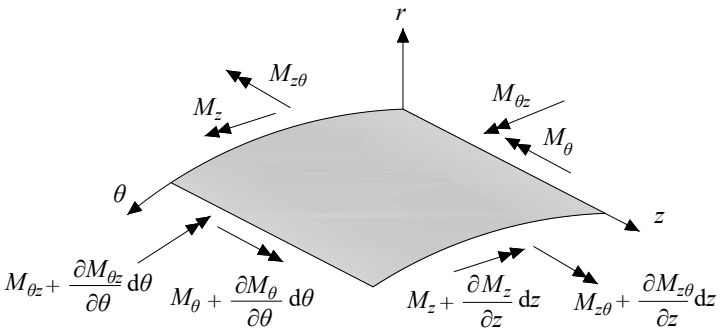

Figure 2.3: Moment resultants in a thin cylindrical shell element.

The last set of governing equations that are valid for any first approximation shell theory corresponds to the constitutive relations. On the condition that the study is restricted to linear elastic isotropic shells, the stress-strain equations for any first approximation theory

read:

$$\sigma_{z,\mathrm{p}} = \frac{E_\mathrm{p}}{1-\nu_\mathrm{p}^2}\left(\varepsilon_{z,\mathrm{p}} + \nu_\mathrm{p}\varepsilon_{\theta,\mathrm{p}}\right) \tag{2.5a}$$

$$\sigma_{\theta,\mathrm{p}} = \frac{E_\mathrm{p}}{1-\nu_\mathrm{p}^2}\left(\varepsilon_{\theta,\mathrm{p}} + \nu_\mathrm{p}\varepsilon_{z,\mathrm{p}}\right) \tag{2.5b}$$

$$\tau_{z\theta,\mathrm{p}} = \tau_{\theta z,\mathrm{p}} = \frac{E_\mathrm{p}}{2\left(1+\nu_\mathrm{p}\right)}\gamma_{z\theta,\mathrm{p}} \tag{2.5c}$$

while the remaining components of the stress tensor $\tau_{zr,\mathrm{p}}$, $\tau_{\theta r,\mathrm{p}}$ and $\sigma_{r,\mathrm{p}}$ are considered equal to zero, in accordance with Love's postulates.

The remaining sets of governing equations correspond to the kinematic relations - relating the strain tensor to the shell displacement field - and the force/moment resultants, that are derived from the integration of stresses along the shell thickness. Based on the chosen shell theory, different relations and assumptions at various stages of the derivations are adopted; yet all the relations given up to this point are applicable to any first approximation shell theory one may employ.

2.2. Wave propagation in thin-walled cylindrical structures

In this section, the propagation of harmonic waves in a thin-walled cylindrical structure, e.g. a (mono)pile, is studied. In general, this topic has attracted significant research interest from the middle of the 20th century up to the present, as thin and/or thick shells constitute major structural elements in applications pertaining to aerospace, biomedical, civil and marine engineering. In particular, the dispersion characteristics of thin cylindrical shells have been studied for various configurations, for instance: (i) *in vacuo* cylindrical shells [146–148], (ii) cylindrical shells supported by an elastic foundation [149–151], (iii) cylindrical shells immersed and/or surrounded by fluid [152–154].

For any thin shell theory, the equations of motion of a cylindrical shell *in vacuo* can be written in the following compact form [139]:

$$\left(\mathscr{L}_\mathrm{DM} + k_\mathrm{p}\,\mathscr{L}_\mathrm{MOD}\right)\begin{bmatrix} u_\mathrm{p} \\ v_\mathrm{p} \\ w_\mathrm{p} \end{bmatrix} = \begin{bmatrix} 0 \\ 0 \\ 0 \end{bmatrix} \tag{2.6}$$

where $\mathscr{L}_\mathrm{DM}$ denotes the differential matrix operator that corresponds to the Donnell-Mushtari shell theory [155–157] and $\mathscr{L}_\mathrm{MOD}$ denotes a modification differential matrix operator. Based on the Donnell-Mushtari theory, $\mathscr{L}_\mathrm{DM}$ is defined as follows:

$$\mathscr{L}_{\mathrm{DM}}(\cdot) = \begin{bmatrix} R_\mathrm{p}^2\dfrac{\partial^2(\cdot)}{\partial z^2} + \dfrac{(1-\nu_\mathrm{p})}{2}\dfrac{\partial^2(\cdot)}{\partial\theta^2} & R_\mathrm{p}\dfrac{(1+\nu_\mathrm{p})}{2}\dfrac{\partial^2(\cdot)}{\partial z\partial\theta} & \nu_\mathrm{p}R_\mathrm{p}\dfrac{\partial(\cdot)}{\partial z} \\ R_\mathrm{p}\dfrac{(1+\nu_\mathrm{p})}{2}\dfrac{\partial^2(\cdot)}{\partial z\partial\theta} & R_\mathrm{p}^2\dfrac{(1-\nu_\mathrm{p})}{2}\dfrac{\partial^2(\cdot)}{\partial z^2} + \dfrac{\partial^2(\cdot)}{\partial\theta^2} & \dfrac{\partial(\cdot)}{\partial\theta} \\ \nu_\mathrm{p}R_\mathrm{p}\dfrac{\partial(\cdot)}{\partial z} & \dfrac{\partial(\cdot)}{\partial\theta} & (1+k_\mathrm{p}\nabla^4)(\cdot) \end{bmatrix} - \frac{R_\mathrm{p}^2}{c_\mathrm{p}^2}\frac{\partial^2(\cdot)}{\partial t^2}\begin{bmatrix} 1 & 0 & 0 \\ 0 & 1 & 0 \\ 0 & 0 & -1 \end{bmatrix} \tag{2.7}$$

where $k_\mathrm{p} = h_\mathrm{p}^2/(12R_\mathrm{p}^2)$ is a non-dimensional thickness parameter, $c_\mathrm{p} = \sqrt{E_\mathrm{p}/(\rho_\mathrm{p}(1-\nu_\mathrm{p}^2))}$ is the (longitudinal) thin plate wave velocity and $\nabla^4(\cdot) = R_\mathrm{p}^4\partial^4(\cdot)/\partial z^4 + 2R_\mathrm{p}^2\partial^4(\cdot)/(\partial z^2\partial\theta^2) + \partial^4(\cdot)/\partial\theta^4$.

The differential matrix operator $\mathscr{L}_{\mathrm{MOD}}$ can lead to any other first approximation shell theory by extending the Donnell-Mushtari theory. A comprehensive review of various thin shell theories can be found in Leissa [139], with focus on free vibrations and relevant theoretical and experimental studies. In the ensuing, the so-called Love-Timoshenko thin shell theory is considered [158, 140, 159], for which $\mathscr{L}_{\text{MOD-LT}}$ is defined as [139]:

$$\mathscr{L}_{\text{MOD-LT}}(\cdot) = \begin{bmatrix} 0 & 0 & 0 \\ 0 & R_\mathrm{p}^2(1-\nu_\mathrm{p})\dfrac{\partial^2(\cdot)}{\partial z^2} + \dfrac{\partial^2(\cdot)}{\partial\theta^2} & -R_\mathrm{p}^2\dfrac{\partial^3(\cdot)}{\partial z^2\partial\theta} - \dfrac{\partial^3(\cdot)}{\partial\theta^3} \\ 0 & -R_\mathrm{p}^2(2-\nu_\mathrm{p})\dfrac{\partial^3(\cdot)}{\partial z^2\partial\theta} - \dfrac{\partial^3(\cdot)}{\partial\theta^3} & 0 \end{bmatrix} \tag{2.8}$$

To study the propagation of harmonic waves the following generic solution is assumed:

$$u_\mathrm{p} = A\cos(n\theta)\mathrm{e}^{-\mathrm{i}\gamma z}\mathrm{e}^{\mathrm{i}\omega t} \tag{2.9a}$$

$$v_\mathrm{p} = B\sin(n\theta)\mathrm{e}^{-\mathrm{i}\gamma z}\mathrm{e}^{\mathrm{i}\omega t} \tag{2.9b}$$

$$w_\mathrm{p} = C\cos(n\theta)\mathrm{e}^{-\mathrm{i}\gamma z}\mathrm{e}^{\mathrm{i}\omega t} \tag{2.9c}$$

where γ is the axial wavenumber, n is the circumferential mode number and A, B and C are constant coefficients. The wave solution given in Eq. (2.9) corresponds to a symmetric waveform with respect to $\theta = 0$; an anti-symmetric waveform can be prescribed by interchanging sines and cosines in Eq. (2.9). Henceforth, the terms symmetric and anti-symmetric configuration will correspond to the preceding definitions.

Upon substitution of Eq. (2.9) into Eq. (2.6), the free vibration problem is recasted as a system of algebraic equations:

$$\begin{bmatrix} L_{11} & L_{12} & L_{13} \\ L_{21} & L_{22} & L_{23} \\ L_{31} & L_{32} & L_{33} \end{bmatrix}\begin{bmatrix} A \\ B \\ C \end{bmatrix} = \begin{bmatrix} 0 \\ 0 \\ 0 \end{bmatrix} \tag{2.10}$$

where the matrix $\mathbf{L}_{\mathrm{LT}}$ is populated with entries L_{ij}, following from the Love-Timoshenko theory. The latter system possesses a non-trivial solution that leads to the dispersion equation for a thin cylindrical shell:

$$\det(\mathbf{L}_{\mathrm{LT}}) = 0 \tag{2.11}$$

At this stage, a distinction is made between two different types of motion, namely axisymmetric ($n = 0$) and non-axisymmetric motion ($n > 0$). A mechanical system (e.g. cylindrical shell) that is symmetric around the longitudinal axis z and its input excitation, initial and boundary conditions possess the same symmetry is called axisymmetric, i.e. no variation along the azimuth is present in the problem ($\partial(\cdot)/\partial\theta = 0$). In the general case of non-axisymmetric motions, Eq. (2.11) becomes an eighth-order polynomial of the axial wavenumber γ (for a given frequency ω) and all three displacement components are coupled [160, 147]. However, under axisymmetric conditions a decoupling occurs and the shell displacement field can be decomposed into two parts, i.e. a coupled axial-radial and a purely circumferential part. The former can be obtained by substituting Eq. (2.9) into Eq. (2.6), while the latter is based on the anti-symmetric configuration of Eq. (2.9); in both cases $n = 0$. Furthermore, this decoupling leads to a sixth-order dispersion equation for the axial-radial wave motion and a second-order dispersion equation for the purely circumferential wave motion.

The focus of the ensuing study is restricted to the propagation of axisymmetric longitudinal waves in a thin-walled cylindrical structure. Customarily, the thin rod approximation may be the first option to describe the one-dimensional wave propagation in a long and thin structural member, by assuming a uni-axial stress state [161]. For a thin cylindrical shell, the propagation of longitudinal waves under axisymmetric conditions ($n = 0$ and symmetric waveform) is governed by the following dispersion equation:

$$k_{\mathrm{p}} R_{\mathrm{p}}^2 c_{\mathrm{p}}^4 \gamma^6 - k_{\mathrm{p}} R_{\mathrm{p}}^2 \omega^2 c_{\mathrm{p}}^2 \gamma^4 + \left(\frac{c_{\mathrm{p}}^4 (1 - \nu_{\mathrm{p}}^2) - R_{\mathrm{p}}^2 \omega^2 c_{\mathrm{p}}^2}{R_{\mathrm{p}}^2} \right) \gamma^2 + \left(\omega^4 - \frac{\omega^2 c_{\mathrm{p}}^2}{R_{\mathrm{p}}^2} \right) = 0 \tag{2.12}$$

In Figs. 2.4 and 2.5, the dispersion curves in the frequency-wavenumber plane are presented for longitudinal waves in a thin rod, flexural waves in a thin plate and coupled longitudinal-flexural waves in a thin cylindrical shell. The properties of the thin cylindrical shell considered in this example are given in Table 2.1. Branch 1 of the cylindrical shell is in agreement with the non-dispersive branch of longitudinal waves in a thin rod up to approximately $\omega/\omega_{\mathrm{r}} = 0.8$, where $\omega_{\mathrm{r}} = c_{\mathrm{p}}/R_{\mathrm{p}}$ denotes the ring frequency of the cylindrical shell (see Fig. 2.4). The harmonic waves corresponding to the aforementioned region of branch 1 possess a dominant axial component and minor radial displacements. For this type of waves, the thin rod approximation is customarily employed in long structural members assumed to be in a uni-axial stress state [161]. For frequencies higher than the ring frequency, the thin rod approaches branch 3 of the shell, where the wave motion is once again axially dominated. However, as can be seen there are certain limitations to that theory, since other motions are present as well. In the vicinity of the ring frequency, the phase wave velocity of branch 1 is significantly reduced and asymptotically approaches that of the thin plate theory in high frequencies and wavenumbers [162]. This behavioural transition in

branch 1 is accompanied by an interchange of the dominant displacement component, i.e. radial motion becomes dominant resembling indeed propagation of flexural waves in a thin plate. Therefore, waves of small wavelengths compared to the radius of the cylindrical shell propagate almost identically in a cylindrical shell and in a thin plate, since the curvature has a negligible effect - effectively the cylindrical shell tends to guide these waves as a thin plate. As regards Fig. 2.5, the imaginary part of the dispersion curves for the thin cylindrical shell are presented. It is remarked that the imaginary parts of the thin rod dispersion curve and the thin plate branch (see Fig. 2.4) are omitted in Fig. 2.5, as they are equal to zero.

ρ_p [kg/m^3]	E_p [Pa]	ν_p [-]	L_p [m]	R_p [m]	h_p [m]
7850	$210{\cdot}10^9$	0.3	10	0.373	0.0159

Table 2.1: Geometrical and material properties of the thin cylindrical shell considered in this study.

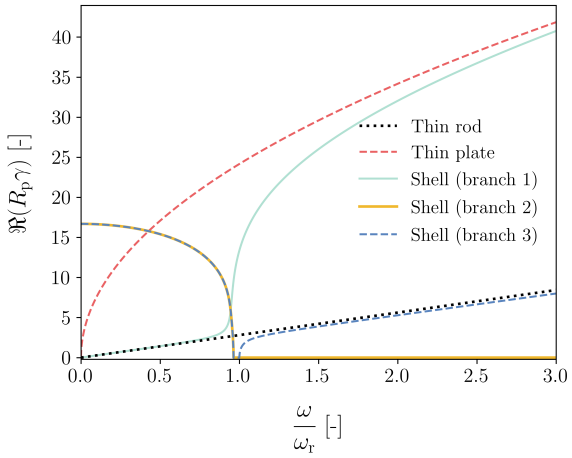

Figure 2.4: Comparison of dispersion curves between a thin rod, a thin plate and a thin cylindrical shell (real part).

Based on the preceding discussion, the dynamics of a thin-walled cylindrical structure (above a certain frequency and/or wavenumber) cannot be adequately described by the thin rod approximation. The latter, also known as elementary theory, comprises a good approximation for disturbances with long wavelengths and low frequencies [163]. Various engineering theories have been proposed to improve the dispersion characteristics of the elementary rod theory and to retain its one-dimensional character, by addressing effects that the thin rod approximation neglected. Rayleigh [164] proposed a correction to improve the thin rod approximation, by taking into account the lateral inertia arising from the contraction and the expansion of the cross-section. The equations of motion for the latter theory were arrived at by Love [140] via Hamilton's principle; accordingly, the said theory is customarily stated as Rayleigh-Love rod theory [163]. Following these developments, the shear stiffness was also introduced on top of the lateral inertia by Bishop [165]. However, none of the preceding approximate theories describes accurately the wave propagation in the

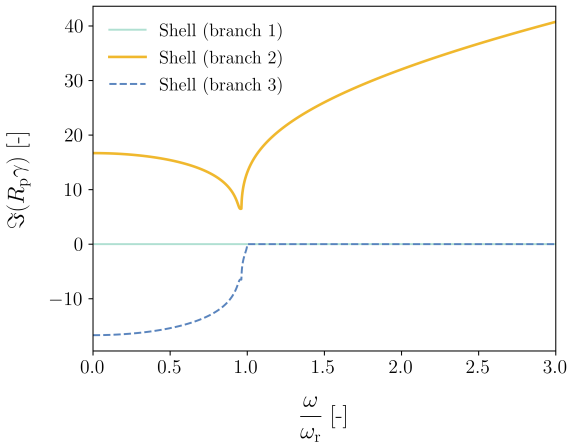

Figure 2.5: Dispersion curves of a thin cylindrical shell (imaginary part).

vicinity of the ring frequency and above. Meijers et al. [166] presented a corrected rod theory that resembles the Rayleigh-Love rod theory, albeit modified such that it approximates the low-frequency dispersion branch of the membrane shell theory. The latter comprises a good approximation for longitudinal waves up to the ring frequency, albeit flexural waves above the ring frequency are not adequately captured.

The thin shell theory may be considered the best engineering approximation for the description of axisymmetric wave propagation in a thin-walled cylindrical structure. The theoretical investigations to substantiate the latter statement have been carried out, by comparing the dispersion curves of thin shell theory against the respective ones derived in the context of three-dimensional elasticity [167–170]. As shown by Le [171], the agreement of three-dimensional elasticity with shell theory is remarkable for axisymmetric wave propagation up to a certain wavenumber; above that threshold discrepancy is observed in the branch corresponding to flexural waves. The ratio $h_\mathrm{p}/R_\mathrm{p}$ constitutes the controlling parameter that may assist in considering whether a thin or thick shell theory is appropriate for the problem at hand [138]. However, in the case of short-wavelength motions that invalidate the linear variation of the displacement field along the shell thickness, neither thin nor thick shell theories are applicable.

2.3. Free vibration of thin cylindrical shells

For engineering applications, the free vibrations of cylindrical shells have been studied extensively and various approaches have been employed to address this classical problem. The preponderance of studies on this topic have employed approximate methods such as differential quadrature [172, 173], the Rayleigh-Ritz method in conjunction with beam functions [174–177] and other standard numerical methods (e.g. finite differences, finite elements) [139]. The main reason for the use of approximate methods in the previous studies appears to be the mathematical complexity of the exact procedure [139]. The exact solution method for the free vibration problem of thin cylindrical shells was developed by Flügge

[178], albeit its numerical implementation was realized at a later stage following the advent of computers [160, 179, 180].

Following the exact solution method as outlined by Flügge [181], the displacement components of the j-th free vibration mode may be expressed as follows:

$$u_{\mathrm{p}}(\theta, z, t) = \cos(n\theta) U_{nj}(z) \mathrm{e}^{\mathrm{i}\omega_{nj} t} \tag{2.13a}$$

$$v_{\mathrm{p}}(\theta, z, t) = \sin(n\theta) V_{nj}(z) \mathrm{e}^{\mathrm{i}\omega_{nj} t} \tag{2.13b}$$

$$w_{\mathrm{p}}(\theta, z, t) = \cos(n\theta) W_{nj}(z) \mathrm{e}^{\mathrm{i}\omega_{nj} t} \tag{2.13c}$$

where $U_{nj}(z)$, $V_{nj}(z)$ and $W_{nj}(z)$ denote the dependency of the three modal displacement components along the longitudinal axis. As can be seen in Eq. (2.13), different modal sets may be obtained based on the circumferential mode number n. In general, the free vibration modes of solids of revolution can be categorized into two different groups, namely the special case of axisymmetric modes ($n = 0$) and the more general case of non-axisymmetric modes ($n > 0$) [182, 183]. Both groups of modes can be obtained via the same mathematical procedure, albeit with certain discrepancies due to the different general solution forms.

2.3.1. Axisymmetric motion ($n = 0$)

For axisymmetric vibrations, the shell motion decouples into two kinds, namely coupled axial-radial motion and circumferential motion [139]. The general solution of the j-th axial-radial mode has the following form:

$$U_{0j}(z) = \sum_{m=1}^{6} A_{0mj} C_{0mj} \mathrm{e}^{-\mathrm{i}\gamma_{0mj} z} \tag{2.14a}$$

$$V_{0j}(z) = 0 \tag{2.14b}$$

$$W_{0j}(z) = \sum_{m=1}^{6} C_{0mj} \mathrm{e}^{-\mathrm{i}\gamma_{0mj} z} \tag{2.14c}$$

where γ_{0mj} encompasses the wavenumbers that correspond to the natural frequency ω_{0j} based on Eq. (2.12), i.e. the dispersion equation for axisymmetric axial-radial waves. The coefficient A_{0mj} is known for each m-th wave component and the coefficient C_{0mj} is determined by the boundary conditions. Evidently, the circumferential component vanishes in Eq. (2.14).

For the j-th circumferential (also termed torsional) mode, the assumed solution may be expressed as:

$$U_{0j}(z) = 0 \tag{2.15a}$$

$$V_{0j}(z) = \sum_{m=1}^{2} B_{0mj} \mathrm{e}^{-\mathrm{i}\gamma_{0mj} z} \tag{2.15b}$$

$$W_{0j}(z) = 0 \tag{2.15c}$$

where the torsional wavenumbers denoted by γ_{0mj} are obtained by a second-order dispersion equation. In this case, the axial and radial components are equal to zero. It is remarked that axial-radial and torsional modes correspond to symmetric and anti-symmetric response configurations, respectively, and the final values B_{0mj} and C_{0mj} are determined by the boundary conditions.

2.3.2. Non-axisymmetric motion ($n > 0$)

In the case of non-axisymmetric motions, the coupling between the three displacement components is retained and the free vibrations modes have the following form:

$$U_{nj}(z) = \sum_{m=1}^{8} A_{nmj} C_{nmj} \mathrm{e}^{-\mathrm{i}\gamma_{nmj} z} \tag{2.16a}$$

$$V_{nj}(z) = \sum_{m=1}^{8} B_{nmj} C_{nmj} \mathrm{e}^{-\mathrm{i}\gamma_{nmj} z} \tag{2.16b}$$

$$W_{nj}(z) = \sum_{m=1}^{8} C_{nmj} \mathrm{e}^{-\mathrm{i}\gamma_{nmj} z} \tag{2.16c}$$

where the coefficients A_{nmj} and B_{nmj} are known and based on the dispersion characteristics of the m-th wave component with wavenumber γ_{nmj}. The determination of C_{nmj}, as in the axisymmetric case, is based on the boundary conditions.

The determination of the unknown coefficients is performed by assembling the boundary conditions, i.e. algebraic equations, in a matrix equation as follows:

$$\mathbf{K}_{\mathrm{LT}} \mathbf{c}_{nj} = \mathbf{0} \tag{2.17}$$

where the vector $\mathbf{c}_{nj} = \begin{bmatrix} C_{n1j} & \cdots & C_{n8j} \end{bmatrix}^{\mathrm{T}}$ encapsulates the unknown coefficients and the matrix $\mathbf{K}_{\mathrm{LT}}$ is a function of frequency. The natural frequency ω_{nj} and, by extension, all other modal quantities are found by requiring $\det(\mathbf{K}_{\mathrm{LT}}) = 0$, thus solving an optimization problem.

In the original method, as put forward by Flügge [181], the longitudinal dependence of the solution is given in terms of $\mathrm{e}^{k_{nmj} z}$. In Eqs. (2.14) to (2.16), the latter term is replaced by $\mathrm{e}^{-\mathrm{i}\gamma_{nmj} z}$, since the variable γ_{nmj} corresponds directly to the axial wavenumber in the context of wave propagation. It is worth noting that the obtained modes for both axisymmetric and non-axisymmetric motions may be complex-valued, which may be perceived as an indication of an incorrect solution. However, that situation may arise for correct solutions as well, due to the numerical implementation of the procedure. At this stage, all the displacement components of a mode shape should be multiplied by a factor $\mathrm{e}^{\mathrm{i}\phi}$, which serves to rotate the mode shapes in the complex space and align them with the real axis [184]. If the latter is not possible for the normal modes of a linear elastic shell, it delineates an inaccurate implementation of the preceding procedure.

2.4. A Semi-analytical Finite Element (SAFE) model for cylindrical shells

In the preceding sections, the analytical treatment of wave propagation and free vibrations of thin cylindrical shells were outlined. However, a reader dealing with engineering problems that include thin cylindrical shells inevitably demands a generic, versatile and efficient numerical modelling framework. The latter is not a minor consideration, in particular when 3-D problems need to be addressed. Available approaches that are fully based on the Finite Element Method (FEM) are abundant and well-established, as for instance the MITC shell elements that constitute the model of choice in most commercial FE codes [185]. Notwithstanding the merits of the preceding approaches, one may wish to resort to other more flexible and efficient techniques for the problem at hand. In view of such considerations, a Semi-analytical Finite Element (SAFE) model is formulated in the ensuing.

The essence of the SAFE method lies in the combination of one- or bi-dimensional finite element discretization with analytical solutions in the remaining coordinates. This approach has been successfully utilized in a wide range of applications, with a view to guided wave propagation for non-destructive evaluation (NDE) and structural health monitoring (SHM) in laminated composite plates and shells among other structures [186–189]. The outlined approach is applied to a cylindrical shell described by the Love-Timoshenko theory, yet the framework is generic and may be applied to other thin as well as thick shell theories in an identical manner.

Consider a thin cylindrical shell segment with length d_l. The equations of motion according to Love-Timoshenko shell theory may be expressed in a compact matrix form as follows:

$$\mathfrak{p}_\mathrm{p} + \mathscr{L}_\mathrm{p}\mathbf{s}_\mathrm{p} - \mathscr{I}_\mathrm{p}\mathbf{A}_\mathrm{p}\frac{\partial^2 \mathfrak{u}_\mathrm{p}}{\partial t^2} = \mathbf{0} \tag{2.18}$$

where the pile displacement/rotation vector $\mathfrak{u}_\mathrm{p}$, the surface forces/moments vector $\mathfrak{p}_\mathrm{p}$ and the force/moment resultants vector $\mathbf{s}_\mathrm{p}$ are defined as follows:

$$\mathfrak{u}_\mathrm{p} = \begin{bmatrix} u_\mathrm{p} & v_\mathrm{p} & w_\mathrm{p} & \beta_z \end{bmatrix}^\mathrm{T} \tag{2.19}$$

$$\mathfrak{p}_\mathrm{p} = \begin{bmatrix} p_{z,\mathrm{p}} & p_{\theta,\mathrm{p}} & p_{r,\mathrm{p}} & m_{z,\mathrm{p}} & m_{\theta,\mathrm{p}} \end{bmatrix}^\mathrm{T} \tag{2.20}$$

$$\mathbf{s}_\mathrm{p} = \mathbf{S}_\mathrm{p}\mathbf{A}_\mathrm{p}\mathfrak{u}_\mathrm{p} = \begin{bmatrix} N_z & N_\theta & N_{z\theta} & N_{\theta z} & Q_z & Q_\theta & M_z & M_\theta & M_{z\theta} & M_{\theta z} \end{bmatrix}^\mathrm{T} \tag{2.21}$$

Furthermore, the differential matrix operators $\mathscr{L}_\mathrm{p}$, $\mathbf{S}_\mathrm{p}$ and $\mathbf{A}_\mathrm{p}$ are defined as:

$$\mathscr{L}_\mathrm{p}(\cdot) = \mathscr{L}_{z,\mathrm{p}}\frac{\partial(\cdot)}{\partial z} + \mathscr{L}_{\theta,\mathrm{p}}\frac{\partial(\cdot)}{\partial \theta} + \mathscr{L}_{0,\mathrm{p}}(\cdot) \tag{2.22}$$

$$\mathbf{S}_\mathrm{p}(\cdot) = \mathbf{S}_{zz,\mathrm{p}}\frac{\partial^2(\cdot)}{\partial z^2} + \mathbf{S}_{\theta\theta,\mathrm{p}}\frac{\partial^2(\cdot)}{\partial \theta^2} + \mathbf{S}_{z\theta,\mathrm{p}}\frac{\partial^2(\cdot)}{\partial z\,\partial \theta} + \mathbf{S}_{z,\mathrm{p}}\frac{\partial(\cdot)}{\partial z} + \mathbf{S}_{\theta,\mathrm{p}}\frac{\partial(\cdot)}{\partial \theta} + \mathbf{S}_{0,\mathrm{p}}(\cdot) \tag{2.23}$$

$$\mathbf{A}_{\mathrm{p}}(\cdot) = \mathbf{A}_{\theta,\mathrm{p}} \frac{\partial(\cdot)}{\partial\theta} + \mathbf{A}_{0,\mathrm{p}}(\cdot) \tag{2.24}$$

In the above definitions, $\mathscr{L}_{\mathrm{p}}$ provides the shell stiffness based on the force/moment resultants, $\mathbf{S}_{\mathrm{p}}$ provides the force/moment resultants based on the shell displacements and rotations and $\mathbf{A}_{\mathrm{p}}$ forms the full displacement/rotation vector $\mathbf{a}_{\mathrm{p}}$, which reads:

$$\mathbf{a}_{\mathrm{p}} = \mathbf{A}_{\mathrm{p}}\mathbf{u}_{\mathrm{p}} = \begin{bmatrix} u_{\mathrm{p}} & v_{\mathrm{p}} & w_{\mathrm{p}} & \beta_z & \beta_\theta \end{bmatrix}^{\mathrm{T}} \tag{2.25}$$

The latter will be employed in the principle of virtual work, which is invoked in the derivation process of the SAFE shell model. Finally, the matrices $\mathscr{I}_{\mathrm{p}}$, $\mathscr{L}_{z,\mathrm{p}}$, $\mathscr{L}_{\theta,\mathrm{p}}$, $\mathscr{L}_{0,\mathrm{p}}$, $\mathbf{A}_{\theta,\mathrm{p}}$, $\mathbf{A}_{0,\mathrm{p}}$, $\mathbf{S}_{zz,\mathrm{p}}$, $\mathbf{S}_{\theta\theta,\mathrm{p}}$, $\mathbf{S}_{z\theta,\mathrm{p}}$, $\mathbf{S}_{z,\mathrm{p}}$, $\mathbf{S}_{\theta,\mathrm{p}}$ and $\mathbf{S}_{0,\mathrm{p}}$ can be found in Appendix A.

For a cylindrical shell, the two mid-surface circumferences at the shell edges comprise its boundary curves and in case of prescribed tractions the associated boundary conditions read [139]:

$$\mathbf{t}_{\mathrm{p}}^{(\mathrm{u})} = -\left(\mathscr{B}_{\mathrm{p}}\mathbf{s}_{\mathrm{p}}\right)^{(\mathrm{u})} \tag{2.26a}$$

$$\mathbf{t}_{\mathrm{p}}^{(\mathrm{l})} = \left(\mathscr{B}_{\mathrm{p}}\mathbf{s}_{\mathrm{p}}\right)^{(\mathrm{l})} \tag{2.26b}$$

where the superscripts (u) and (l) correspond to the upper ($z = z_{\mathrm{u}}$) and lower ($z = z_{\mathrm{l}}$) shell boundaries, respectively. The internal force/moment resultants along the boundary curve are defined as:

$$\mathscr{B}_{\mathrm{p}}\mathbf{s}_{\mathrm{p}} = \begin{bmatrix} N_z & N_{z\theta} + \dfrac{M_{z\theta}}{R_{\mathrm{p}}} & Q_z + \dfrac{1}{R}\dfrac{\partial M_{z\theta}}{\partial\theta} & M_z \end{bmatrix}^{\mathrm{T}} \tag{2.27}$$

where the differential matrix operator $\mathscr{B}_{\mathrm{p}}$ is defined as:

$$\mathscr{B}_{\mathrm{p}}(\cdot) = \mathscr{B}_{\theta,\mathrm{p}} \frac{\partial(\cdot)}{\partial\theta} + \mathscr{B}_{0,\mathrm{p}}(\cdot) \tag{2.28}$$

The matrices $\mathscr{B}_{\theta,\mathrm{p}}$ and $\mathscr{B}_{0,\mathrm{p}}$ can be found in Appendix A. Furthermore, the external force/moment vector $\mathbf{t}_{\mathrm{p}}$ at the boundary reads:

$$\mathbf{t}_{\mathrm{p}} = \begin{bmatrix} t_{z,\mathrm{p}} & t_{\theta,\mathrm{p}} & t_{r,\mathrm{p}} & t_{zz,\mathrm{p}} \end{bmatrix}^{\mathrm{T}} \tag{2.29}$$

Upon arranging all the necessary quantities in compact matrix form, we proceed to formulate a SAFE model for a thin cylindrical shell. In this problem, analytical solutions in θ are combined with a finite element discretization in z, resulting in a series of nodal rings (see Fig. 2.6). First, a cylindrical shell segment is considered with the following assumed solution:

$$\mathbf{u}_{\mathrm{p}} = \mathbf{\Theta}_n\mathbf{N}_{\mathrm{p}}\mathbf{x}_{\mathrm{p}}, \quad \mathbf{x}_{\mathrm{p}} = \begin{bmatrix} \mathbf{x}_{\mathrm{p}}^{(\mathrm{u})} \\ \mathbf{x}_{\mathrm{p}}^{(\mathrm{l})} \end{bmatrix} \tag{2.30}$$

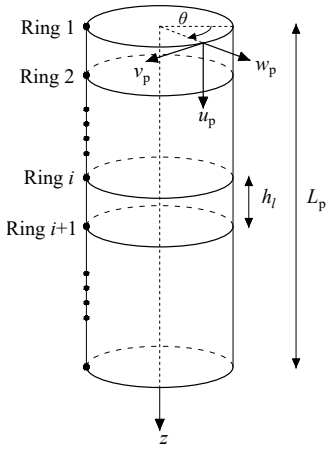

Figure 2.6: A thin cylindrical shell with axial discretization into nodal rings based on the SAFE method.

The diagonal matrix $\mathbf{\Theta}_n$ ensures that the response is periodic in θ. Both symmetric and anti-symmetric configurations with respect to $\theta = 0$ are admissible and can be expressed as:

$$\mathbf{\Theta}_n^{\mathrm{s}} = \begin{bmatrix} \cos(n\theta) & 0 & 0 & 0 \\ 0 & -\sin(n\theta) & 0 & 0 \\ 0 & 0 & \cos(n\theta) & 0 \\ 0 & 0 & 0 & \cos(n\theta) \end{bmatrix} \tag{2.31a}$$

$$\mathbf{\Theta}_n^{\mathrm{a}} = \begin{bmatrix} \sin(n\theta) & 0 & 0 & 0 \\ 0 & \cos(n\theta) & 0 & 0 \\ 0 & 0 & \sin(n\theta) & 0 \\ 0 & 0 & 0 & \sin(n\theta) \end{bmatrix} \tag{2.31b}$$

The symmetric and anti-symmetric azimuthal matrices are related as follows:

$$\frac{\mathrm{d}\mathbf{\Theta}_n^{\mathrm{s}}}{\mathrm{d}\theta} = -n\mathbf{\Theta}_n^{\mathrm{a}} \tag{2.32a}$$

$$\frac{\mathrm{d}\mathbf{\Theta}_n^{\mathrm{a}}}{\mathrm{d}\theta} = n\mathbf{\Theta}_n^{\mathrm{s}} \tag{2.32b}$$

In the ensuing, the azimuthal matrix $\mathbf{\Theta}_n$ will be used as a placeholder, since the generic developments to be presented are valid for both symmetric and anti-symmetric cases.

The interpolation matrix $\mathbf{N}_\mathrm{p}$ encapsulates the interpolation polynomials used to approximate the response of the shell element along the z-axis based on the nodal ring values, i.e. $\mathbf{x}_\mathrm{p}^{(\mathrm{u})}$ and $\mathbf{x}_\mathrm{p}^{(\mathrm{l})}$:

$$\mathbf{N}_\mathrm{p} = \begin{bmatrix} N_1^l(z) & 0 & 0 & 0 & N_2^l(z) & 0 & 0 & 0 \\ 0 & N_1^l(z) & 0 & 0 & 0 & N_2^l(z) & 0 & 0 \\ 0 & 0 & N_1^c(z) & -N_2^c(z) & 0 & 0 & N_3^c(z) & -N_4^c(z) \\ 0 & 0 & -\dfrac{\mathrm{d}N_1^c(z)}{\mathrm{d}z} & \dfrac{\mathrm{d}N_2^c(z)}{\mathrm{d}z} & 0 & 0 & -\dfrac{\mathrm{d}N_3^c(z)}{\mathrm{d}z} & \dfrac{\mathrm{d}N_4^c(z)}{\mathrm{d}z} \end{bmatrix} \tag{2.33}$$

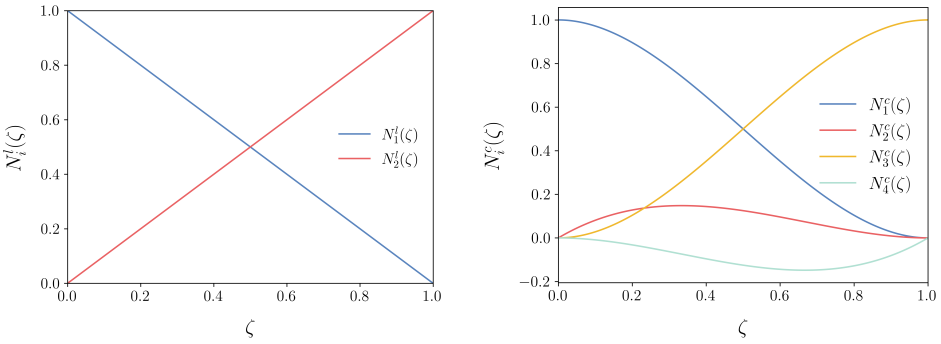

(a) (b)

Figure 2.7: (a) Linear Lagrange polynomials are used to approximate u_p and v_p along z and (b) cubic Hermite polynomials are used to approximate w_p and β_z along z (given as functions of $\zeta = z/d_l$).

The axial u_p and circumferential v_p displacements are interpolated based on linear Lagrange polynomials (see Fig. 2.7a), which are defined as:

$$N_1^l(z) = \frac{d_l - z}{d_l} \tag{2.34a}$$

$$N_2^l(z) = \frac{z}{d_l} \tag{2.34b}$$

The radial displacement w_p and the rotation angle β_z are approximated by cubic Hermite polynomials (see Fig. 2.7b):

$$N_1^c(z) = 1 - \frac{3z^2}{d_l^2} + \frac{2z^3}{d_l^3} \tag{2.35a}$$

$$N_2^c(z) = z - \frac{2z^2}{d_l} + \frac{z^3}{d_l^2} \tag{2.35b}$$

$$N_3^c(z) = \frac{3z^2}{d_l^2} - \frac{2z^3}{d_l^3} \tag{2.35c}$$

$$N_4^c(z) = -\frac{z^2}{d_l} + \frac{z^3}{d_l^2} \tag{2.35d}$$

Without further delay, the principle of virtual work is formulated for a cylindrical shell segment in order to derive the SAFE equations [190]. Accordingly, we require that the virtual work performed by the residual surface forces/moments throughout the shell domain and by the residual line forces/moments along the boundary curves to be zero:

$$\int_0^{2\pi}\left(\left(\delta\mathbf{u}_\mathrm{p}^{(\mathrm{u})}\right)^\mathrm{T}\mathbf{r}_\mathrm{p}^{(\mathrm{u})}+\left(\delta\mathbf{u}_\mathrm{p}^{(\mathrm{l})}\right)^\mathrm{T}\mathbf{r}_\mathrm{p}^{(\mathrm{l})}+\int_{z_\mathrm{u}}^{z_\mathrm{l}}\delta\mathbf{a}_\mathrm{p}^\mathrm{T}\mathbf{r}_{\mathrm{p,V}}\,\mathrm{d}z\right)R_\mathrm{p}\,\mathrm{d}\theta=0 \tag{2.36}$$

where $\mathbf{r}_\mathrm{p}^{(\mathrm{u})}$ and $\mathbf{r}_\mathrm{p}^{(\mathrm{l})}$ denote the residual force/moment resultants at the upper ($z=z_\mathrm{u}$) and lower ($z=z_\mathrm{l}$) shell segment boundaries, respectively, and $\mathbf{r}_{\mathrm{p,V}}$ denotes the residual surface forces/moments in the shell domain. The aforementioned residuals are expressed as follows:

$$\mathbf{r}_\mathrm{p}^{(\mathrm{u})}=\mathbf{t}_\mathrm{p}^{(\mathrm{u})}+\left(\mathscr{B}_\mathrm{p}\mathbf{s}_\mathrm{p}\right)^{(\mathrm{u})} \tag{2.37a}$$

$$\mathbf{r}_\mathrm{p}^{(\mathrm{l})}=\mathbf{t}_\mathrm{p}^{(\mathrm{l})}-\left(\mathscr{B}_\mathrm{p}\mathbf{s}_\mathrm{p}\right)^{(\mathrm{l})} \tag{2.37b}$$

$$\mathbf{r}_{\mathrm{p,V}}=\mathfrak{p}_\mathrm{p}+\mathscr{L}_\mathrm{p}\mathbf{s}_\mathrm{p}-\mathscr{I}_\mathrm{p}\mathbf{A}_\mathrm{p}\frac{\partial^2\mathfrak{u}_\mathrm{p}}{\partial t^2} \tag{2.37c}$$

In the absence of boundary forces/moments and surface loading in the shell, Eq. (2.36) is expanded as follows:

$$\int_0^{2\pi}\left[-\left(\delta\mathbf{u}_\mathrm{p}^\mathrm{T}\mathscr{B}_\mathrm{p}\mathbf{s}_\mathrm{p}\right)\Big|_{(\mathrm{u})}^{(\mathrm{l})}+\int_{z_\mathrm{u}}^{z_\mathrm{l}}\delta\mathbf{a}_\mathrm{p}^\mathrm{T}\left(\mathscr{L}_\mathrm{p}\mathbf{s}_\mathrm{p}-\mathscr{I}_\mathrm{p}\mathbf{A}_\mathrm{p}\frac{\partial^2\mathfrak{u}_\mathrm{p}}{\partial t^2}\right)\mathrm{d}z\right]R_\mathrm{p}\,\mathrm{d}\theta=0 \tag{2.38}$$

The line integral that corresponds to the boundary terms can be recasted into a surface integral, leading to:

$$\int_0^{2\pi}\int_{z_\mathrm{u}}^{z_\mathrm{l}}\left[-\left(\delta\mathbf{u}_\mathrm{p}^\mathrm{T}\mathscr{B}_\mathrm{p}\frac{\partial\mathbf{s}_\mathrm{p}}{\partial z}\right)-\left(\frac{\partial(\delta\mathbf{u}_\mathrm{p}^\mathrm{T})}{\partial z}\mathscr{B}_\mathrm{p}\mathbf{s}_\mathrm{p}\right)+\delta\mathbf{a}_\mathrm{p}^\mathrm{T}\left(\mathscr{L}_\mathrm{p}\mathbf{s}_\mathrm{p}-\mathscr{I}_\mathrm{p}\mathbf{A}_\mathrm{p}\frac{\partial^2\mathfrak{u}_\mathrm{p}}{\partial t^2}\right)\right]R_\mathrm{p}\,\mathrm{d}z\mathrm{d}\theta=0 \tag{2.39}$$

By factoring out the virtual displacement/rotation vector $\delta\mathbf{x}_\mathrm{p}^\mathrm{T}$, given that the principle of virtual work should hold for any arbitrary variation, Eq. (2.36) can been finally reformed as:

$$\begin{aligned}\int_0^{2\pi}\int_{z_\mathrm{u}}^{z_\mathrm{l}}&\left((\mathbf{N}_n^\theta)^\mathrm{T}\mathscr{B}_\mathrm{p}\mathbf{S}_\mathrm{p}\mathbf{A}_\mathrm{p}\frac{\mathrm{d}\mathbf{N}_n^\theta}{\mathrm{d}z}+\frac{\mathrm{d}(\mathbf{N}_n^\theta)^\mathrm{T}}{\mathrm{d}z}\mathscr{B}_\mathrm{p}\mathbf{S}_\mathrm{p}\mathbf{A}_\mathrm{p}\mathbf{N}_n^\theta-(\mathbf{N}_n^\theta)^\mathrm{T}\mathbf{A}_\mathrm{p}^\mathrm{T}\mathscr{L}_\mathrm{p}\mathbf{S}_\mathrm{p}\mathbf{A}_\mathrm{p}\mathbf{N}_n^\theta\right)R_\mathrm{p}\,\mathrm{d}z\mathrm{d}\theta\,\mathbf{x}_\mathrm{p}\\&+\int_0^{2\pi}\int_{z_\mathrm{u}}^{z_\mathrm{l}}(\mathbf{N}_n^\theta)^\mathrm{T}\mathbf{A}_\mathrm{p}^\mathrm{T}\mathscr{I}_\mathrm{p}\mathbf{A}_\mathrm{p}\mathbf{N}_n^\theta R_\mathrm{p}\,\mathrm{d}z\mathrm{d}\theta\,\frac{\mathrm{d}^2\mathbf{x}_\mathrm{p}}{\mathrm{d}t^2}=0\end{aligned} \tag{2.40}$$

Upon the outlined series of mathematical operations, the element mass and stiffness matrices $\mathbf{I}_{\mathrm{p},n}^l$ and $\mathbf{L}_{\mathrm{p},n}^l$, respectively, are derived and expressed as follows (see Appendix A):

$$\mathbf{I}_{\mathrm{p},n}^{l} = \int_{0}^{2\pi}\int_{z_{\mathrm{u}}}^{z_{\mathrm{l}}} (\mathbf{N}_{n}^{\theta})^{\mathrm{T}}\mathbf{A}_{\mathrm{p}}^{\mathrm{T}}\mathscr{I}_{\mathrm{p}}\mathbf{A}_{\mathrm{p}}\mathbf{N}_{n}^{\theta} R_{\mathrm{p}}\,\mathrm{d}z\mathrm{d}\theta \tag{2.41}$$

$$\mathbf{L}_{\mathrm{p},n}^{l} = \int_{0}^{2\pi}\int_{z_{\mathrm{u}}}^{z_{\mathrm{l}}} \left((\mathbf{N}_{n}^{\theta})^{\mathrm{T}}\mathscr{B}_{\mathrm{p}}\mathbf{S}_{\mathrm{p}}\mathbf{A}_{\mathrm{p}}\frac{\mathrm{d}\mathbf{N}_{n}^{\theta}}{\mathrm{d}z} + \frac{\mathrm{d}(\mathbf{N}_{n}^{\theta})^{\mathrm{T}}}{\mathrm{d}z}\mathscr{B}_{\mathrm{p}}\mathbf{S}_{\mathrm{p}}\mathbf{A}_{\mathrm{p}}\mathbf{N}_{n}^{\theta} - (\mathbf{N}_{n}^{\theta})^{\mathrm{T}}\mathbf{A}_{\mathrm{p}}^{\mathrm{T}}\mathscr{L}_{\mathrm{p}}\mathbf{S}_{\mathrm{p}}\mathbf{A}_{\mathrm{p}}\mathbf{N}_{n}^{\theta} \right) R_{\mathrm{p}}\,\mathrm{d}z\mathrm{d}\theta \tag{2.42}$$

In the presence of external loads in the shell surface and/or along the boundary curves, the vector of consistent forces/moments at the element nodal rings $\mathbf{p}_{\mathrm{p},n}^{l}$ may be expressed as:

$$\mathbf{p}_{\mathrm{p},n}^{l} = \int_{0}^{2\pi} \left(\begin{bmatrix} \boldsymbol{\Theta}_{n}^{\mathrm{T}}\mathbf{t}_{\mathrm{p}}^{(\mathrm{u})} \\ \boldsymbol{\Theta}_{n}^{\mathrm{T}}\mathbf{t}_{\mathrm{p}}^{(\mathrm{l})} \end{bmatrix} + \int_{z_{\mathrm{u}}}^{z_{\mathrm{l}}} (\mathbf{N}_{n}^{\theta})^{\mathrm{T}}\mathbf{A}_{\mathrm{p}}^{\mathrm{T}}\mathbf{p}_{\mathrm{p}}\,\mathrm{d}z \right) R_{\mathrm{p}}\mathrm{d}\theta \tag{2.43}$$

It is noted that $\mathbf{N}_{n}^{\theta} = \boldsymbol{\Theta}_{n}\mathbf{N}_{\mathrm{p}}$ has been introduced in all previous equations for notation compactness.

The final SAFE equations are formulated by overlapping all the obtained vectors and matrices in the classical finite element sense and rearranging rows and columns to organize per degrees of freedom instead of nodal rings. In that manner, the discretized equations of motion of the cylindrical shell based on the SAFE approach read:

$$\mathbf{I}_{\mathrm{p},n}\frac{\mathrm{d}^{2}\mathbf{u}_{\mathrm{p},n}}{\mathrm{d}t^{2}} + \mathbf{L}_{\mathrm{p},n}\mathbf{u}_{\mathrm{p},n} = \mathbf{p}_{\mathrm{p},n} \tag{2.44}$$

where $\mathbf{I}_{\mathrm{p},n}$ is the shell mass matrix, $\mathbf{L}_{\mathrm{p},n}$ is the shell stiffness matrix, $\mathbf{u}_{\mathrm{p},n}$ is the displacement/rotation vector at the nodal rings and $\mathbf{p}_{\mathrm{p},n}$ is the vector of consistent forces/moments at the nodal rings. Specifically, the displacements/rotations and forces/moments vectors read:

$$\mathbf{u}_{\mathrm{p},n} = \begin{bmatrix} \mathbf{u}_{n} \\ \mathbf{v}_{n} \\ \mathbf{w}_{n} \\ \boldsymbol{\beta}_{z,n} \end{bmatrix}, \quad \mathbf{p}_{\mathrm{p},n} = \begin{bmatrix} \mathbf{p}_{zn,\mathrm{p}} \\ \mathbf{p}_{\theta n,\mathrm{p}} \\ \mathbf{p}_{rn,\mathrm{p}} \\ \mathbf{m}_{zzn,\mathrm{p}} \end{bmatrix} \tag{2.45}$$

As can be seen, all the aforementioned quantities are valid for any circumferential mode number n and hold for both symmetric and anti-symmetric problems. In a general problem with arbitrary dependence on θ and/or coupling of the response components of different n, concurrent solution of multiple equations in the form of Eq. (2.44) is necessary. For that purpose, the general solution at the nodal rings can be written as:

$$\mathbf{u}_{\mathrm{p}} = \begin{bmatrix} \mathbf{u} \\ \mathbf{v} \\ \mathbf{w} \\ \boldsymbol{\beta}_{z} \end{bmatrix} = \sum_{n=0}^{\infty} \left[\left(\boldsymbol{\Theta}_{n}^{\mathrm{s}} \otimes \mathbf{I}_{N_{l}}\right)\mathbf{u}_{\mathrm{p},n}^{\mathrm{s}} + \left(\boldsymbol{\Theta}_{n}^{\mathrm{a}} \otimes \mathbf{I}_{N_{l}}\right)\mathbf{u}_{\mathrm{p},n}^{\mathrm{a}} \right] \tag{2.46}$$

where $\otimes$ is the Kronecker product and $\mathbf{I}_{N_l}$ is the $N_l \times N_l$ identity matrix with N_l being the number of nodal rings of the shell.

To accelerate the numerical solution of problems with the SAFE approach, the shell response may be decomposed in terms of *in vacuo* modes as follows (e.g. for a symmetric form):

$$\mathbf{u}^{\mathrm{s}}_{\mathrm{p},n} = \mathbf{\Phi}^{\mathrm{s}}_{\mathrm{p},n}\mathbf{q}^{\mathrm{s}}_{n} \tag{2.47}$$

where $\mathbf{q}^{\mathrm{s}}_{n} = \mathbf{q}^{\mathrm{s}}_{n}(t)$ is the vector of modal coordinates and the modal matrix $\mathbf{\Phi}^{\mathrm{s}}_{\mathrm{p},n}$ is defined as follows:

$$\mathbf{\Phi}^{\mathrm{s}}_{\mathrm{p},n} = \begin{bmatrix} \mathbf{U}^{\mathrm{s}}_{n} \\ \mathbf{V}^{\mathrm{s}}_{n} \\ \mathbf{W}^{\mathrm{s}}_{n} \\ \mathbf{B}^{\mathrm{s}}_{n} \end{bmatrix} \tag{2.48}$$

with the modal sub-matrices $\mathbf{U}^{\mathrm{s}}_{n}$, $\mathbf{V}^{\mathrm{s}}_{n}$, $\mathbf{W}^{\mathrm{s}}_{n}$ and $\mathbf{B}^{\mathrm{s}}_{n}$ that read:

$$\mathbf{U}^{\mathrm{s}}_{n} = \begin{bmatrix} \mathbf{u}^{\mathrm{s}}_{n,1} & \mathbf{u}^{\mathrm{s}}_{n,2} & \cdots \end{bmatrix} \tag{2.49a}$$

$$\mathbf{V}^{\mathrm{s}}_{n} = \begin{bmatrix} \mathbf{v}^{\mathrm{s}}_{n,1} & \mathbf{v}^{\mathrm{s}}_{n,2} & \cdots \end{bmatrix} \tag{2.49b}$$

$$\mathbf{W}^{\mathrm{s}}_{n} = \begin{bmatrix} \mathbf{w}^{\mathrm{s}}_{n,1} & \mathbf{w}^{\mathrm{s}}_{n,2} & \cdots \end{bmatrix} \tag{2.49c}$$

$$\mathbf{B}^{\mathrm{s}}_{n} = \begin{bmatrix} \boldsymbol{\beta}^{\mathrm{s}}_{n,1} & \boldsymbol{\beta}^{\mathrm{s}}_{n,2} & \cdots \end{bmatrix} \tag{2.49d}$$

2.5. Validation of the SAFE cylindrical shell model

In Section 2.4, a SAFE model for cylindrical shells has been presented that is valid for both axisymmetric ($n = 0$) and non-axisymmetric motions ($n > 0$). In the problem of our interest, i.e. pile installation, only axisymmetric modes ($n = 0$) will be used. However, we proceed to demonstrate the remarkable potential of the developed SAFE model for both axisymmetric and non-axisymmetric motions. For that purpose, the SAFE approach is compared against a finite element (FE) model developed in COMSOL Multiphysics® software [191]. A free-free cylindrical shell is considered, which is modelled in COMSOL by means of MITC shell elements using the Shell module [185]. It is remarked that the natural frequencies of the COMSOL model were obtained for a certain frequency range and then categorized based on the respective circumferential mode number n. The pile properties are identical to the ones presented in Table 2.1.

In Fig. 2.8, the natural frequencies of the first thirty axial-radial axisymmetric modes ($n = 0$) are found by the SAFE shell model and compared with those obtained from COMSOL. Similarly, for the non-axisymmetric case the first thirty modes for $n = 1$ are shown in Fig. 2.9, with a view to the direct applicability of this type of motion to tubular structures subject to lateral loading (e.g. monopiles). Evidently, the agreement is such that the two sets (SAFE and COMSOL) are virtually indistinguishable for both $n = 0$ and $n = 1$, showcasing the remarkable accuracy of the SAFE method in the prediction of natural frequencies.

To further supplement the validation study, the mode shapes for the two modal sets under consideration (i.e. $n = 0$ and $n = 1$) are also compared. In Figs. 2.10 and 2.11, the

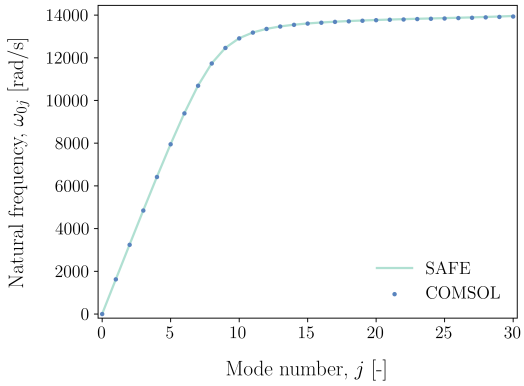

Figure 2.8: Comparison of the shell natural frequencies obtained from the SAFE and the FE (COMSOL) models for axial-radial modes ($n = 0$).

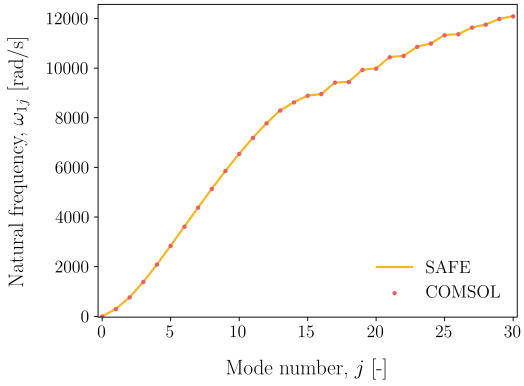

Figure 2.9: Comparison of the shell natural frequencies obtained from the SAFE and the FE (COMSOL) models for $n = 1$.

axisymmetric axial-radial mode shapes are displayed for both the SAFE and the COMSOL model. Similarly, in Figs. 2.12 and 2.13 the axial and radial modal displacements for the set of $n = 1$ modes are compared. It is noted that the mode index j in these examples corresponds to flexible-body mode shapes, as rigid-body modes are trivially found and thus were excluded herein. As can be seen, the agreement of the two models in terms of mode shapes is remarkable both in axial and radial components. This additional validation neatly corroborates the results of the natural frequencies comparison for both $n = 0$ and $n = 1$.

In Fig. 2.14, a collection of mode shapes obtained via the SAFE method is visualized to showcase its applicability to both axisymmetric and non-axisymmetric motions of arbitrary circumferential mode numbers n. These normal modes can be obtained by substituting the associated circumferential mode numbers n and the solution form of Eq. (2.47) in Eq. (2.44) in the absence of external forcing. In that manner, a generalized linear eigenvalue problem is obtained, which can be numerically solved via standard techniques [192].

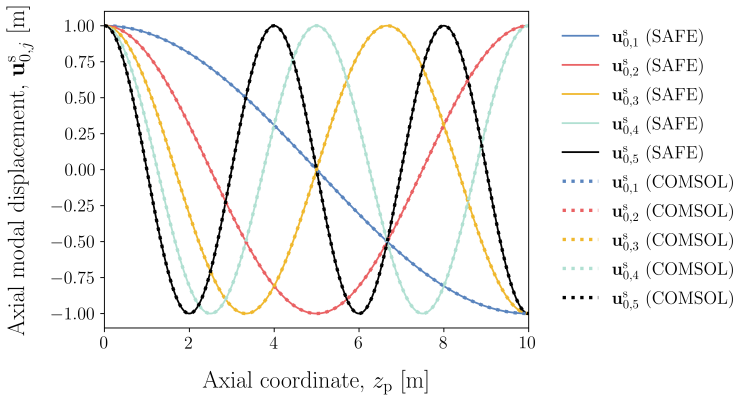

Figure 2.10: Comparison of the axial modal displacements $\mathbf{u}^{s}_{0,j}$ obtained from the SAFE and the FE (COMSOL) models for $n = 0$.

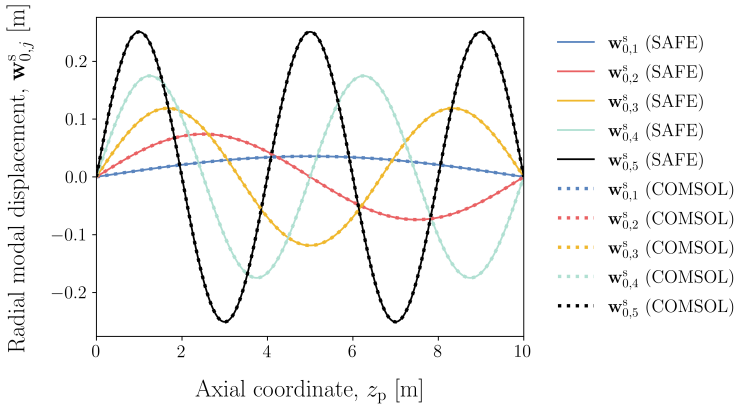

Figure 2.11: Comparison of the radial modal displacements $\mathbf{w}^{s}_{0,j}$ obtained from the SAFE and the FE (COMSOL) models for $n = 0$.

Conclusively, the accuracy of the proposed SAFE model has been showcased in terms of natural frequencies and mode shapes. It is clear that the SAFE method is a highly attractive numerical framework as it provides: (i) computational savings, i.e. a 1-D FE discretization may be applied to 2-D and 3-D problems, (ii) versatility of coupling to other FE-based approaches, as its numerical core lies in the FEM, and (iii) remarkable accuracy, due to the use of analytical solutions in place of additional discretization.

2.6. Conclusions

This chapter has focused on the vibrations of thin-walled cylindrical structures, in view of the need for accurate and computationally efficient modelling of large-diameter monopiles. The standard 1-D pile modelling approaches were established for slender small-diameter

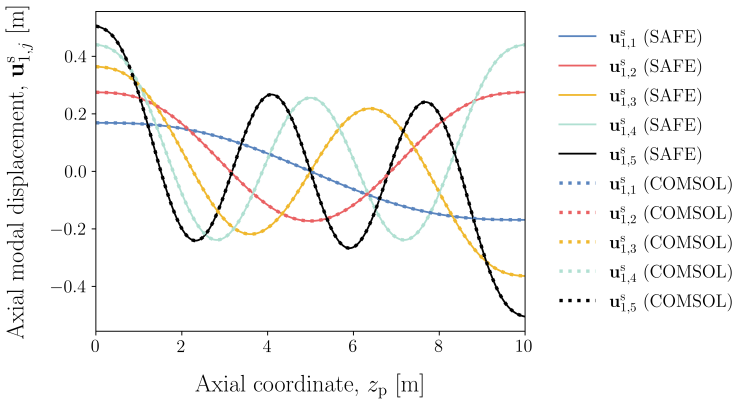

Figure 2.12: Comparison of the axial modal displacements $\mathbf{u}^{s}_{1,j}$ obtained from the SAFE and the FE (COMSOL) models for $n = 1$.

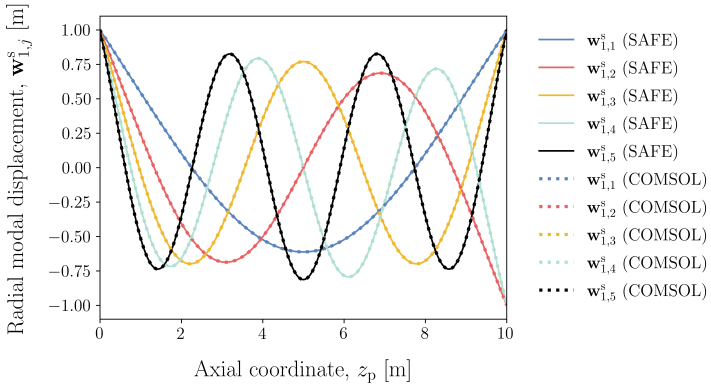

Figure 2.13: Comparison of the radial modal displacements $\mathbf{w}^{s}_{1,j}$ obtained from the SAFE and the FE (COMSOL) models for $n = 1$.

piles, while their applicability to large tubular structures is questionable. To overcome these limitations, a thin cylindrical shell theory has been proposed as an optimal choice for a physically accurate and computationally efficient pile model. Furthermore, the wave dispersion characteristics of thin-walled cylindrical waveguides have been explored, with emphasis on thin shell theory.

To facilitate the numerical modelling of thin and thick cylindrical shells, a Semi-analytical Finite Element (SAFE) model has been developed and numerically validated. By means of this development, we introduced a valuable tool for future studies, aiming to investigate the vibrations of these structures for a multitude of engineering applications. In the ensuing chapters, the previous advancements will be utilized in order to incorporate a thin cylindrical shell model in pile installation analysis.

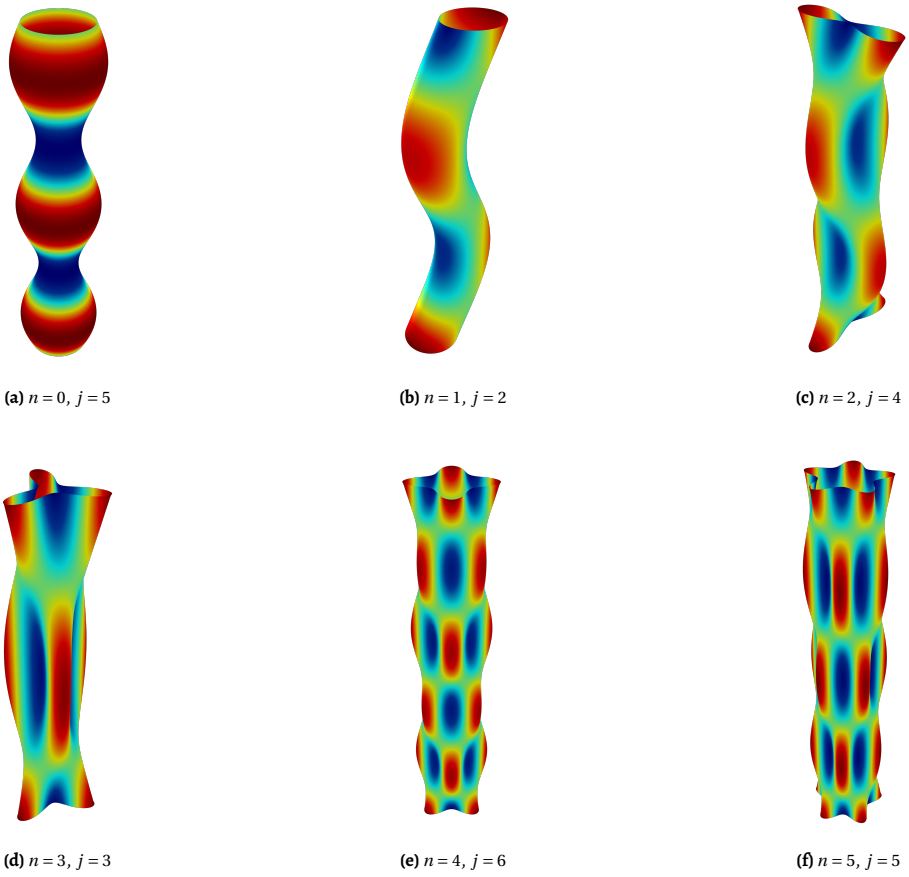

(a) $n = 0,\ j = 5$ **(b)** $n = 1,\ j = 2$ **(c)** $n = 2,\ j = 4$

(d) $n = 3,\ j = 3$ **(e)** $n = 4,\ j = 6$ **(f)** $n = 5,\ j = 5$

Figure 2.14: Shell mode shapes for various circumferential mode numbers n obtained via the SAFE model; the modal index j starts from 1 and includes only flexible-body modes.

3

Installation of large-diameter monopiles: wave dispersion and non-local soil reaction

During the last decade, the offshore wind industry grew ceaselessly and engineering challenges continuously arose in that area. Installation of foundation piles, commonly termed as monopiles, is one of the most critical phases in the construction of offshore wind farms. Prior to installation, a drivability study is performed, by means of pile driving models. Since the latter have been developed for small-diameter piles, their applicability for the analysis of large-diameter monopiles is questionable. The focal points of this chapter are associated with two physical mechanisms present in pile installation and their significance for large-diameter monopiles, albeit they are commonly neglected for ease of numerical modelling. First, the dispersion of elastic waves in a pile during installation is addressed, showcasing the need for an accurate description of the pile motion based on a thin shell theory. Secondly, the non-locality of soil reaction is discussed, with a view to set the stage for the later developments dealing with the dynamic response of a 3-D soil medium.

To showcase the significance of these effects, a 3-D axisymmetric pile driving model with non-local soil reaction is presented. This model captures properly the elastic wave propagation in the pile and utilizes a simple approach to introduce non-local soil reaction, as an extension of its local counterpart. A numerical case study of impact piling is performed to showcase the response disparities stemming from these effects and being already of importance for the size of monopiles currently installed.

This chapter is structured as follows. A brief review of modelling approaches utilized in drivability analysis of piles installed via impact hammers is presented in Section 3.1. In Section 3.2, the descriptions of the 1-D pile driving model and the non-local 3-D model are given. The comparison of the results obtained from the two modelling approaches is presented in Section 3.3, highlighting the effects of wave dispersion and non-local soil

Parts of this chapter have been published in Tsetas et al. [193].

reaction for various cases. Conclusively, in Section 3.4 the findings are discussed, alongside the importance of the introduced effects and insights for further development.

3.1. Drivability analysis in impact piling

Installation of monopile foundations for offshore wind turbines (OWTs) is a considerably challenging operation and the associated cost comprises a significant part of the total budget for an offshore wind farm [28, 194]. For that reason, in the design stage, close attention is required to various aspects, one of which is the analysis of pile drivability. Inaccurate pile drivability predictions can cause time delays, excessive financial costs, or even greater project risks, e.g. pile refusal [195]. Thus, it is evident that reliable numerical tools are needed for pile driving analysis, primarily for offshore monopiles due to the aforementioned possible complications. In view of the ceaseless advancements in offshore wind in recent years [25], the monopiles used as foundations for OWTs have increased in both length and diameter, and their installation process has raised various challenges.

For the prediction of pile drivability, an analysis is performed that takes into account the pile characteristics, the soil profile at the location of installation and the impact/vibratory hammer to drive the pile to the required depth [30]. The vast majority of pile driving models used in engineering practice are based on the model proposed by Smith [196]; a 1-D model that describes the pile as a thin rod and the soil reaction by elasto-plastic springs and viscous dashpots. Subsequently, various modifications have been proposed towards rational pile driving models, by improving certain aspects of Smith's model, such as the empirical character of the soil reaction parameters [80, 81]. For that purpose, dynamic models that represent the linear soil reaction based on approximate impedance formulas [66, 67] have been used in conjunction with non-linear relations to account for the pile penetration process (pile slip). However, the linear reaction of a soil continuum is frequency-dependent and spatially non-local. The latter fact is mostly neglected in pile driving analysis and frequency-independent values are assigned to local elements, in order to facilitate the numerical simulation in the time domain. As a result, local and frequency-independent springs and dashpots are arranged together with non-linear elements, e.g. frictional sliders, to represent the soil reaction during installation. It is evident that the preceding approaches comprised significant steps towards less empirical, rational pile driving models.

In the advent of large-diameter monopiles used in offshore wind, the validity of the existing approaches to analyse pile drivability was examined. Byrne et al. [94] investigated the applicability of available design approaches with a focus on the static resistance to driving (SRD), since these approaches are largely empirical and have been developed for piles of relatively small diameter (less than 2 m) [94, 197]. Furthermore, Byrne et al. [94] introduced a modification factor in the aforementioned approaches, which resulted in improved drivability predictions. However, a subsequent and more extensive study revealed that both the existing and the modified approaches were proven not to provide reliable predictions of the blow counts [95].

Albeit the preceding works mainly focused on the determination of the SRD and its influence on drivability predictions, other aspects of available pile driving models have also been examined. Due to the increase in the diameter of monopiles, various works questioned the validity of the classical rod theory, which is exclusively used to describe the pile dynamics during installation [198, 199]. Since the wave motions excited in a pile during a hammer

impact may pertain in the frequency range where dispersive effects are not negligible, a more accurate description of the pile structure may be required. In thin-walled tubular structures, frequencies in the vicinity of the so-called ring frequency correspond to predominantly radial motions [149, 148] - which cannot be captured in current models - and are related to strong Poisson effects that can significantly affect the soil reaction along the pile shaft [200].

In view of these considerations, a 3-D axisymmetric model is developed herein, as a step towards pile driving models that are suitable for large-diameter monopiles. The dispersion of longitudinal waves is taken into account by modelling the pile as a thin cylindrical shell according to the Love-Timoshenko theory. Furthermore, the effect of non-local dynamic soil reaction is introduced, by formulating a non-local foundation model based on the stiffness and damping parameters of its local counterpart. To demonstrate the effects of these two aspects, a 1-D pile driving model with local soil reaction, as customarily used in engineering practice, is formulated and a numerical study is performed to compare these two modelling approaches. It is observed that pile penetration is significantly affected by wave dispersion and this effect becomes more prominent with ascending pile diameter. In the case of large-diameter piles, foundation non-locality leads to a stronger deviation from the local reaction models in terms of pile responses. Since for large-diameter cases, both examined aspects significantly alter the drivability predictions of standard approaches, their incorporation in pile driving models for large-diameter monopiles is deemed critical.

3.2. Modelling of pile driving

In Section 3.2.1, a 1-D pile driving model is formulated, based on approaches widely used in engineering practice. A 3-D axisymmetric model is presented in Section 3.2.2, where the pile is modelled as a thin cylindrical shell and non-locality is introduced in soil reaction. Details about the numerical solution of the two models are given in Section 3.2.3.

3.2.1. 1-D pile driving model

An open-ended pipe pile is modelled as a linear elastic homogeneous rod occupying the domain $0 \leq z \leq L_\mathrm{p}$, where L_p denotes the pile length (see Fig. 3.1). The soil reaction is represented by a combination of elastic springs, viscous dashpots and plastic sliders, as will be described in the ensuing. The equation of motion of the rod reads:

$$\rho_\mathrm{p} A_\mathrm{p} \frac{\partial^2 u_\mathrm{p}(z,t)}{\partial t^2} = E_\mathrm{p} A_\mathrm{p} \frac{\partial^2 u_\mathrm{p}(z,t)}{\partial z^2} - \mathrm{H}(z-l_1)\, p_\mathrm{sh} \tag{3.1}$$

in which ρ_p is the mass density of the pile, A_p is the area of the pile cross-section, $u_\mathrm{p}(z,t)$ is the axial displacement of the pile, E_p is the Young's modulus of the pile, $\mathrm{H}(\cdot)$ is the Heaviside function, l_1 is the non-embedded pile length and p_sh is the soil resistance along the pile shaft. The latter is defined as [80]:

$$p_\mathrm{sh} = \begin{cases} k_\mathrm{sh}\left(u_\mathrm{p}(z,t) - u_\mathrm{eq,sh}(z,t)\right) + c_\mathrm{sh}\frac{\partial u_\mathrm{p}(z,t)}{\partial t}\,, & \text{for } \left|k_\mathrm{sh}\left(u_\mathrm{p}(z,t) - u_\mathrm{eq,sh}(z,t)\right) + c_\mathrm{sh}\frac{\partial u_\mathrm{p}(z,t)}{\partial t}\right| \leq 2\pi R_\mathrm{o} q_\mathrm{sh}(z) \\ 2\pi R_\mathrm{o} q_\mathrm{sh}(z)\,\mathrm{sgn}\left(\frac{\partial u_\mathrm{p}(z,t)}{\partial t}\right), & \text{for } \left|k_\mathrm{sh}\left(u_\mathrm{p}(z,t) - u_\mathrm{eq,sh}(z,t)\right) + c_\mathrm{sh}\frac{\partial u_\mathrm{p}(z,t)}{\partial t}\right| > 2\pi R_\mathrm{o} q_\mathrm{sh}(z) \end{cases} \tag{3.2}$$

In Eq. (3.2), k_{sh} is the stiffness of the soil springs along the pile shaft, $u_{eq,sh}(z,t)$ is the equilibrium position of each point along the pile shaft once plastic deformation develops at the pile-soil interface, c_{sh} is the soil dashpot coefficient along the pile shaft, R_o is the outer radius of the pile and $q_{sh}(z)$ is the ultimate shaft resistance. The spring and dashpot coefficients in this study are chosen in accordance with Deeks and Randolph [201] (viscous effects neglected in plastic regime) and further modified as $k_{sh} = 2\pi G_s$ and $c_{sh} = 2\pi R_o\sqrt{\rho_s G_s}$, to account also for the inner shaft resistance of the open-ended piles, as proposed by Liyanapathirana et al. [202]. The parameters G_s and ρ_s denote the shear modulus and mass density of the soil, respectively.

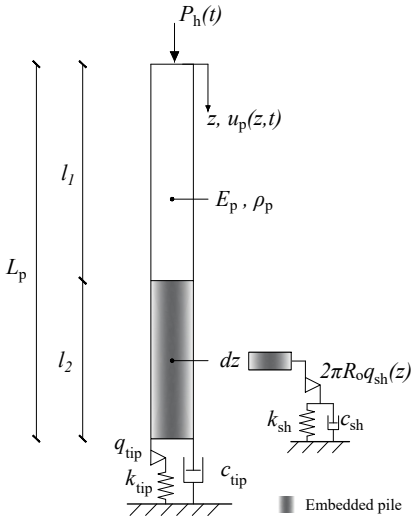

Figure 3.1: A 1-D pile driving model, with the pile described as a rod.

The mathematical statement is supplemented by the initial and boundary conditions as follows:

$$u_p(z,0) = 0, \quad \left.\frac{\partial u_p(z,t)}{\partial t}\right|_{t=0} = 0, \quad N_1(0,t) = -P_h(t), \quad N_1(L_p,t) = -P_{tip}, \tag{3.3}$$

in which N_1 is the axial force and $P_h(t)$ is the force exerted on the pile head by the hammer impact, computed analytically by the model of Deeks and Randolph [85]. Similarly, the soil reaction P_{tip} at the pile tip of an open-ended pipe pile ($z = L_p$) reads [81]:

$$P_{tip} = \begin{cases} k_{tip}(u_p(L_p,t) - u_{eq,tip}(t)) + c_{tip}\left.\frac{\partial u_p(z,t)}{\partial t}\right|_{z=L_p}, & \text{for } |k_{tip}(u_p(L_p,t) - u_{eq,tip}(t))| \le q_{tip}A_p \\ q_{tip}A_p \operatorname{sgn}\left(\left.\frac{\partial u_p(z,t)}{\partial t}\right|_{z=L_p}\right) + c_{tip}\left.\frac{\partial u_p(z,t)}{\partial t}\right|_{z=L_p}, & \text{for } |k_{tip}(u_p(L_p,t) - u_{eq,tip}(t))| > q_{tip}A_p \end{cases} \tag{3.4}$$

and

$$k_{\text{tip}} = 2G_{\text{s}}R_{\text{o}} / \left((1-\nu_{\text{s}})\,\eta_{\text{r}}\right) \tag{3.5a}$$

$$c_{\text{tip}} = 3.4\left(R_{\text{o}}^2 - R_{\text{i}}^2\right)\sqrt{\rho_{\text{s}}G_{\text{s}}} / (1-\nu_{\text{s}}) \tag{3.5b}$$

in which k_{tip} is the soil spring stiffness at the pile tip, $u_{\text{eq,tip}}(t)$ is the equilibrium position of the pile tip after plastic deformation has occurred, c_{tip} is the soil dashpot coefficient at the pile tip, R_{i} is the inner radius of the pile, ν_{s} is the soil Poisson's ratio, η_{r} is a function of the ratio of the inner to outer radius of the pile $R_{\text{i}}/R_{\text{o}}$ - according to Egorov [61] - and q_{tip} is the ultimate tip resistance.

The ultimate shaft resistance at the pile-soil interface $q_{\text{sh}}(z)$, for a cohensionless layer of sand, is estimated as a function of depth z according to the Mohr-Coulomb failure criterion [203]:

$$q_{\text{sh}}(z) = K_{\text{o}}\sigma_{\text{v}}^{'}(z)\tan\delta_{\text{s}}' \tag{3.6}$$

in which K_{o} is the coefficient of lateral earth pressure, $\sigma_{\text{v}}^{'}(z)$ is the effective vertical soil stress as a function of depth (for $z \geq l_1$ and $\sigma_{\text{v}}'(l_1) = 0$) and δ_{s}' is the critical friction angle of the pile-soil interface. It is noted that in the present study, the shaft resistance is assumed for all piles identical at the inner and outer surface of the pile shaft, leading to a total shaft resistance $q_{\text{sh}}(z) = 2K_{\text{o}}\sigma_{\text{v}}'(z)\tan\delta_{\text{s}}'$. Similarly, at the pile tip soil failure takes place according to the Mohr-Coulomb criterion and an associated flow rule, based on the work of Kumar and Chakraborty [204]. Accordingly, the ultimate tip resistance reads:

$$q_{\text{tip}} = c_{\text{c}}N_c + q_{\text{o}}N_{q_{\text{o}}} + \gamma_{\text{s}}\left(R_{\text{o}} - R_{\text{i}}\right)N_{\gamma_{\text{s}}} \tag{3.7}$$

in which the terms N_c, $N_{q_{\text{o}}}$ and $N_{\gamma_{\text{s}}}$ denote the bearing capacity factors of soil cohesion c_{c}, soil surcharge pressure q_{o} and soil unit weight γ_{s}, respectively [204].

3.2.2. 3-D axisymmetric pile driving model with non-local soil reaction

An open-ended pipe pile, due to its cylindrical geometry and its small wall thickness compared to its other dimensions, may be described adequately as a thin cylindrical shell up to a certain frequency range. In fact, the accurate description of elastic wave propagation in such a structure requires a thin shell theory [139]. Specifically, the motion of a thin-walled cylindrical structure is primarily radial and strong dispersive effects are present in the frequency region around the so-called shell ring frequency f_{r} [205]; classical rod theory cannot capture such effects [149, 148]. Alternative rod theories may be used to introduce dispersive effects (e.g. Rayleigh-Love rod), albeit such theories are mostly inaccurate in the vicinity of the ring frequency and may falsely predict a cut-off frequency. On the other hand, thin shell theories are in excellent agreement with the results of three-dimensional elasticity theory, for the greater part of the frequency spectrum in the case of axisymmetric waves [138].

In great soil depths, large soil reaction may be encountered during offshore monopile installation, thus the importance of accurate description of the pile motion cannot be overemphasized. Excitation of strong radial motions can affect the soil resistance during

installation and render the drivability predictions inaccurate, as this effect is altogether neglected in current pile driving models. For small-diameter piles that have been mainly used offshore in the past, that issue had not arisen for reasons that will become apparent in the ensuing.

In view of the above considerations, a drivability model that describes the pile by means of a thin shell theory is developed. As the pile, the force by the hammer impact, and the soil reaction are symmetric around the pile longitudinal axis, the model used is considered axisymmetric. Therefore, all the quantities involved in the problem are independent of the azimuth θ, i.e. $\partial(\cdot)/\partial\theta = 0$. Given the aforementioned considerations, the pile dynamic equilibria of the coupled axial-radial motion during impact driving, according to the Love-Timoshenko shell theory [159] read:

$$\rho_\mathrm{p} h_\mathrm{p} \frac{\partial^2 u_\mathrm{p}(z,t)}{\partial t^2} = \frac{E_\mathrm{p} h_\mathrm{p}}{\left(1-\nu_\mathrm{p}^2\right)} \frac{\partial^2 u_\mathrm{p}(z,t)}{\partial z^2} + \frac{E_\mathrm{p} h_\mathrm{p} \nu_\mathrm{p}}{\left(1-\nu_\mathrm{p}^2\right) R_\mathrm{p}} \frac{\partial w_\mathrm{p}(z,t)}{\partial z} - \frac{\mathrm{H}(z-l_1)\, p_\mathrm{sh}}{2\pi R_\mathrm{p}} \tag{3.8a}$$

$$\rho_\mathrm{p} h_\mathrm{p} \frac{\partial^2 w_\mathrm{p}(z,t)}{\partial t^2} = -\frac{E_\mathrm{p} h_\mathrm{p} \nu_\mathrm{p}}{\left(1-\nu_\mathrm{p}^2\right) R_\mathrm{p}} \frac{\partial u_\mathrm{p}(z,t)}{\partial z} - \frac{E_\mathrm{p} h_\mathrm{p}}{\left(1-\nu_\mathrm{p}^2\right) R_\mathrm{p}^2} w_\mathrm{p}(z,t) - \frac{E_\mathrm{p} h_\mathrm{p}^3}{12\left(1-\nu_\mathrm{p}^2\right)} \frac{\partial^4 w_\mathrm{p}(z,t)}{\partial z^4} \tag{3.8b}$$

in which h_p is the pile wall thickness, ν_p is the Poisson's ratio of the pile and $w_\mathrm{p}(z,t)$ is the radial displacement of the pile. It is remarked that the soil reaction in the radial direction may also be considered. However, in the ensuing study the radial soil reaction is not introduced, such that the two models are directly comparable and the effect of wave dispersion can be evaluated.

Similarly to Eq. (3.3), the initial conditions are set equal to zero. For the thin cylindrical shell the axial force resultants are prescribed at the top and the bottom of the pile, while the remaining boundaries are formulated as free [206]. Accordingly, the boundary conditions read:

$$\begin{aligned} N_z(0,t) &= -\frac{P_\mathrm{h}(t)}{2\pi R_\mathrm{p}}, \quad N_{z\theta}(0,t) = 0, \quad Q_z(0,t) = 0, \quad M_z(0,t) = 0, \\ N_z(L_\mathrm{p},t) &= -\frac{P_\mathrm{tip}}{2\pi R_\mathrm{p}}, \quad N_{z\theta}(L_\mathrm{p},t) = 0, \quad Q_z(L_\mathrm{p},t) = 0, \quad M_z(L_\mathrm{p},t) = 0 \end{aligned} \tag{3.9}$$

in which $N_z(z,t)$, $N_{z\theta}(z,t)$ and $Q_z(z,t)$ denote the axial, in-plane shear and out-plane shear force resultants, respectively, and $M_z(z,t)$ denotes the moment resultant of the thin cylindrical shell [139]. The natural boundary conditions from Eq. (3.3) have been reformulated into Eq. (3.9), such that the prescribed forces at the boundaries, $P_\mathrm{h}(t)$ and P_tip, are uniformly distributed along the pile circumference. Finally, the ultimate shaft and tip resistances are identical to the ones described in Section 3.2.1 and the described model is displayed in Fig. 3.2.

As stated before, one of the main challenges in pile drivability predictions lies in the strong need for a simple and accurate description of the soil reaction. Available models employ local and frequency-independent springs and dashpots, arranged together with non-linear elements to account for the soil reaction in a computationally efficient manner.

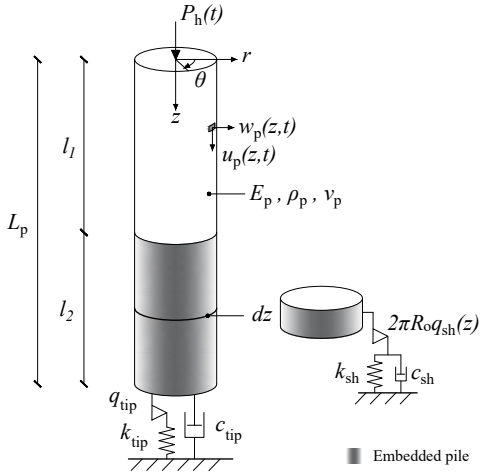

Figure 3.2: A 3-D axisymmetric pile driving model, in which the pile is described as a thin cylindrical shell.

The significance of modelling accurately the linear part of these phenomenological models is enhanced when a pile is close to refusal during driving and essentially the linear regime is strongly present [84]. In view of the aforementioned, the employment of a non-local soil reaction model comprises a significant step towards computationally efficient and more realistic foundation models [207], while it has been recently applied for capturing the lateral response of monopiles [208].

In the present study, the approach adopted is similar to Friswell et al. [207]. Accordingly, the derivation of non-local foundation models follows from the weighted average of state variables (e.g. displacement, velocity) over a spatial domain via convolution integrals; the associated spatial kernel functions are defined by a characteristic length measure. In the ensuing, the spatial kernel is assumed to be a Gaussian function $g_G(z,\xi)$, normalized as shown in [209], with the following form:

$$g_G(z,\xi) = \frac{\alpha_G}{\sqrt{2\pi}} e^{-\frac{\alpha_G^2 (z-\xi)^2}{2}} \tag{3.10}$$

in which α_G is the inverse of the influence distance of the spatial kernel function $g_G(z,\xi)$ (see Fig. 3.3). At this point let us remark that the local foundation models can also be described in this form and essentially comprise a special case with spatial kernel equal to the Dirac delta function, $g_G(z,\xi) = \delta(z-\xi)$. The latter means that the foundation is locally reacting. According to the previous, the non-local soil reaction along the pile shaft $\bar{p}_{sh}$ reads:

$$\bar{p}_{\mathrm{sh}} = \begin{cases} \int_{l_1}^{L_\mathrm{p}} g_\mathrm{G}(z,\xi)\left(k_\mathrm{sh}\left(u_\mathrm{p}(\xi,t) - u_{\mathrm{eq,sh}}(\xi,t)\right) + c_\mathrm{sh}\frac{\partial u_\mathrm{p}(\xi,t)}{\partial t}\right)\mathrm{d}\xi = G_\mathrm{G}(z,t)\,, & \text{for } |G_\mathrm{G}(z,t)| \le 2\pi R_\mathrm{o} q_\mathrm{sh} \\ 2\pi R_\mathrm{o} q_\mathrm{sh} \operatorname{sgn}\left(\dfrac{\partial u_\mathrm{p}(z,t)}{\partial t}\right), & \text{for } |G_\mathrm{G}(z,t)| > 2\pi R_\mathrm{o} q_\mathrm{sh} \end{cases} \tag{3.11}$$

The present non-local soil reaction model comprises an extension of its local counterpart, by coupling of the locally reacting elements through prescribed spatial kernel functions. The accuracy of such models can be evaluated properly, only by comparison with the dynamic reaction of the three-dimensional soil continuum, which is not considered in this chapter.

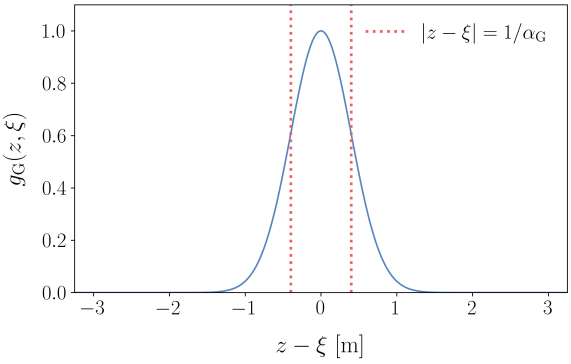

Figure 3.3: The Gaussian function as spatial kernel $g_\mathrm{G}(z,\xi)$ with $\alpha_\mathrm{G} = \sqrt{2\pi}$.

3.2.3. Numerical solution method

For the 1-D model presented in Section 3.2.1, henceforth called 1-D FD model for brevity, the method of central finite differences, of accuracy $\mathcal{O}(\Delta z^2)$, is employed for the spatial discretization. The boundary conditions are treated by introducing fictitious nodes [210] and the non-linear partial differential equation (PDE) governing the pile motion, is decomposed into a set of non-linear ordinary differential equations (ODEs) representing the dynamic equilibria of the pile nodes.

For the 3-D axisymmetric model, henceforth referred to as 3-D LT model for brevity, the spatial discretization is performed by means of the Galerkin method [211]. A series discretization method is advantageous for this system, compared to a method such as finite differences that leads to ODEs at nodal points and thus increases the computational complexity, due to the dimensions of the problem. The Galerkin method circumvents the problem of dimensions, albeit requires a more laborious analytical treatment to utilize its benefits in our case. First, the reformulation of the boundary conditions is performed, as we have a time-dependent boundary condition at $z = 0$ and a non-linear boundary condition at $z = L_\mathrm{p}$. The concentrated body force method (CBFM) is used to reformulate the boundary conditions into stress-free boundaries and to translate the boundary tractions into the equation of motion by means of the Dirac delta function $\delta(\cdot)$ [212]. At this point, the

axisymmetric free vibration modes of the free-free cylindrical shell *in vacuo* are found and employed in our solution as trial and test functions. Therefore, the solution of Eqs. (3.8a) and (3.8b) is approximated by the series:

$$u_{\mathrm{p}} = \sum_{m=0}^{N_m} U_{0m}(z)\, q_{0m}(t) \tag{3.12a}$$

$$w_{\mathrm{p}} = \sum_{m=0}^{N_m} W_{0m}(z)\, q_{0m}(t) \tag{3.12b}$$

in which $q_{0m}(t)$ is the m-th generalized coordinate and N_m is the upper limit of the truncated summation, adequate to provide a sufficiently accurate solution. By substituting Eqs. (3.12a) and (3.12b) into Eqs. (3.8a) and (3.8b), the residual is obtained and by integrating over the shell domain the product of each test function with the residual, the weighted residual is derived. By setting the latter equal to zero, a set of N_m non-linear coupled ODEs of $q_{0m}(t)$ is formulated. Conclusively, for both 1-D FD and 3-D LT models the resulting sets of ODEs are arranged in the state-space form, in order to solve them via numerical integration. The explicit Runge-Kutta method of accuracy $\mathcal{O}(\Delta t^4)$ is used in both cases [213].

For both models, the frequency at which the force amplitude is equal to 10% of the maximum amplitude (see Section 3.3.2) and the corresponding wavelength are used to determine the discretization parameters. For the 1-D FD model, the time step is defined as $\Delta t = \Delta z/(10 c_{\mathrm{p}})$, in which Δz denotes the spatial mesh size, equal to 1/8 of the smallest wavelength to be analysed, and c_{p} is the longitudinal wave velocity in the pile [214]. In the 3-D LT model, the upper frequency limit is used to select the truncation limit N_m in Eq. (3.12) and the time step is set equal to $\Delta t = \pi/(5\omega_m)$ (10 time steps for the highest frequency component ω_m). Further refinement of the previous discretization parameters is performed until convergence is met, defined as:

$$\epsilon_i = \frac{\left| u_{\mathrm{p},i+1}(z,t) - u_{\mathrm{p},i}(z,t) \right|}{\left| u_{\mathrm{p},i+1}(z,t) \right|} < 1\% \tag{3.13}$$

in which ϵ_i is the relative error of the displacement field between the i-th and $(i+1)$-th analyses, used as the convergence criterion.

3.3. Results

In Section 3.3.1 the validity of the 3-D LT model is verified, by reducing it into a physically equivalent model to 1-D FD, for direct comparison. Furthermore, in Sections 3.3.2 and 3.3.3 numerical examples that consider the influence of wave dispersion and non-local soil reaction, respectively, are presented.

3.3.1. Validation of the 3-D LT model

At first, a set of numerical analyses for a single hammer blow are performed to showcase the validity of the 3-D LT model. For this purpose, the 1-D FD model formulated in Section 3.2.1 is used as reference and its results are compared with the respective ones obtained from the 3-D LT model, upon proper reduction to an equivalent classical rod with local soil reaction.

By setting the Poisson's ratio of the pile $\nu_p = 0$ in Eq. (3.8a) and discarding Eq. (3.8b), the equation of motion of the classical rod theory is retrieved. Furthermore, by considering $\alpha_G \to \infty$, the spatial kernel becomes $g_G(z,\xi) = \delta(z-\xi)$ and the soil reaction is rendered local. Under these considerations, the pile is equivalently described by the classical rod theory and the soil reaction is local, in both models. In view of the previous, the numerical results of the 1-D FD and the reduced 3-D LT models should be identical. The parameters of the validation case are shown in Table 3.1 and the hammer force function $P_h(t)$, together with the amplitude of its Fourier transform $|\widetilde{P}_h(f)|$, are depicted in Fig. 3.4.

Pile	Young's modulus	E_p	210 GPa
	Mass density	ρ_p	7850 kg/m^3
	Poisson's ratio	ν_p	0.3
	Length	L_p	42 m
	Radius	R_p	1.1 m
	Wall thickness	h_p	0.03 m
	Initial embedment depth	l_2	25.2 m
Soil	Shear modulus	G_s	18.52 MPa
	Mass density	ρ_s	1900 kg/m^3
	Poisson's ratio	ν_s	0.35
	Friction angle	ϕ'	35^o
	Soil-pile interface friction angle	δ'	31.5^o
Hammer	Ram mass	m_r	10000 kg
	Anvil mass	m_a	1000 kg
	Cushion stiffness	k_c	70.87x10^6 kN/m
	Ram impact velocity	v_0	5 m/s

Table 3.1: Parameters of the validation case.

In Fig. 3.5 the axial tip displacement $u_p(L_p, t)$ is presented for a single hammer blow, as obtained by the two models in consideration. Evidently, the response obtained by the two approaches is in excellent agreement. Therefore, in the following analyses the capabilities of the 3-D LT model can be utilized fully, to study the dispersion of elastic waves in the pile and the introduction of non-locality in the soil reaction along the pile shaft.

3.3.2. Influence of wave dispersion

To isolate the effect of wave dispersion, the 3-D LT model used in the following examples, has local soil reaction and differs from the 1-D FD solely in the pile description as a thin cylindrical shell. For the following numerical examples, all the parameter values are given in Table 3.1, except for R_p, h_p, l_2 and the hammer parameters. The initial embedment depths of $l_2 = 0.4L_p, 0.5L_p, 0.6L_p$ are considered, while various pile radii are used (see Table 3.2), to identify the effect of these parameters on wave dispersion. In Table 3.2 each column provides a pair of pile radius R_p and wall thickness h_p leading to eleven different pile geometries.

Regarding the properties of the hammer, attention is needed in order to have results

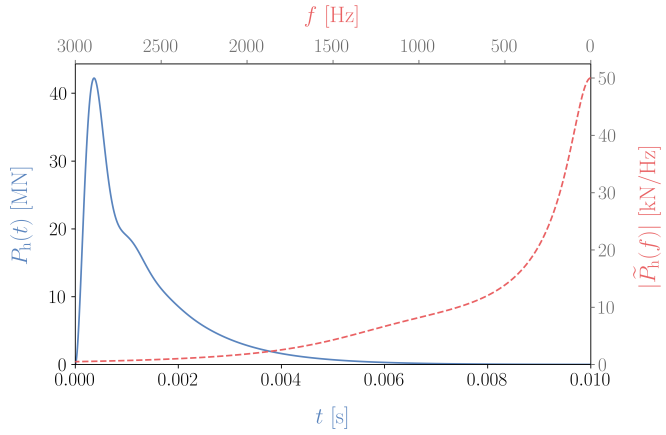

Figure 3.4: Hammer force function $P_h(t)$ (in blue) and the amplitude of its Fourier transform $|\widetilde{P}_h(f)|$ (in red) for a pile with $R_p = 1.1$ m and $h_p = 0.03$ m.

R_p	1.1 m	1.4 m	1.7 m	2.0 m	2.3 m	2.6 m	2.9 m	3.2 m	3.5 m	3.8 m	4.1 m
h_p	3 cm	3 cm	3 cm	4 cm	4 cm	4 cm	4 cm	5 cm	5 cm	5 cm	5 cm

Table 3.2: Set of variable pile parameters.

that can be compared on a rational basis. For that purpose, normalization of the hammer force was performed for all pile driving cases, such that the maximum axial stress at the pile head was equal to 57% of the yield stress, $f_y = 355$ MPa. The dimensionless mass ratio $m_a^* = m_a / m_r$ and the dimensionless cushion stiffness $k_c^* = k_c m_r / Z_p^2$ with Z_p denoting the impedance of a semi-infinite rod, were used in order to achieve the normalization in all cases [85]. The aforementioned parameters were set to $m_a^* = 0.1$ and $k_c^* = 10$ in all the cases studied, while the ram impact velocity v_0 was equal to 5 m/s. Therefore, depending on the pile geometry, the values of ram mass m_r, anvil mass m_a and cushion stiffness k_c were scaled in order to preserve the dimensionless quantities and the maximum axial stress level constant. According to the previous, the Fourier transform of the hammer force normalized over the maximum amplitude at zero frequency as $\overline{P}_h(f) = |\widetilde{P}_h(f)|/|\widetilde{P}_h(0)|$, is identical for all piles considered. In Fig. 3.6 the normalized amplitude of the hammer force spectrum is depicted together with the normalized amplitude at the ring frequency of each pile of this study, indicated by the red markers.

In Fig. 3.7 the ultimate pile set ratio $u_{LT}(L_p, t_f) / u_{FD}(L_p, t_f)$ is displayed, in which $u_{LT}(L_p, t_f)$ and $u_{FD}(L_p, t_f)$ denote the tip displacement of 3-D LT and 1-D FD models, respectively, at the final time moment of the analysis t_f. It is noted that t_f was adequate for the imparted energy into the pile to dissipate through the soil reaction and the final pile set to be obtained. As can be observed for all the examined pile radii and embedment depths, there is deviation from the response of the 1-D FD model (i.e. ratio equal to 1.0). Consequently, wave dispersion does have an effect even for small-diameter piles, albeit its influence on the final pile set is not as pronounced as in the large-diameter cases. With ascending pile radius

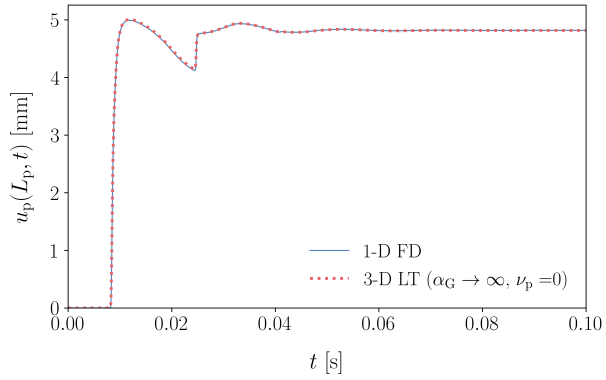

Figure 3.5: Axial tip displacement comparison between the 1-D FD and the reduced 3-D LT model ($\alpha_G \to \infty$ and $\nu_p = 0$).

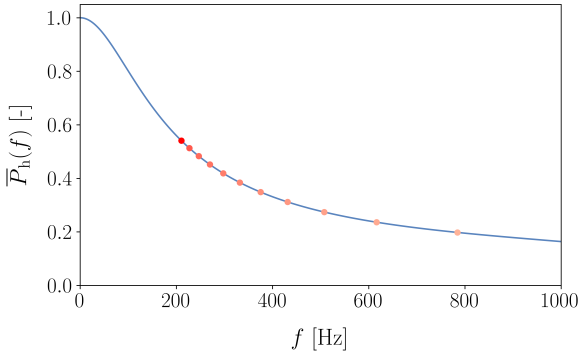

Figure 3.6: Normalized amplitude of the hammer force spectrum $\overline{P}_h(f)$ (blue line), together with the corresponding normalized amplitudes at the ring frequency f_r of all the examined piles (red markers).

R_p, the amount of energy imparted in frequencies around the ring frequency f_r becomes significant. As a result, the increase of $\overline{P}_h(f_r)$ leads clearly to reduction of the ultimate set ratio, as direct consequence of dispersion effects. Embedment depth l_2 seems to be beneficial for the ultimate set ratio and mitigate partially these effects, which is rational since additional damping is provided from the increased length of the shaft in contact with the soil. Wave dispersion is strongly present in high-frequency motions, thus increased embedment depth contributes to their decay and results in a weaker influence on the pile response overall. Notwithstanding the remarks about embedment depth, it seems that for large radii ($R_p \geq 3.0$ m) - or better for high $\overline{P}_h(f_r)$ - the set ratio is less sensitive to its influence. For these pile geometries, the ring frequency f_r is significantly excited by the hammer impact as $\overline{P}_h(f_r)$ approaches 0.5 and relevant induced pile motions obtain large amplitudes. The aforementioned observations and relevant remarks are better understood through Figs. 3.8 and 3.9.

The tip displacement obtained by the two considered models, for the extreme scenarios

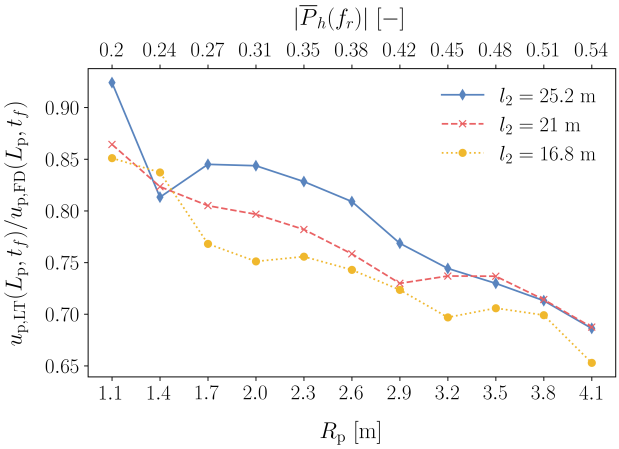

Figure 3.7: Ratios of ultimate set obtained by 3-D LT model to 1-D FD model, $u_{p,LT}(L_p, t_f)/u_{p,FD}(L_p, t_f)$, for the all considered pile radii R_p and initial embedment depths l_2.

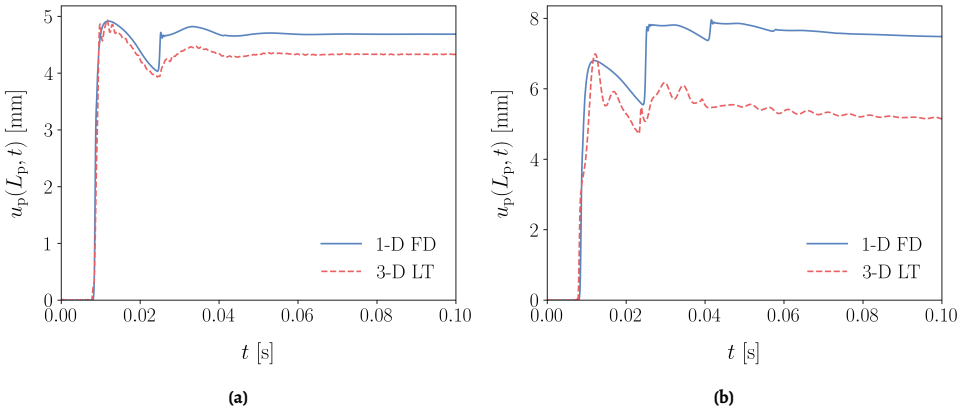

Figure 3.8: Tip displacement $u_p(L_p, t)$ obtained by the 1-D FD and 3-D LT models for a pile with $l_2 = 25.2$ m, (**a**) $R_p = 1.1$ m and (**b**) $R_p = 4.1$ m

of the smallest and the largest pile radii, are shown in Fig. 3.8. Evidently, the two responses for $R_p = 4.1$ m (Fig. 3.8b) deviate much more than for $R_p = 1.1$ m (Fig. 3.8a). In Fig. 3.8a, the displacements mainly diverge for the two approaches after the second arrival of the impact-induced stress wave at the pile tip (after $t = 0.02$ s), but follow the same trend. On the contrary, in Fig. 3.8b the response becomes dissimilar already after the first arrival of the stress wave at the pile tip, as the frequency content of this motion is much richer in components that display dispersive behaviour. The amplitude of the discrete Fourier transform (DFT) spectra of the velocities for the cases analysed in Fig. 3.8, are given in Fig. 3.9 to supplement the previous observations.

In Fig. 3.9a, the amplitude of the axial velocity spectrum for both models is in good agreement approximately up to 600 Hz. At that point, the amplitude of the axial velocity

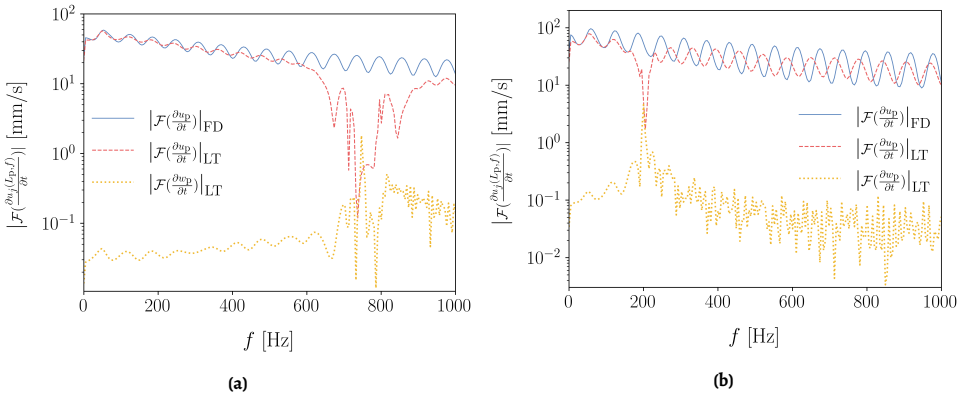

Figure 3.9: Amplitude of axial velocity spectra $\left|\frac{\partial u_p(L_p,f)}{\partial t}\right|$ and radial velocity spectra $\left|\frac{\partial w_p(L_p,f)}{\partial t}\right|$ (for the 3-D LT model) for a pile with $l_2 = 0.6L_p$, (**a**) $R_p = 1.1$ m and (**b**) $R_p = 4.1$ m.

in the 3-D LT model drops significantly and energy in axial motion is reduced at these frequencies. However, it is not the case that energy is not present in this region of the frequency spectrum in the pile motion. As can be observed, the radial velocity amplitudes surge in this region of the spectrum and even surpass the amplitudes of the axial velocity in some frequencies. For this case the ring frequency is f_r =784.48 Hz, which supports our observations as the frequency region of strong dispersive effects is traced around this value. Considering further the case of $R_p = 4.1$ m, in Fig. 3.9b the velocity spectrum shows some differences with respect to Fig. 3.9a. First, the drop corresponding to the vicinity of the ring frequency occurs much lower in the frequency axis, as f_r =210.47 Hz and even in the low frequency region of the axial velocity spectrum, discrepancy exists between the two models. The latter already indicates that dispersion is present in lower frequencies compared to Fig. 3.9a, and its effect is more eminent as the energy imparted from the hammer impact is greater in this frequency region (see Fig. 3.6). For $R_p = 1.1$ m, the velocity amplitudes are in good agreement up to a certain frequency (approximately 600 Hz), albeit for $R_p = 4.1$ m they clearly deviate along the whole spectrum indicating the inaccurate description of wave propagation in the 1-D FD model. The preceding remarks lead to the strong discrepancy observed between 1-D FD and 3-D LT results in Fig. 3.8b.

3.3.3. Influence of non-local soil reaction

At this point, the introduction of non-locality in the soil reaction of the 3-D LT model is examined. For that purpose, the 3-D LT model with local soil reaction and its non-local counterpart are compared. The exact spatial distribution of the non-local soil reaction is not known and in this work the Gaussian function is assumed as the spatial kernel *a priori*, with three different values of influence distance considered, namely $1/\alpha_G = L_p/100, L_p/200, L_p/500$. In Fig. 3.10, the axial tip displacement $u_p(L_p, t)$ is presented for $R_p = 1.1$ m and $R_p = 4.1$ m ($l_2 = 25.2$ m). As can be seen, the divergence of the displacement obtained by the non-local model compared to the local one is much stronger for the large-diameter pile.

To better evaluate the effects of non-locality, in Fig. 3.11 for each pile the displacement

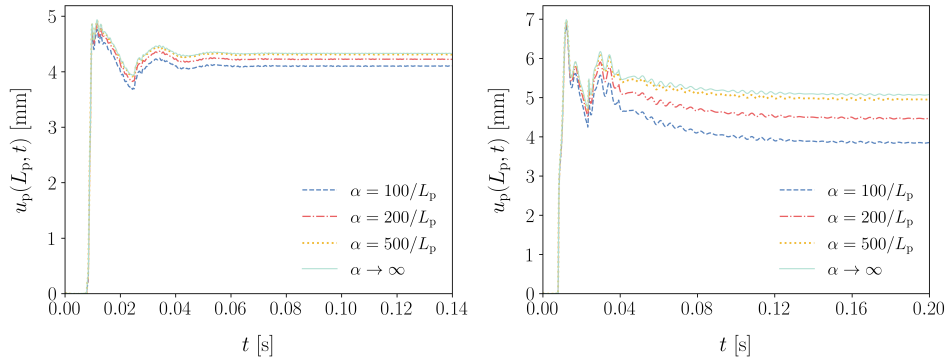

(a) $R_p = 1.1$ m **(b)** $R_p = 4.1$ m

Figure 3.10: Axial tip displacement $u_p(L_p, t)$ obtained by the local and non-local reaction models for $l_2 = 25.2$ m and various values of α_G.

ratio of non-local to local models, $\overline{u}_p(t) = u_p(L_p, t) / u_p(L_p, t)\big|_{\alpha_G \to \infty}$ is examined for four different pile radii. The effect of non-locality seems to become more eminent for large-diameter piles and the deviation even between the non-local models for different values of α_G becomes quite important. On the other hand, for $R_p = 1.1$ m and $R_p = 2.0$ m all the non-local reaction models considered present a ratio, $\overline{u}_p(t)$, from 0.9 to 1.0, practically meaning that for the values of α_G considered, local and non-local reactions do not significantly alter the final pile penetration. In all cases, the non-locality seems to reduce the final pile penetration for the considered soil profile. Furthermore, the increase of α_G (decrease of influence distance) tends to provide a response that converges to the one of the local reaction model, which is rational. To summarize, Fig. 3.11 reveals that the non-locality of the soil reaction can affect the pile response in variable degree and the pile radius seems to be a significant factor that determines the amount of this influence by altering the pile motion characteristics.

Apart from the pile radius, the parameter of the embedment depth l_2, is finally considered. In Fig. 3.12, the results for the smallest ($R_p = 1.1$ m) and the largest ($R_p = 4.1$ m) pile radii of this study are shown, for $l_2 = 16.8$ m and $l_2 = 25.2$ m. At a first glance, the different values of l_2 do not appear to significantly alter the displacement ratios, $\overline{u}_p(t)$. For both piles the larger l_2 value seems to lead to a minor reduction of $\overline{u}_p(t)$. Finally, the introduction of the soil reaction in the radial direction and the study of its effect on pile penetration comprise additional steps not considered herein, as this work focuses on dispersive wave propagation and non-local soil reaction in the direction of driving.

3.4. Conclusions

In this chapter, a 3-D axisymmetric pile driving model with non-local soil reaction is developed, as an extension of standard local 1-D modelling approaches. The pile description is based on the Love-Timoshenko theory for thin cylindrical shells and the non-local soil reaction is formulated as a convolution integral of local soil reaction models and the Gaussian function as spatial kernel. Furthermore, the 1-D basis model is formulated according

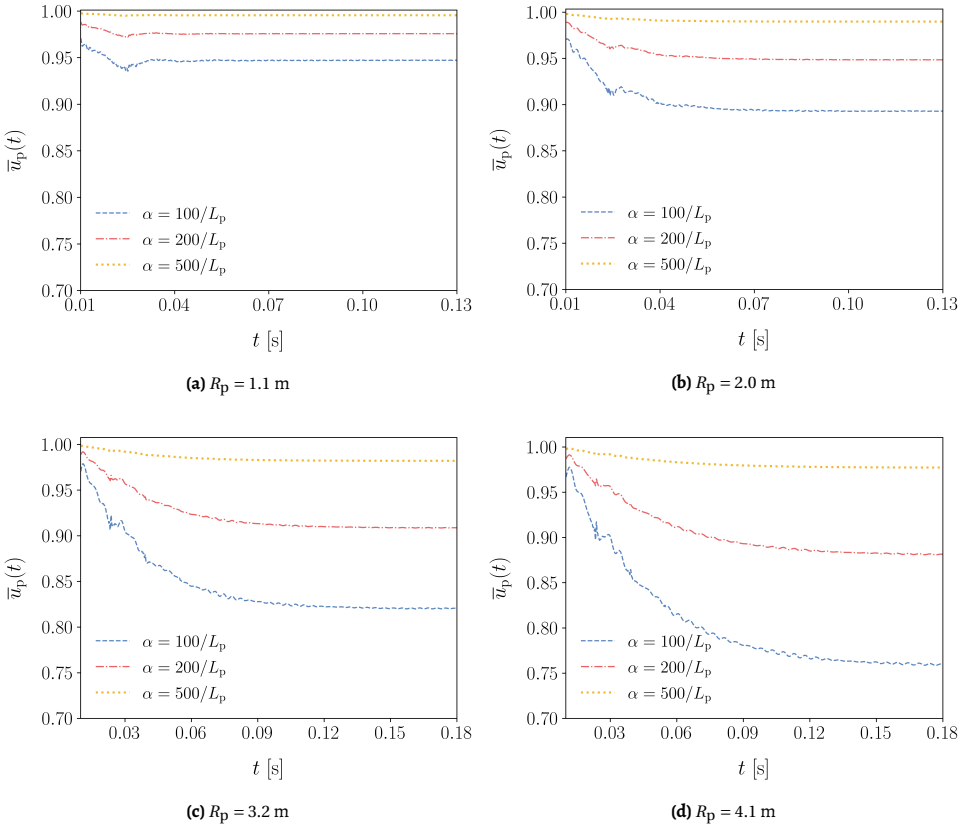

(a) $R_\mathrm{p} = 1.1$ m

(b) $R_\mathrm{p} = 2.0$ m

(c) $R_\mathrm{p} = 3.2$ m

(d) $R_\mathrm{p} = 4.1$ m

Figure 3.11: Displacement ratio of non-local to local reaction models, $\overline{u}_\mathrm{p}(t) = u_\mathrm{p}(L_\mathrm{p}, t) / \left. u_\mathrm{p}(L_\mathrm{p}, t)\right|_{\alpha\to\infty}$ for a pile with $l_2 = 25.2$ m.

to widely adopted approaches in pile driving and is compared against the 3-D model, with a view to investigate the effects of elastic wave dispersion and non-locality of the soil reaction.

First, the effect of elastic wave dispersion in the pile was studied, for various pile geometries and initial embedment depths. The main argument of the significance of wave dispersion in drivability of large-diameter monopiles was ascertained, as the effect of dispersion was even found to increase with ascending pile radius. Embedment depth provided some mitigation of this effect for small-to-medium pile radii, while for large-diameter piles the effect of wave dispersion was sustained even for large pile embedments. In the vicinity of the ring frequency pile motion is predominantly radial and significantly excited by the hammer impact for large-diameter monopiles. This effect cannot be captured by 1-D models and can alter the soil resistance to driving (not considered herein). In the current effort to modify, or even reinvent, the existing drivability approaches for large-diameter monopiles, the proper description of the pile motion is essential. Otherwise, certain response features in field data from monopile installation, resulting from wave dispersion, may be falsely attributed to other mechanisms, e.g. non-linear soil behaviour, and lead us further away

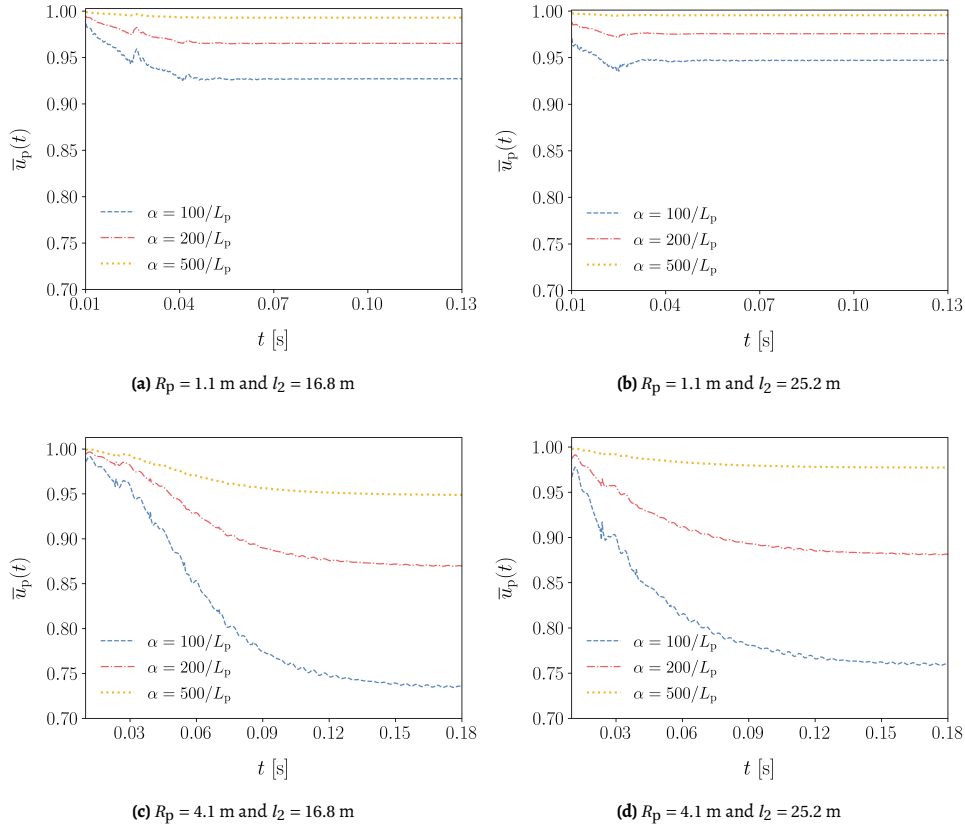

(a) $R_p = 1.1$ m and $l_2 = 16.8$ m

(b) $R_p = 1.1$ m and $l_2 = 25.2$ m

(c) $R_p = 4.1$ m and $l_2 = 16.8$ m

(d) $R_p = 4.1$ m and $l_2 = 25.2$ m

Figure 3.12: Displacement ratio of non-local to local reaction models, $\overline{u}_p(t) = u_p(L_p, t) / \left. u_p(L_p, t) \right|_{\alpha_G \to \infty}$.

from an accurate approach to predict monopile drivability.

Conclusively, the introduction of non-local soil reaction has been realized. A system of integro-differential equations is obtained, which is solved by means of the Galerkin method and numerical integration. The effect of non-locality was found to be more influential in the case of large diameters, where the pile motion deviates significantly from the non-dispersive purely axial motion considered in standard rod-based models. Furthermore, the variable embedment depth yielded minor differences between local and non-local models. Decrease of the influence distance $1/\alpha_G$ showcased the trend to converge to the response of the local reaction model, which is the expected behaviour. The results for various influence distances comprise an indication of the degree to which non-locality may affect the overall behaviour. The refinement of the non-local soil reaction by also introducing frequency-dependence, based on the response of the three-dimensional soil continuum is considered the optimal next step. In that manner, a non-local - both in space and time - soil reaction model may be employed in modelling approaches for impact piling, as well as for other installation methods.

4

Wave propagation in layered soil media

The paradigm of the previous chapter showcased the significance of wave dispersion in the pile and its accurate description, in particular in the case of large-diameter monopiles. However, another aspect of pile drivability modelling was touched upon, namely the soil reaction modelling. With a view to modelling approaches applicable to engineering practice, certain physical mechanisms are commonly discarded for the sake of simplicity and computational convenience. Specifically, the reaction provided by a continuum (e.g. 3-D soil medium) should be rigorously characterized by spatial and temporal non-locality. In the previous chapter, a standard local and frequency-independent reaction model was transformed via a spatial kernel to a non-local one. However, the spatially non-local model was neither rigorously based on the 3-D soil medium at hand, nor possessed any form of frequency dependence. In addition to these considerations, spatial and temporal non-locality are essentially coupled through the dispersion characteristics of the soil medium, thus complicating further the potential application of this process in soil-structure interaction problems. In view of these considerations, it appears that to incorporate the true non-local - in space and time - reaction provided by the soil medium at hand, the most sensible approach is also the direct one, i.e. to treat the problem of the 3-D soil medium.

In the ensuing, the propagation of mechanical disturbances in a linear elastic soil medium is studied. With a view to pile installation, a modelling framework that can seamlessly treat arbitrarily layered soil media is indispensable. For that purpose, the Thin-Layer Method (TLM) is considered as the optimal choice, in order to eradicate the formidable complications introduced by soil layering. Beginning from the resolution of wave motion in terms of displacement potentials, the formulation of the TLM is presented, leading to the generalized eigenvalue problem of cylindrical waves and the respective normal modes of wave propagation. The outlined developments are suitable to analyse problems that deal with a layered soil stratum of finite depth overlying a rigid bedrock. To extend the applicability of the present TLM formulation, the approximation of the underlying half-space is accomplished by coupling the TLM with Perfectly Matched Layers (PMLs). Subsequently, we proceed to

derive explicit expressions for the Green's functions in the frequency-space domain in the context of the TLM. The latter are valid both for the original and the PMLs-augmented TLM formulation, which is also verified by a set of numerical examples presented at the end of the chapter.

4.1. Wave propagation in a linear isotropic elastic solid

Consider a linear elastic isotropic medium described in a cylindrical coordinate system (r, θ, z) with unit basis vectors $\mathbf{e}_r$, $\mathbf{e}_\theta$, $\mathbf{e}_z$. The dynamic equilibrium equations governing the displacement vector field, commonly termed as Navier equations, may be expressed in the frequency domain as [215]:

$$(\lambda_\mathrm{s} + G_\mathrm{s})\,\nabla(\nabla\cdot\widetilde{\mathbf{u}}_\mathrm{s}) + G_\mathrm{s}\nabla^2\widetilde{\mathbf{u}}_\mathrm{s} + \omega^2\rho_\mathrm{s}\widetilde{\mathbf{u}}_\mathrm{s} = 0 \tag{4.1}$$

where λ_s and G_s are the Lamé parameters and ρ_s is the mass density. The displacement vector $\widetilde{\mathbf{u}}_\mathrm{s}$ is defined as:

$$\widetilde{\mathbf{u}}_\mathrm{s} = \begin{bmatrix} \widetilde{u}_{r,\mathrm{s}}(r,\theta,z,\omega) & \widetilde{u}_{\theta,\mathrm{s}}(r,\theta,z,\omega) & \widetilde{u}_{z,\mathrm{s}}(r,\theta,z,\omega) \end{bmatrix}^\mathrm{T} \tag{4.2}$$

The Fourier transform pair of a general function $f(t)$ is defined as follows:

$$f(t) = \frac{1}{2\pi}\int_{-\infty}^{+\infty} \widetilde{f}(\omega)\mathrm{e}^{\mathrm{i}\omega t}\,\mathrm{d}\omega \tag{4.3a}$$

$$\widetilde{f}(\omega) = \int_{-\infty}^{+\infty} f(t)\mathrm{e}^{-\mathrm{i}\omega t}\,\mathrm{d}t \tag{4.3b}$$

We proceed to analyse the propagation of mechanical waves in the absence of body loads and boundary effects. The displacement vector field governing the wave motion of a linear elastic solid may be decomposed into an irrotational and a solenoidal vector field, based on Lamé potentials [216]:

$$\widetilde{\mathbf{u}}_\mathrm{s} = \nabla\widetilde{\phi}_\mathrm{s} + \nabla\times\widetilde{\boldsymbol{\psi}}_\mathrm{s} \tag{4.4}$$

Upon substitution of Eq. (4.4) into Eq. (4.1), the following set of identities from vector calculus are invoked:

$$\nabla^2\left(\nabla\widetilde{\phi}_\mathrm{s}\right) = \nabla\left(\nabla\cdot(\nabla\widetilde{\phi}_\mathrm{s})\right) = \nabla\left(\nabla^2\widetilde{\phi}_\mathrm{s}\right) \tag{4.5a}$$

$$\nabla^2\left(\nabla\times\widetilde{\boldsymbol{\psi}}_\mathrm{s}\right) = \nabla\times\left(\nabla^2\widetilde{\boldsymbol{\psi}}_\mathrm{s}\right) \tag{4.5b}$$

$$\nabla\cdot\left(\nabla\times\widetilde{\boldsymbol{\psi}}_\mathrm{s}\right) = 0 \tag{4.5c}$$

Subsequently, a series of mathematical operations and term rearrangements are applied to the Navier equations leading to the following:

$$\nabla\left((\lambda_\mathrm{s}+2G_\mathrm{s})(\nabla^2\widetilde{\phi}_\mathrm{s})+\omega^2\rho_\mathrm{s}\widetilde{\phi}_\mathrm{s}\right)+\nabla\times\left(G_\mathrm{s}(\nabla^2\widetilde{\boldsymbol{\psi}}_\mathrm{s})+\omega^2\rho_\mathrm{s}\widetilde{\boldsymbol{\psi}}_\mathrm{s}\right)=0 \tag{4.6}$$

In the preceding equation, it is evident that the equations of motion are satisfied if both terms vanish, thus resulting to:

$$\nabla^2\widetilde{\phi}_\mathrm{s}+\frac{\omega^2}{c_\mathrm{P}^2}\widetilde{\phi}_\mathrm{s}=0 \tag{4.7}$$

$$\nabla^2\widetilde{\boldsymbol{\psi}}_\mathrm{s}+\frac{\omega^2}{c_\mathrm{S}^2}\widetilde{\boldsymbol{\psi}}_\mathrm{s}=0 \tag{4.8}$$

where $c_\mathrm{P}=\sqrt{(\lambda_\mathrm{s}+2G_\mathrm{s})/\rho_\mathrm{s}}$ and $c_\mathrm{S}=\sqrt{G_\mathrm{s}/\rho_\mathrm{s}}$ denote, respectively, the P- and S-wave velocities.

4.1.1. Propagation of dilatational (P) waves in a linear elastic solid

The scalar Helmholtz equation that governs the propagation of dilatational waves in a linear elastic medium reads:

$$\nabla^2\widetilde{\phi}_\mathrm{s}+k_\mathrm{P}^2\widetilde{\phi}_\mathrm{s}=0 \tag{4.9}$$

where $k_\mathrm{P}=\omega/c_\mathrm{P}$ denotes the P wavenumber. A solution is sought in the form of separation of variables as follows:

$$\widetilde{\phi}_\mathrm{s}=R_\phi(r)\Theta_\phi(\theta)Z_\phi(z) \tag{4.10}$$

By substituting Eq. (4.10) into Eq. (4.9) and upon separating variables twice, the following three equations are obtained:

$$\frac{\mathrm{d}^2R_\phi}{\mathrm{d}r^2}+\frac{1}{r}\frac{\mathrm{d}R_\phi}{\mathrm{d}r}+\left(k_\mathrm{P}^2-k_z^2-\frac{n^2}{r^2}\right)R_\phi=0 \tag{4.11}$$

$$\frac{\mathrm{d}^2\Theta_\phi}{\mathrm{d}\theta^2}+n^2\Theta_\phi=0 \tag{4.12}$$

$$\frac{\mathrm{d}^2Z_\phi}{\mathrm{d}z^2}+k_z^2Z_\phi=0 \tag{4.13}$$

where k_z is the vertical wavenumber and n is the azimuthal index. The general solutions to the preceding equations are readily available and may be written as:

$$R_\phi(r)=d_1J_n(k_\alpha r)+d_2Y_n(k_\alpha r) \tag{4.14}$$

$$\Theta_\phi(\theta)=d_3\cos(n\theta)+d_4\sin(n\theta) \tag{4.15}$$

$$Z_\phi(z)=d_5\mathrm{e}^{\mathrm{i}k_zz}+d_6\mathrm{e}^{-\mathrm{i}k_zz} \tag{4.16}$$

where $J_n(k_\alpha r)$ and $Y_n(k_\alpha r)$ denote, respectively, the Bessel functions of first and second kinds of order n, $k_\alpha=\sqrt{k_\mathrm{P}^2-k_z^2}$ is the radial wavenumber and d_i are arbitrary constants.

It is noted that the harmonic variation in the azimuth should also satisfy the periodicity/continuity condition: $\Theta_\phi(\theta) = \Theta_\phi(\theta + 2\pi)$. Therefore, the azimuthal index n may acquire only non-negative integer values. Conclusively, the scalar potential $\widetilde{\phi}_\mathrm{s}$ may be expressed as:

$$\widetilde{\phi}_\mathrm{s} = (d_1 J_n(k_\alpha r) + d_2 Y_n(k_\alpha r))(d_3 \cos(n\theta) + d_4 \sin(n\theta))(d_5 \mathrm{e}^{\mathrm{i}k_z z} + d_6 \mathrm{e}^{-\mathrm{i}k_z z}) \tag{4.17}$$

4.1.2. Propagation of distortional (S) waves in a linear elastic solid

The propagation of distortional (S) waves in a linear elastic medium is governed by the vector Helmholtz equation:

$$\nabla^2 \widetilde{\boldsymbol{\psi}}_\mathrm{s} + k_\mathrm{S}^2 \widetilde{\boldsymbol{\psi}}_\mathrm{s} = 0 \tag{4.18}$$

where $k_\mathrm{S} = \omega / c_\mathrm{S}$ is the S wavenumber. In the context of elastodynamics, different solution forms have been put forward for $\widetilde{\boldsymbol{\psi}}_\mathrm{s}$. The solution of Eq. (4.1) by means of potentials is customarily employed on the basis of the Helmholtz decomposition theorem. Accordingly, a solution in the form of Eq. (4.4) is assumed together with the so-called gauge condition that requires $\widetilde{\boldsymbol{\psi}}_\mathrm{s}$ to be solenoidal, i.e. $\nabla \cdot \widetilde{\boldsymbol{\psi}}_\mathrm{s} = 0$. Based on these considerations the solution to the vector Helmholtz equation reads [217, 161, 163, 218, 219]:

$$\widetilde{\boldsymbol{\psi}}_\mathrm{s} = \nabla \times \left(\widetilde{\chi}\mathbf{e}_z\right) + \nabla \times \nabla \times \left(\widetilde{\eta}\mathbf{e}_z\right) \tag{4.19}$$

where $\widetilde{\chi}$ and $\widetilde{\eta}$ are scalar potentials. The gauge condition poses an additional constraint that relates the three displacement components to the four components (in total) of $\widetilde{\phi}_\mathrm{s}$ and $\widetilde{\boldsymbol{\psi}}_\mathrm{s}$. However, $\widetilde{\boldsymbol{\psi}}_\mathrm{s}$ needs not to be necessarily solenoidal and another solution form can be employed for Eq. (4.18) that reads [220, 221, 163, 222]:

$$\widetilde{\boldsymbol{\psi}}_\mathrm{s} = \widetilde{\chi}\mathbf{e}_z + \nabla \times (\widetilde{\eta}\mathbf{e}_z) \tag{4.20}$$

Both Eqs. (4.19) and (4.20), upon substitution into Eq. (4.18), reduce the vector Helmholtz equation to the following two scalar Helmholtz equations:

$$\nabla^2 \widetilde{\chi} + k_\mathrm{S}^2 \widetilde{\chi} = 0 \tag{4.21}$$

$$\nabla^2 \widetilde{\eta} + k_\mathrm{S}^2 \widetilde{\eta} = 0 \tag{4.22}$$

Therefore, the general solution to Eqs. (4.21) and (4.22) has identical form to Eq. (4.17) and the general solution of $\widetilde{\boldsymbol{\psi}}_\mathrm{s}$ may be found by direct substitution. Similar to the solenoidal gauge condition that Eq. (4.19) is subject to, an additional constraint to reduce the number of independent components of potentials is essential for Eq. (4.20). For that purpose, a generalized gauge condition can be formulated as follows [163]:

$$\left(\nabla^2 + k_\mathrm{S}^2\right)\left(\nabla \cdot \widetilde{\boldsymbol{\psi}}_\mathrm{s}\right) = 0 \tag{4.23}$$

As can be seen, the solenoidal gauge condition corresponds to the trivial solution of Eq. (4.23), i.e. $\nabla \cdot \widetilde{\boldsymbol{\psi}}_\mathrm{s} = 0$, whereas Eq. (4.20) satisfies Eq. (4.23) in a non-trivial manner.

The preceding developments were based on the resolution of the displacement field in terms of Lamé potentials. It is worth noting that another representation can be formulated based on the so-called Somigliana potentials [223]. However, the displacement field is mostly expressed in terms of Lamé potentials, due to their compactness and simplicity [220]. Naturally, Lamé and Somigliana potentials are related to each other, with the latter fulfilling the solenoidal gauge condition.

Considering that the general solutions for the two displacement potentials $\widetilde{\phi}_{\mathrm{s}}$ and $\widetilde{\boldsymbol{\psi}}_{\mathrm{s}}$ have been obtained, the general solution to the displacement field can be formulated by substitution. For purposes that will become evident in the ensuing developments, the general solution of the displacement field is arranged in a compact matrix form as follows [219]:

$$\widetilde{\mathbf{u}}_{\mathrm{s}} = \mathbf{T}_n \mathbf{C}_n \widetilde{\mathbf{f}} \tag{4.24}$$

where the diagonal matrix $\mathbf{T}_n$ is an azimuthal matrix that expands the displacement field into a Fourier series in θ. The displacement field may be either symmetric or anti-symmetric with respect to $\theta = 0$, with the corresponding azimuthal matrices defined as:

$$\mathbf{T}_n^{\mathrm{s}} = \begin{bmatrix} \cos(n\theta) & 0 & 0 \\ 0 & -\sin(n\theta) & 0 \\ 0 & 0 & \cos(n\theta) \end{bmatrix} \tag{4.25a}$$

$$\mathbf{T}_n^{\mathrm{a}} = \begin{bmatrix} \sin(n\theta) & 0 & 0 \\ 0 & \cos(n\theta) & 0 \\ 0 & 0 & \sin(n\theta) \end{bmatrix} \tag{4.25b}$$

Conclusively, the Bessel matrix $\mathbf{C}_n$ is defined as follows:

$$\mathbf{C}_n = \begin{bmatrix} \dfrac{\mathrm{d}J_n(kr)}{\mathrm{d}(kr)} & \dfrac{n}{kr} J_n(kr) & 0 \\ \dfrac{n}{kr} J_n(kr) & \dfrac{\mathrm{d}J_n(kr)}{\mathrm{d}(kr)} & 0 \\ 0 & 0 & J_n(kr) \end{bmatrix} \tag{4.26}$$

where k is the radial wavenumber variable and $J_n(kr)$ denotes the Bessel function of the first kind of order n. The form of $\mathbf{C}_n$ implies that P and S waves have common radial wavenumber, satisfying compatibility and equilibrium conditions to adjoin adjacent soil layers with a view to problems of horizontally stratified media. Finally, $\widetilde{\mathbf{f}}$ provides both the dependency in frequency and in the vertical coordinate in terms of exponential functions - the latter are omitted here for reasons that will become apparent in the ensuing.

4.2. Normal modes of a layered soil medium via the Thin-Layer Method (TLM)

In the following, the development of the Thin-Layer Method (TLM) is presented. As a generic framework, the TLM is a superbly efficient computational method to analyse dynamic

problems in two and three dimensions [224]. The main field of application is the analysis of wave motion in layered media, where the TLM has been instrumental in a vast number of contributions in the last decades. The fundamental concept of the TLM lies in the partial discretization of the problem at hand only along the direction of layering. In particular, a finite element discretization is performed along one spatial coordinate combined with analytical solutions in the remaining directions. In essence, the TLM corresponds to the discrete version of the normal modes approach, that is widely used in acoustic, elastic and acousto-elastic problems [218, 225], and by virtue of its discrete formulation the modes are obtained via a quadratic eigenvalue problem circumventing the need for complex search techniques.

Lysmer [226] was the first to employ a form of the TLM, albeit the development of its present formulation is attributed to Waas [227] and Kausel [75]. Following these seminal works, a number of studies followed focusing on various aspects of wave propagation in layered soil media and soil-structure interaction problems [228–232]. Subsequent developments were realized extending the application of the TLM to fluid [233–235], poro-elastic [236, 237] and anisotropic media [238]. More recently, the TLM - owing to its versatility - has been coupled to other powerful frameworks as, for instance, the stochastic finite element method (SFEM) for the analysis of stochastic media (stochastic TLM) [239–241], and the domain reduction method (DRM) [242, 243] for the simulation of seismic scenarios with topographic features [244]. This is by no means an exhaustive list of the most significant developments in the topic, but merely a brief outline of some of the major works that have formed the TLM up to the present.

Without further delay, let us consider a soil layer of infinite horizontal extent comprised of a linear elastic isotropic material with mass density ρ_s and Lamé constants λ_s and G_s. The equations of motion in cylindrical coordinates (r, θ, z) may be expressed in matrix form as follows [219]:

$$\mathfrak{p}_\mathrm{s} + \mathbf{L}_{\sigma,\mathrm{s}}^\mathrm{T} \boldsymbol{\sigma}_\mathrm{s} - \rho_\mathrm{s} \frac{\partial^2 \mathbf{u}_\mathrm{s}}{\partial t^2} = \mathbf{0} \tag{4.27}$$

where $\mathbf{u}_\mathrm{s}$ is the displacement vector, $\mathfrak{p}_\mathrm{s}$ is the body force vector and $\boldsymbol{\sigma}_\mathrm{s}$ is the soil stress tensor. The preceding quantities are defined as:

$$\mathbf{u}_\mathrm{s} = \begin{bmatrix} u_{r,\mathrm{s}} & u_{\theta,\mathrm{s}} & u_{z,\mathrm{s}} \end{bmatrix}^\mathrm{T} \tag{4.28}$$

$$\mathfrak{p}_\mathrm{s} = \begin{bmatrix} p_{r,\mathrm{s}} & p_{\theta,\mathrm{s}} & p_{z,\mathrm{s}} \end{bmatrix}^\mathrm{T} \tag{4.29}$$

$$\boldsymbol{\sigma}_\mathrm{s} = \mathbf{D}_\mathrm{s} \boldsymbol{\varepsilon}_\mathrm{s} = \begin{bmatrix} \sigma_{r,\mathrm{s}} & \sigma_{\theta,\mathrm{s}} & \sigma_{z,\mathrm{s}} & \tau_{\theta z,\mathrm{s}} & \tau_{rz,\mathrm{s}} & \tau_{r\theta,\mathrm{s}} \end{bmatrix}^\mathrm{T} \tag{4.30}$$

where the constitutive matrix $\mathbf{D}_\mathrm{s}$ and the strain tensor $\boldsymbol{\varepsilon}_\mathrm{s}$ read:

$$\mathbf{D}_\mathrm{s} = \begin{bmatrix} \lambda_\mathrm{s}+2G_\mathrm{s} & \lambda_\mathrm{s} & \lambda_\mathrm{s} & 0 & 0 & 0 \\ \lambda_\mathrm{s} & \lambda_\mathrm{s}+2G_\mathrm{s} & \lambda_\mathrm{s} & 0 & 0 & 0 \\ \lambda_\mathrm{s} & \lambda_\mathrm{s} & \lambda_\mathrm{s}+2G_\mathrm{s} & 0 & 0 & 0 \\ 0 & 0 & 0 & G_\mathrm{s} & 0 & 0 \\ 0 & 0 & 0 & 0 & G_\mathrm{s} & 0 \\ 0 & 0 & 0 & 0 & 0 & G_\mathrm{s} \end{bmatrix} \tag{4.31}$$

$$\boldsymbol{\varepsilon}_{\mathrm{s}} = \mathbf{L}_{\varepsilon,\mathrm{s}}\mathbf{u}_{\mathrm{s}} = \begin{bmatrix} \varepsilon_{r,\mathrm{s}} & \varepsilon_{\theta,\mathrm{s}} & \varepsilon_{z,\mathrm{s}} & \gamma_{\theta z,\mathrm{s}} & \gamma_{rz,\mathrm{s}} & \gamma_{r\theta,\mathrm{s}} \end{bmatrix}^{\mathrm{T}} \tag{4.32}$$

The differential matrix operators $\mathbf{L}_{\sigma,\mathrm{s}}$ and $\mathbf{L}_{\varepsilon,\mathrm{s}}$ may be written as:

$$\mathbf{L}_{\sigma,\mathrm{s}}(\cdot) = \mathbf{L}_{r,\mathrm{s}}\frac{\partial(\cdot)}{\partial r} + \mathbf{L}_{\theta,\mathrm{s}}\frac{1}{r}\frac{\partial(\cdot)}{\partial\theta} + \mathbf{L}_{z,\mathrm{s}}\frac{\partial(\cdot)}{\partial z} + \left(\mathbf{L}_{r,\mathrm{s}} - \mathbf{L}_{1,\mathrm{s}}\right)\frac{1}{r}(\cdot) \tag{4.33a}$$

$$\mathbf{L}_{\varepsilon,\mathrm{s}}(\cdot) = \mathbf{L}_{r,\mathrm{s}}\frac{\partial(\cdot)}{\partial r} + \mathbf{L}_{\theta,\mathrm{s}}\frac{1}{r}\frac{\partial(\cdot)}{\partial\theta} + \mathbf{L}_{z,\mathrm{s}}\frac{\partial(\cdot)}{\partial z} + \mathbf{L}_{1,\mathrm{s}}\frac{1}{r}(\cdot) \tag{4.33b}$$

and the partition matrices $\mathbf{L}_{r,\mathrm{s}}$, $\mathbf{L}_{\theta,\mathrm{s}}$, $\mathbf{L}_{z,\mathrm{s}}$ and $\mathbf{L}_{1,\mathrm{s}}$ are defined as follows:

$$\mathbf{L}_{r,\mathrm{s}} = \begin{bmatrix} 1 & 0 & 0 \\ 0 & 0 & 0 \\ 0 & 0 & 0 \\ 0 & 0 & 0 \\ 0 & 0 & 1 \\ 0 & 1 & 0 \end{bmatrix}, \quad \mathbf{L}_{\theta,\mathrm{s}} = \begin{bmatrix} 0 & 0 & 0 \\ 0 & 1 & 0 \\ 0 & 0 & 0 \\ 0 & 0 & 1 \\ 0 & 0 & 0 \\ 1 & 0 & 0 \end{bmatrix} \tag{4.34a}$$

$$\mathbf{L}_{z,\mathrm{s}} = \begin{bmatrix} 0 & 0 & 0 \\ 0 & 0 & 0 \\ 0 & 0 & 1 \\ 0 & 1 & 0 \\ 1 & 0 & 0 \\ 0 & 0 & 0 \end{bmatrix}, \quad \mathbf{L}_{1,\mathrm{s}} = \begin{bmatrix} 0 & 0 & 0 \\ 1 & 0 & 0 \\ 0 & 0 & 0 \\ 0 & 0 & 0 \\ 0 & 0 & 0 \\ 0 & -1 & 0 \end{bmatrix} \tag{4.34b}$$

For a soil layer bounded by two horizontal planes (see Fig. 4.1), the boundary conditions in the presence of external tractions read:

$$\mathbf{t}_{\mathrm{s}}^{(\mathrm{u})} = -\mathbf{s}_{z}^{(\mathrm{u})} \tag{4.35a}$$

$$\mathbf{t}_{\mathrm{s}}^{(\mathrm{l})} = \mathbf{s}_{z}^{(\mathrm{l})} \tag{4.35b}$$

where the superscripts (u) and (l) correspond to the upper ($z = z_{\mathrm{u}}$) and lower ($z = z_{\mathrm{l}}$) horizontal planes, respectively. The traction vector $\mathbf{t}_{\mathrm{s}}$ and the stress vector along a horizontal surface $\mathbf{s}_z$ are defined as:

$$\mathbf{t}_{\mathrm{s}} = \begin{bmatrix} t_{r,\mathrm{s}} & t_{\theta,\mathrm{s}} & t_{z,\mathrm{s}} \end{bmatrix}^{\mathrm{T}} \tag{4.36}$$

$$\mathbf{s}_{z} = \begin{bmatrix} \tau_{zr,\mathrm{s}} & \tau_{z\theta,\mathrm{s}} & \sigma_{z,\mathrm{s}} \end{bmatrix}^{\mathrm{T}} = \mathbf{L}_{z,\mathrm{s}}^{\mathrm{T}}\boldsymbol{\sigma}_{\mathrm{s}} \tag{4.37}$$

To deal with our numerical problem the spatial discretization of the soil domain is needed. At this point the physical domain is discretized into thin horizontal layers of infinite lateral extent, and the displacement field $\mathbf{u}_{\mathrm{s}}$ can be approximated within each thin layer l as:

$$\mathbf{u}_{\mathrm{s}} = \mathbf{T}_{n}\mathbf{C}_{n}\mathbf{N}_{\mathrm{s}}\mathbf{x}_{\mathrm{s}} \tag{4.38}$$

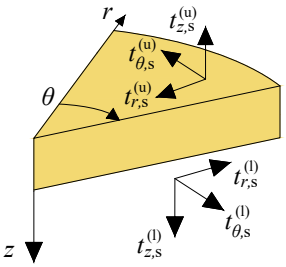

Figure 4.1: A horizontal soil layer of infinite lateral extent with $\mathbf{t}_{\mathrm{s}}^{(\mathrm{u})}$ and $\mathbf{t}_{\mathrm{s}}^{(\mathrm{l})}$ being the traction applied at the upper and lower horizontal boundary surfaces, respectively.

As can be seen, the chosen dependencies in the radial ($\mathbf{C}_n$) and circumferential ($\mathbf{T}_n$) directions are based on the exact solutions that were derived in Section 4.1. Finally, the soil displacements are interpolated along z based on the vector of interface values $\mathbf{x}_{\mathrm{s}}$ and the interpolation matrix $\mathbf{N}_{\mathrm{s}}$ which can be expressed as:

$$\mathbf{N}_{\mathrm{s}} = \begin{bmatrix} N_1^l(z)\mathbf{I}_3 & N_2^l(z)\mathbf{I}_3 \end{bmatrix}, \quad \mathbf{x}_{\mathrm{s}} = \begin{bmatrix} \mathbf{x}_{\mathrm{s}}^{(\mathrm{u})} \\ \mathbf{x}_{\mathrm{s}}^{(\mathrm{l})} \end{bmatrix} \tag{4.39}$$

where $N_1^l(z)$ and $N_2^l(z)$ are linear Lagrange polynomials and $\mathbf{I}_3$ is a 3×3 identity matrix. The interpolation matrix $\mathbf{N}_{\mathrm{s}}$ for quadratic interpolation polynomials can be found in Appendix B.

By substituting Eq. (4.38) into Eqs. (4.27) and (4.35) and considering that the adopted solution is approximate, residual body forces and surface tractions at the boundaries are generated. By invoking the principle of virtual work and requiring that residual body forces and surface tractions perform virtual work equal to zero, we obtain:

$$\int_0^{+\infty}\int_0^{2\pi}\left(\left(\delta\mathbf{u}_{\mathrm{s}}^{(\mathrm{u})}\right)^{\mathrm{T}}\mathbf{r}_{\mathrm{s}}^{(\mathrm{u})} + \left(\delta\mathbf{u}_{\mathrm{s}}^{(\mathrm{l})}\right)^{\mathrm{T}}\mathbf{r}_{\mathrm{s}}^{(\mathrm{l})} + \int_{z_{\mathrm{u}}}^{z_{\mathrm{l}}}\delta\mathbf{u}_{\mathrm{s}}^{\mathrm{T}}\mathbf{r}_{\mathrm{s,V}}\mathrm{d}z\right) r\,\mathrm{d}\theta\,\mathrm{d}r = 0 \tag{4.40}$$

where $\mathbf{r}_{\mathrm{s,V}}$ is the vector of residual body forces in the interior of the thin layer and $\mathbf{r}_{\mathrm{s}}^{(\mathrm{u})}$, $\mathbf{r}_{\mathrm{s}}^{(\mathrm{l})}$ are the vectors of residual surface tractions at the upper ($z = z_{\mathrm{u}}$) and lower ($z = z_{\mathrm{l}}$) bounding horizontal planes, respectively. The residuals $\mathbf{r}_{\mathrm{s}}^{(\mathrm{u})}$, $\mathbf{r}_{\mathrm{s}}^{(\mathrm{l})}$ and $\mathbf{r}_{\mathrm{s,V}}$ are defined as:

$$\mathbf{r}_{\mathrm{s}}^{(\mathrm{u})} = \mathbf{t}_{\mathrm{s}}^{(\mathrm{u})} + \mathbf{s}_z^{(\mathrm{u})} \tag{4.41a}$$

$$\mathbf{r}_{\mathrm{s}}^{(\mathrm{l})} = \mathbf{t}_{\mathrm{s}}^{(\mathrm{l})} - \mathbf{s}_z^{(\mathrm{l})} \tag{4.41b}$$

$$\mathbf{r}_{\mathrm{s,V}} = \mathbf{p}_{\mathrm{s}} + \mathbf{L}_{\sigma,\mathrm{s}}^{\mathrm{T}}\mathbf{D}_{\mathrm{s}}\mathbf{L}_{\varepsilon,\mathrm{s}}\mathbf{u}_{\mathrm{s}} - \rho_{\mathrm{s}}\frac{\partial^2\mathbf{u}_{\mathrm{s}}}{\partial t^2} \tag{4.41c}$$

At this point, Eq. (4.27) in the absence of external body forces may be expanded as follows [219]:

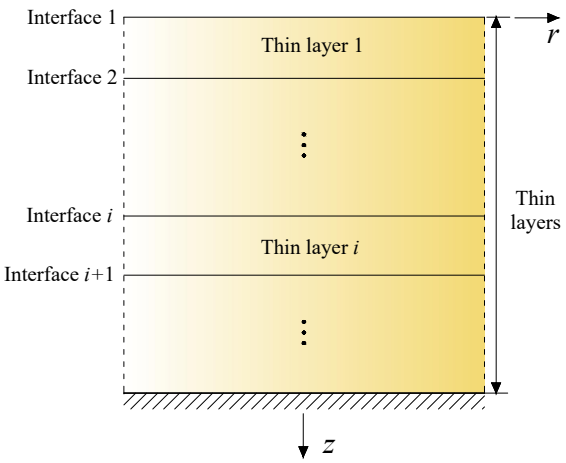

Figure 4.2: A layered soil stratum discretized according to the TLM, overlying a rigid bedrock.

$$\mathbf{D}_{rr}\frac{\partial^2\mathbf{u}_\mathrm{s}}{\partial r^2}+\mathbf{D}_{\theta\theta}\frac{1}{r^2}\frac{\partial^2\mathbf{u}_\mathrm{s}}{\partial\theta^2}+\mathbf{D}_{zz}\frac{\partial^2\mathbf{u}_\mathrm{s}}{\partial z^2}+(\mathbf{D}_{r\theta}+\mathbf{D}_{\theta r})\frac{1}{r}\frac{\partial^2\mathbf{u}_\mathrm{s}}{\partial r\partial\theta}$$
$$+(\mathbf{D}_{rz}+\mathbf{D}_{zr})\frac{\partial^2\mathbf{u}_\mathrm{s}}{\partial r\partial z}+(\mathbf{D}_{\theta z}+\mathbf{D}_{z\theta})\frac{1}{r}\frac{\partial^2\mathbf{u}_\mathrm{s}}{\partial z\partial\theta}+\mathbf{D}_{rr}\frac{1}{r}\frac{\partial\mathbf{u}_\mathrm{s}}{\partial r}$$
$$+(\mathbf{D}_{\theta 1}-\mathbf{D}_{1\theta})\frac{1}{r^2}\frac{\partial\mathbf{u}_\mathrm{s}}{\partial\theta}+(\mathbf{D}_{rz}+\mathbf{D}_{z1}-\mathbf{D}_{1z})\frac{1}{r}\frac{\partial\mathbf{u}_\mathrm{s}}{\partial z}-\mathbf{D}_{11}\frac{\mathbf{u}_\mathrm{s}}{r^2}-\rho_\mathrm{s}\frac{\partial^2\mathbf{u}_\mathrm{s}}{\partial t^2}=\mathbf{0} \tag{4.42}$$

where all the partition matrices $\mathbf{D}_{ij}$ are defined in Appendix B.

By substituting Eq. (4.38) into Eq. (4.42), it is possible to factor out the azimuthal and radial dependencies:

$$\mathbf{T}_n\mathbf{C}_n\left(\mathbf{D}_{zz}\frac{\partial^2\chi_\mathrm{s}}{\partial z^2}-k\left(\mathbf{D}_{rz}+2\mathbf{D}_{z1}-\mathbf{D}_{zr}-2\mathbf{D}_{1z}\right)\frac{\partial\chi_\mathrm{s}}{\partial z}-k^2\mathbf{D}_{rr}\chi_\mathrm{s}-\rho_\mathrm{s}\frac{\partial^2\chi_\mathrm{s}}{\partial t^2}\right)=\mathbf{0} \tag{4.43}$$

where $\chi_\mathrm{s}=\mathbf{N}_\mathrm{s}\mathbf{x}_\mathrm{s}$ and for notation convenience the vector $\mathbf{w}_\mathrm{s}$ is also defined as:

$$\mathbf{w}_\mathrm{s}=\mathbf{D}_{zz}\frac{\partial^2\chi_\mathrm{s}}{\partial z^2}-k\left(\mathbf{D}_{rz}+2\mathbf{D}_{z1}-\mathbf{D}_{zr}-2\mathbf{D}_{1z}\right)\frac{\partial\chi_\mathrm{s}}{\partial z}-k^2\mathbf{D}_{rr}\chi_\mathrm{s}-\rho_\mathrm{s}\frac{\partial^2\chi_\mathrm{s}}{\partial t^2} \tag{4.44}$$

So the vector of residual body forces in the layer can be written as:

$$\mathbf{r}_{\mathrm{s,V}}=\mathbf{p}_\mathrm{s}+\mathbf{T}_n\mathbf{C}_n\mathbf{w}_\mathrm{s} \tag{4.45}$$

In a similar manner, the stresses in the principal surface z may also be rewritten as [219]:

$$\mathbf{s}_z = \mathbf{D}_{zr}\frac{\partial \mathbf{u}_\mathrm{s}}{\partial r} + \mathbf{D}_{z\theta}\frac{1}{r}\frac{\partial \mathbf{u}_\mathrm{s}}{\partial \theta} + \mathbf{D}_{zz}\frac{\partial \mathbf{u}_\mathrm{s}}{\partial z} + \mathbf{D}_{z1}\frac{\mathbf{u}_\mathrm{s}}{r} \tag{4.46}$$

Based on the assumed solution, Eq. (4.46) can be expressed in the following compact form:

$$\mathbf{s}_z = \mathbf{T}_n\mathbf{C}_n\mathbf{S}_z\boldsymbol{\chi}_\mathrm{s} \tag{4.47}$$

where $\mathbf{S}_z$ denotes a differential matrix operator that is defined as:

$$\mathbf{S}_z(\cdot) = \mathbf{D}_{zz}\frac{\partial(\cdot)}{\partial z} + k(\mathbf{D}_{zr} - 2\mathbf{D}_{z1})(\cdot) \tag{4.48}$$

Returning back to the principle of virtual work, we employ Eqs. (4.45) and (4.47) and in the absence of surface loads at the boundary surfaces and external body loads in the domain, Eq. (4.40) may be recasted as follows:

$$\int_0^{+\infty}\int_0^{2\pi}\left(-\delta\mathbf{u}_\mathrm{s}^\mathrm{T}\mathbf{T}_n\mathbf{C}_n\mathbf{S}_z\boldsymbol{\chi}_\mathrm{s}\Big|_{(\mathrm{u})}^{(\mathrm{l})} + \int_{z_\mathrm{u}}^{z_\mathrm{l}}\delta\mathbf{u}_\mathrm{s}^\mathrm{T}\mathbf{T}_n\mathbf{C}_n\mathbf{w}_\mathrm{s}\,\mathrm{d}z\right) r\,\mathrm{d}\theta\,\mathrm{d}r = 0 \tag{4.49}$$

Recasting the surface integral that corresponds to the boundary terms into a volume integral and performing a series of mathematical operations, we obtain:

$$\int_0^{+\infty}\int_0^{2\pi}\delta\mathbf{x}_\mathrm{s}^\mathrm{T}\mathbf{H}_n^\mathrm{T}\mathbf{H}_n\left(-\int_{z_\mathrm{u}}^{z_\mathrm{l}}\mathbf{N}_\mathrm{s}^\mathrm{T}\mathbf{S}_z\frac{\mathrm{d}\mathbf{N}_\mathrm{s}}{\mathrm{d}z}\mathbf{x}_\mathrm{s}\,\mathrm{d}z - \int_{z_\mathrm{u}}^{z_\mathrm{l}}\frac{\mathrm{d}\mathbf{N}_\mathrm{s}^\mathrm{T}}{\mathrm{d}z}\mathbf{S}_z\mathbf{N}_\mathrm{s}\mathbf{x}_\mathrm{s}\,\mathrm{d}z + \int_{z_\mathrm{u}}^{z_\mathrm{l}}\mathbf{N}_\mathrm{s}^\mathrm{T}\mathbf{w}_\mathrm{s}\,\mathrm{d}z\right) r\,\mathrm{d}\theta\,\mathrm{d}r = 0 \tag{4.50}$$

where the matrix $\mathbf{H}_n$ is defined as:

$$\mathbf{H}_n = \begin{bmatrix} \mathbf{T}_n\mathbf{C}_n & \mathbf{0} \\ \mathbf{0} & \mathbf{T}_n\mathbf{C}_n \end{bmatrix} \tag{4.51}$$

The principle of virtual work holds for any arbitrary variation $\delta\mathbf{x}_\mathrm{s}^\mathrm{T}$ and given that the matrix $\mathbf{H}_n^\mathrm{T}\mathbf{H}_n$ is not singular, the following may be deduced upon transformation to the frequency domain:

$$\int_{z_\mathrm{u}}^{z_\mathrm{l}}\left(k^2\left(\mathbf{N}_\mathrm{s}^\mathrm{T}\mathbf{D}_{rr}\mathbf{N}_\mathrm{s}\right) + k\left(\frac{\mathrm{d}\mathbf{N}_\mathrm{s}^\mathrm{T}}{\mathrm{d}z}\left(\mathbf{D}_{zr} - 2\mathbf{D}_{z1}\right)\mathbf{N}_\mathrm{s} + \mathbf{N}_\mathrm{s}^\mathrm{T}\left(\mathbf{D}_{rz} - 2\mathbf{D}_{1z}\right)\frac{\mathrm{d}\mathbf{N}_\mathrm{s}}{\mathrm{d}z}\right)\right.$$
$$\left. + \frac{\mathrm{d}\mathbf{N}_\mathrm{s}^\mathrm{T}}{\mathrm{d}z}\mathbf{D}_{zz}\frac{\mathrm{d}\mathbf{N}_\mathrm{s}}{\mathrm{d}z} - \rho_\mathrm{s}\omega^2\mathbf{N}_\mathrm{s}^\mathrm{T}\mathbf{N}_\mathrm{s}\right)\tilde{\mathbf{x}}_\mathrm{s}\,\mathrm{d}z = \mathbf{0} \tag{4.52}$$

Based on the latter expression the TLM matrices $\mathbf{A}^l$, $\mathbf{B}^l$, $\mathbf{G}^l$ and $\mathbf{M}^l$ are defined as follows:

$$\mathbf{A}^l = \int_{z_\mathrm{u}}^{z_\mathrm{l}}\mathbf{N}_\mathrm{s}^\mathrm{T}\mathbf{D}_{rr}\mathbf{N}_\mathrm{s}\,\mathrm{d}z \tag{4.53}$$

$$\mathbf{B}^l = \int_{z_u}^{z_l} \frac{\mathrm{d}\mathbf{N}_s^{\mathrm{T}}}{\mathrm{d}z} \left(\mathbf{D}_{zr} - 2\mathbf{D}_{z1}\right) \mathbf{N}_s \, \mathrm{d}z + \int_{z_u}^{z_l} \mathbf{N}_s^{\mathrm{T}} \left(\mathbf{D}_{rz} - 2\mathbf{D}_{1z}\right) \frac{\mathrm{d}\mathbf{N}_s}{\mathrm{d}z} \, \mathrm{d}z \tag{4.54}$$

$$\mathbf{G}^l = \int_{z_u}^{z_l} \frac{\mathrm{d}\mathbf{N}_s^{\mathrm{T}}}{\mathrm{d}z} \mathbf{D}_{zz} \frac{\mathrm{d}\mathbf{N}_s}{\mathrm{d}z} \, \mathrm{d}z \tag{4.55}$$

$$\mathbf{M}^l = \rho_s \int_{z_u}^{z_l} \mathbf{N}_s^{\mathrm{T}} \mathbf{N}_s \, \mathrm{d}z \tag{4.56}$$

The above matrices characterize a single thin layer l and their explicit expressions are given for linear and quadratic approximation polynomials in Appendix B. By overlapping all the thin layer matrices in the usual finite element sense, the matrices for the layered soil medium are formed in the context of the TLM (see Fig. 4.2). Subsequently, we group the degrees of freedom instead of the layer interfaces by rearranging rows and columns, which leads to the following matrix equation:

$$\left(k^2 \mathbf{A}^* + k\mathbf{B}^* + \mathbf{G}^* - \omega^2 \mathbf{M}^*\right) \boldsymbol{\Phi} = \mathbf{0} \tag{4.57}$$

where the soil matrices $\mathbf{A}^*$, $\mathbf{B}^*$, $\mathbf{G}^*$ and $\mathbf{M}^*$ are defined as:

$$\mathbf{A}^* = \begin{bmatrix} \mathbf{A}_r & \mathbf{0} & \mathbf{0} \\ \mathbf{0} & \mathbf{A}_\theta & \mathbf{0} \\ \mathbf{0} & \mathbf{0} & \mathbf{A}_z \end{bmatrix}, \; \mathbf{B}^* = \begin{bmatrix} \mathbf{0} & \mathbf{0} & \mathbf{B}_{rz} \\ \mathbf{0} & \mathbf{0} & \mathbf{0} \\ \mathbf{B}_{zr} & \mathbf{0} & \mathbf{0} \end{bmatrix} \tag{4.58}$$

$$\mathbf{G}^* = \begin{bmatrix} \mathbf{G}_r & \mathbf{0} & \mathbf{0} \\ \mathbf{0} & \mathbf{G}_\theta & \mathbf{0} \\ \mathbf{0} & \mathbf{0} & \mathbf{G}_z \end{bmatrix}, \; \mathbf{M}^* = \begin{bmatrix} \mathbf{M}_r & \mathbf{0} & \mathbf{0} \\ \mathbf{0} & \mathbf{M}_\theta & \mathbf{0} \\ \mathbf{0} & \mathbf{0} & \mathbf{M}_z \end{bmatrix} \tag{4.59}$$

It is noted that all the above sub-matrices are symmetric, except for $\mathbf{B}_{zr}$ and $\mathbf{B}_{rz}$ for which $\mathbf{B}_{zr} = \mathbf{B}_{rz}^{\mathrm{T}}$ holds.

As can be seen, Eq. (4.57) describes a quadratic eigenvalue problem in the radial wavenumber k. A standard solution technique for quadratic eigenvalue problems is linearization, by transforming the original equation into a generalized linear eigenvalue problem of double dimension and then solving the latter by means of standard techniques [192, 245, 246]. However, the special structure of the matrices in Eqs. (4.58) and (4.59) may be exploited and two uncoupled generalized linear eigenvalue problems may be obtained for the normal modes of generalized Rayleigh (SV-P) and Love (SH) waves, respectively. So the generalized Rayleigh (SV-P) eigenvalue problem becomes a linear non-symmetric eigenvalue problem in k^2:

$$\left(k^2 \bar{\mathbf{A}} + \bar{\mathbf{C}}\right) \begin{bmatrix} \boldsymbol{\Phi}_r \\ k\boldsymbol{\Phi}_z \end{bmatrix} = \begin{bmatrix} \mathbf{0} \\ \mathbf{0} \end{bmatrix} \tag{4.60}$$

where the matrices $\bar{\mathbf{A}}$ and $\bar{\mathbf{C}}$ are defined as:

$$\bar{\mathbf{A}} = \begin{bmatrix} \mathbf{A}_r & \mathbf{0} \\ \mathbf{B}_{zr} & \mathbf{A}_z \end{bmatrix} \tag{4.61a}$$

$$\bar{\mathbf{C}} = \begin{bmatrix} \mathbf{G}_r - \omega^2 \mathbf{M}_r & \mathbf{B}_{rz} \\ \mathbf{0} & \mathbf{G}_z - \omega^2 \mathbf{M}_z \end{bmatrix} \tag{4.61b}$$

and similarly the generalized Love (SH) eigenvalue problem becomes linear and symmetric as follows:

$$\left(k^2 \mathbf{A}_\theta + \mathbf{C}_\theta\right) \boldsymbol{\Phi}_\theta = \mathbf{0} \tag{4.62}$$

where $\mathbf{C}_\theta = \mathbf{G}_\theta - \omega^2 \mathbf{M}_\theta$ and $\boldsymbol{\Phi}_r$, $\boldsymbol{\Phi}_\theta$ and $\boldsymbol{\Phi}_z$ are the radial, circumferential and vertical modal displacements at the interfaces (i.e. eigenvectors), respectively.

4.3. Half-space approximation in the TLM via Perfectly Matched Layers (PMLs)

The numerical simulation of wave propagation in infinite or semi-infinite media necessitates in most cases the truncation of the physical domain into a finite computational one [247]. The bounded domain is necessarily accompanied by artificial boundary conditions that aim to minimize the reflections of incident waves in order to obtain an accurate solution. The number of available approaches for that purpose is vast, yet they can be broadly categorized into two groups: (i) non-local and (ii) local boundaries [248]. The former correspond to rigorous and highly accurate, even exact in certain cases (e.g. boundary elements [249, 250]), approaches that reproduce the spatial and temporal non-locality of the unbounded medium reaction. However, non-local approaches may become cumbersome and computationally impractical, thus one may resort to less accurate yet simple local boundary conditions [251]. In the latter approaches, larger computational domains may be required compared to non-local ones and the range of applicability is reduced, yet these drawbacks are tolerated on the premise of simplicity and compactness.

In the context of the TLM, the original contributions in the topic focused on layered soil strata supported by rigid bedrock and the effect of the underlying half-space was compensated by appropriate enlargement of the computational domain [227, 75, 252, 253, 229, 230]. Hull and Kausel [254] introduced a second-order paraxial approximation to the half-space dynamic stiffness that was shown to be in agreement with the paraxial boundary condition developed by Clayton and Engquist [255]. Following that development, the study of unbounded domains in the context of the TLM was customarily performed in conjunction with paraxial boundaries (PBs) [256–259] and further aspects of PBs have been elaborated in [260].

Presently, the Perfectly Matched Layers (PMLs) comprise one of the most successful techniques to describe semi-infinite media with finite computational domains augmented with absorbing boundary layers. The concept of PMLs was introduced in a seminal work by Berenger [261] for the absorption of electromagnetic waves and their excellent performance rendered them supreme in electromagnetic wave propagation. Their potential was early recognized by the community of solid mechanics and they were widely adopted in problems

of elastodynamics [262–265]. In the ensuing, we will briefly outline the coupling of PMLs to the TLM [266, 267] in order to formulate an approach for wave propagation in semi-infinite layered media that combines the merits of these two powerful techniques.

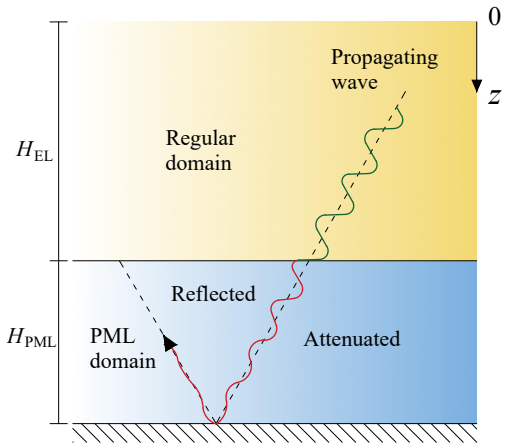

Figure 4.3: Attenuation of propagating waves inside the PML region.

The key principle of PMLs lies in the transformation of the spatial coordinates into complex-valued coordinates by means of complex stretching functions. In our case, the vertical coordinate z is transformed to a complex-valued stretched coordinate $\bar{z}$ as follows:

$$\bar{z} = \int_0^z \varepsilon_s\left(z', \omega\right) \, \mathrm{d}z' \tag{4.63}$$

where $\varepsilon_s(z, \omega)$ denotes the complex-valued stretching function and the form that leads to the standard PML formulation reads:

$$\varepsilon_s(z, \omega) = \alpha_s(z) + \frac{\beta_s(z)}{\mathrm{i}\omega} \tag{4.64}$$

where $\alpha_s(z)$ is the scaling function and $\beta_s(z)$ is the attenuation function; the former controls the amplitude decay of evanescent waves, while the latter is responsible for the attenuation of propagating waves. In principle, there are different classes of stretching functions $\varepsilon_s(z, \omega)$ that can be employed and define the PML formulation in the problem. A different form of complex-valued stretching function has been proposed, giving rise to the so-called complex-frequency-shifted (CFS) PMLs [268–271], with a view to achieving long-time numerical stability in time domain simulations. In general, the CFS-PMLs require the evaluation of convolution integrals for inversion to time domain, so a non-convolutional formulation of CFS-PMLs has also been recently developed to circumvent that complexity [271]. Conclusively, the last category of complex-valued stretching functions is based on the combination of the regular and CFS formulations that leads to a higher-order PML model.

In the ensuing, the standard PML formulation is employed according to Eq. (4.64). Both scaling and attenuation function should increase monotonically with z and ensure continuity of the vertical coordinate at the interface between the regular and the PML domains, i.e. $\alpha_s(H_{\text{EL}}) = 1$ and $\beta_s(H_{\text{EL}}) = 0$ [272]. To comprehend the rationale of these general rules it suffices to consider a harmonic wave propagating in a 1-D PML medium:

$$\exp(\mathrm{i}\omega t)\exp\left(-\mathrm{i}\gamma\bar{z}\right) = \exp(\mathrm{i}\omega t)\exp\left(-\mathrm{i}\Re(\gamma)\Re(\bar{z}) + \mathrm{i}\Im(\gamma)\Im(\bar{z})\right)\exp\left(\Re(\gamma)\Im(\bar{z}) + \Im(\gamma)\Re(\bar{z})\right) \tag{4.65}$$

where γ denotes the wavenumber and:

$$\Re(\bar{z}) = \int_0^z \alpha_s(z')\,\mathrm{d}z' \tag{4.66}$$

$$\Im(\bar{z}) = -\frac{1}{\omega}\int_0^z \beta_s(z')\,\mathrm{d}z' \tag{4.67}$$

As can be seen in Eq. (4.65), the last exponential term is effectively controlling the amplitude of the waveform in the PML region. For a propagating wave ($\Re(\gamma) > 0$ and $\Im(\gamma) = 0$), the argument of the preceding term becomes negative and decreases monotonically, based on the preceding rules for the attenuation function $\beta_s(z)$. Therefore, the initially propagating wave becomes an evanescent wave with strongly increasing attenuation along the propagation direction (see Fig. 4.3). In the case of an evanescent wave ($\Im(\gamma) < 0$), the contribution of the scaling function $\alpha_s(z)$ is to artificially enlarge the domain, accelerating the amplitude decrease of the waveform inside the PML. Admittedly, this simple yet effective example demonstrates the basic principle of PMLs and offers a glimpse of their superb capability to attenuate both propagating and evanescent waves.

Based on the previous considerations, the scaling and attenuation functions are customarily expressed as follows [271]:

$$\alpha_s(z) = \begin{cases} 1, & 0 \le z \le H_{\text{EL}} \\ 1 + \alpha_0\left(\dfrac{z - H_{\text{EL}}}{H_{\text{PML}}}\right)^{m_{\text{PML}}}, & H_{\text{EL}} \le z \le H_{\text{EL}} + H_{\text{PML}} \end{cases} \tag{4.68}$$

$$\beta_s(z) = \begin{cases} 0, & 0 \le z \le H_{\text{EL}} \\ \beta_0\left(\dfrac{z - H_{\text{EL}}}{H_{\text{PML}}}\right)^{m_{\text{PML}}}, & H_{\text{EL}} \le z \le H_{\text{EL}} + H_{\text{PML}} \end{cases} \tag{4.69}$$

where H_{EL} is the thickness of the regular domain, H_{PML} is the thickness of the PML domain and m_{PML} is the degree of the polynomial attenuation inside the PMLs. The scalar tuning parameters α_0 and β_0 control the scaling and attenuation inside the PMLs, respectively.

By employing the stretching function used by Collino and Tsogka [263] and substituting it in Eq. (4.63), the complex-valued stretched coordinate $\bar{z}$ is obtained:

$$\bar{z} = z - \mathrm{i}\mathrm{H}(z - H_{\text{EL}})\frac{\beta_0 H_{\text{PML}}}{\omega(m_{\text{PML}} + 1)}\left(\frac{z - H_{\text{EL}}}{H_{\text{PML}}}\right)^{m_{\text{PML}}+1} \tag{4.70}$$

where H(·) is the Heaviside function. Therefore, Eq. (4.70) describes both the vertical coordinate in the elastic domain and its complex-valued stretched counterpart in the PML domain.

The treatment up to this point has set the stage for the introduction of PMLs in the TLM. Consider a PML domain with thickness H_{PML} that is discretized into N_{PML} thin layers of equal thickness. Following the procedure developed by Kausel and de Oliveira Barbosa [266], PMLs may be readily incorporated in the TLM by simply replacing the thickness of the l-th thin layer h_l in the PML domain with a complex-valued stretched thickness $\bar{h}_l$ (see Fig. 4.4), defined as:

$$\bar{h}_l = H_{\text{PML}} \left[\frac{1}{N_{\text{PML}}} - \mathrm{i} \frac{\beta_0}{\omega (m_{\text{PML}}+1)} \left(\left(\frac{l}{N_{\text{PML}}} \right)^{m_{\text{PML}}+1} - \left(\frac{l-1}{N_{\text{PML}}} \right)^{m_{\text{PML}}+1} \right) \right], \quad 1 \le l \le N_{\text{PML}} \tag{4.71}$$

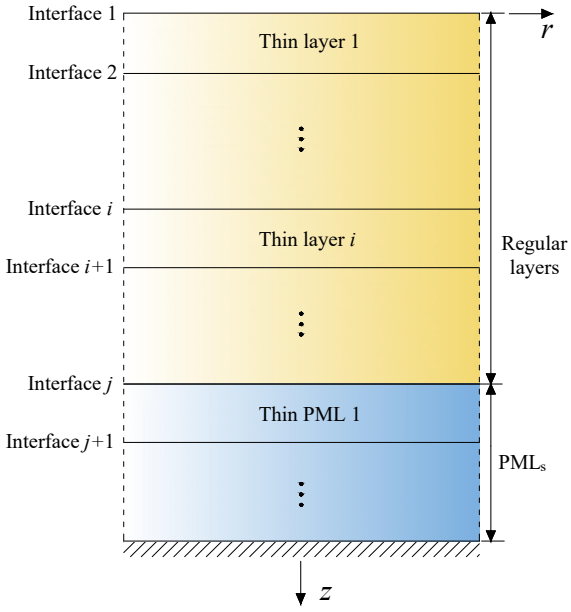

Figure 4.4: A layered soil half-space modelled via the TLM+PMLs.

In essence, the substitution of the layer thickness h_l with its complex-valued counterpart $\bar{h}_l$ is reflected in the TLM matrices given in Eqs. (4.53) to (4.56). In particular, the TLM matrices corresponding to thin PMLs may be expressed as:

$$\bar{\mathbf{A}}^l = \frac{\bar{h}_l}{h_l}\mathbf{A}^l, \quad \bar{\mathbf{B}}^l = \mathbf{B}^l, \quad \bar{\mathbf{G}}^l = \frac{h_l}{\bar{h}_l}\mathbf{G}^l, \quad \bar{\mathbf{M}}^l = \frac{\bar{h}_l}{h_l}\mathbf{M}^l \tag{4.72}$$

It follows that the generalized Rayleigh (SV-P) and Love (SH) eigenvalue problems will result in new eigenvalues and normal modes. Next to the physical modes, the so-called Berenger modes are obtained, which contribute to the overall response in a manner that resembles the branch cut integrals of the half-space [267]. Conclusively, a comparison of PMLs against PBs showcased their superior performance, rendering PMLs the approach of choice for half-space approximation in the TLM [267, 273].

4.4. Green's functions for spatially arbitrary sources in layered soil media

Elastodynamics problems and their solution has traditionally attracted the interest of the mechanics community for more than a century [274–276]. The response elicited by dynamic loads acting on or within a medium, customarily termed as fundamental solution (full-space) or Green's function (half-space), has been the subject of a vast number of studies with applications ranging from seismology and geophysics to acoustics [161, 218, 225]. In the ensuing, the focus lies on the Green's functions of a linear elastic layered medium, which has been a classical topic in the field of soil dynamics and soil-structure interaction.

Numerous techniques are available for the derivation of Green's functions for layered media, albeit most elastodynamics problems are addressed by: (i) the transfer matrix method [277, 278], (ii) the method of wavenumber integration [279–283], (iii) the stiffness matrix method [252, 284, 265] and (iv) the Thin-Layer Method (TLM) [78, 253, 285, 232]. An extensive review of the preceding - as well as many other - approaches and their relevant developments up to the present has been recently presented by Dineva et al. [286]. As may be already apparent, in the ensuing the Green's functions for a layered medium are obtained via the TLM based on the framework developed by Kausel [78].

We proceed to derive the Green's functions in the frequency-space domain due to a spatially arbitrary dynamic load. First, the displacement vector $\widetilde{\mathbf{u}}_{\mathrm{s}}^{(i)}$ at i-th elevation (layer interface) is defined in the frequency-space domain as:

$$\widetilde{\mathbf{u}}_{\mathrm{s}}^{(i)} = \begin{bmatrix} \widetilde{u}_{r,\mathrm{s}}^{(i)} \\ \widetilde{u}_{\theta,\mathrm{s}}^{(i)} \\ \widetilde{u}_{z,\mathrm{s}}^{(i)} \end{bmatrix} = \sum_{n=0}^{\infty} \mathbf{T}_n \int_0^{\infty} k\mathbf{C}_n \widehat{\mathbf{u}}_{\mathrm{s},n}^{(i)} \, \mathrm{d}k \tag{4.73}$$

where $\widehat{\mathbf{u}}_{\mathrm{s},n}^{(i)}$ denotes the displacement vector at elevation $z^{(i)}$ in the frequency-(radial-azimuthal)-wavenumber domain. In the ensuing, the symbols $\widetilde{(\cdot)}$ and $\widehat{(\cdot)}$ refer to quantities in the frequency-space and frequency-(radial-azimuthal)-wavenumber domains, respectively. Transformation to the latter can be achieved by means of the discrete Fourier transform in the azimuth θ and the Hankel transform in the radial coordinate r:

$$\widehat{\mathbf{u}}_{\mathrm{s},n}^{(i)} = \begin{bmatrix} \widehat{u}_{r,\mathrm{s},n}^{(i)} \\ \widehat{u}_{\theta,\mathrm{s},n}^{(i)} \\ \widehat{u}_{z,\mathrm{s},n}^{(i)} \end{bmatrix} = a_n \int_0^{\infty} r\mathbf{C}_n \int_0^{2\pi} \mathbf{T}_n \widetilde{\mathbf{u}}_{\mathrm{s}}^{(i)} \, \mathrm{d}\theta \, \mathrm{d}r \tag{4.74}$$

where $a_0 = \dfrac{1}{2\pi}$ and $a_n = \dfrac{1}{\pi}$ $(n \neq 0)$. The azimuthal matrix $\mathbf{T}_n$ is a placeholder that can be

substituted by its symmetric ($\mathbf{T}_n^{\mathrm{s}}$) or anti-symmetric ($\mathbf{T}_n^{\mathrm{a}}$) form, depending on the case considered. For the external load vector, an analogous transformation pair is defined at the j-th layer interface, involving the exact same transformations employed in Eqs. (4.73) and (4.74), as follows:

$$\widetilde{\mathbf{p}}_{\mathrm{s}}^{(j)} = \begin{bmatrix} \widetilde{p}_{r,\mathrm{s}}^{(j)} \\ \widetilde{p}_{\theta,\mathrm{s}}^{(j)} \\ \widetilde{p}_{z,\mathrm{s}}^{(j)} \end{bmatrix} = \sum_{n=0}^{\infty} \mathbf{T}_n \int_0^{\infty} k\mathbf{C}_n \widehat{\mathbf{p}}_{\mathrm{s},n}^{(j)} \, \mathrm{d}k \tag{4.75}$$

in the frequency-space domain and:

$$\widehat{\mathbf{p}}_{\mathrm{s},n}^{(j)} = \begin{bmatrix} \widehat{p}_{r,\mathrm{s},n}^{(j)} \\ \widehat{p}_{\theta,\mathrm{s},n}^{(j)} \\ \widehat{p}_{z,\mathrm{s},n}^{(j)} \end{bmatrix} = a_n \int_0^{\infty} r\mathbf{C}_n \int_0^{2\pi} \mathbf{T}_n \widetilde{\mathbf{p}}_{\mathrm{s}}^{(j)} \, \mathrm{d}\theta \, \mathrm{d}r \tag{4.76}$$

in the frequency-(radial-azimuthal)-wavenumber domain.

As shown in Section 4.2, the problem of spatially arbitrary wave motion in a three-dimensional layered medium can be decomposed in terms of the azimuthal index n and the generalized Rayleigh (SV-P) and Love (SH) wave motions. The overall response is constructed by superposition of these components. So we proceed to formulate the Green's functions on the basis of these considerations, for the SV-P and SH cases.

The following equilibrium equation is formed, on the basis of the TLM, between external sources of the SV-P type and displacements in the frequency-(radial-azimuthal)-wavenumber domain:

$$\left(k^2\bar{\mathbf{A}} + \bar{\mathbf{C}}\right) \begin{bmatrix} \widehat{\mathbf{u}}_{r,n} \\ k\widehat{\mathbf{u}}_{z,n} \end{bmatrix} = \begin{bmatrix} \widehat{\mathbf{p}}_{r,n} \\ k\widehat{\mathbf{p}}_{z,n} \end{bmatrix} \tag{4.77}$$

Upon introducing the matrices $\mathbf{Y}$ and $\mathbf{Z}$, we premultiply Eq. (4.77) by $\mathbf{Y}^{\mathrm{T}}$ and substitute $\mathbf{Z}\mathbf{Z}^{-1} = \mathbf{I}$:

$$\mathbf{Y}^{\mathrm{T}} \left(k^2\bar{\mathbf{A}} + \bar{\mathbf{C}}\right) \mathbf{Z}\mathbf{Z}^{-1} \begin{bmatrix} \widehat{\mathbf{u}}_{r,n} \\ k\widehat{\mathbf{u}}_{z,n} \end{bmatrix} = \mathbf{Y}^{\mathrm{T}} \begin{bmatrix} \widehat{\mathbf{p}}_{r,n} \\ k\widehat{\mathbf{p}}_{z,n} \end{bmatrix} \tag{4.78}$$

where the matrices $\mathbf{Y}$ and $\mathbf{Z}$ encapsulate the left and right eigenvectors, respectively:

$$\mathbf{Y} = \begin{bmatrix} \boldsymbol{\Phi}_r \mathbf{K}_{\mathrm{R}} \\ \boldsymbol{\Phi}_z \end{bmatrix}, \quad \mathbf{Z} = \begin{bmatrix} \boldsymbol{\Phi}_r \\ \boldsymbol{\Phi}_z \mathbf{K}_{\mathrm{R}} \end{bmatrix} \tag{4.79}$$

In Eq. (4.79), $\mathbf{K}_{\mathrm{R}} = \mathrm{diag}\{k_{\mathrm{R},1} \;\; k_{\mathrm{R},2} \;\; \cdots\}$ is a diagonal matrix containing the wavenumbers $k_{\mathrm{R},m}$ associated with the generalized Rayleigh (SV-P) modes; the latter are found by Eq. (4.60). As can be seen in Eq. (4.79), the left and right eigenmatrices $\mathbf{Y}$ and $\mathbf{Z}$ are defined on the basis of the modal matrices $\boldsymbol{\Phi}_r$ and $\boldsymbol{\Phi}_z$:

$$\boldsymbol{\Phi}_r = \begin{bmatrix} \boldsymbol{\phi}_{r,1} & \boldsymbol{\phi}_{r,2} & \cdots \end{bmatrix} \tag{4.80a}$$

$$\boldsymbol{\Phi}_z = \begin{bmatrix} \boldsymbol{\phi}_{z,1} & \boldsymbol{\phi}_{z,2} & \cdots \end{bmatrix} \tag{4.80b}$$

The previous steps are necessary in order to invoke the following orthogonality and normalization relations employed by Waas [227] and Kausel [78]:

$$\mathbf{Y}^{\mathrm{T}}\bar{\mathbf{A}}\mathbf{Z}=\mathbf{K}_{\mathrm{R}},\quad \mathbf{Y}^{\mathrm{T}}\bar{\mathbf{C}}\mathbf{Z}=-\mathbf{K}_{\mathrm{R}}^{3} \tag{4.81}$$

By employing Eq. (4.81) and carrying out the relevant mathematical operations we obtain:

$$\begin{bmatrix} \widehat{\mathbf{u}}_{r,n} \\ k\widehat{\mathbf{u}}_{z,n} \end{bmatrix}=\mathbf{Z}\left(k^{2}\mathbf{I}-\mathbf{K}_{\mathrm{R}}^{2}\right)^{-1}\mathbf{K}_{\mathrm{R}}^{-1}\mathbf{Y}^{\mathrm{T}}\begin{bmatrix} \widehat{\mathbf{p}}_{r,n} \\ k\widehat{\mathbf{p}}_{z,n} \end{bmatrix} \tag{4.82}$$

Finally, it can be shown that the response of the soil medium in the presence of spatially arbitrary SV-P sources can be brought into the following form in the frequency-(radial-azimuthal)-wavenumber domain:

$$\begin{bmatrix} \widehat{\mathbf{u}}_{r,n} \\ \widehat{\mathbf{u}}_{z,n} \end{bmatrix}=\begin{bmatrix} \boldsymbol{\Phi}_{r}\mathbf{D}_{\mathrm{R}}\boldsymbol{\Phi}_{r}^{\mathrm{T}} & k\boldsymbol{\Phi}_{r}\mathbf{K}_{\mathrm{R}}^{-1}\mathbf{D}_{\mathrm{R}}\boldsymbol{\Phi}_{z}^{\mathrm{T}} \\ \frac{1}{k}\boldsymbol{\Phi}_{z}\mathbf{D}_{\mathrm{R}}\mathbf{K}_{\mathrm{R}}\boldsymbol{\Phi}_{r}^{\mathrm{T}} & \boldsymbol{\Phi}_{z}\mathbf{D}_{\mathrm{R}}\boldsymbol{\Phi}_{z}^{\mathrm{T}} \end{bmatrix}\begin{bmatrix} \widehat{\mathbf{p}}_{r,n} \\ \widehat{\mathbf{p}}_{z,n} \end{bmatrix} \tag{4.83}$$

where $\mathbf{D}_{\mathrm{R}}=\left(k^{2}\mathbf{I}-\mathbf{K}_{\mathrm{R}}^{2}\right)^{-1}$.

The corresponding procedure for the displacement field due to SH-type sources is similar, yet simpler. First, the modal matrix $\boldsymbol{\Phi}_{\theta}$ is obtained from the generalized Love (SH) eigenvalue problem:

$$\boldsymbol{\Phi}_{\theta}=\begin{bmatrix} \boldsymbol{\Phi}_{\theta,1} & \boldsymbol{\Phi}_{\theta,2} & \cdots \end{bmatrix} \tag{4.84}$$

Based on the TLM, for SH-type sources in the frequency-(radial-azimuthal)-wavenumber domain the equilibrium equation reads:

$$\left(k^{2}\mathbf{A}_{\theta}+\mathbf{C}_{\theta}\right)\widehat{\mathbf{u}}_{\theta,n}=\widehat{\mathbf{p}}_{\theta,n} \tag{4.85}$$

The corresponding orthogonality and normalization relations for the generalized Love (SH) modes read:

$$\boldsymbol{\Phi}_{\theta}^{\mathrm{T}}\mathbf{A}_{\theta}\boldsymbol{\Phi}_{\theta}=\mathbf{I},\quad \boldsymbol{\Phi}_{\theta}^{\mathrm{T}}\mathbf{C}_{\theta}\boldsymbol{\Phi}_{\theta}=-\mathbf{K}_{\mathrm{L}}^{2} \tag{4.86}$$

Premultiplying with $\boldsymbol{\Phi}_{\theta}^{\mathrm{T}}$, employing $\boldsymbol{\Phi}_{\theta}\boldsymbol{\Phi}_{\theta}^{-1}=\mathbf{I}$ and following the same steps as in the SV-P case, the displacements in the presence of spatially arbitrary SH sources in the frequency-(radial-azimuthal)-wavenumber domain may be expressed as:

$$\widehat{\mathbf{u}}_{\theta,n}=\boldsymbol{\Phi}_{\theta}\mathbf{D}_{\mathrm{L}}\boldsymbol{\Phi}_{\theta}^{\mathrm{T}}\widehat{\mathbf{p}}_{\theta,n} \tag{4.87}$$

where $\mathbf{D}_{\mathrm{L}}=\left(k^{2}\mathbf{I}-\mathbf{K}_{\mathrm{L}}^{2}\right)^{-1}$ and $\mathbf{K}_{\mathrm{L}}=\mathrm{diag}\left\{k_{\mathrm{L},1}\;\; k_{\mathrm{L},2}\;\; \cdots\right\}$ is a diagonal matrix containing the wavenumbers $k_{\mathrm{L},m}$ associated with the generalized Love (SH) modes as found by Eq. (4.62).

At this point, it is possible to formulate a complete expression of the soil response in terms of any spatially arbitrary source, as a combination of SV-P and SH sources, as follows:

$$\widehat{\mathbf{u}}_{\mathrm{s},n}=\begin{bmatrix}\widehat{\mathbf{u}}_{r,n}\\ \widehat{\mathbf{u}}_{\theta,n}\\ \widehat{\mathbf{u}}_{z,n}\end{bmatrix}=\begin{bmatrix}\boldsymbol{\Phi}_r\mathbf{D}_{\mathrm{R}}\boldsymbol{\Phi}_r^{\mathrm{T}} & \mathbf{0} & k\boldsymbol{\Phi}_r\mathbf{K}_{\mathrm{R}}^{-1}\mathbf{D}_{\mathrm{R}}\boldsymbol{\Phi}_z^{\mathrm{T}}\\ \mathbf{0} & \boldsymbol{\Phi}_\theta\mathbf{D}_{\mathrm{L}}\boldsymbol{\Phi}_\theta^{\mathrm{T}} & \mathbf{0}\\ \frac{1}{k}\boldsymbol{\Phi}_z\mathbf{D}_{\mathrm{R}}\mathbf{K}_{\mathrm{R}}\boldsymbol{\Phi}_r^{\mathrm{T}} & \mathbf{0} & \boldsymbol{\Phi}_z\mathbf{D}_{\mathrm{R}}\boldsymbol{\Phi}_z^{\mathrm{T}}\end{bmatrix}\begin{bmatrix}\widehat{\mathbf{p}}_{r,n}\\ \widehat{\mathbf{p}}_{\theta,n}\\ \widehat{\mathbf{p}}_{z,n}\end{bmatrix} \tag{4.88}$$

Based on Eq. (4.88), the displacement vector $\widehat{\mathbf{u}}_{\mathrm{s},n}^{(i)}$ at the i-th layer interface due to a harmonic spatially arbitrary load $\widehat{\mathbf{p}}_{\mathrm{s},n}^{(j)}$ at the j-th layer interface may be explicitly written as:

$$\widehat{\mathbf{u}}_{\mathrm{s},n}^{(i)}=\begin{bmatrix}\displaystyle\sum_{m=1}^{N_{\mathrm{R}}}\left(\frac{\phi_{r,m}^{(i)}\phi_{r,m}^{(j)}}{k^2-k_{\mathrm{R},m}^2}\widehat{p}_{r,\mathrm{s},n}^{(j)}+\frac{k\phi_{r,m}^{(i)}\phi_{z,m}^{(j)}}{k_{\mathrm{R},m}(k^2-k_{\mathrm{R},m}^2)}\widehat{p}_{z,\mathrm{s},n}^{(j)}\right)\\ \displaystyle\sum_{m=1}^{N_{\mathrm{L}}}\frac{\phi_{\theta,m}^{(i)}\phi_{\theta,m}^{(j)}}{k^2-k_{\mathrm{L},m}^2}\widehat{p}_{\theta,\mathrm{s},n}^{(j)}\\ \displaystyle\sum_{m=1}^{N_{\mathrm{R}}}\left(\frac{k_{\mathrm{R},m}\phi_{z,m}^{(i)}\phi_{r,m}^{(j)}}{k(k^2-k_{\mathrm{R},m}^2)}\widehat{p}_{r,\mathrm{s},n}^{(j)}+\frac{\phi_{z,m}^{(i)}\phi_{z,m}^{(j)}}{k^2-k_{\mathrm{R},m}^2}\widehat{p}_{z,\mathrm{s},n}^{(j)}\right)\end{bmatrix} \tag{4.89}$$

Transformation of Eq. (4.89) to the frequency-space domain is achieved based on Eq. (4.73).

In the following chapters, the Green's functions due to axisymmetric ($n=0$) circular ring sources will be of interest. Without further delay, let us derive the Green's functions due to the following harmonic unit ring sources:

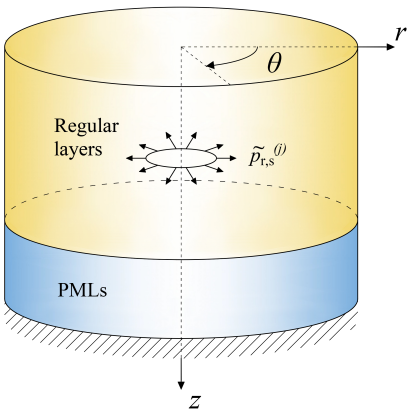

Figure 4.5: Schematic of a radial ring source at elevation z_j.

(i) A unit radial ring load (see Fig. 4.5)

The load vector for a harmonic radial ring source at the j-th layer interface in the frequency-space domain reads:

$$\widetilde{\mathbf{p}}_{\mathrm{s}}^{(j)}=\begin{bmatrix}\delta(r-R)\\ 0\\ 0\end{bmatrix} \tag{4.90}$$

Upon application of the transform given in Eq. (4.76), the load vector in the frequency-(radial-azimuthal)-wavenumber is obtained as:

$$\widehat{\mathbf{p}}_{\mathrm{s},0}^{(j)} = \frac{1}{2\pi}\int_0^{\infty} r\mathbf{C}_0 \int_0^{2\pi} \mathbf{T}_0^{\mathrm{s}} \begin{bmatrix} \delta(r-R) \\ 0 \\ 0 \end{bmatrix} \mathrm{d}\theta\,\mathrm{d}r = \begin{bmatrix} -RJ_1(kR) \\ 0 \\ 0 \end{bmatrix} \tag{4.91}$$

Combining Eqs. (4.73), (4.89) and (4.91), the displacements at the i-th layer interface in the frequency-space domain read:

$$\widetilde{\mathbf{u}}_{\mathrm{s}}^{(i)} = \mathbf{T}_0^{\mathrm{s}} \int_0^{\infty} k\mathbf{C}_0 \widehat{\mathbf{u}}_{\mathrm{s},0}^{(i)}\,\mathrm{d}k = R \begin{bmatrix} \sum_{m=1}^{N_{\mathrm{R}}} \phi_{r,m}^{(i)}\phi_{r,m}^{(j)} \int_0^{\infty} k \dfrac{J_1(kr)J_1(kR)}{k^2 - k_{\mathrm{R},m}^2}\,\mathrm{d}k \\ 0 \\ \sum_{m=1}^{N_{\mathrm{R}}} \phi_{z,m}^{(i)}\phi_{r,m}^{(j)} k_{\mathrm{R},m} \int_0^{\infty} \dfrac{-J_0(kr)J_1(kR)}{k^2 - k_{\mathrm{R},m}^2}\,\mathrm{d}k \end{bmatrix} \tag{4.92}$$

(ii) A unit torsional ring load (see Fig. 4.6)

The transformation pair of the load vector for a harmonic torsional ring source at the j-th layer interface reads:

$$\widetilde{\mathbf{p}}_{\mathrm{s}}^{(j)} = \begin{bmatrix} 0 \\ \delta(r-R) \\ 0 \end{bmatrix}, \quad \widehat{\mathbf{p}}_{\mathrm{s},0}^{(j)} = \begin{bmatrix} 0 \\ -RJ_1(kR) \\ 0 \end{bmatrix} \tag{4.93}$$

Subsequently, the associated displacement vector at the i-th layer interface may be expressed in the frequency-space domain as:

$$\widetilde{\mathbf{u}}_{\mathrm{s}}^{(i)} = \mathbf{T}_0^{\mathrm{a}} \int_0^{\infty} k\mathbf{C}_0 \widehat{\mathbf{u}}_{\mathrm{s},0}^{(i)}\,\mathrm{d}k = R \begin{bmatrix} 0 \\ \sum_{m=1}^{N_L} \phi_{\theta,m}^{(i)}\phi_{\theta,m}^{(j)} \int_0^{\infty} k \dfrac{J_1(kr)J_1(kR)}{k^2 - k_{\mathrm{L},m}^2}\,\mathrm{d}k \\ 0 \end{bmatrix} \tag{4.94}$$

(iii) A unit vertical ring load (see Fig. 4.7)

Finally, for a harmonic vertical ring source at the j-th layer interface the load vector transformation pair is defined as:

$$\widetilde{\mathbf{p}}_{\mathrm{s}}^{(j)} = \begin{bmatrix} 0 \\ 0 \\ \delta(r-R) \end{bmatrix}, \quad \widehat{\mathbf{p}}_{\mathrm{s},0}^{(j)} = \begin{bmatrix} 0 \\ 0 \\ RJ_0(kR) \end{bmatrix} \tag{4.95}$$

and the corresponding displacement vector at the i-th layer interface reads:

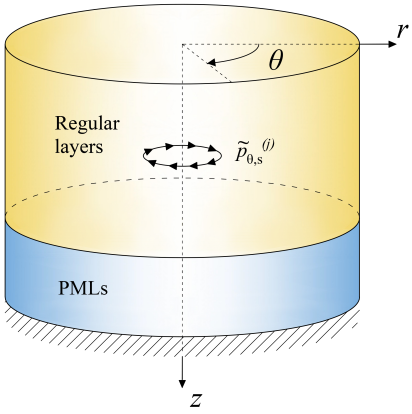

Figure 4.6: Schematic of a torsional ring source at elevation z_j.

$$\widetilde{\mathbf{u}}_{\mathrm{s}}^{(i)} = \mathbf{T}_0^{\mathrm{s}} \int_0^{\infty} k\mathbf{C}_0 \widehat{\mathbf{u}}_{\mathrm{s},0}^{(i)} \, \mathrm{d}k = R \begin{bmatrix} \sum_{m=1}^{N_{\mathrm{R}}} \phi_{r,m}^{(i)} \phi_{z,m}^{(j)} \dfrac{1}{k_{\mathrm{R},m}} \displaystyle\int_0^{\infty} -k^2 \frac{J_1(kr) J_0(kR)}{k^2 - k_{\mathrm{R},m}^2} \, \mathrm{d}k \\ 0 \\ \sum_{m=1}^{N_{\mathrm{R}}} \phi_{z,m}^{(i)} \phi_{z,m}^{(j)} \displaystyle\int_0^{\infty} k \frac{J_0(kr) J_0(kR)}{k^2 - k_{\mathrm{R},m}^2} \, \mathrm{d}k \end{bmatrix} \tag{4.96}$$

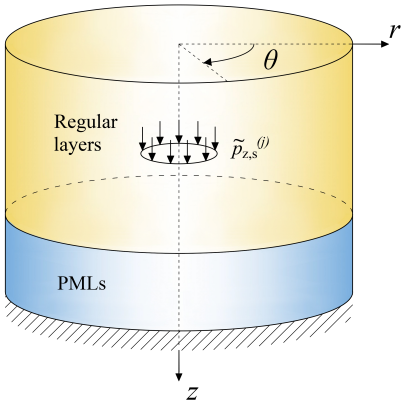

Figure 4.7: Schematic of a vertical ring source at elevation z_j.

As can be seen, Eqs. (4.92), (4.94) and (4.96) involve certain integrals corresponding to inverse Hankel transforms - the latter are analytically tractable (see [78, 253]). Therefore, one can truly obtain the Green's functions in the frequency-space domain in an explicit form

in the context of the TLM for circular ring sources. Furthermore, a collection of Green's functions for various other source types have explicit expressions in the context of the TLM and can be found in [78, 285].

Conclusively, one may utilize the preceding framework to compute the soil response at a set of receivers in the frequency-space domain for any input excitation of interest. A rearrangement of the obtained displacements and the applied loads per degree of freedom leads to the following:

$$\widetilde{\mathbf{u}}_{\mathrm{s}} = \begin{bmatrix} \widetilde{\mathbf{u}}_{r,\mathrm{s}} \\ \widetilde{\mathbf{u}}_{\theta,\mathrm{s}} \\ \widetilde{\mathbf{u}}_{z,\mathrm{s}} \end{bmatrix} = \begin{bmatrix} \widetilde{\mathbf{F}}_{rr} & \widetilde{\mathbf{F}}_{r\theta} & \widetilde{\mathbf{F}}_{rz} \\ \widetilde{\mathbf{F}}_{\theta r} & \widetilde{\mathbf{F}}_{\theta\theta} & \widetilde{\mathbf{F}}_{\theta z} \\ \widetilde{\mathbf{F}}_{zr} & \widetilde{\mathbf{F}}_{z\theta} & \widetilde{\mathbf{F}}_{zz} \end{bmatrix} \begin{bmatrix} \widetilde{\mathbf{p}}_{r,\mathrm{s}} \\ \widetilde{\mathbf{p}}_{\theta,\mathrm{s}} \\ \widetilde{\mathbf{p}}_{z,\mathrm{s}} \end{bmatrix} \tag{4.97}$$

As can be seen in Eq. (4.97), the flexibility matrix in the frequency-space domain possesses additional coupling matrices, compared to the flexibility matrix in the frequency-(radial-azimuthal)-wavenumber domain given by Eq. (4.88). These coupling matrices are associated with dynamic loads that excite simultaneously SV-P and SH waves, which are amenable to decoupling in the (radial-azimuthal)-wavenumber domain, yet not in the spatial one. This occurrence corresponds to non-axisymmetric motions ($n > 0$), thus in the problems of interest in the following chapters $\widetilde{\mathbf{F}}_{r\theta} = \widetilde{\mathbf{F}}_{\theta r} = \widetilde{\mathbf{F}}_{z\theta} = \widetilde{\mathbf{F}}_{\theta z} = \mathbf{0}$.

Conclusively, energy dissipation in the soil material may be included by means of the correspondence principle in the preceding developments [287]. Therefore, hysteretic soil damping is considered in the form of complex-valued Lamé constants, where the damping ratio ξ_{s} is taken identical for both dilatational and distortional waves, i.e. $\lambda_{\mathrm{s}}^{*} = \lambda_{\mathrm{s}}\left(1 + 2\mathrm{i}\xi_{\mathrm{s}}\mathrm{sgn}(\omega)\right)$ and $G_{\mathrm{s}}^{*} = G_{\mathrm{s}}\left(1 + 2\mathrm{i}\xi_{\mathrm{s}}\mathrm{sgn}(\omega)\right)$.

4.5. Validation of Green's functions via the TLM+PMLs

In the preceding sections, a framework to obtain the Green's functions of a linear elastic layered half-space in an accurate and computationally efficient manner has been formulated based on the TLM coupled with PMLs (TLM+PMLs). The Green's functions constitute an indispensable element of the pile installation models to be presented in Chapters 6 and 7. For that purpose, we proceed to validate the results obtained via the TLM+PMLs, by means of a numerical example, against a 3-D FE model developed in COMSOL Multiphysics® software [191]. In particular,

	ρ_{s} [kg/m^3]	G_{s} [MPa]	ν_s [-]	ξ_{s} [-]
Upper soil layer	2000	20	0.3	0.025
Bottom half-space	1800	23	0.499	0.025

Table 4.1: Soil parameters for the validation case of the Green's functions.

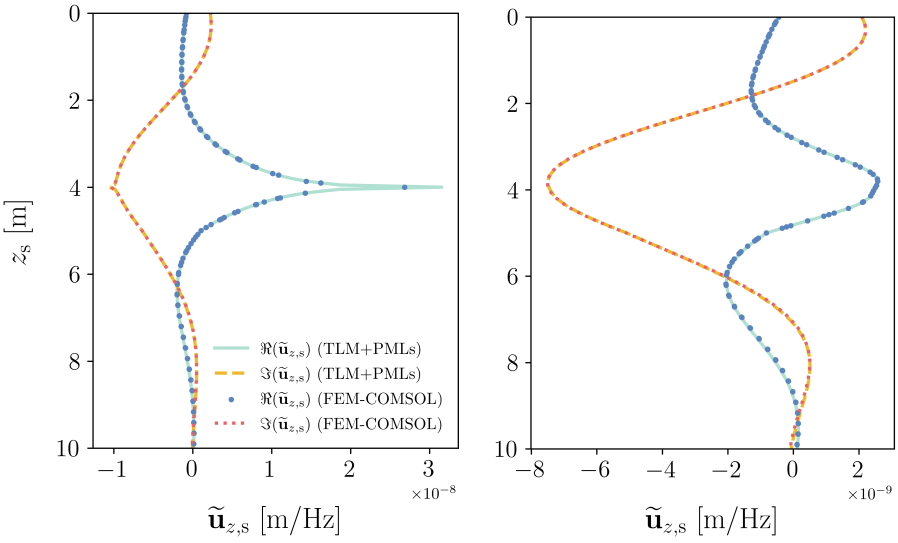

Figure 4.8: Comparison of Green's functions ($\widetilde{\mathbf{u}}_{z,s}$) obtained via the TLM+PMLs and the FE (COMSOL) model for a unit vertical ring load applied at $r = 0.4$ m (source) and receiver radius at (a) $r = 0.4$ m and (b) $r = 0.8$ m.

The case study is based on a two-layer soil profile as described in Table 4.1. Three types of harmonic ring sources, namely vertical, radial and circumferential, with frequency $f = 23$ Hz are applied at $z = 4$ m and $r = 0.4$ m, while the Green's functions are evaluated along the vertical axis and at different radii. The upper layer is unsaturated with a thickness $H_{\text{EL},1} = 5$ m and underlain by a water-saturated half-space. In the TLM+PMLs, the half-space is substituted by a linear elastic layer with thickness $H_{\text{EL},2} = 5$ m and a PML domain with thickness $H_{\text{PML}} = 5$ m. For the half-space approximation in the COMSOL model, a linear elastic layer with large depth ($H_{\text{EL},2} = 25$ m) is modelled and supported below by a horizontal low-reflecting boundary. Similarly, the radial extent of the FE model is finite with a domain radius of 50 m and bounded by a cylindrical low-reflecting boundary. In the TLM+PMLs, such an approach is altogether avoided, due to analytical solutions employed in the radial direction that satisfy naturally the radiation condition at infinity. It is noted that the Solid Mechanics module was used for the COMSOL model and the computations were performed in the frequency domain.

In Figs. 4.8 and 4.9, the vertical ($\widetilde{\mathbf{u}}_{z,s}$) and radial ($\widetilde{\mathbf{u}}_{r,s}$) Green's functions due to a vertical ring source are displayed, respectively. Furthermore, the Green's functions are computed for all cases at two different receiver radii, i.e. $r = 0.4$ m and $r = 0.8$ m. As can be seen, the agreement between the results of the TLM+PMLs and the FE (COMSOL) model is remarkable for both vertical and radial displacements; a discrepancy appears solely in Fig. 4.8a for the source-receiver concurrence, which is expected due to a singularity at that point.

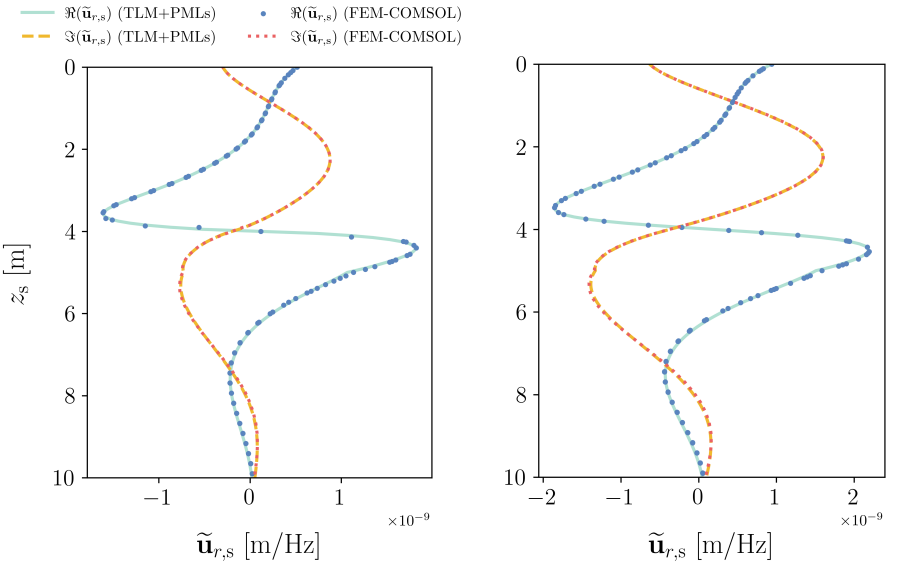

Figure 4.9: Comparison of Green's functions ($\widetilde{\mathbf{u}}_{r,\mathrm{s}}$) obtained via the TLM+PMLs and the FE (COMSOL) models for a unit vertical ring load applied at $r = 0.4$ m (source) and receiver radius at (a) $r = 0.4$ m and (b) $r = 0.8$ m.

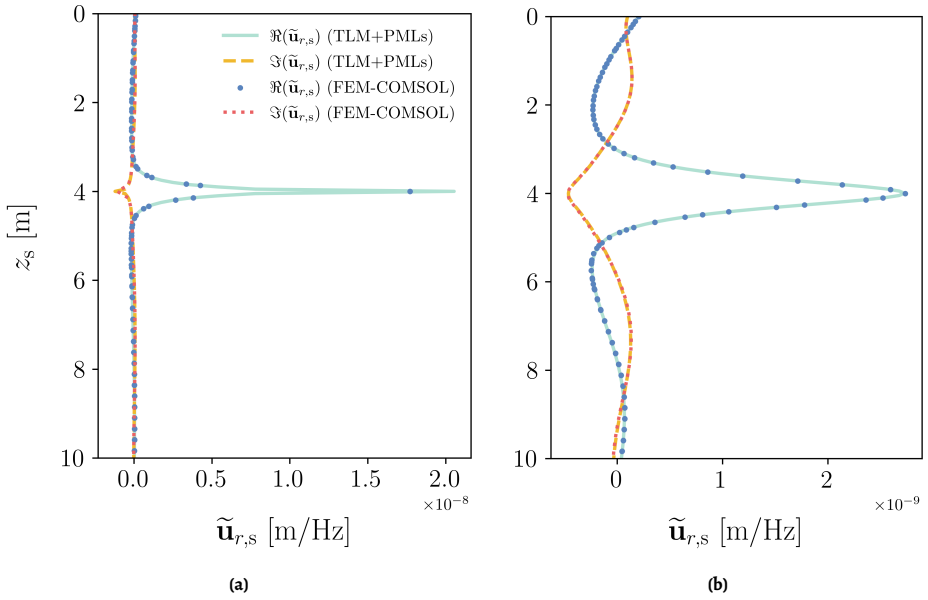

Figure 4.10: Comparison of Green's functions ($\widetilde{\mathbf{u}}_{r,\mathrm{s}}$) obtained via the TLM+PMLs and the FE (COMSOL) models for a unit radial ring load applied at $r = 0.4$ m (source) and receiver radius at (a) $r = 0.4$ m and (b) $r = 0.8$ m.

Figures 4.10 and 4.11 depict the radial ($\widetilde{\mathbf{u}}_{r,\mathrm{s}}$) and vertical ($\widetilde{\mathbf{u}}_{z,\mathrm{s}}$) components of the Green's functions due to a radial ring source for the source/receiver radii given above. Similarly to the case of the vertical ring source, there is great agreement for both displacement components and at all receiver locations. Conclusively, Fig. 4.12 presents the Green's functions due to a circumferential ring source, which also displays virtually identical results for the two models; in this case, the sole displacement component is the circumferential one ($\widetilde{\mathbf{u}}_{\theta,\mathrm{s}}$). By means of these three examples, the validation of the presented TLM+PMLs framework is showcased, with a particular emphasis on the computation of three types of Green's functions for ring sources that will be utilized in the following chapters.

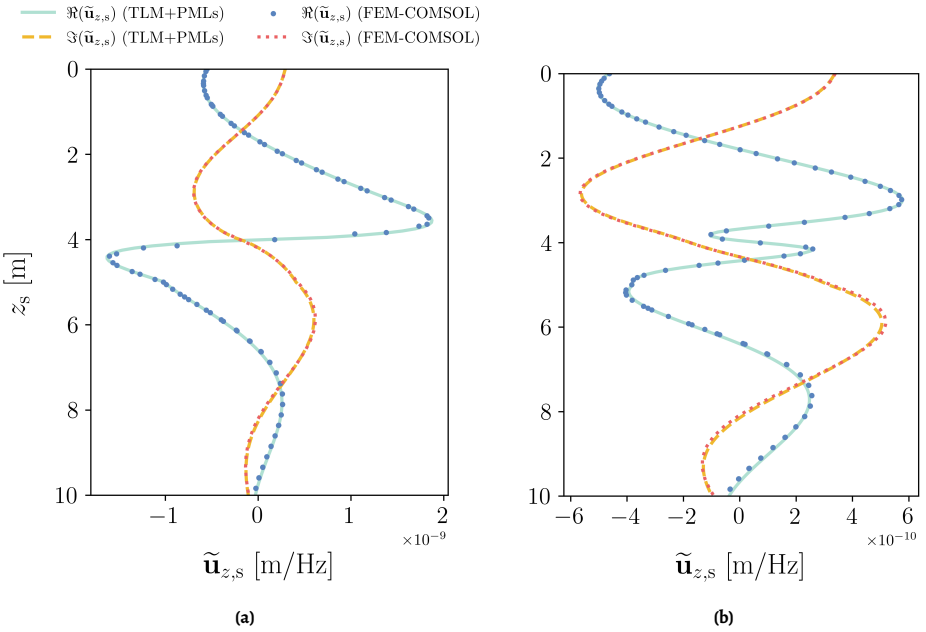

Figure 4.11: Comparison of Green's functions ($\widetilde{\mathbf{u}}_{z,\mathrm{s}}$) obtained via the TLM+PMLs and the FE (COMSOL) models for a unit radial ring load applied at $r = 0.4$ m (source) and receiver radius at (a) $r = 0.4$ m and (b) $r = 0.8$ m.

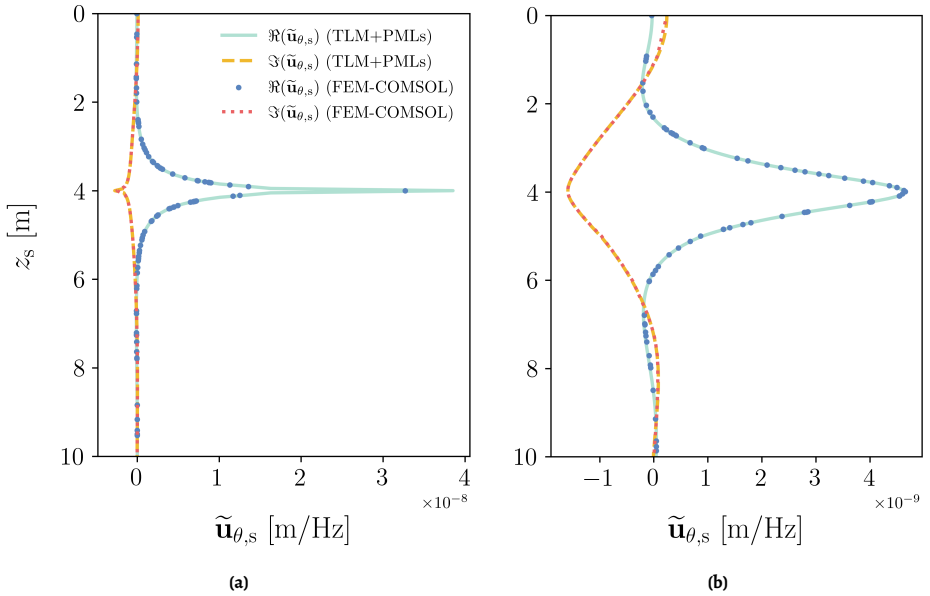

Figure 4.12: Comparison of Green's functions ($\widetilde{\mathbf{u}}_{\theta,\mathrm{s}}$) obtained via the TLM+PMLs and the FE (COMSOL) models for a unit circumferential ring load applied at $r = 0.4$ m (source) and receiver radius at (a) $r = 0.4$ m and (b) $r = 0.8$ m.

4.6. Conclusions

In this chapter, we treated the propagation of mechanical disturbances in a 3-D layered soil medium, with a view to overcome the limitations of local and frequency-independent soil reaction analogues. As a point of departure, the wave motion in linear elastic solids was studied, laying the foundations for the subsequent numerical developments. In particular, the TLM has been proposed, as a superbly efficient numerical scheme for the analysis of wave propagation in linear elastic layered media. Additionally, the incorporation of PMLs in the TLM has been presented, as an advantageous method to approximate the underlying half-space via complex-valued coordinate stretching.

By means of the TLM+PMLs framework, the Green's functions for ring sources in the frequency-space domain are obtained and validated. The previous developments are presented in a generic manner, as their applicability vastly exceeds the topic of this thesis. In the ensuing chapters, the Green's functions derived via the TLM+PMLs are integrated in a numerical framework for pile driving analysis, thus facilitating the computation of pile and soil responses during installation.

5

Gentle Driving of Piles (GDP) at a sandy site combining axial and torsional vibrations: field tests

In the preceding chapters, the theoretical background related to dynamic pile and soil behaviours during driving has been presented, along with relevant numerical approaches. The latter components will be merged into a computationally efficient framework for pile installation analysis purposes. However, let us first elucidate the motivation for these developments, i.e. the demand for sustainable methods of offshore monopile installation. In the last decade, alarming concerns have emerged regarding the environmental impact of the most commonly adopted monopile installation method, i.e. impact hammer driving. Two courses of action have been followed to tackle this problem: i) introduction of mitigation measures in impact piling and ii) use of alternative installation techniques. The former approach has a major practical drawback, irrespectively of the mitigation efficiency, i.e. the increase of offshore wind energy cost. Therefore, mitigation measures effectively lead the sector further away from its main goal, namely cheaper and more accessible wind energy. To that end, alternative pile installation techniques have been progressively drawing attention in the last decade and an increasing number of research projects are focusing on their investigation.

Gentle Driving of Piles (GDP) is a new technology for the vibratory installation of tubular (mono)piles, in line with the preceding objective. Its founding principle is that both high installation performance and low levels of noise emissions can be achieved by applying to the pile a combination of axial and torsional vibrations. Preliminary development and demonstration of the proposed technology have been the main objectives of the GDP research programme. To this end, onshore medium-scale pile installation tests have been performed in sand, using both impact and vibratory driving methods (including GDP). Following the development of a purpose-built GDP device and the geotechnical characterisation of the test

Parts of this chapter have been published in Tsetas et al. [51].

site, the main body of this chapter describes the execution and the experimental findings of the GDP field tests. Focus is on the installation performance of GDP piles, which is discussed with the aid of structural and ground monitoring data. The comparison between piling data associated with GDP and standard axial vibratory driving showcases the potential of the proposed installation technology, particularly with regard to the beneficial effect of the torsional vibration component.

5.1. Sustainable installation of offshore monopiles - the 'Gentle Driving of Piles' method

Ever more countries worldwide are working to shift their energy mix towards renewables. In this regard, offshore wind energy will continue to play an increasingly relevant role as an abundant, cost-effective resource [26], on the condition that the pace of its technological development is further expedited. Presently, 15-24% of the investment for the construction of an offshore wind farm relates to the design, production and installation of substructures [24]. Continual improvement of engineering methodologies in this area is therefore key to achieving further cost reduction [288, 289, 194].

Based on the latest European Wind Energy Association (EWEA) report [26], over 80% of the existing offshore wind turbines (OWTs) in European wind farms are founded on so-called monopile foundations, which are most commonly installed by means of impact hammering. The impact technology is to date very well established in the offshore industry [27]. However, impact installation in certain soil conditions (e.g., dense sands) may be slower than desired [44, 48], which causes increased installation costs and, potentially, higher pile damage under many hammer blows [46, 166]. Moreover, the high levels of underwater noise emissions generated during pile installation are known to be harmful to marine life [290]. This alarming concern has motivated over the years the enforcement of strict regulations to limit its negative environmental effects [35]. Such regulations include the adoption of costly soundproofing measures (e.g. bubble curtains, isolation casings, and cofferdams) [291, 36].

An interesting alternative to impact piling is provided by vibratory technologies, which can achieve quiet(er)/fast pile installation through the application of low-amplitude axial vibrations. The input excitation is induced through the harmonic rotation of eccentric masses, usually at a frequency no larger than 40 Hz. Vibratory driving devices (or simply 'vibro-hammers') have been manufactured and studied since the 1940s [44], and their benefits in terms of driving performance and noise emissions are known since then [45, 46, 292, 290]. The use of piling loads lower than in impact driving can effectively reduce both damage and radial expansion of the pile during driving – the latter (Poisson effect) is a major culprit for noise emissions and larger soil resistance to driving [200]. Despite its obvious benefits, vibratory driving is not yet widely adopted for offshore piling. Its use is hindered by a number of factors, including the incompleteness (and inconclusiveness) of available field observations. Major knowledge gaps are also associated with dynamic soil behaviour during vibro-driving [47] and the effects of vibro-installation on the operational performance of the pile [293, 50, 48].

To boost the improvement of vibratory installation methods, a new technology – the Gentle Driving of Piles (GDP) – has been recently proposed in the Netherlands as the core of a joint industry project led by the Delft University of Technology (TU Delft) [49]. GDP tar-

gets enhanced piling performance and reduced noise emissions through the simultaneous application of low-frequency/axial and high-frequency/torsional vibrations. This thread of research was originally inspired by observing that torsional vibrations do not induce radial pile expansion during driving, which was foreseen to play in favour of both driving and acoustic performances. A preliminary demonstration of the proposed technology was pursued by performing medium-scale field tests on identical test piles installed using impact and vibratory driving methods, including GDP. The tests were performed in sandy soil at the Port of Rotterdam and comprised two distinct stages, the first to investigate the driving performance, and the second to explore installation effects in the response of the test piles to repeated lateral loading [54]. The GDP field campaign adds to the research carried out within other major programmes on monopile foundations, such as PISA [288] in the UK, REDWIN [294] and WAS-XL [295] in Norway, Vibro [296, 48] in Germany, and DISSTINCT [297], MIDAS [298] and BLUE Piling [299] in the Netherlands.

The GDP project was initiated to achieve a preliminary demonstration of the proposed pile driving method at medium scale – particularly, with respect to the inclusion of a high-frequency torsional vibration component. In what follows, the installation performance of the GDP method is described in detail with the aid of selected field measurements, and in comparison to other piling data associated with standard axial vibro-driving. Although the GDP project was originally motivated by offshore wind developments, this work aims to attract the interest of the piling community, and foster further studies for an even broader range of applications and geotechnical conditions.

5.2. The GDP shaker

The design of the GDP shaker built on the idea of installing monopiles by combining low-frequency/axial and high-frequency/torsional motions. The effectiveness of such a pile driving approach was envisioned in light of the following considerations:

(i) high-frequency torsional motion is expected to reduce the axial frictional resistance along the pile shaft. Since torsional vibration mobilises soil shear resistance in the circumferential direction, less frictional resources are left to oppose axial pile penetration [300, 301];

(ii) as a consequence of point (i), the axial vibratory load that is necessary to drive the pile can be reduced, so the amplitude of the generated stress waves will decrease in comparison to the case of axial vibro-driving. Therefore, the amplitude of the radial pile motion (Poisson effect) will also decrease, as a result of the so-called ring frequency effect [205, 193];

(iii) the mentioned decrease in radial pile expansion during installation is believed to be beneficial for two reasons. First, it is expected to enable faster penetration, due to lower soil confinement; secondly, less radial expansion of the pile results in reduced underwater noise emissions.

It is worth recalling that, under axisymmetric loading conditions (e.g. in the presence of a torque), the circumferential motion of an elastic cylindrical structure (pile) is uncoupled

from its axial and radial deformations [180]. Therefore, a pile subjected to torsional vibrations can only transmit shear (SH) waves to the surrounding media [219]. Such shear waves cannot propagate in seawater [225], nor do they contribute to underwater noise.

Importantly, the preference for torsional vibrations at high frequency relates to the short wavelengths that are accordingly transmitted to the soil, which decay in amplitude within a short distance from the pile. Therefore, the torsional mobilisation of the soil resistance (also reduced by pore pressure build-up [301]) is expected to occur locally around the pile shaft, and likely with a lower impact on the post-installation lateral response than in the case of low-frequency axial vibrations.

(a) (b)

Figure 5.1: The GDP shaker: (a) view at the manufacturing site; (b) shaker connected to a test pile via a bolted flange connection

.

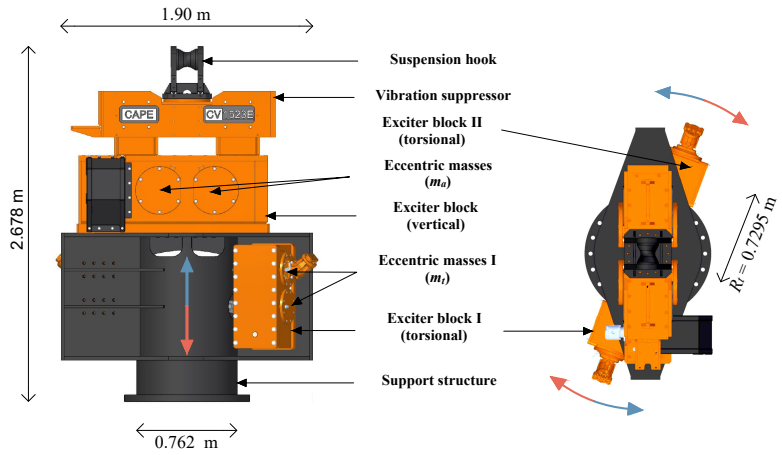

Figure 5.2: Detailed design of the GDP shaker.

A novel GDP shaker was designed and purpose-built for the execution of GDP tests (see Fig. 5.1). As shown in Fig. 5.2, the shaker is formed by three gear trains directly connected to masses that can counter-rotate with a given (constant) eccentricity. Such masses are accommodated within exciter blocks, which are in turn bolted to a support structure. In its first design, the GDP shaker operated by means of hydraulic motors and was connected to each test pile via a bolted flange connection, which was a preliminary solution adopted for the GDP experimental campaign (see Fig. 5.1b).

Similarly to conventional vibratory hammers, the eccentric masses in the GDP shaker are set to counter-rotate in order to generate a dynamic load along a certain direction. In the case of the GDP shaker, the exciter block at the top of the support structure can generate a harmonic load $F_a(t)$ along the pile axis with frequency Ω_a. To induce torsional and axial vibrations of different amplitude and frequency, a separate set of exciter blocks was needed. To this end, two additional exciter blocks were mechanically connected through a shaft with the twofold goal of (i) assembling all units into a single substructure and (ii) positioning them properly. Furthermore, vibratory loads were generated based on a control system that ensured synchronisation, so as to obtain the application of a torque $M_t(t)$ of frequency Ω_t at the top of the pile (Fig. 5.2). Overall, the GDP shaker can apply to the pile head load combinations of the following type:

$$F_a(t) = m_a e_a \Omega_a^2 \sin(\Omega_a t) \tag{5.1}$$

$$M_t(t) = R_t m_t e_t \Omega_t^2 \sin(\Omega_t t) \tag{5.2}$$

where $m_a e_a$ and $m_t e_t$ denote, respectively, the axial and torsional eccentric moments* associated with the eccentric masses in both exciter blocks. The distance between the centre of the pile cross-section and the torsional eccentric masses is denoted by R_t (see Fig. 5.2). According to Eqs. (5.1) and (5.2), the resulting load amplitudes are mainly governed by the frequency as the eccentric moments ($m_a e_a$ and $m_t e_t$) and the radius (R_t) are fixed.

Figure 5.3 illustrates the axial and torsional inputs generated based on the counter-rotation of the respective eccentric masses, along with their representation as part of a pile-soil interaction model. The axial load is associated with the force resultant of $F_{a1}(t)$ and $F_{a2}(t)$, whereas the torque is the net moment resultant of $F_{t1}(t)$, $F_{t2}(t)$, $F_{t3}(t)$, and $F_{t4}(t)$; it is remarked that the net force resultant of the latter set of forces is always equal to zero. Further details regarding GDP shaker specifications may be found in Gómez and Metrikine [302].

The final design of the GDP shaker stemmed directly from the conceptual foundation of the GDP method, though with constraints imposed by practical limitations. In the installation tests described in the following, the axial vibration frequency of GDP was set to be similar to the frequency adopted for a parallel axial vibro-driving test, so as to gain insight into the effect of the torsional vibrations. On the other hand, the GDP torsional frequency was maximised within the manufacturing constraints of the GDP shaker. In particular, the choice of the torsional frequency was driven by the need of maintaining comparable power capacity for the installation tests associated both with GDP and axial vibro-driving. The

*Although not rigorously moments, $m_a e_a$ and $m_t e_t$ are usually referred to as such within the vibro-driving community.

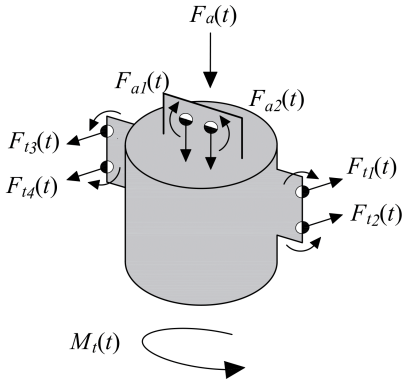

Figure 5.3: Generation of axial and torsional loads through the rotating eccentric masses in the GDP shaker.

final design of the GDP shaker enabled the application of axial and torsional vibratory loads with frequencies up to 23 Hz and 80 Hz, respectively.

The main technical specifications of the GDP shaker and the standard vibratory hammer (CV-25) used in the GDP campaign are summarised in Table 5.1.

	GDP shaker		Vibro-hammer CV-25
	Axial shaker	Torsional shaker	Axial shaker
Total mass [kg]	5150		4100
Eccentric moment *me* [kg m]	15	4	25
Rotational speed [rpm]	1400	4800	1800
Operational power [kW]	72	188	263

Table 5.1: Technical specifications of the GDP shaker and the axial vibro-hammer CV-25.

5.3. Geotechnical site characterisation

The GDP experimental campaign was planned to achieve a preliminary proof of concept for the proposed pile driving technology. To this end, medium-scale onshore field tests in sandy soil were performed. Both geotechnical and logistical considerations led to the selection of the Maasvlakte II site at the Port of Rotterdam, which offers space and facilities for field tests and is presently supporting an increasing number of offshore-related demonstration projects. This part of the port comprises North Sea sand that was used to create a reclaimed/compacted site. The GDP field tests took place at the Maasvlakte II over a surface of 60 × 60 m^2 in the so-called *area E*. Site location and access routes are shown in Fig. 5.4.

5.3.1. Site investigation

The geotechnical investigation of the test site was carried out between June and September 2019 in two phases of *preliminary* and *detailed* site investigation (PSI and DSI, respectively). First, the PSI was performed to identify suitable locations for installing the test piles, mostly in light of site homogeneity considerations. During the PSI, 25 cone penetration tests with pore water pressure measurements (CPTu's) were performed down to a target depth of 10 m over a regular grid with a spacing of about 12.5 m. After reaching the target depth, dissipation tests were executed for the CPTu's at the four corners of the site to measure the depth of the ground water table. Each dissipation test lasted for one hour, which was deemed sufficient for the achievement of hydraulic steady-state conditions. Based on these tests, the depth of the water table was estimated to range, at the time of the PSI, between 3.5 and 4.5 m depth below the ground surface (phreatic fluctuations are to be expected at the test site due to its proximity to open waters).

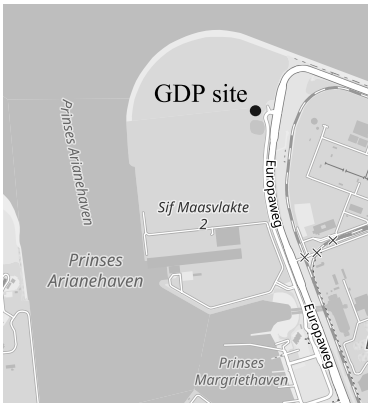

Figure 5.4: GDP test site and its access routes – edited after [303].

After selecting all pile locations based on the PSI, the DSI phase was carried out by performing additional tests around and at the centre of each pile location (see Fig. 5.5). Eight test piles were installed along with a larger reaction pile (RP). The latter would later serve the post-installation loading tests [54]. The embedded length was 8 m for all piles, i.e. 2 m less than the target depth of the CPTu's. Four of the test piles, henceforth referred to as *Main Test Piles* (MTPs), were extensively instrumented and installed with a radial, centre-to-centre distance of 12 m from the RP. The other four piles, labelled as *Auxiliary Test Piles* (ATPs), were installed uninstrumented for preliminary testing purposes, at a distance of 16 m from the RP (see Fig. 5.5). As detailed in the following, the four MTPs were installed using different driving methods, namely impact hammering (IH), axial vibro-driving (VH), and GDP. For the two standard driving methods, the Hydrohammer S-90 and the vibro-hammer CV-25 were used for the IH and VH piles, respectively.

The DSI programme included:

- four CPTu tests at the ATP locations (target depth: 10 m);
- four Seismic CPTu (SCPTu) tests at the MTP locations (target depth: 10 m);

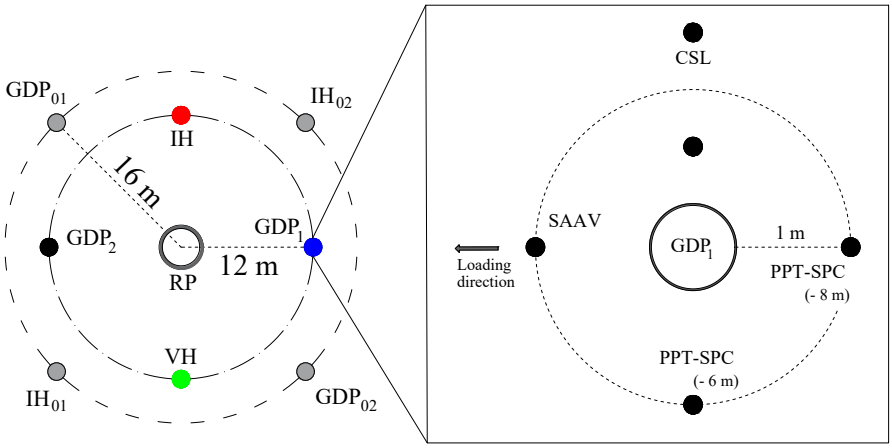

Figure 5.5: Site layout (left – ATPs in grey) and soil monitoring around the MTPs (right). For better readability, the site layout on the left is shown with MTP diameters and distances from the central RP that are not to scale.

- four hydro-profiling tests with mini pump tests (HPT-MPT) around the MTPs (target depth: 15 m).
- borehole sampling around the MTPs. A total of eight boreholes (two per MTP) of 10 m depth and 15 cm diameter were dug and simultaneously sustained with hollow PVC tubes, which would then enable the execution of Cross-hole Sonic Logging (CSL) tests;
- three boreholes (15 cm diameter) around each MTP to host ground monitoring instrumentation, including Shape Acceleration Arrays (SAAVs), soil pressure cells (SPCs), and pore water pressure transducers (PPTs). As shown in Fig. 5.5, two pairs of SPC and PPT sensors were installed in two different boreholes to reach different target depths (6 m and 8 m).

The layout and locations of DSI tests and boreholes are shown on the right side of Fig. 5.5 for the case of the MTP GDP_1. Both PSI and DSI data confirmed the predominantly sandy nature of the soil deposit from the ground surface (NAP +5 m – *Normaal Amsterdams Peil*, i.e. *Amsterdam Ordnance Datum*) down to approximately 10 m below (NAP -5m). The upper 5 m consist of the dredged material employed to create the Maasvlakte II site, which overlays a layer of sand and clayey/silty sand from the holocenic Naaldwijk formation [304].

The whole SCPTu dataset is visualised in Fig. 5.6 after post-processing according to Robertson's soil classification framework (*SBTn charts*) [305, 306]. Robertson's approach relies on the notion of *normalised soil behaviour type*, which is identified for any soil at hand based on the values of relevant dimensionless indices – namely, the normalised cone resistance (Q_{tn}) and the normalised friction ratio (F_r). In Fig. 5.6, all data points from the four soil profiles lie mostly in zone 6 (sand), with some excursions into zone 5 (sand-mixtures)

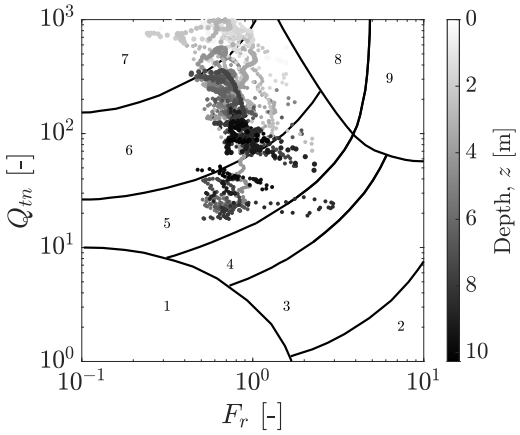

Figure 5.6: Robertson's soil classification at the four MTP locations.

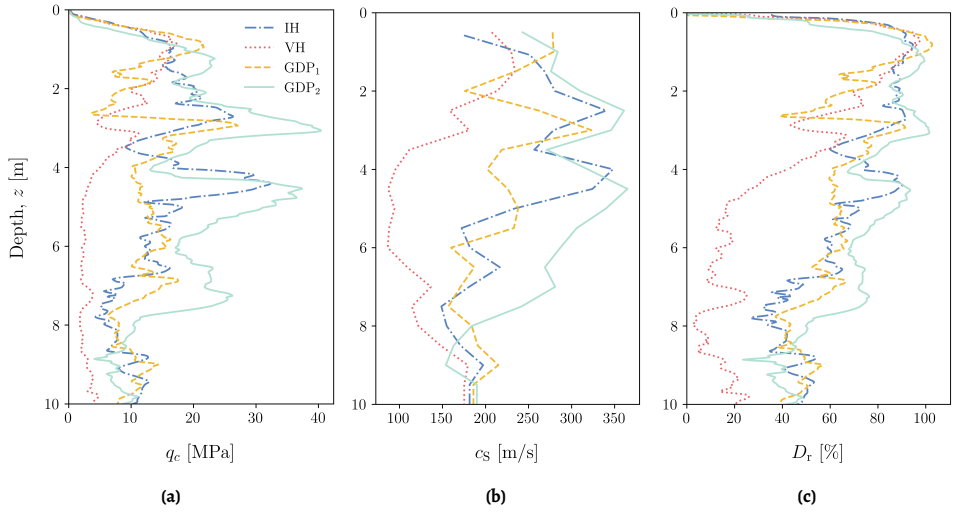

Figure 5.7: Profiles of (a) cone tip resistance (q_c), (b) shear wave velocity (c_S) and (c) relative density (D_r).

and zone 7 (gravelly sand to sand). The cone penetration data from the four MTP locations indicate altogether reasonably consistent profiles of soil type/properties – see Figs. 5.7a and 5.7c.

The profiles in Fig. 5.7 of (a) cone resistance (q_c), (b) shear wave velocity (c_S), and (c) relative density (D_r) (obtained following [307]) suggest that the site comprises very dense sand ($D_r = 80 - 100\%$) in the upper 5 m, and medium-dense to dense sand ($D_r = 60 - 80\%$) in the 5 m below. An exception can be observed at the VH pile location (Fig. 5.7), where the SCPTu data show much lower cone resistance and relative density ($D_r < 40\%$) in the lower 5

m. Obviously, the effects of this site anomaly will require special attention when comparing the results of different pile tests.

The c_S profiles obtained from seismic measurements are largely consistent with the corresponding q_c-D_r distributions, with c_S values mostly in the range from 200 to 300 m/s (and occasionally up to 350 m/s). The VH location exhibits the same aforementioned anomaly also in terms of c_S – note that a significant portion of the profile exhibits c_S values lower than 150 m/s.

Soil samples were also extracted from the aforementioned boreholes for further characterisation of the soil at the Maasvlakte II site. Visual observation, borehole analysis, and particle size distribution (PSD) tests (see Fig. 5.8) confirmed the presence of two different sand types, respectively in the upper and lower 5 m of the deposit. Overall, sieving and micrometric analyses revealed that sand, slightly silty and slightly gravelly, with very spherical and moderately round particles, was present down to 10 m below the ground surface. Two distinct batches of soil were created by mixing borehole material associated with either sand type: soil from the upper layer (0-5 m) was used for Batch 1 (B1), while Batch 2 (B2) was made of soil from the lower layer (5-10 m). As reported in Table 5.2, rather similar index properties were found for B1 and B2 sand samples.

	g_s [−]	e_{max} [−]	e_{min} [−]	D_{50} [mm]	C_u [−]	C_c [−]
B1	2.65	0.82	0.44	0.317	2.346	0.912
B2	2.65	0.83	0.46	0.244	2.161	0.845

Table 5.2: Index properties of Maasvlakte II sand (g_s – specific gravity; e_{max} – maximum void ratio; e_{min} – minimum void ratio; D_{50} – median particle diameter; C_u – coefficient of uniformity; C_c – coefficient of curvature).

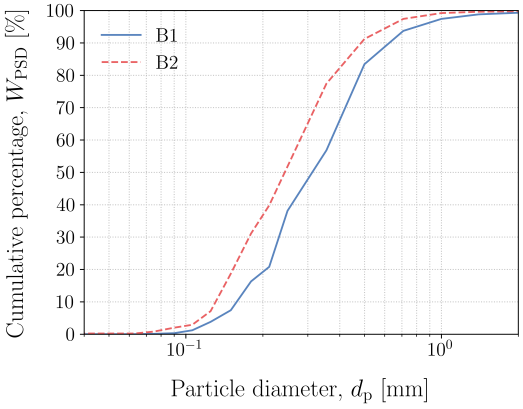

Figure 5.8: Particle size distribution (PSD) curves for two representative soil samples from batches B1 and B2.

5.4. Installation tests and pile-soil monitoring

5.4.1. Field testing programme

As mentioned in the previous section, nine piles in total were used for field testing purposes, namely four MTPs, four ATPs, and one RP, with geometrical specifications reported in Table 5.3. The distinction between MTPs and ATPs relates to their different roles in the GDP experimental campaign. The ATPs were exploited for preliminary testing of the GDP shaker, so that relevant driving settings could be first adjusted during the installation of non-instrumented test piles. After the installation of the ATPs, it was decided to target for MTPs axial and torsional vibration frequencies approximately equal to 16.5 Hz and 63 Hz, respectively. The latter pair of values was chosen to exploit as much as possible the vibratory capacity of the GDP shaker, though without compromising the testing agenda or operational safety. An axial frequency of around 24.8 Hz was adopted for the installation of the VH pile. The ATPs also served post-installation tests, in that they enabled the calibration of specific settings for the subsequent lateral loading tests [54]. Since the main goal of the GDP campaign was to monitor and analyse the performance of the MTPs, they were fully instrumented prior to all tests. The present experimental data were exclusively recorded on/around the MTPs, with a focus on the GDP piles.

		Test piles	Reaction pile
Length	L_p	10 m	10 m
Embedded length	L_e	8 m	8 m
Outer diameter	D_p	0.762 m	1.6 m
Aspect ratio	$L_\mathrm{p}/D_\mathrm{p}$	13.12	6.25
Wall thickness	h_p	0.0159 m	0.02 m

Table 5.3: Geometrical characteristics of the piles indicated in Fig. 5.5.

Extensive instrumentation of all MTPs and the soil in their surrounding was set in place to monitor the complex soil-pile response during driving – see Fig. 5.5. As previously mentioned, the final pile locations were selected based on the results of the PSI and DSI, with mutual distances limited by the length of the lateral loading frame that was employed afterwards [54]. The circular arrangement shown in Fig. 5.5 allowed to minimise the interference between consecutive pile driving tests. In chronological order, the MTPs were installed as follows: (i) GDP_2 (30/10/2019), (ii) GDP_1 (30/10/2019), (iii) VH (31/10/2019) and (iv) IH (4/11/2019). The installation sequence may generally be relevant to assessing the interference of consecutive pile installations over a limited soil surface. However, since all pile-to-pile distances were larger than $10D_\mathrm{p}$ at the GDP test site, it is argued that such interference must have been negligible in all instances [114, 308].

The same installation protocol was followed for all piles, regardless of the specific driving method. In particular, such a protocol included the following three phases (see Fig. 5.9): (i) in the first phase, the top flange of the pile was connected to the shaker (for VH and GDP piles), then the pile was upended by a crane and positioned vertically at the corresponding installation location. The pile was stabilised by means of lateral restraints, and driven for 0.5 m into the soil. At that point the installation was paused to check that all sensors

were functioning properly; (ii) in the second phase, each pile, still laterally restrained, was driven further down to 3 m of total penetration; (iii) in the third phase, lateral restraints were removed and each pile was driven up to the target penetration depth of 8 m. In the remainder of this work, only data measured during the third phase of the installation protocol are presented. Such data are believed to be most meaningful in that they relate to pile penetration in water-saturated soil. It is worth noting that both axial and torsional vibration frequencies – and therefore the corresponding load amplitudes (cf. to Equations (5.1)-(5.2)) – were kept constant during the installation tests.

(a) (b) (c)

Figure 5.9: (a) First, (b) second and (c) third installation phases of an ATP.

5.4.2. Pile instrumentation

During the installation of the MTPs, a number of measurements were performed simultaneously, both on the piles and in the surrounding soil, in order to monitor the dynamic behaviour of the complete pile-soil system. As the GDP method comprises a combination of axial and torsional vibrations, non-zero components of motion in all directions were anticipated. Accordingly, the following sensing instrumentation was deployed:

- two tri-axial micro-electro-mechanical systems (MEMS) accelerometers to record the dynamic motion of the pile during installation. The MEMS accelerometers were positioned 1.56 m below the pile head at diametrically opposite locations (see Fig. 5.10 and their technical specifications in Table 5.4);

- fiber Bragg grating (FBG) sensors (12 per side) to monitor pile strains along the length (see specifications in Table 5.5). The same technology has been recently adopted for pile monitoring during impact driving tests [309]. Two types of FBG configurations were adopted, namely in-line FBGs and FBG rosettes (see Fig. 5.10). In-line FBGs were installed at multiple cross sections along the length, two per cross section at diametrically opposite locations to monitor axial strains. FBG rosettes were placed at three selected locations along the length, two per cross-section and diametrically opposite, in order to monitor strains along the longitudinal and two inclined directions,

at angles of 60° and 120° with respect to the horizontal plane;

– two FBG temperature sensors to measure temperature variations on the pile surface during pile penetration. The main purpose of such measurements was to obtain quantitative factors for temperature compensation of the FBG measurements. The temperature sensors were positioned next to the location of the last FBG sensor (approximately 35 cm above the pile tip);

– one potentiometer (draw-wire type) to record the penetration of each pile into the soil by measuring its axial displacement. The measurement range of the potentiometer was ±10 m and its accuracy equal to 0.1 mm.

Type of sensor	MEMS ADXLL377
Number of sensors per pile	2 (1 per side)
Measurement range	±200 g
Bandwidth (x, y axes)	0.5 Hz – 1300 Hz
Bandwidth (z axis)	0.5 Hz – 1000 Hz
Sensitivity (x axis)	5.8 mV/g
Sensitivity (y axis)	6.5 mV/g
Sensitivity (z axis)	7.2 mV/g

Table 5.4: Technical specifications of tri-axial MEMS accelerometers

Type of FBG strain sensor	Sylex FFA-01
Number of sensors per pile	24 (12 per side)
Measurement range	±3000 μm/m
FBG wavelength range	1510 nm - 1590 nm
Fiber coating	Polyimide

Table 5.5: Technical specifications of in-line FBG strain sensors.

All the pile sensors operated at a sampling frequency equal to 1 kHz. Additional details about sensor specifications are provided in Tables 5.4 and 5.5.

5.4.3. Ground monitoring

The response of the soil surrounding the MTPs was monitored during pile driving tests by means of the following ground monitoring instrumentation:

– Eight VWPC2100 *RST Instruments* sensors containing both soil pressure cells (SPCs) and pore water pressure transducers (PPTs) were deployed to simultaneously record the evolution in time of the total radial stress (σ_r) and the pore pressure (p_w), with accuracy and resolution of 5.0 kPa and 0.25 kPa, respectively. For each MTP and prior to pile driving, the sensors were installed at two different depths (6 m and 8 m below the ground surface, see Fig. 5.5);

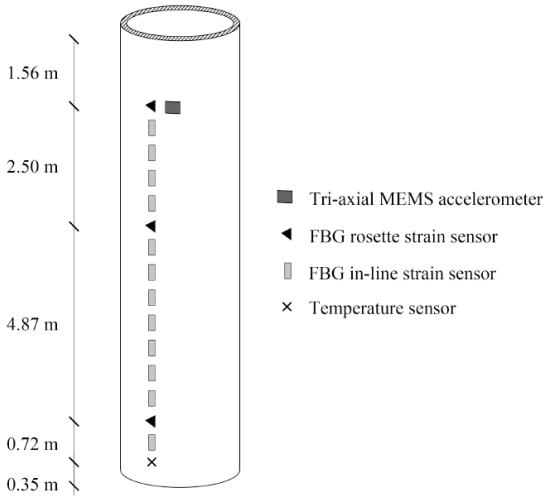

Figure 5.10: Pile instrumentation.

– shape-acceleration arrays (SAAVs) located at the front side of each pile with respect to the lateral loading direction (see Fig. 5.5) to record lateral soil displacements during installation. The SAAV sensors comprised a cable-shaped series of half-meter rigid segments from 0.5 m to 8.5 m, which would detect lateral soil displacement through the tilt of the individual segments.

After installing the above soil sensors in boreholes dug during the DSI, all SPCs, PPTs and SAAVs were set to sample data at 1 kHz for all pile installation tests.

Finally, cross-hole sonic logging (CSL) tests were performed before and after pile driving tests, in order to evaluate possible installation effects in the soil by means of P-wave measurements. For these tests, two 10-meter long PVC access tubes were installed at a distance of 0.5 m and 1.5 m from the pile wall (see Fig. 5.5), while two ultrasonic transmitter/receiver probes were lowered to the bottom of the tubes. The transmitted P-waves (50 kHz nominal frequency) were recorded by the receiver probe at a sample rate of 0.5 MHz. To assess repeatability, CSL tests were performed twice for each pile before and after installation.

5.5. Field observations during GDP installation

This section presents relevant field observations associated with the dynamic response of the MTPs and the surrounding soil during the installation tests – namely, during the third phase of the installation protocol described above. The following analysis of field data is a preliminary effort to demonstrate the potential of the GDP method, particularly in comparison to standard axial vibratory driving (VH). Due to site inhomogeneity and the inherent differences between the considered driving methods (IH, VH, GDP), further interpretation of the whole dataset may only be achieved through future numerical modelling work.

5.5.1. Pile penetration rates

Figure 5.11 displays the penetration time series for the VH and the two GDP piles. The red and blue lines correspond to the displacement of GDP_1 and VH as measured by the potentiometer (PM), respectively, while the respective measurement for GDP_2 is not available due to sensor failure during driving. The markers in the same figure represent the "slow" measurements of the driving logging (DL) system, which includes displacement values recorded every 25 cm of pile penetration. Average penetration rates equal to 20.9 mm/s, 37.1 mm/s and 18.7 mm/s were determined for VH, GDP_1, and GDP_2, respectively, based on the driving logging system; the more reliable data returned by the potentiometer transducer for VH and GDP_1 indicate average penetration rates of 19.8 mm/s and 34.3 mm/s, respectively. The good agreement between the data from the potentiometer and the driving log led to consider the latter reliable also for the GDP_2 installation.

As can be observed in Fig. 5.11, GDP_1 had a shorter installation time compared to VH and GDP_2 (and therefore a larger penetration rate). Since the two GDP piles were driven with identical installation settings, the higher installation rate of GDP_1 was presumably due to the lower cone resistance (q_c) and relative density (D_r) at the corresponding soil location – see Fig. 5.7. Although VH was installed in weaker soil, GDP_1 penetrated at an almost double average rate. Further, while GDP_2 was driven into the stiffest soil (among the four MTP locations), its average penetration rate was found to be very similar to that of VH (see Fig. 5.11). These facts seem to support that combining axial and torsional vibrations was indeed beneficial from a pile driving perspective.

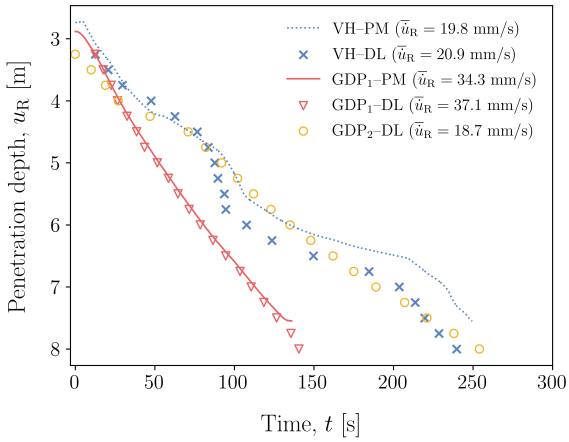

Figure 5.11: Pile penetration curves (u_R) for VH, GDP_1 and GDP_2, with average penetration rates ($\bar{u}_R$) obtained from potentiometer (PM) and driving log (DL) data.

It was also possible to obtain more detailed information about the penetration rates by numerically differentiating the pile penetration time series – which could be done using the potentiometer data, therefore only for VH and GDP_1. The differentiated time series are given in Figs. 5.12a and 5.12b alongside their low-pass filtered counterparts (a moving average filter with a cut-off frequency of 2 Hz). Figure 5.12b indicates that the penetration rate of GDP_1 was on average fairly constant during installation. In contrast, VH penetrated

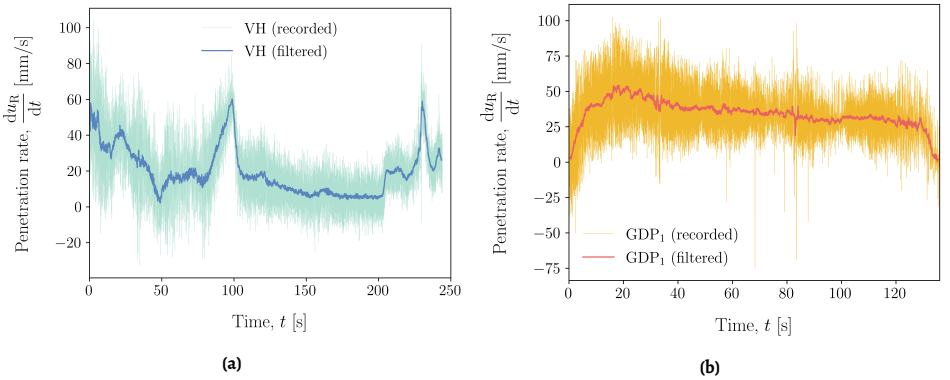

Figure 5.12: Time evolution of the pile penetration rate $\left(\frac{du_R}{dt}\right)$ obtained for (a) VH and (b) GDP$_1$ from potentiometer (PM) data.

5

at a more variable rate, with some abrupt changes during the penetration process – see for instance the peak around 100 s. Considering the penetration depth reached by the pile tip of VH after such time (between 4 and 5 m), it is likely that the transition from unsaturated to saturated soil had a temporary influence on the penetration rate. It is again apparent that GDP$_1$ driving outperformed VH, especially considering that the latter was installed in weaker soil (see Fig. 5.7). Overall, the penetration rates observed at the GDP site resemble quite closely the (high) values reported by [310] during the axial vibro-driving of similarly sized open-ended pipe piles. Importantly, no refusal was experienced during GDP driving, as is testified by the rather steady penetration rates in Fig. 5.11.

5.5.2. Power and energy consumption

In addition to pile penetration measurements, the power consumption of the GDP shaker and the axial vibro-hammer was also monitored to assess the efficiency of the different methods. In agreement with the GDP shaker specifications in Table 5.1, two independent exciter blocks were used for the axial and the torsional excitation. In Fig. 5.13a, the power consumption of the hydraulic power unit (HPU) is plotted against time for the axial excitation provided by the GDP shaker and the axial vibro-hammer; the torsional HPU power consumption is shown in Fig. 5.13b, exclusively for the two GDP piles.

It is readily apparent that the power consumed to impose torsional vibrations is substantially larger than its axial counterpart for both GDP$_1$ and GDP$_2$. Generally, the HPU power consumed for axial loading of both GDP piles was found to be almost identical, and significantly lower than the power consumed to axially vibrate the VH pile (see Fig. 5.13a). In contrast, the power associated with the torsional loading of the GDP piles is larger than that consumed for the VH pile, as one would expect in light of the higher frequency of torsion. Overall, the power consumed by the GDP shaker lies inside the power capacity of the VH device, as was indeed a target of the first GDP shaker design in order to enable fair comparisons.

It is also worth noting that GDP$_2$ consumed through torsion more power than GDP$_1$, as

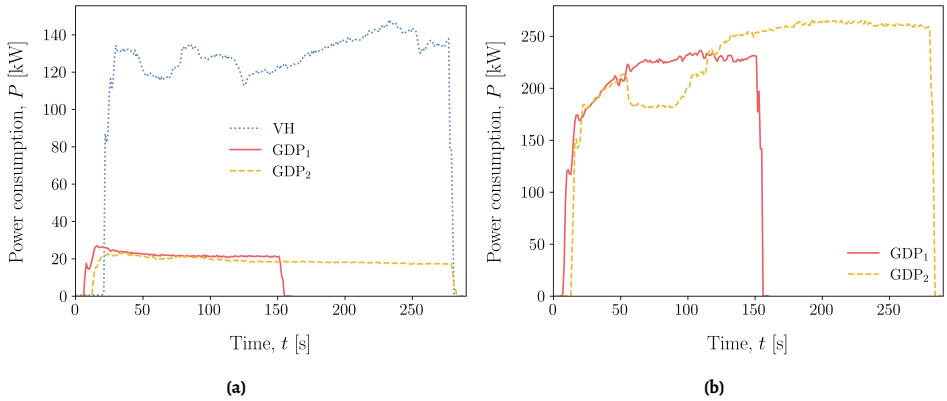

Figure 5.13: HPU power consumption (P) associated with (a) axial and (b) torsional loads applied to VH, GDP$_1$, and GDP$_2$.

a likely outcome of the denser soil profile at the GDP$_2$ location – this is also confirmed by the longer installation time (see Fig. 5.13b). Further, a drop in torsional power consumption is visible for GDP$_2$ between 50 s to 100 s: since power was delivered to maintain a given vibration frequency (which was constant during driving), a local reduction in soil resistance may have caused a temporary power drop of the kind shown in Fig. 5.13. As time elapsed, the power consumed to axially vibrate both GDP piles slightly decreased with the penetration depth, while the torsional power tended to increase in time for both piles. Overall, these trends indicate that the soil resistance to pile driving was mainly overcome through the torsional mechanism. This observation strongly supports the conceptual foundation of the GDP method, i.e. the beneficial effect of torsional vibrations in overcoming the frictional soil resistance along the pile shaft.

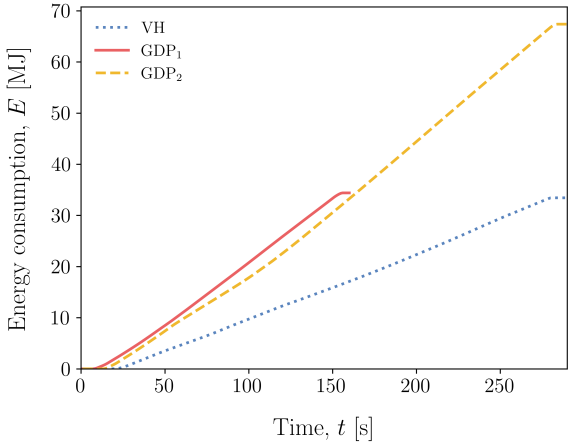

Figure 5.14: Time evolution of the total energy consumption (E) during the installation of VH, GDP$_1$, and GDP$_2$ (both axial and torsional components included for GDP piles).

As a final comparison between VH and GDP driving performances, the total energy consumption (both axial and torsional for GDP) is plotted against the installation time in Fig. 5.14. The efficiency of the GDP method is clearly supported by the fact that GDP_1 consumed approximately the same total energy as VH (only 2.8% larger), even though GDP_1 was driven in substantially stronger soil. On the other hand, GDP_2 required approximately twice as much energy as needed for GDP_1, which was mostly due to the stronger soil encountered at that location (see Fig. 5.7). A detailed discussion of energy efficiency matters and their quantification both for VH and GDP piles is provided by Gómez et al. [52]. For clarity, the values of average cone resistance along the soil profile, total energy consumption, and the average penetration rate are summarised in Table 5.6 for VH, GDP_1, and GDP_2.

	VH	GDP_1	GDP_2
Average cone resistance, $\overline{q}_c$	5.75 MPa	11.9 MPa	18.6 MPa
Total energy consumption, E	33.44 MJ	34.39 MJ	67.38 MJ
Average penetration rate, $\left(\overline{\frac{\mathrm{d}u_\mathrm{R}}{\mathrm{d}t}}\right)$	19.8 mm/s	34.3 mm/s	18.7 mm/s

Table 5.6: Comparison of geotechnical properties and driving performance for VH, GDP_1, and GDP_2.

5.5.3. Pile response during driving

To portray relevant features of the dynamic pile response during GDP, acceleration spectra have been obtained from the output of the two MEMS accelerometers. In particular, the amplitudes of the acceleration spectra (denoted by $|\mathscr{F}(\cdot)|$) are shown in Fig. 5.15 both for GDP_1 and GDP_2, and for each spatial direction, i.e. axial, radial and circumferential. The driving frequency of the GDP shaker in the axial direction was measured at 16.3 Hz and 16.5 Hz for piles GDP_1 and GDP_2, respectively. These frequencies correspond to well-visible peaks in Figs. 5.15a and 5.15b. Next to these primary amplitude peaks, which are directly related to the main driving frequencies, the pile response is amplified at multiple other harmonics. The reason for this observation is twofold. First, the shaker itself excites the system at multiple super-harmonics (of the main driving frequency) due to minor imperfections in the rotation of the eccentric masses. This statement applies to both vibration modes excited in the pile, i.e., axial and torsional. Secondly, the dynamic response of the system is inherently non-linear even at low vibration amplitudes, and this fact may cause further amplification of the mentioned super-harmonics [311]. The extent to which each of these two mechanisms contributes to the energy content in the super-harmonics has not been quantified – however, the first mechanism is believed to be dominant. It is also interesting to note that frequencies (including super-harmonics) associated with the torsional vibration are clearly visible in the other acceleration spectra. By comparing the spectra in Fig. 5.15 for the two GDP piles, it can be stated that the acceleration response is almost identical regardless of moderately different soil conditions, which indicates strong dependence on the GDP excitation.

The amplitudes of the circumferential acceleration spectra show for both GDP piles a distinct peak at the main torsional driving frequency, i.e., at 62.6 Hz and 63 Hz for piles GDP_1

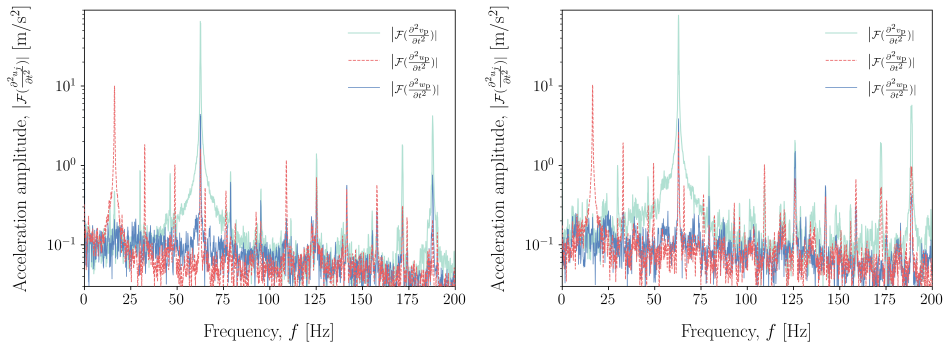

Figure 5.15: Amplitudes of acceleration spectra $\left|\mathscr{F}\left(\frac{\partial^2 u_j}{\partial t^2}\right)\right|$ in all directions for piles (a) GDP_1 and (b) GDP_2.

and GDP_2, respectively. Once again, the frequencies of 125 Hz and 188 Hz (approximately), corresponding to the first and second super-harmonics, are associated with prominent spectral amplitudes.

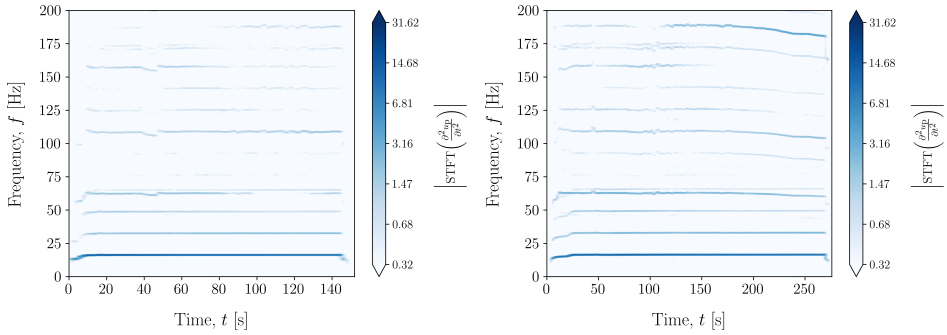

Figure 5.16: Amplitudes of the STFT in axial direction $\left|\mathrm{STFT}\left(\frac{\partial^2 u_p}{\partial t^2}\right)\right|$ for (a) GDP_1 and (b) GDP_2.

The acceleration spectra in Fig. 5.15 provide a detailed picture of the frequency content during the time interval taken into account. Such an interval was chosen to be a 10 s time window approximately in the middle of the third driving phase. Such a choice was motivated by the abrupt variation in frequency content at the beginning and the end of the driving process, due to the (de)activation of the GDP shaker. It is however worth recalling that the acceleration signals recorded during pile penetration may not be *a priori* regarded as stationary. In Figs. 5.16 and 5.17 the amplitudes of the discrete short-time Fourier transforms (STFTs) of the sensor-averaged pile accelerations - denoted by |STFT(·)| - are shown in spectrogram form [312]. Specifically, the axial and circumferential components of motion are presented, as they are the most relevant to the GDP vibratory excitation. In the resulting

time-frequency analysis, a trade-off between resolution in time and frequency had to be found, as a consequence of the Gabor limit [313].

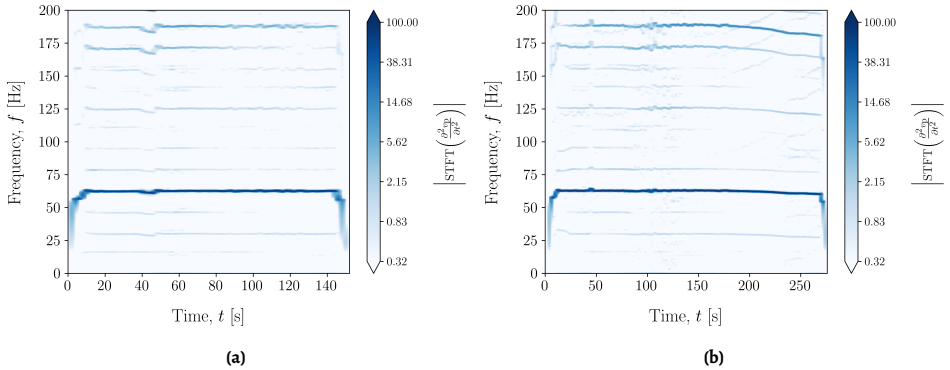

Figure 5.17: Amplitudes of the STFT in circumferential direction $\left|\mathrm{STFT}\left(\frac{\partial^2 v_\mathrm{p}}{\partial t^2}\right)\right|$ for (a) GDP_1 and (b) GDP_2.

Figure 5.16 confirms that the frequency content was relatively constant during the main part of the installation (phase three), as was expected based on the installation settings (constant frequency) and the steady pile penetration trends observed in Fig. 5.11. The existence of the previously identified super-harmonics is confirmed throughout the whole installation process. For GDP_1, Fig. 5.16a shows that the super-harmonics associated with the axial driving frequency slightly decreased in amplitude towards the end of driving – conversely, this observation does not apply to the main driving frequency above 16 Hz and its first super-harmonic at 33 Hz, which seem to have maintained a fairly constant amplitude. The amplitude of the frequency component close to the torsional excitation frequency decreased significantly towards the end of driving.

The results of the time-frequency analysis performed for the circumferential acceleration signals are reported in Fig. 5.17. In this case, the main driving frequency is clearly apparent, and its energy level is considerably larger than that associated with the super-harmonics. This is in full agreement with what has been observed in Fig. 5.15. The amplification of the second torsional super-harmonic towards the end of GDP_2 installation is further supported by Fig. 5.17b. Similarly to the case of the axial acceleration (Fig. 5.16), the spectrogram of the circumferential acceleration (Fig. 5.17) corroborates that the torsional driving frequency (and the associated amplitude) remained nearly constant during GDP installation, as per the intended installation settings.

5.5.4. Ground monitoring data

Further insight into the mechanics of GDP can be obtained by inspecting the ground monitoring data. In Fig. 5.18, pore water pressure variations Δp_w (with respect to local, pre-installation values) are plotted against time for both GDP piles and at two different depths (6 m and 8 m below the ground surface). The vertical lines in all subplots of Fig. 5.18 indicate the times when the pile reaches a penetration depth of 6 m (location of the first PPT) and 8 m (location of the second PPT and target penetration depth). A common feature of

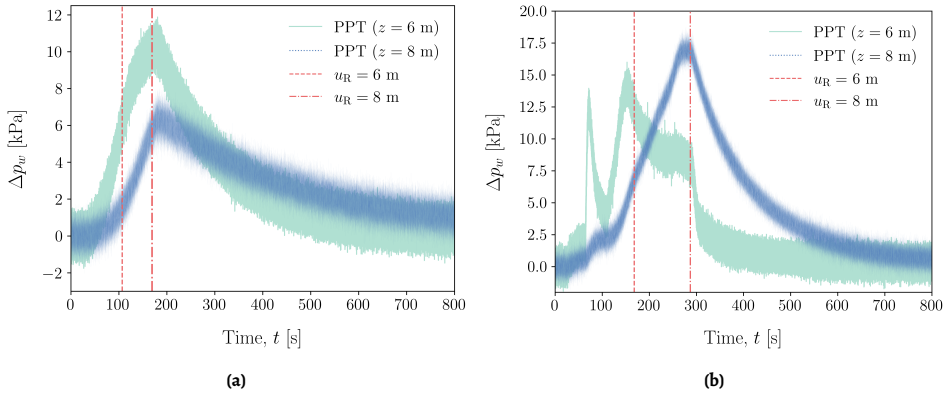

Figure 5.18: Pore water pressure variations (Δp_w) recorded during the installation of (a) GDP_1 and (b) GDP_2 at depths, z, equal to 6 m and 8 m below the ground surface. The vertical dashed lines indicate the times when the pile tip penetration (u_R) equals the depths of the two PPT sensors.

all Δp_w trends in Fig. 5.18 is the gradual increase in pore water pressure during driving, which is consistent with previous observations regarding vibratory driving in saturated granular soils [301]. Subsequently, excess pore pressures attenuate as pile driving reaches its conclusion: pore pressure dissipation takes only a few minutes in a soil as permeable as that at the Maasvlakte site. The outlook of Fig. 5.18a (for GDP_1) and Fig. 5.18b (for GDP_2) reveals maximum pore pressure variations in the order of 10 kPa for both piles and reference depths, although larger Δp_w emerge for the pile installed in denser soil (GDP_2). A sudden increase in pore water pressure is visible at 60 s (approximately 4 m penetration), followed by a temporary drop in excess pore pressure at $z = 6$ m in Fig. 5.18b. The former increase may be attributed to a local inhomogeneity in the GDP_2 soil profile between 3 m and 5 m – cf. to the q_c profile in Fig. 5.7a – while the ensuing drop seems to be closely related to the decrease in torsional power consumption (and therefore in mobilisation of soil resistance) that has been previously observed for GDP_2 in Fig. 5.13. Figure 5.18b does not show a similar behaviour at $z = 8$ m, which may be due to the larger distance of the PPT from the pile tip during the relevant time interval.

At the same depths where pore water pressures were measured, variations in total horizontal/radial soil stresses ($\Delta\sigma_r$) were also monitored (see Fig. 5.19). The soil pressure measurements for GDP_2 in Fig. 5.19b show different trends at the two reference depths. Nonetheless, $\Delta\sigma_r$ evolves to reach soil pressures lower than the estimated pre-installation values both at 6 m and 8 m below the ground surface – more prominently at the shallower location ($z = 6$ m). The overall reduction in radial (total) confinement is likely associated with vibration-induced sand densification. Such a densification is indeed expected to be more significant at shallower soil locations, i.e., where the soil experiences a larger number of dynamic loading cycles.

As for $\Delta\sigma_r$ measurements around GDP_1, it should be noted that a significantly larger reduction was measured for no obvious reason – see Fig. 5.19a. Although decreasing $\Delta\sigma_r$ is consistently found in both GDP piles, full reliability of soil pressure data around GDP_1 may not be taken for granted. In principle, the stiffness of the SPCs should be similar to the soil

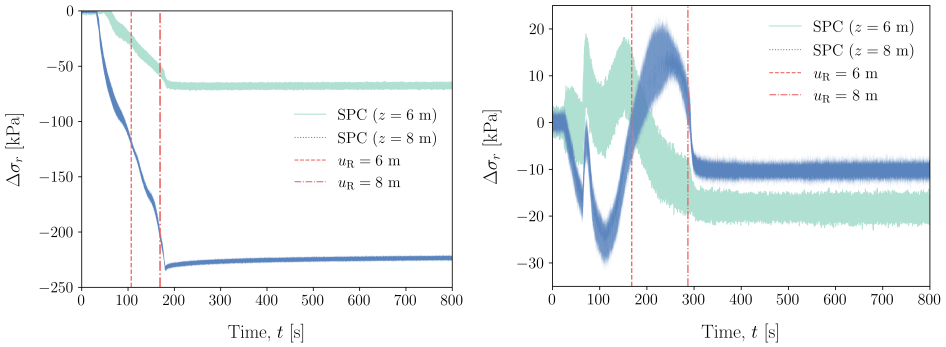

Figure 5.19: Total radial soil stress variations ($\Delta\sigma_r$) recorded during the installation of (a) GDP_1 and (b) GDP_2 at depths, z, equal to 6 m and 8 m below the ground surface. The vertical dashed lines indicate the times when the pile tip penetration (u_R) equals the depths of the two SPC sensors.

stiffness to avoid arching effects and properly capture soil stress conditions. A number of factors, such as local soil inhomogeneity and/or sensor installation in a soil of quite different stiffness, might have produced inaccuracies in the measured data.

5.5.5. Impact of GDP on soil stiffness

During the PSI and the DSI, well-established in-situ procedures such as CPTu, SCPTu, and HPT-MPT were performed. However, it was the first time – to the authors' knowledge – that CSL tests were planned for geotechnical investigation purposes; CSL tests are most usually performed to detect mechanical anomalies in drilled shafts and diaphragm walls [314]. Specifically, CSL tests were performed before and after pile installation to evaluate the impact of GDP on the stiffness of the surrounding soil. Since compression wave velocity c_P is related to the stiffness of the medium, variations in wave velocity can be used for general quantification of installation effects. Depth-profiles of average compression wave velocity (tests were performed twice) before and after pile installation are reported in Fig. 5.20. The c_P profiles in the upper soil layers exhibit significant scatter, and are generally unreliable as a consequence of unsaturated soil conditions. Conversely, deeper c_P measurements appear to be reliable and in agreement with expectations. In particular, appreciable c_P enhancement can be observed in the lower water-saturated soil, which indicates an overall stiffening of the soil around the pile. This finding is consistent with the $\Delta\sigma_r$ trends shown in Fig. 5.19, and reinforces the belief that GDP driving can induce soil densification/stiffening with no apparent evidence of soil degradation.

5.6. Concluding remarks

Recent research related to the GDP project ('Gentle Driving of Piles') has been presented in this chapter. GDP is a TU Delft-led research project on the development of a new vibratory driving technology for monopiles. Its stepping stone is the idea that both efficient installation and low noise emissions can be achieved by applying to the pile a combination of

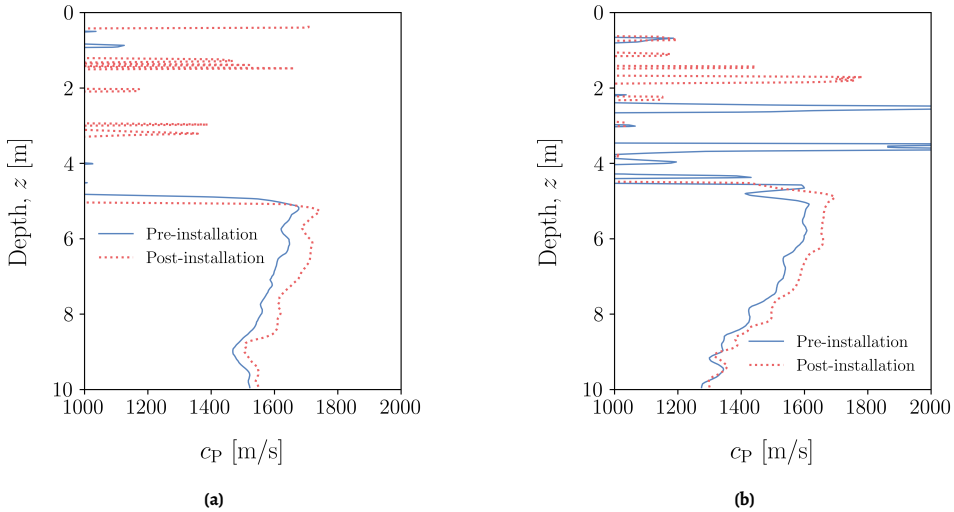

Figure 5.20: CSL test results: c_P profiles obtained before (solid lines) and after (dotted lines) pile installation in the vicinity of (a) GDP_1 and (b) GDP_2.

low-frequency/axial and high-frequency/torsional vibrations. To achieve a first demonstration of the GDP concept, medium-scale field tests were performed at the sandy Maasvlakte II site in Rotterdam. Such tests included installation experiments with different driving methods (impact hammering, axial vibro-driving and GDP), followed by cyclic/dynamic loading of the same piles.

The main experimental evidence presented in this chapter may be summarised as follows:

- two test piles have been smoothly installed at the reference site via GDP, with fairly constant/high penetration rates and no instances of pile refusal;
- the comparison between GDP and axial vibro-installation has highlighted the remarkable potential of the GDP method. Compared to standard axial vibro-driving, the GDP method enabled faster installation in stiffer soil with comparable total energy consumption (cf. GDP_1 installation data to VH);
- the values of HPU power consumed to impose axial and torsional vibrations have proven consistent with typical magnitude levels for vibro-piling. Particularly, the evolution in time of such power values has suggested that the torsional mechanism contributed the most to pile penetration;
- the frequency and time-frequency analyses of pile acceleration signals have indicated that frequencies mainly associated with the vibrations of the GDP shaker were excited during driving, which has turned out to be a nearly stationary process under the reference site conditions;

- the hydro-mechanical response of the soil during driving has been found to be in line with expectations for vibratory driving processes. Pore pressures in the order of a few kPa built up and rapidly dissipated in the permeable soil at hand. A gradual relaxation in the total radial soil stress has been observed as a likely outcome of vibration-induced soil densification;
- the results of in-situ CSL tests have shown an increase in P-wave soil velocity after pile installation, which may be associated with an overall increase in soil stiffness due to the mentioned densification.

The field campaign has preliminarily demonstrated the potential of the GDP method as a pile installation technology with high installation performance and low environmental impact. The results presented from the installation tests, along with those regarding the post-installation performance of the test piles [54], encourage further development of the GDP method and its future extension to full-scale offshore conditions. To that end, a set of numerical tools that can serve for quantitative analysis, interpretation of the installation tests and design purposes are indispensable for future development and constitute the focus of the ensuing chapters.

6

A non-linear 3-D pile-soil model for vibratory pile installation in layered media

The scope of the GDP field campaign encompassed various objectives, with a view to further the body of knowledge on the topic of pile installation. It is apparent that the proof of concept of the GDP method comprised the main novel contribution of the experimental campaign by itself. Furthermore, the collected dataset and the field observations served another central purpose of the GDP project, i.e. the comparison of standard pile driving techniques (and GDP) in terms of installation and post-installation performances. These two aspects are associated with major open research questions in vibratory pile installation. Focusing on the installation process, we endeavour to advance the state of modelling approaches in vibratory driving, by joining the numerical developments of the preceding chapters and utilizing the experimental results of the GDP campaign.

In the ensuing, a vibratory pile driving model is developed that aims to bridge the gap between the available medium- and high-fidelity approaches and comprises the main novel contribution of this chapter. The former approaches possess multiple empirical components and are largely based on simplifications, whereas the latter are hindered by computational and practical aspects. As a consequence, an established modelling approach - applicable to engineering practice - to study vibratory pile installation cannot be distinguished. Therefore, a modelling framework that can adequately address the physics of the process, while retaining computational efficiency and engineering applicability is indispensable. With a view to achieving this aim, the theoretical elements presented in Chapters 2 and 4 are integrated into a non-linear dynamic pile-soil interaction model. Furthermore, the soil model parameters are calibrated based on standard *in-situ* geotechnical measurements, thus rendering the overall approach SCPT-based. Finally, installation data from the GDP field tests (Chapter 5) are compared with model predictions - showcasing the predictive

Parts of this chapter have been published in Tsetas et al. [315].

capabilities of the model - and this framework is further utilized to investigate certain aspects of the vibratory installation process.

6.1. Numerical modelling of vibratory pile driving

Bottom-fixed foundations are primarily used to support OWTs and amongst the available concepts, the monopile is the foremost one [25]. The installation of offshore monopiles is most commonly performed by means of impact hammering. However, in view of the environmental concerns related to impact piling and the challenges entailed in the continuous size increase of monopiles, the investigation and further development of alternative installation methods with low environmental impact are indispensable. At present, the offshore wind industry is increasingly adopting vibratory techniques, albeit their use in the past was hindered by a number of factors, including the incompleteness (and inconclusiveness) of available field observations. To further accelerate this shift, knowledge gaps and open questions regarding pile drivability, installation efficiency and post-installation effects need to be addressed [48, 50, 52].

The available modelling approaches for vibratory pile installation can be broadly divided into two categories. The first category comprises high-fidelity models. In these approaches, computational schemes such as the total Lagrangian [134], the updated Lagrangian [127] and the Coupled-Eulerian Lagrangian formulation [136] have been employed in conjunction with advanced soil constitutive models (e.g. hypoplasticity), whereas the pile is treated as a rigid body. Significant insights can be gained with such approaches, regarding the post-installation soil stress state and the mechanisms of vibratory driving. However, the limitations of these models lie in their excessive computational cost, which renders them rather prohibitive for engineering purposes, and the large number of constitutive soil parameters that need to be calibrated. The previous cannot be retrieved by standard *in-situ* measurements, thus such models require additional extensive laboratory testing.

On the other hand, a range of medium-fidelity models exists for vibratory driving, albeit no established approach can be distinguished. One-dimensional (1-D) radial models have been widely used, where the pile is modelled as a rigid body and the soil is discretized into concentric rigid cylinders [107, 109]. Such an approach disregards the pile flexible motion and precludes the consideration of soil layering. Furthermore, 1-D wave equation models have been adopted from the area of impact piling [316, 47]. In these approaches, the pile is modelled as a thin rod and the soil reaction is considered through local and frequency-independent mechanical analogues [84]. However, these approaches were originally developed for small-diameter piles and their applicability to offshore monopiles has been questioned in terms of pile [193] and soil reaction modelling [95]. It is evident that an engineering-oriented model that captures adequately the mechanics of vibratory installation is essential.

In response to the preceding shortcomings, a computationally efficient model is presented, that amalgamates rigorous theoretical elements and promising prediction capabilities in an engineering-oriented framework. A SAFE cylindrical shell model is utilized to represent the pile and the dynamic response of a layered soil half-space is expressed in terms of Green's functions for ring sources. The latter are obtained via the Thin-Layer Method (TLM) [285], coupled with Perfectly Matched Layers (PMLs) to approximate the underlying half-space [267, 317]. Furthermore, the non-linear pile-soil interaction is addressed through

a history-dependent frictional interface and a visco-elasto-plastic tip reaction model, both characterized on the basis of standard geotechnical *in-situ* measurements (i.e. SCPT). The solution to the non-linear pile-soil interaction problem is obtained by means of sequential application of the Harmonic Balance Method (HBM) [318, 319], leading to a computationally efficient yet accurate scheme. This approach is one of the major contributions of this chapter, being uniquely inspired by the physics of the installation process, rendering the computational cost similar to a 1-D medium-fidelity approach and is applicable to a broader class of non-linear systems that possess quasi-periodicity due to amplitude modulation.

6.2. Pile-soil model description

The present model describes the process of vibratory pile installation. The pile is represented as a thin cylindrical shell and the soil medium as a layered half-space. As regards the input excitation, either a harmonic (or periodic) load can be directly applied at the pile head, or a mechanical analogue of a few degrees-of-freedom (DoFs) can be coupled with the pile by virtue of the FE-based framework employed. In the latter case, the harmonic (or periodic) load is applied at a certain component and the overall interaction is taken into account. Considering that all the components of our model are symmetric around the vertical axis, i.e. pile, soil and input excitation, the overall 3-D model is axisymmetric and circumferential motion is absent. A schematic of the described model is shown in Fig. 6.1 and a flowchart that outlines the overall computational framework is presented in Fig. 6.2.

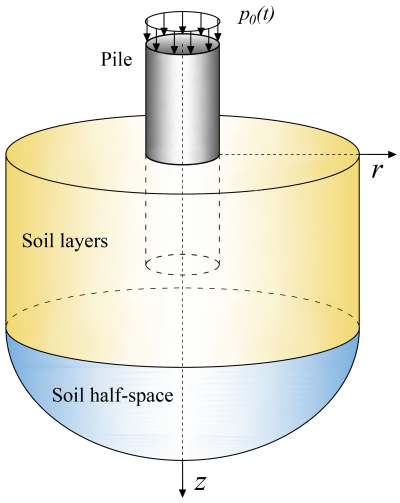

Figure 6.1: A pipe pile partially embedded in a layered soil medium.

6.2.1. Modelling of a tubular pile as a thin cylindrical shell

Consider a thin cylindrical shell with wall thickness h_p, length L_p and mid-surface radius R_p. The thin shell is comprised of linear isotropic elastic material with Young's modulus

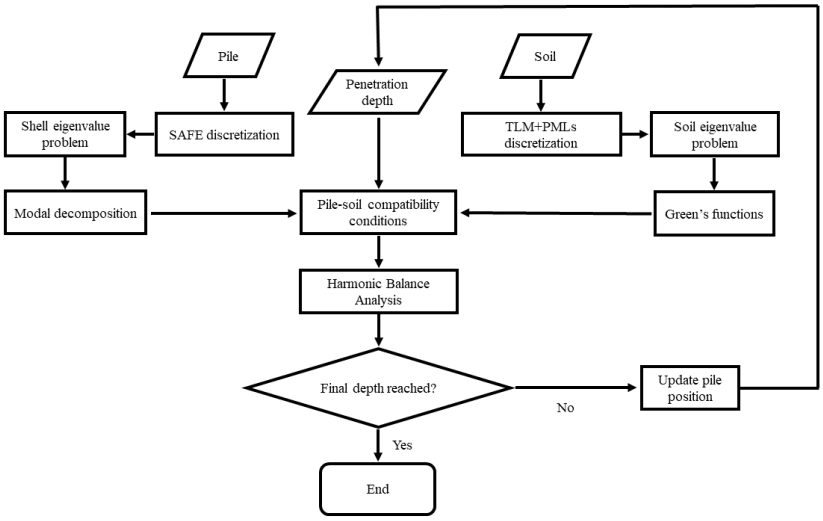

Figure 6.2: A flowchart of the present computational framework for vibratory pile installation.

E_p, Poisson's ratio ν_p and mass density ρ_p. The SAFE method is employed to model the thin cylindrical shell (see Fig. 6.3); the development of this approach has been presented in detail in Chapter 2. The process of vibratory pile installation corresponds to an axisymmetric problem ($n = 0$) in symmetric configuration, due to the absence of circumferential motion/loading. Given these considerations, the SAFE shell governing equations reduce to:

$$\mathbf{I}^{\mathrm{s}}_{\mathrm{p},0}\frac{\mathrm{d}^2\mathbf{u}^{\mathrm{s}}_{\mathrm{p},0}}{\mathrm{d}t^2}+\mathbf{L}^{\mathrm{s}}_{\mathrm{p},0}\mathbf{u}^{\mathrm{s}}_{\mathrm{p},0}=\mathbf{p}^{\mathrm{s}}_{\mathrm{p},0} \tag{6.1}$$

where $\mathbf{I}^{\mathrm{s}}_{\mathrm{p},0}$ is the shell mass matrix, $\mathbf{L}^{\mathrm{s}}_{\mathrm{p},0}$ is the shell stiffness matrix, $\mathbf{u}^{\mathrm{s}}_{\mathrm{p},0}$ is the displacement/rotation vector at the nodal rings and $\mathbf{p}^{\mathrm{s}}_{\mathrm{p},0}$ is the vector of consistent forces/moments at the nodal rings. Specifically, the displacements/rotations and forces/moments vectors read:

$$\mathbf{u}^{\mathrm{s}}_{\mathrm{p},0}=\begin{bmatrix}\mathbf{u}^{\mathrm{s}}_{0}\\ \mathbf{w}^{\mathrm{s}}_{0}\\ \boldsymbol{\beta}^{\mathrm{s}}_{z,0}\end{bmatrix},\quad \mathbf{p}^{\mathrm{s}}_{\mathrm{p},0}=\begin{bmatrix}\mathbf{p}^{\mathrm{s}}_{z0,\mathrm{p}}\\ \mathbf{p}^{\mathrm{s}}_{r0,\mathrm{p}}\\ \mathbf{m}^{\mathrm{s}}_{zz0,\mathrm{p}}\end{bmatrix} \tag{6.2}$$

To further improve the computational aspects of the problem, the shell response is decomposed in terms of the normal modes *in vacuo*:

$$\mathbf{u}^{\mathrm{s}}_{\mathrm{p},0}=\boldsymbol{\Phi}^{\mathrm{s}}_{\mathrm{p},\mathrm{o}}\mathbf{q}^{\mathrm{s}}_{\mathrm{o}} \tag{6.3}$$

where $\boldsymbol{\Phi}^{\mathrm{s}}_{\mathrm{p},\mathrm{o}}$ is the modal matrix of the symmetric form for $n = 0$ and $\mathbf{q}^{\mathrm{s}}_{\mathrm{o}}$ denotes the respective generalized coordinates. In particular, the modal matrix $\boldsymbol{\Phi}^{\mathrm{s}}_{\mathrm{p},\mathrm{o}}$ reads:

$$\mathbf{\Phi}^{\mathrm{s}}_{\mathrm{p},0} = \begin{bmatrix} \mathbf{U}^{\mathrm{s}}_0 \\ \mathbf{W}^{\mathrm{s}}_0 \\ \mathbf{B}^{\mathrm{s}}_0 \end{bmatrix} \tag{6.4}$$

where the modal sub-matrices $\mathbf{U}^{\mathrm{s}}_0$, $\mathbf{W}^{\mathrm{s}}_0$ and $\mathbf{B}^{\mathrm{s}}_0$ are defined as follows:

$$\mathbf{U}^{\mathrm{s}}_0 = \begin{bmatrix} \mathbf{u}^{\mathrm{s}}_{0,1} & \mathbf{u}^{\mathrm{s}}_{0,2} & \cdots \end{bmatrix} \tag{6.5a}$$

$$\mathbf{W}^{\mathrm{s}}_0 = \begin{bmatrix} \mathbf{w}^{\mathrm{s}}_{0,1} & \mathbf{w}^{\mathrm{s}}_{0,2} & \cdots \end{bmatrix} \tag{6.5b}$$

$$\mathbf{B}^{\mathrm{s}}_0 = \begin{bmatrix} \boldsymbol{\beta}^{\mathrm{s}}_{0,1} & \boldsymbol{\beta}^{\mathrm{s}}_{0,2} & \cdots \end{bmatrix} \tag{6.5c}$$

As can be seen, the circumferential modal sub-matrix $\mathbf{V}^{\mathrm{s}}_0$ (equal to zero) is erased for convenience in Eq. (6.4), as well as in all subsequent shell expressions. The system of ordinary differential equations that govern the shell response is transformed to the space of generalized coordinates $\mathbf{q}^{\mathrm{s}}_{\mathrm{o}}$ and reads:

$$\left(\mathbf{\Phi}^{\mathrm{s}}_{\mathrm{p,o}}\right)^{\mathrm{T}} \mathbf{I}^{\mathrm{s}}_{\mathrm{o}} \mathbf{\Phi}^{\mathrm{s}}_{\mathrm{p,o}} \frac{\mathrm{d}^2 \mathbf{q}^{\mathrm{s}}_{\mathrm{o}}}{\mathrm{d}t^2} + \left(\mathbf{\Phi}^{\mathrm{s}}_{\mathrm{p,o}}\right)^{\mathrm{T}} \mathbf{L}^{\mathrm{s}}_{\mathrm{o}} \mathbf{\Phi}^{\mathrm{s}}_{\mathrm{p,o}} \mathbf{q}^{\mathrm{s}}_{\mathrm{o}} = \left(\mathbf{\Phi}^{\mathrm{s}}_{\mathrm{p,o}}\right)^{\mathrm{T}} \mathbf{p}^{\mathrm{s}}_{\mathrm{p,o}} \tag{6.6}$$

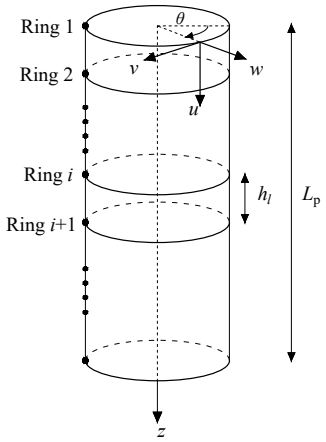

Figure 6.3: A thin cylindrical shell with axial discretization into nodal rings based on the SAFE method.

At this point, it is noted that the vector of consistent forces/moments $\mathbf{p}^{\mathrm{s}}_{\mathrm{p},0}$ encompasses both external excitation applied to the shell body and the soil reaction terms. Finally, the pile displacements/rotation vector $\mathbf{u}_{\mathrm{p}}$ and line load vector $\mathbf{p}_{\mathrm{p}}$, based on the premises of axisymmetric response and symmetric configuration, can be obtained as follows:

$$\mathbf{u}_{\mathrm{p}} = \begin{bmatrix} \mathbf{u}^{\mathrm{s}}_0 \\ \mathbf{0} \\ \mathbf{w}^{\mathrm{s}}_0 \\ \boldsymbol{\beta}^{\mathrm{s}}_{z,0} \end{bmatrix}, \quad \mathbf{p}_{\mathrm{p}} = \frac{1}{2\pi R_{\mathrm{p}}} \begin{bmatrix} \mathbf{p}^{\mathrm{s}}_{z0,\mathrm{p}} \\ \mathbf{0} \\ \mathbf{p}^{\mathrm{s}}_{r0,\mathrm{p}} \\ \mathbf{m}^{\mathrm{s}}_{zz0,\mathrm{p}} \end{bmatrix} \tag{6.7}$$

6.2.2. Wave motion in a layered half-space via the TLM+PMLs

To attain a physically sound description of the dynamic soil response and to retain computational efficiency, the TLM+PMLs approach is employed to model a layered soil half-space. On the premise of linear elastic response of the soil medium, this approach can treat arbitrarily layered soil profiles with exemplary accuracy and efficiency; the relevant formulations are extensively presented in Chapter 4. In this problem, only vertical and radial motions (and loads) are present in both pile and soil, leading us to consider only the generalized Rayleigh (SV-P) modes of the soil medium. Specifically, the generalized eigenvalue problem for the SV-P waves is written as:

$$\left(k^2\bar{\mathbf{A}}+\bar{\mathbf{C}}\right)\begin{bmatrix}\boldsymbol{\Phi}_r\\ k\boldsymbol{\Phi}_z\end{bmatrix}=\begin{bmatrix}\mathbf{0}\\ \mathbf{0}\end{bmatrix} \tag{6.8}$$

where k is the radial wavenumber variable, and $\boldsymbol{\Phi}_r$ and $\boldsymbol{\Phi}_z$ denote the radial and vertical modal displacements at the layer interfaces, respectively. The TLM matrices $\bar{\mathbf{A}}$ and $\bar{\mathbf{C}}$ are defined as:

$$\bar{\mathbf{A}}=\begin{bmatrix}\mathbf{A}_r & \mathbf{0}\\ \mathbf{B}_{zr} & \mathbf{A}_z\end{bmatrix} \tag{6.9a}$$

$$\bar{\mathbf{C}}=\begin{bmatrix}\mathbf{G}_r-\omega^2\mathbf{M}_r & \mathbf{B}_{rz}\\ \mathbf{0} & \mathbf{G}_z-\omega^2\mathbf{M}_z\end{bmatrix} \tag{6.9b}$$

The original formulation of the TLM is suitable to analyse wave propagation in a layered medium with fixed base (e.g. bedrock). For that purpose, we proceed to couple the TLM with PMLs [266, 267], as outlined in Section 4.3. As a result, PMLs may be readily incorporated in the TLM as thin layers with complex-valued stretched thickness $\bar{h}_l$ and the respective TLM matrices are reformed as follows:

$$\bar{\mathbf{A}}^l=\frac{\bar{h}_l}{h_l}\mathbf{A}^l,\quad \bar{\mathbf{B}}^l=\mathbf{B}^l,\quad \bar{\mathbf{G}}^l=\frac{h_l}{\bar{h}_l}\mathbf{G}^l,\quad \bar{\mathbf{M}}^l=\frac{\bar{h}_l}{h_l}\mathbf{M}^l \tag{6.10}$$

Based on the presented TLM+PMLs approach, the Green's functions of a linear elastic layered half-space are computed in the frequency-space domain. In particular, the present model requires the evaluation of the Green's functions due to: (i) unit radial ring sources at $r = R_\mathrm{p}$ and (ii) unit vertical ring sources at $r = R_\mathrm{p}$ (see Fig. 6.4). The explicit expressions of the Green's functions in the frequency-(radial-azimuthal)-wavenumber domain read [78, 253]:

$$\begin{bmatrix}\widehat{\mathbf{u}}_{r,n}\\ \widehat{\mathbf{u}}_{z,n}\end{bmatrix}=\begin{bmatrix}\boldsymbol{\Phi}_r\mathbf{D}_\mathrm{R}\boldsymbol{\Phi}_r^\mathrm{T} & k\boldsymbol{\Phi}_r\mathbf{K}_\mathrm{R}^{-1}\mathbf{D}_\mathrm{R}\boldsymbol{\Phi}_z^\mathrm{T}\\ \frac{1}{k}\boldsymbol{\Phi}_z\mathbf{D}_\mathrm{R}\mathbf{K}_\mathrm{R}\boldsymbol{\Phi}_r^\mathrm{T} & \boldsymbol{\Phi}_z\mathbf{D}_\mathrm{R}\boldsymbol{\Phi}_z^\mathrm{T}\end{bmatrix}\begin{bmatrix}\widehat{\mathbf{p}}_{r,n}\\ \widehat{\mathbf{p}}_{z,n}\end{bmatrix} \tag{6.11}$$

where $\widehat{\mathbf{u}}_{r,n}$ and $\widehat{\mathbf{u}}_{z,n}$ are the soil displacements and $\widehat{\mathbf{p}}_{r,n}$ and $\widehat{\mathbf{p}}_{z,n}$ are the external loads, both expressed in the frequency-(radial-azimuthal)-wavenumber domain. The matrices $\mathbf{K}_\mathrm{R}=\mathrm{diag}\{k_{\mathrm{R},1}\ \ k_{\mathrm{R},2}\ \cdots\}$ and $\mathbf{D}_\mathrm{R}=\left(k^2\mathbf{I}-\mathbf{K}_\mathrm{R}^2\right)^{-1}$ are diagonal matrices based solely on the generalized Rayleigh (SV-P) wavenumbers $k_{\mathrm{R},m}$ and the modal matrices $\boldsymbol{\Phi}_r$ and $\boldsymbol{\Phi}_z$ are defined as:

$$\boldsymbol{\Phi}_r = \begin{bmatrix} \boldsymbol{\phi}_{r,1} & \boldsymbol{\phi}_{r,2} & \cdots \end{bmatrix} \tag{6.12a}$$

$$\boldsymbol{\Phi}_z = \begin{bmatrix} \boldsymbol{\phi}_{z,1} & \boldsymbol{\phi}_{z,2} & \cdots \end{bmatrix} \tag{6.12b}$$

The transformation to the frequency-space domain is the subsequent step in this process. Detailed discussion and the relevant developments can be found in Section 4.4 to avoid repetition of content. Without entering into lengthy details, the soil displacements $\widetilde{\mathbf{u}}_r$ and $\widetilde{\mathbf{u}}_z$ are readily obtained in the frequency-space domain by virtue of the dynamic flexibility matrix $\widetilde{\mathbf{F}}_\mathrm{s}$ as follows:

$$\begin{bmatrix} \widetilde{\mathbf{u}}_{r,\mathrm{s}} \\ \widetilde{\mathbf{u}}_{z,\mathrm{s}} \end{bmatrix} = \begin{bmatrix} \widetilde{\mathbf{F}}_{rr} & \widetilde{\mathbf{F}}_{rz} \\ \widetilde{\mathbf{F}}_{zr} & \widetilde{\mathbf{F}}_{zz} \end{bmatrix} \begin{bmatrix} \widetilde{\mathbf{p}}_{r,\mathrm{s}} \\ \widetilde{\mathbf{p}}_{z,\mathrm{s}} \end{bmatrix} \tag{6.13}$$

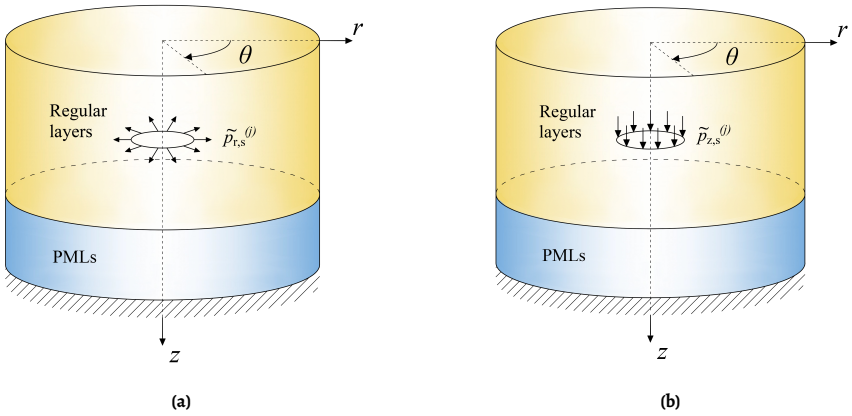

Figure 6.4: Schematic of a (a) unit radial and (b) unit vertical ring source at elevation z_j.

In the present problem, the ring loads $\widetilde{\mathbf{p}}_{r,\mathrm{s}}$ and $\widetilde{\mathbf{p}}_{z,\mathrm{s}}$ correspond to the pile-soil interaction loads applied from both the pile shaft and tip. They are formulated similarly to external loads for reasons that will become apparent in the ensuing computational treatment.

6.2.3. Pile-soil compatibility conditions

The numerical method to be employed is based on the solution of the pile-soil system at discrete depths coinciding with the vertical mesh of pile and soil. Consider the pile at a certain embedment depth, where nodal rings and layer interfaces corresponding to the region of pile-soil contact are defined by the superscripts c and the remaining rings and interfaces (out-of-contact) are defined by the superscript nc. Therefore, vectors of quantities related to both pile and soil are partitioned into in-contact and out-of-contact parts, e.g. $\mathbf{p}_{z,\mathrm{s}} = \begin{bmatrix} \left(\mathbf{p}^{\mathrm{c}}_{z,\mathrm{s}}\right)^{\mathrm{T}} & \left(\mathbf{p}^{\mathrm{nc}}_{z,\mathrm{s}}\right)^{\mathrm{T}} \end{bmatrix}^{\mathrm{T}}$ and $\mathbf{p}_{z,\mathrm{p}} = \begin{bmatrix} \left(\mathbf{p}^{\mathrm{nc}}_{z,\mathrm{p}}\right)^{\mathrm{T}} & \left(\mathbf{p}^{\mathrm{c}}_{z,\mathrm{p}}\right)^{\mathrm{T}} \end{bmatrix}^{\mathrm{T}}$. The latter partitioning into in-contact and out-of-contact quantities is employed in the following for both displacement and traction components. Evidently, the pile-soil interface is comprised by the lower part of

the pile nodal rings (embedded) and the upper part of soil layer interfaces, irrespectively of the size of the contact region.

The pile and soil motions are described by Eq. (6.6) and Eq. (6.13), respectively, and the compatibility conditions that complete the mathematical formulation are:
(i) continuity of radial displacements at the pile-soil interface:

$$\mathbf{w}^{\mathrm{c}} = \mathbf{u}^{\mathrm{c}}_{r,\mathrm{s}}\Big|_{r=R_{\mathrm{p}}} \tag{6.14}$$

(ii) compatibility of vertical tractions applied at the pile-soil interface and the pile tip:

$$\mathbf{p}^{\mathrm{c}}_{z,\mathrm{s}} = -\mathbf{p}^{\mathrm{c}}_{z,\mathrm{p}}, \quad p^{(\mathrm{t})}_{z,\mathrm{s}} = -p^{(\mathrm{t})}_{z,\mathrm{p}} \tag{6.15}$$

in which the superscript (t) denotes the tip related component. It is remarked that the load at the tip and the last entry of the load vector at the shaft, correspond to the same nodal ring/layer interface, albeit they are split for computational purposes.
(iii) compatibility of radial tractions applied at pile and soil:

$$\mathbf{p}^{\mathrm{c}}_{r,\mathrm{s}} = -\mathbf{p}^{\mathrm{c}}_{r,\mathrm{p}} \tag{6.16}$$

The above conditions require the compatibility of tractions applied to both pile and soil along the shaft and at the tip, whereas continuity of displacements is retained only for the radial displacements. As regards the vertical motion, there is continuous pile sliding along the interface during installation, thus the vertical pile and soil velocities (and displacements) are different.

The frictional forces along the pile shaft are described according to a hereditary Coulomb friction law. Several numerical schemes are available for frictional contact problems; in the present work the hyperbolic tangent regularization is employed to retain computational efficiency and accuracy [320, 119, 321]

$$p^{(i)}_{z,\mathrm{s}} = -p^{(i)}_{z,\mathrm{p}} = f^{(i)}_{\mathrm{s,ult}} l^{(i)} \tanh\left(\frac{1}{v_{\mathrm{tol}}}\left(\frac{\partial u^{(i)}_{\mathrm{p}}}{\partial t} - \frac{\partial u^{(i)}_{z,\mathrm{s}}}{\partial t}\Big|_{r=R_{\mathrm{p}}}\right)\right) \tag{6.17}$$

where v_{tol} is a velocity tolerance parameter, $l^{(i)}$ is the length of influence derived from the finite element projection and $f^{(i)}_{\mathrm{s,ult}}$ defines the amplitude of the static (and kinetic) friction. It is remarked that Eq. (6.17) includes the friction forces resulting from both the inner and outer pile surfaces. A distinction between the two is beyond the scope of the present model.

In the present friction law, a memory mechanism is incorporated that leads to reduction of the friction amplitude under cyclic loading conditions. The latter effect is known to occur due to soil strength degradation and reduction of effective stresses in the immediate vicinity of the pile shaft [301]. Moriyasu et al. [322] performed field tests with different driving frequencies and found that the shaft degradation follows closely the number of loading cycles. A more detailed investigation on the quantitative and qualitative character of shaft friction degradation will follow in Section 6.4.3. We proceed to formulate such a hereditary law that incorporates that effect with the least number of parameters as follows:

$$f^{(i)}_{\mathrm{s,ult}} = f^{(i)}_{\mathrm{s},0}\left(\beta_{\infty} + (1-\beta_{\infty})\mathrm{e}^{-c_N N^{(i)}_{\mathrm{cycl}}}\right) \tag{6.18}$$

where β_∞ is the ratio of the ultimately degraded friction amplitude to the initial one ($f_{s,0}^{(i)}$), c_N is a memory parameter that controls the rate of degradation and $N_{\text{cycl}}^{(i)}$ is the number of loading cycles accumulated at the soil interface (i) during driving. Therefore, the accumulation of loading cycles at a specific point in the soil, as the pile penetrates into the ground, leads to reduction of the friction force at this particular point.

The ring load at the pile tip includes a contribution of both shaft friction as well as tip reaction, due to the adopted discretization. For the tip reaction, the following local description is considered:

$$p_{z,\text{s}}^{(\text{t})} = -p_{z,\text{p}}^{(\text{t})} = \begin{cases} k_\text{t}(u_\text{p}^{(\text{t})} - u_\text{pl}) + c_\text{t}\dfrac{\partial u_\text{p}^{(\text{t})}}{\partial t}, & |k_\text{t}(u_\text{p}^{(\text{t})} - u_\text{pl})| < f_{\text{t,ult}} h_\text{p} \\ f_{\text{t,ult}} h_\text{p} \operatorname{sgn}\left(\dfrac{\partial u_\text{p}^{(\text{t})}}{\partial t}\right) + c_\text{t}\dfrac{\partial u_\text{p}^{(\text{t})}}{\partial t}, & |k_\text{t}(u_\text{p}^{(\text{t})} - u_\text{pl})| = f_{\text{t,ult}} h_\text{p} \end{cases} \tag{6.19}$$

where u_pl is the plastic tip displacement, $f_{\text{t,ult}}$ is the plastic tip resistance and the stiffness and damping coefficients are defined as k_t and c_t, respectively. The latter are extracted from the diagonal entry of the soil dynamic stiffness matrix $\widetilde{\mathbf{K}}_\text{s}$ that corresponds to the pile tip; the matrix $\widetilde{\mathbf{K}}_\text{s}$ is obtained via inversion of $\widetilde{\mathbf{F}}_\text{s}$ given in Eq. (6.13). The present tip reaction model parallels that of a mechanical analogue comprised of a spring-slider in parallel with a viscous dashpot. However, in the present model the parameters k_t and c_t are derived from the exact dynamic stiffness of the layered soil medium and rely solely on standard soil properties, instead of being computed on the basis of approximate formulas and empirical parameters.

6.3. A solution to the coupled problem via the Harmonic Balance Method (HBM)

In this problem, a time domain solution would be strictly prohibitive for engineering purposes, due to the excessive computational cost. For that purpose, a novel solution scheme is proposed uniquely inspired by the physics of the installation process, based on sequential application of the Harmonic Balance Method (HBM).

6.3.1. A sequential HBM: application to vibratory pile driving

The HBM has been successfully employed in various applications, such as buckling analysis of composite plates [323], vibrations of beams on non-linear and visco-elastic foundations [324] and bladed disks in turbomachinery [325]. However, its use in soil-structure interaction problems has not been realized as yet. In vibratory pile installation, the excitation induced by the vibrator is harmonic (or periodic), thus the HBM is appealing. Yet, the overall problem is not periodic as the pile penetration into the soil leads to an increase of the pile embedment and varying soil reactions along the shaft and at the tip. To tackle this challenge, we propose a solution based on sequential HB analyses for different pile positions, that once assembled together can provide the total solution. The present approach is structured as follows:

(i) First, we define a compatible vertical mesh for the pile (SAFE) and soil (TLM), e.g. uniform mesh of identical size.

(ii) For each compatible position, i.e. elevations at which pile nodal rings and soil layer interfaces coincide, a solution is sought via the HBM. This solution is valid for a time interval significantly larger than the HB fundamental period, as the pile position and the overall response vary in a much slower rate than the driving frequency (different time scales). Therefore, the HB coefficients of the solution for each pile position along the mesh can be found in a sequential manner.

(iii) The HB coefficients are considered to vary linearly (in time) in the transition from each position to the subsequent one, given that the adjacent positions are close enough to allow for such an approximation.

(iv) The solutions from the sequential HB analysis are assembled into the total solution, leading effectively to a piece-wise linear amplitude modulation of the involved harmonics and thus an overall quasi-periodic system response.

A visual representation of the process described is also shown in Fig. 6.5. Two adjacent positions are denoted by states i and $i+1$ and linear interpolation of the resulting HB coefficients takes place to transition from state i to state $i+1$. It is noted that by degrees-of-freedom (DoFs) we consider all the quantities that are approximated by the HBM.

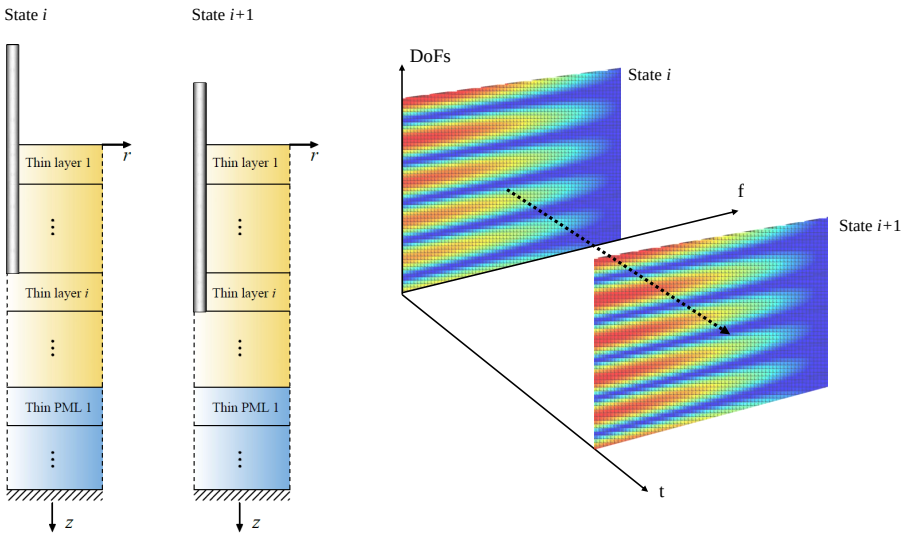

Figure 6.5: Schematic of the sequential HB approach for two pile positions i and $i+1$, accompanied by the linear interpolation of the HB coefficients in the frequency-time plane.

We proceed to define our solution ansatz according to the HBM. For the pile generalized coordinates the following ansatz is considered:

$$q_{0,m}^{\mathrm{s}} = \begin{cases} c_{0,0}\, t + \sum_{j=1}^{N_{\mathrm{h}}} \left(c_{0,j} \cos(j\Omega t) + s_{0,j} \sin(j\Omega t) \right), & m = 0 \\ c_{m,0} + \sum_{j=1}^{N_{\mathrm{h}}} \left(c_{m,j} \cos(j\Omega t) + s_{m,j} \sin(j\Omega t) \right), & m > 0 \end{cases} \tag{6.20}$$

where $\mathbf{c}_m = \begin{bmatrix} c_{m,0} & c_{m,1} & \cdots \end{bmatrix}^{\mathrm{T}}$ and $\mathbf{s}_m = \begin{bmatrix} s_{m,1} & s_{m,2} & \cdots \end{bmatrix}^{\mathrm{T}}$ denote the vectors encapsulating the Fourier coefficients of the m-th mode related to the cosine and sine terms, respectively. As can be seen, the ansatz that corresponds to the rigid body mode ($m = 0$) is periodic in velocity, such that linear pile progression into the soil with time can be addressed [326].

To obtain the soil response, it is chosen to approximate the non-linear reaction forces at the soil-pile interface and at the tip as Fourier series. Furthermore, to reduce the dimensionality of the friction forces along the pile-soil interface, a matrix decomposition of the following form is applied:

$$\mathbf{p}_{z,\mathrm{s}}^{\mathrm{c}} = \boldsymbol{\Psi} \left(\boldsymbol{\alpha}_0 + \sum_{j=1}^{N_{\mathrm{h}}} \left(\boldsymbol{\alpha}_j \cos(j\Omega t) + \boldsymbol{\beta}_j \sin(j\Omega t) \right) \right) \tag{6.21}$$

in which $\boldsymbol{\alpha}_j = \begin{bmatrix} \alpha_{j,0} & \alpha_{j,1} & \cdots \end{bmatrix}^{\mathrm{T}}$ and $\boldsymbol{\beta}_j = \begin{bmatrix} \beta_{j,1} & \beta_{j,2} & \cdots \end{bmatrix}^{\mathrm{T}}$ are the vectors of the Fourier coefficients related to the j-th cosine and sine terms and the matrix $\boldsymbol{\Psi}$ encapsulates the basis vectors employed to approximate the spatial distribution of the interface forces. In particular, these basis vectors are obtained by projection of the respective function class to the vertical finite element mesh; a multitude of functions is suitable for that purpose, e.g. Lagrange polynomials, Fourier-based shape functions and B-splines [327]. As follows from the HBM, the tip reaction is also assumed to be periodic:

$$p_{z,\mathrm{s}}^{(\mathrm{t})} = \alpha_{\mathrm{t},0} + \sum_{j=1}^{N_{\mathrm{h}}} \left(\alpha_{\mathrm{t},j} \cos(j\Omega t) + \beta_{\mathrm{t},j} \sin(j\Omega t) \right) \tag{6.22}$$

where $\boldsymbol{\alpha}_{\mathrm{t}} = \begin{bmatrix} \alpha_{\mathrm{t},0} & \alpha_{\mathrm{t},1} & \cdots \end{bmatrix}^{\mathrm{T}}$ and $\boldsymbol{\beta}_{\mathrm{t}} = \begin{bmatrix} \beta_{\mathrm{t},1} & \beta_{\mathrm{t},2} & \cdots \end{bmatrix}^{\mathrm{T}}$ denote the vectors encapsulating the Fourier coefficients of the tip reaction related to the cosine and sine terms, respectively.

In all the above equations, the involved quantities are in the space-time domain, albeit in Eq. (6.13) the soil response and the applied loads are in the frequency-space domain. Based on the premise of periodic response, transformation to the time domain via the inverse Fourier transform is analytically tractable - indicatively, the tip reaction (Eq. (6.22)) is transformed in the frequency domain as follows:

$$\widetilde{p}_{z,\mathrm{s}}^{(\mathrm{t})} = \int_{-\infty}^{+\infty} p_{z,\mathrm{s}}^{(\mathrm{t})} \mathrm{e}^{-\mathrm{i}\omega t}\, \mathrm{d}t = 2\pi\delta(\omega)\alpha_{\mathrm{t},0} + \sum_{j=1}^{N_{\mathrm{h}}} \left(\pi\alpha_{\mathrm{t},j} (\delta(\omega - j\Omega) + \delta(\omega + j\Omega)) - \mathrm{i}\pi\beta_{\mathrm{t},j} (\delta(\omega - j\Omega) - \delta(\omega + j\Omega)) \right) \tag{6.23}$$

By substituting the assumed solutions into the dynamic equilibria of pile and soil and the compatibility conditions, it can be shown that the following residuals are required to vanish:

$$\mathbf{r}_{\mathrm{c}} = \boldsymbol{\Psi}^{\mathrm{T}} \left(\mathbf{p}^{\mathrm{c}}_{z,\mathrm{s}} + \mathbf{p}^{\mathrm{c}}_{z,\mathrm{p}} \right) \tag{6.24a}$$

$$r_{\mathrm{t}} = p^{(\mathrm{t})}_{z,\mathrm{s}} + p^{(\mathrm{t})}_{z,\mathrm{p}} \tag{6.24b}$$

$$\mathbf{r}_q = \left(\boldsymbol{\Phi}^{\mathrm{s}}_{\mathrm{p,o}} \right)^{\mathrm{T}} \left(\mathbf{I}^{\mathrm{s}}_{\mathrm{o}} \boldsymbol{\Phi}^{\mathrm{s}}_{\mathrm{p,o}} \frac{\mathrm{d}^2 \mathbf{q}^{\mathrm{s}}_{\mathrm{o}}}{\mathrm{d}t^2} + \mathbf{L}^{\mathrm{s}}_{\mathrm{o}} \boldsymbol{\Phi}^{\mathrm{s}}_{\mathrm{p,o}} \mathbf{q}^{\mathrm{s}}_{\mathrm{o}} - \mathbf{p}^{\mathrm{s}}_{\mathrm{p,o}} \right) \tag{6.24c}$$

which can be arranged in the following residual vector:

$$\mathbf{r} = \begin{bmatrix} \mathbf{r}_{\mathrm{c}} \\ r_{\mathrm{t}} \\ \mathbf{r}_q \end{bmatrix} \tag{6.25}$$

Following the HBM, we require that the Fourier coefficients of the residual vector $\mathbf{r}$ vanish up to the truncation limit and are obtained via a Fourier-Galerkin projection as follows:

$$\mathbf{R}_{\mathrm{F}} = \frac{1}{T} \int_0^T \mathbf{r}\mathbf{h} \, \mathrm{d}t \tag{6.26}$$

where $\mathbf{R}_{\mathrm{F}}$ is a matrix that encapsulates the Fourier coefficients of the residuals, T is the period corresponding to the fundamental frequency, i.e. the driving frequency Ω, and the row vector $\mathbf{h}$ encapsulates the test functions (i.e. Fourier harmonics) $h_j(t)$ defined as:

$$h_j(t) = \frac{1}{2} \left[\left(1 + (-1)^j \right) \cos\left(\frac{j\Omega t}{2} \right) + \left(1 + (-1)^{j+1} \right) \sin\left(\frac{j+1}{2} \Omega t \right) \right], \quad j = 0, \ldots, 2N_{\mathrm{h}} \tag{6.27}$$

The outlined approach corresponds to the classical HBM, i.e. a Galerkin method, as the Fourier series is chosen both as the set of trial and test functions. With a view to successful and/or accelerated convergence of the method, the notion of HB as a weighted residual method can be expanded by introducing various sets of trial and test functions (e.g. B-splines, periodized wavelets) and exploring the possibility of differentiation between the two sets, thus leading to a Petrov-Galerkin scheme [328]. These ideas will not be pursued in this work, albeit they are considered highly promising for systems characterized by responses of bounded continuity.

It is noted that the non-linear reaction forces in the present problem cannot be analytically expanded in terms of the assumed Fourier coefficients, thus the Alternating Frequency-Time (AFT) HBM is applied [329, 330]. The latter is based on the evaluation of the non-linear forcing terms in the time domain and the subsequent application of the Discrete Fourier Transform (DFT) via the Fast Fourier Transform (FFT) algorithm. The AFT-HBM entails an iterative process that in our solution approach is posed as a vector optimization problem and customarily is solved by the Newton-Raphson or similar algorithms [319, 329, 331]. In our solution scheme, the Powell's hybrid method is found to be superior both in terms of accuracy and computational performance and is employed in the ensuing analyses [332].

Briefly, the overall process can be summarized as follows:

(i) a periodic ansatz is considered for the pile generalized coordinates (Eq. (6.20)) and the vertical tractions (Eqs. (6.21) and (6.22)), thus the pile and soil displacement fields can be obtained via Eqs. (6.3) and (6.13), respectively. It is remarked that the radial soil displacements are directly obtained via Eq. (6.14).

(ii) a residual is formed by the assumed tractions and the tractions resulting from the pile-soil relative motion according to Coulomb's friction (Eq. (6.17)). Similarly, the residual of the SAFE equations of motion in the modal domain is formed.

(iii) the Fourier coefficients of the preceding residuals are required to vanish - implying vanishing of the residuals - according to the HBM. The vectors of Fourier coefficients ($\mathbf{c}_m$, $\mathbf{s}_m$, $\boldsymbol{\alpha}_j$, $\boldsymbol{\beta}_j$, $\boldsymbol{\alpha}_\mathrm{t}$, $\boldsymbol{\beta}_\mathrm{t}$) obtained from the vector optimization problem and leading to $\mathbf{R}_\mathrm{F} = \mathbf{0}$ provide the final solution to the problem.

Conclusively, the described procedure corresponds to the solution of the system at a single embedment depth. For each subsequent depth, it follows that the involved vector and matrix quantities need to be updated in accordance with Fig. 6.2. It is remarked that the presented numerical model is an effective engineering-oriented model of the vibratory pile installation process. Therefore, the large soil deformations that may develop in the pile vicinity and the associated physical processes are not fully considered in the model herein, as they are not not encompassed in the model purposes. Essentially, the present model represents an effective framework, in which the following conditions are necessary for pile penetration to occur: i) gross sliding at the pile shaft (Eq. (6.17)) and ii) plastic deformation at the pile tip (Eq. (6.19)). In that manner, sequential non-linear equilibria of the pile-soil model are computed and their assemblage with the presented HB-based scheme leads to the overall solution.

6.3.2. Validation of the sequential HB scheme: 1-D benchmark problem

In Section 6.3.1, a new solution scheme based on the HBM has been presented for the problem at hand. To focus on the validation of the proposed sequential HB solution scheme, we formulate a corresponding 1-D problem [333]. Specifically, two rods in frictional contact are considered, where the first rod may slide along the second. Modal decomposition is applied to rod 1 and rod 2 is described via its Green's functions in the frequency domain. Therefore, all the problem components are corresponding fully to the respective ones in the pile-soil problem of interest. However, the advantage of this benchmark problem is that it lends itself to direct solution in the time domain via numerical integration, alleviating the rest of the complexities associated with the installation process. For the process of numerical integration, an explicit Runge–Kutta method (RK45) is employed [213].

ρ_i [kg/m^3]	A_i [m^2]	E_i [Pa]	P_0 [N]	P_1 [N]	Ω_1 [rad/s]	f_c [N/m]
7850	0.03726	$210{\cdot}10^9$	$10{\cdot}10^3$	$100{\cdot}10^3$	157.08	$8.379{\cdot}10^3$

Table 6.1: Parameters of 1-D validation example ($i = 1, 2$).

In brief, two linear homogeneous elastic rods are considered with domains $0 \leq z_1 \leq L_1$ and $0 \leq z_2 \leq L_2$, respectively (see Fig. 6.6), and their equations of motion read:

$$\rho_1 A_1 \frac{\partial^2 u_1}{\partial t^2} = E_1 A_1 \frac{\partial^2 u_1}{\partial z_1^2} + f \tag{6.28a}$$

$$\rho_2 A_2 \frac{\partial^2 u_2}{\partial t^2} = E_2 A_2 \frac{\partial^2 u_2}{\partial z_2^2} - f \tag{6.28b}$$

where E_i, A_i, ρ_i, $u_i(z_i, t)$ denote the modulus of elasticity, the area of the cross section, the mass density per unit length and the axial displacements of the rods ($i = 1, 2$), while f is the distributed Coulomb friction force. Conclusively, the boundary conditions read as follows:

$$N_1(0,t) = -P(t) = -P_0 - P_1 \sin(\Omega_1 t), \quad N_1(L_1,t) = 0, \quad N_2(0,t) = 0, \quad u_2(L_2,t) = 0 \tag{6.29}$$

where $N_1(z_1, t)$ and $N_2(z_2, t)$ denote the axial forces of rods 1 and 2, respectively, and $P(t)$ is the external force at the top of rod 1. In this example, two identical rods are considered and the contact region is equal to 50% of their length. The excitation at the top of rod 1 is comprised by a static component P_0 and a harmonic component of amplitude P_1 and frequency Ω_1. The contact interface is described by Coulomb friction with static (and kinetic) friction amplitude of f_c, which is constant along the longitudinal axis. The properties of the overall system can be found in Table 6.1.

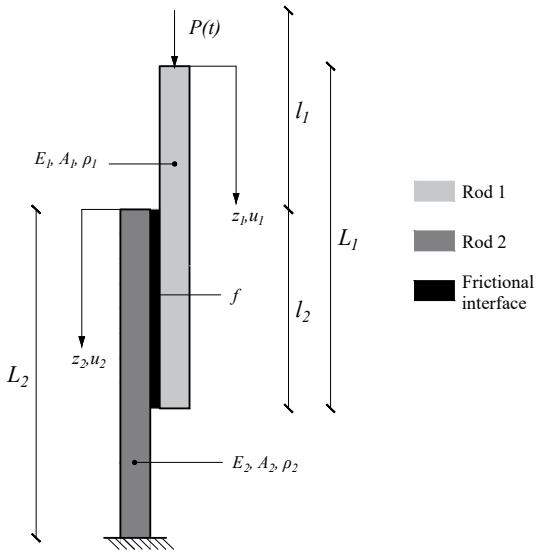

Figure 6.6: Two rods in frictional contact.

In Fig. 6.7a, the displacement at the top of rod 1 is shown. The dashed red line corresponds to the first HB solution found at the initial position of rod 1 and is used to indicate the

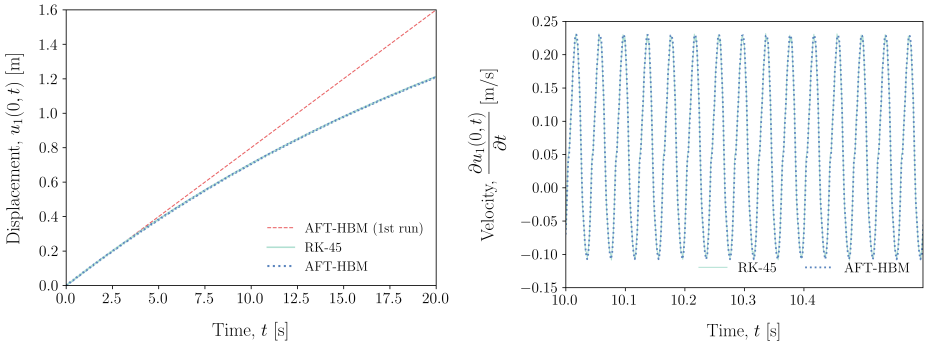

(a) (b)

Figure 6.7: (a) Comparison of displacements at the top of rod 1 for the full analysis and (b) zoomed-in comparison of velocities at the top of rod 1 for a time window in the middle of the analysis, obtained via numerical integration (RK-45) and the sequential AFT-HBM.

initial (and maximum) penetration rate. As rod 1 progresses and the contact length increases, the penetration rate reduces due to the increase in the total friction force. As can be seen, the proposed sequential HB scheme captures remarkably the overall penetration process. A more detailed view of the comparison can be found in Fig. 6.7b, where the velocities of the two rods are shown in a time window of 0.6 s located at the middle of the analysis ($t = 10$ s). The results of the two approaches are in great agreement and showcase the accuracy of the presented sequential HB scheme in a problem with non-stationary motion.

6.4. Numerical results and comparison with field data

The presented numerical model is used to study the vibratory-driven pile from the GDP experimental campaign [51, 54]. First, input data from *in-situ* tests are used to characterize the relevant model parameters. Subsequently, model predictions are compared with field data and further investigations are performed that pertain to soil reaction evolution and memory mechanisms, pile dynamics and effect of driving frequency.

6.4.1. Input data

In the GDP campaign different installation methods (impact, axial vibratory and GDP) were tested and the pile considered herein is the only one installed via axial vibratory driving (VH). The driven pile properties and the specifications of the vibratory device used are given in Tables 6.2 and 6.3, respectively. For both pile and soil, hysteretic damping is considered with ratios $\xi_p = 0.001$ and $\xi_s = 0.025$ (for both P- and S-waves), respectively. In the installation tests, for the upper 3 m of penetration the pile was laterally restrained to eliminate any inclination and controlled by a crane, thus the interval from 3 m to 8 m is considered in this study. The dynamic excitation at the pile top is introduced in the model based on strain measurements via fiber Bragg grating (FBG) sensors; the FBG sensors were located 1.62 m from the pile top. In our solution approach via the HBM, the dynamic excitation is considered nearly stationary, i.e. periodic for time intervals significantly larger than the

fundamental period during which we apply the HBM. The latter has been found to hold for both vibratory methods (VH and GDP) in the GDP field tests [52, 51]. Furthermore, a time-frequency analysis of the top axial strain ($\epsilon_{zz,\mathrm{p}}$) by means of a discrete short-time Fourier transform (STFT) is also performed to support that finding. As can be seen in Fig. 6.8, the frequency content and the associated amplitudes remain fairly constant during installation, indicating a quasi-periodic excitation due to amplitude modulation of the involved harmonics.

ρ_p [kg/m^3]	E_p [Pa]	ν_p [-]	L_p [m]	R_p [m]	h_p [m]
7850	$210{\cdot}10^9$	0.3	10	0.373	0.0159

Table 6.2: Properties of the piles driven in the GDP field campaign.

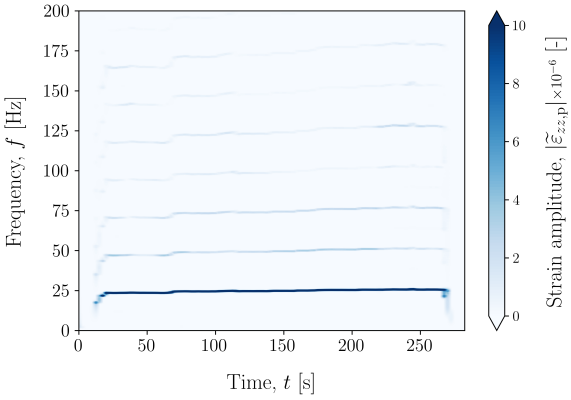

Figure 6.8: Amplitude of the axial strain ($|\widetilde{\varepsilon}_{zz,\mathrm{p}}|$) STFT for the VH pile.

For the characterization of the soil properties, Seismic Cone Penetration Tests with pore water pressure measurements (SCPTu's) were performed (see Fig. 6.9) and the depth of the water table was found at 4.5 m. From the SCPTu measurements, the basic soil properties that characterize the linear elastic layered medium can be obtained. Therefore, the Green's functions can be directly computed, as well as the values of k_t and c_t that follow from the dynamic stiffness matrix. In general, ultimate shaft (friction amplitude) and tip resistances are known to correlate strongly with the cone tip resistance q_c measured during CPT tests [334–336]. The relevant studies were focused on static axial pile capacity and recent field tests by Moriyasu et al. [322] investigated such correlations also in the case of vibro-driving of pipe piles. Based on the latter tests, an initial friction amplitude of $f_{\mathrm{s},0}^{(i)} = 0.012 q_c(z_i)$ is

Mass [kg]	Eccentric moment [kgm]	Rotational speed [rpm]	Operational power [kW]
4100	25	1800	204

Table 6.3: Technical specifications of the vibro-hammer CV-25.

adopted in our analysis. Regarding the ratio of ultimately degraded to initial shaft resistance, a value of $\beta_\infty = 0.2$ is selected for the sandy soil considered [101, 337]. In the latter studies the ultimately degraded value is typically reached at approximately 10000 loading cycles, while a range from approximately 7000 to 15000 cycles was observed by Moriyasu et al. [322]. For the proposed memory mechanism, this range of loading cycles corresponds to c_N values between 0.0003 and 0.0005. As regards to the tip reaction during vibratory driving, field observations are scarce, so we investigate a range of $f_{\mathrm{t,ult}}$ values. As will be shown in the ensuing, this uncertainty has insignificant effect on the pile drivability.

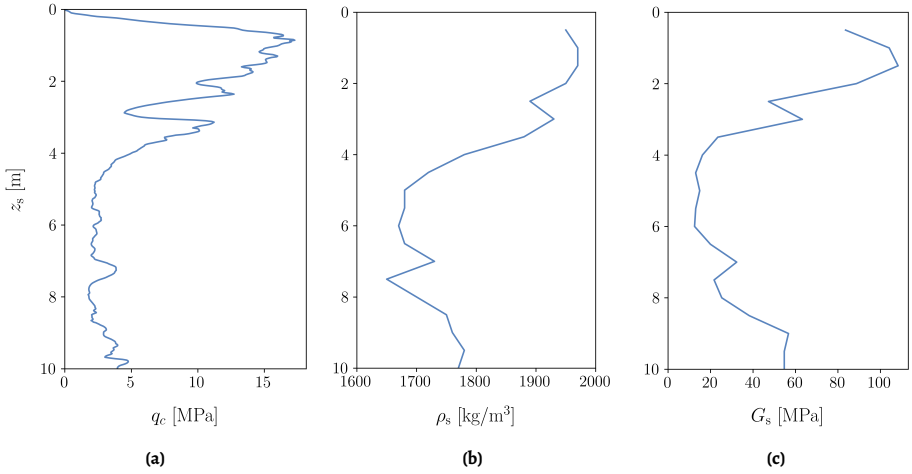

Figure 6.9: Profiles of (a) cone tip resistance (q_c), (b) mass density (ρ_s), and (c) shear modulus (G_s) obtained from the SCPTu tests.

6.4.2. Field measurements and model predictions

In Fig. 6.10, the pile penetration is shown, as measured by the potentiometer transducer (PM) and the driving logging (DL) system. The former measurement has a high sampling rate ($f = 1000$ Hz) and is considered more reliable than the latter, which is a sparse measurement (recorded per 25 cm of penetration). As can be seen, the predictions of the model provide fairly similar penetration trends and form an upper and lower bound (of soil reaction), respectively. The best prediction was found for $c_N = 0.0004$ for the overall duration of installation (in least squares sense). This result is promising for the predictive potential of our model, which is expected to further improve with the inflow of additional field data. Furthermore, the small number of non-standard parameters that need to be calibrated and its robust theoretical formulation for both pile and soil are considered advantageous for engineering practice.

For the analyses shown in Fig. 6.10, $f_{\mathrm{t,ult}} = 0.5q_c$ was considered in the tip reaction model, due to its fair comparison with the FBG-measured reaction 0.5 m from the pile tip as shown in Fig. 6.11a. We proceed to showcase that the plastic tip resistance is of minor importance for the overall penetration process of the studied pile. In Fig. 6.11b, the penetration for different analyses is shown, where a range of $f_{\mathrm{t,ult}}$ from $0.3q_c$ to $0.7q_c$ has been considered. Based

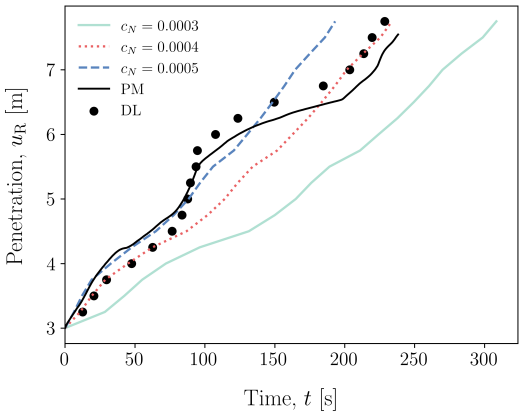

Figure 6.10: Comparison of vibratory installation model predictions with field data as recorded by a potentiometer (PM) and the vibratory device logging system (DL).

on the two extrema ($f_{t,ult} = 0.3q_c$ and $f_{t,ult} = 0.7q_c$), an increase of the plastic tip resistance $f_{t,ult}$ by 133.3% led to a minor increase of 12.8% in the total installation time. Therefore, for the present pile, the elasto-plastic component of the tip reaction has a secondary effect on the installation rate and the pile-soil friction at the shaft provides the main resistance to driving. This observation is expected to be even more prominent in the installation of offshore monopiles given the significantly larger embedment depth. For that purpose, field campaigns that include in their scope the identification of the memory mechanism that leads to soil-pile friction reduction are considered of major importance for better understanding the vibratory installation process.

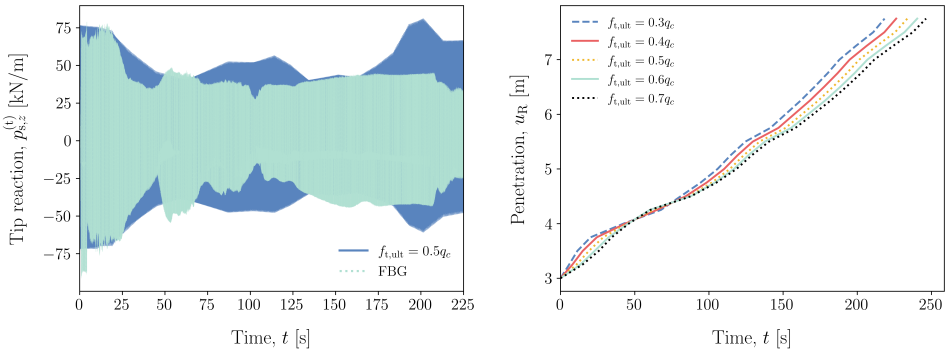

Figure 6.11: (a) Comparison of tip reaction $p_{z,s}^{(t)}$ from vibratory installation model ($f_{t,ult} = 0.5q_c$) with the FBG-based axial force resultant close to the pile tip. (b) Comparison of penetration model predictions for different ultimate tip resistance $f_{t,ult}$ values.

The preceding discussion was focused on the identification of plastic tip resistance $f_{t,ult}$

and its minor effect on the pile penetration. However, this finding does not necessarily imply that the overall tip reaction, including both the elasto-plastic and the viscous components, is necessarily of minor significance for the installation rate. To elaborate further, the comparison of the tip and the total shaft reactions is depicted in Fig. 6.12a. As can be seen, the total shaft reaction is arguably the major component, albeit without rendering the tip reaction negligible. In Fig. 6.12b, the total shaft and tip reactions are given as fractions of the total soil reaction ($p_{z,\mathrm{s}}^{(\mathrm{t})} + \sum_i p_{z,\mathrm{s}}^{(i)}$). The arithmetic means of the two ratios are approximately 77% and 23% for the shaft and tip components, respectively, showcasing the dominance of the former as well as the appreciable magnitude of the latter.

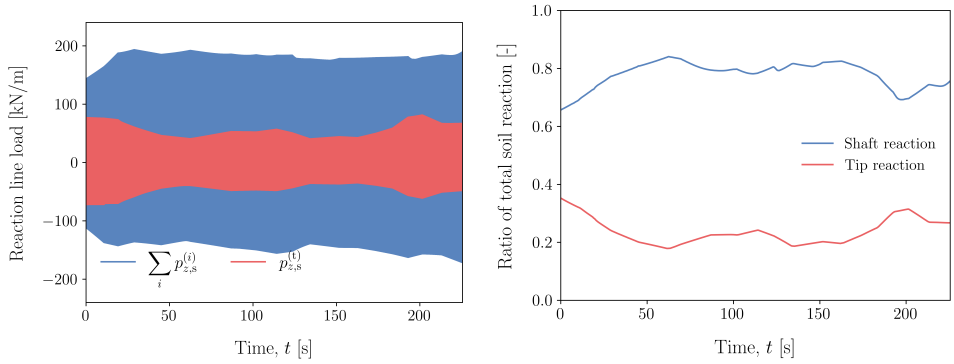

Figure 6.12: (a) Total shaft and tip reactions and (b) ratios of total shaft and tip reactions to total soil reaction during driving.

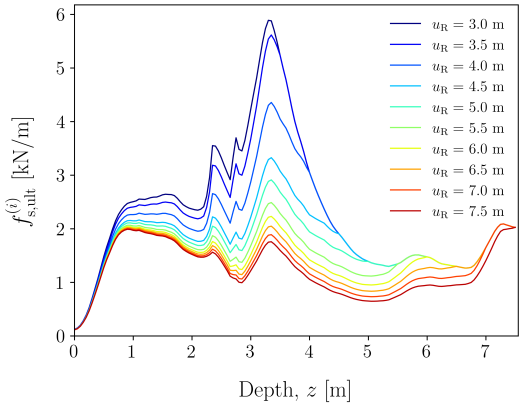

Figure 6.13: Friction amplitude distribution along soil depth z for different embedment depths (per 0.5 m), showcasing the memory effect on the shaft friction reduction.

An interesting remark in Fig. 6.12a is the relatively small variation of the total shaft reaction as the pile progresses into the soil. This occurrence results from the combination of

the friction amplitude distribution with depth z, directly related to the cone tip resistance q_c profile, and the degradation of the friction amplitude at each soil material point in contact with the pile shaft. The latter mechanism has been described in Section 6.3.1 and the effect of the memory parameter c_N on penetration is shown in Fig. 6.10. To better visualize the function of the cyclic memory mechanism, Fig. 6.13 presents the distribution of the friction amplitude $f_{\text{s,ult}}^{(i)}$ along depth z for different instances during driving, i.e. every 0.5 m of pile penetration. The gradual reduction of friction amplitude with the accumulation of loading cycles (and thus pile penetration) is clear. Furthermore, the "saturation" of the degradation effect in the shallow soil layers is visible, as the associated soil horizons have been exposed to a greater number of loading cycles.

The dynamic pile response during installation is also of great interest in order to assess the model capabilities and identify its limitations. For that purpose, the time-frequency analysis of the axial acceleration at the pile head is considered for the model output and the accelerometer recording. Specifically, a short-time Fourier transform (STFT) is applied to both signals and the amplitudes of both STFTs are shown in Fig. 6.14. As can be seen, the nearly stationary nature of the response is supported by both field data and numerical results, and good agreement in terms of acceleration amplitudes is found up to the second super-harmonic. From the third super-harmonic onward, the acceleration recording possesses lower amplitudes compared to the model prediction. Considering that these super-harmonics result from the non-linear pile-soil interaction - with major contributor the shaft friction - this observation may be interpreted as an indication that the pile response is smoother than the model predicts. This outcome is most likely owed to the non-smooth character of Coulomb friction and points out a presumably smoother friction model for the shaft reaction. For drivability purposes, the Coulomb friction model appears satisfactory and circumvents the complications of identifying additional friction model parameters, as Coulomb friction is characterized by the lowest possible number of parameters, i.e. only one.

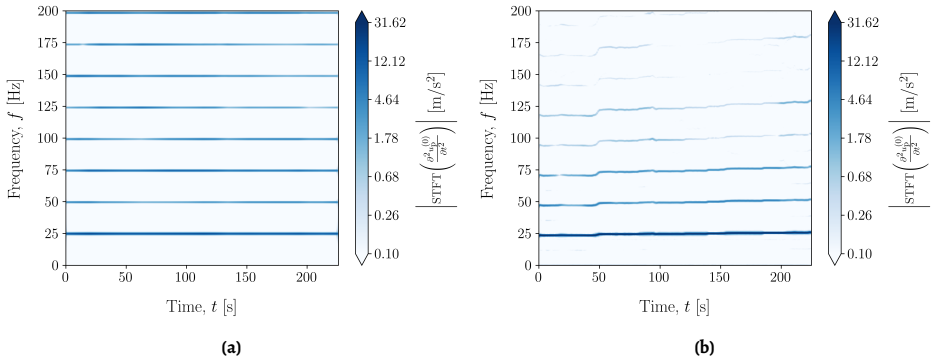

Figure 6.14: Amplitude of the axial acceleration STFT (a) obtained from the installation model and (b) recorded during installation of the VH pile.

6.4.3. Comparison of different memory mechanisms for the frictional interface: friction fatigue - the h/R effect

The decrease of the ultimate shaft friction that corresponds to a fixed (spatially) soil material point is not solely occurring during vibratory pile installation. Heerema [338] observed that pile progression was accompanied by shaft friction reduction during impact piling tests in clayey soil and termed this phenomenon as "friction fatigue". A mechanism was proposed to account for friction fatigue based on the distance between the pile tip and the considered soil horizon, whereas the phenomenon was attributed to the decrease of horizontal soil stresses [338]. The reduction of radial effective stresses was recorded in pile jacking experiments and the ratio h/R was identified as the control parameter[339, 340], where h and R denote the distance of a soil material point from the pile tip and the pile radius, respectively. Sheng et al. [117] captured the so-called h/R effect in pile jacking via advanced FE simulations and found that the radial stress decrease above the tip level was associated with soil softening around the pile (upon the tip passage). Friction fatigue has been further considered in studies related to static pile capacity [93, 92, 341].

The preceding outline indicates that friction fatigue has received appreciable attention in certain topics related to pile foundations. However, studies of this phenomenon in the context of vibratory driving are scarce. White and Lehane [335] performed centrifuge tests and studied, among other techniques, the two-way cyclic jacked installation and its influence on the penetration process. It was found that shaft friction degradation was better characterized based on the number of cycles accumulated at a fixed soil material point than the normalized distance from the tip h/R. In a recent experimental campaign focused on vibratory pile installation tests, Moriyasu et al. [322] corroborated the previous finding and showed that the number of accumulated cycles was a better control parameter than the h/R ratio. Based on the preceding findings, we were motivated to formulate a hereditary Coulomb friction law that accounts for shaft friction degradation, with the number of accumulated loading cycles being the control variable (see Section 6.2.3). To further investigate the plausibility of normalized distance-based friction reduction, we proceed to formulate an associated memory mechanism as follows:

$$f_{\mathrm{s,ult}}^{(i)} = f_{\mathrm{s,0}}^{(i)} \left(\beta_{\infty} + (1 - \beta_{\infty}) \mathrm{e}^{-c_{\mathrm{D}} l_{\mathrm{D}}^{(i)}} \right) \tag{6.30}$$

where $l_{\mathrm{D}}^{(i)}$ is the normalized distance of the soil interface (i) from the pile tip and c_{D} is the memory parameter that controls the rate of degradation, whereas $f_{\mathrm{s,0}}^{(i)}$ and β_{∞} have the same definitions as in the case of the cyclic memory mechanism.

As can be seen in Fig. 6.15a, a range of c_{D} values from $0.8R_{\mathrm{p}}$ to $1.0R_{\mathrm{p}}$ has been used in numerical analyses. The model results showcase an appreciable mismatch compared to the field data, both in quantitative and qualitative terms; for c_{D} values outside the present range the deviation was even larger. In particular, the model displays a monotonic increase in penetration rate for all c_{D} values, which is largely dissimilar to the installation record. The absolute penetration error between numerical results (u_{R}) and field data ($u_{\mathrm{R,DM}}$) is shown in Fig. 6.15b for all c_{D} values, as well as for cyclic memory model with $c_N = 0.0004$. Based on the considered model and memory mechanisms, the cyclic formulation leads to a significantly better match with the field data compared to the normalized distance-based model. The absolute error is confined to significantly lower levels during almost the whole

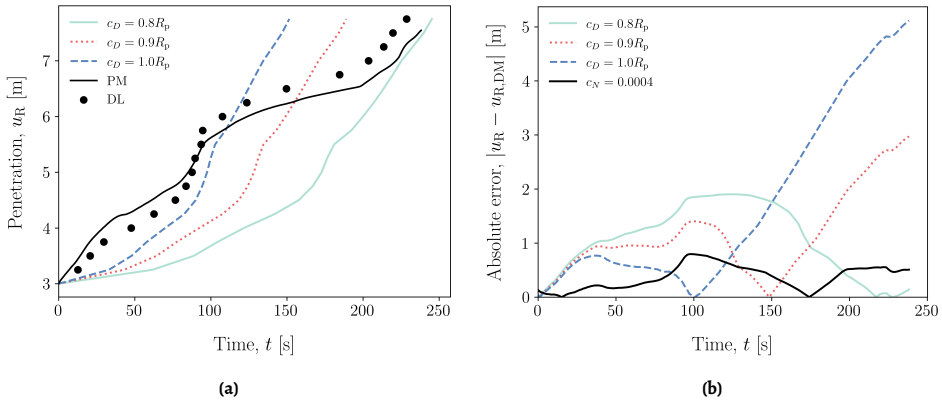

Figure 6.15: (a) Comparison of model predictions with normalized distance-based memory mechanism against field data - both potentiometer (PM) and driving logging system (DL) - in terms of pile penetration. (b) Comparison of model predictions with normalized distance-based and cyclic memory mechanisms in terms of absolute penetration error.

course of pile installation. Conclusively, this numerical study further corroborates that the number of accumulated loading cycles is superior to the h/R ratio as a control variable for shaft friction reduction during vibratory pile driving.

Naturally, the proposed cyclic memory mechanism is an effective one and more dependencies may be important with a view to future model refinement, e.g. driving frequency, loading amplitude and soil properties. Both experimental and numerical studies are required to better understand the physical mechanisms at hand and develop a reduced-order formulation suitable for engineering-oriented models.

6.4.4. Effect of driving frequency on penetration rate

An interesting aspect of vibratory driving is the effect of the driving frequency on the penetration rate. We proceed to analyse the penetration of the VH pile for a range of driving frequencies without altering any other parameter (e.g. excitation amplitude). In Fig. 6.16, the average penetration rates for all driving frequencies and degradation rate values c_N are shown. The general trend indicates that the average penetration rate is a monotonic function of frequency for the examined range, i.e. from 16 Hz to 60 Hz. This observation persists for all three c_N values considered and a plateau region becomes apparent above 45 Hz. A similar trend has also been reported by Xiao and Ge [109], based on numerical analyses. Field experiments that will investigate the effect of driving frequency are necessary to test the validity of the trend presented in Fig. 6.16, as well as the effect of driving frequency on the post-installation performance.

6.4.5. Computational aspects of the model

The present model development provides a new path in vibratory pile installation modelling, by virtue of its physical rigour and computational performance. Therefore, some additional details regarding the latter are required. For both pile and soil a vertical mesh of size $h = 0.05$ m was considered, while 5 trial functions (i.e. *in vacuo* normal modes) were adequate to

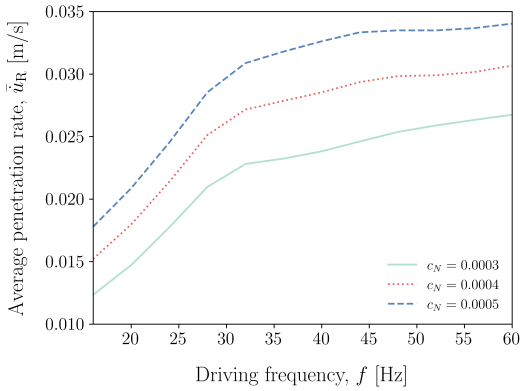

Figure 6.16: Comparison of average penetration rates for different driving frequencies, based on model predictions.

obtain an accurate pile response. In the HB analyses, terms up to the 15-th super-harmonic were retained (31 terms in total) in each Fourier series. A parametric study of 54 numerical analyses for the VH pile was performed on a computer desktop with a 10-core 3.3 GHz processor. A parallel implementation of the described task had a run time of 3 hours, leading to a remarkable CPU time of 3~4 minutes per analysis (for 5 m of pile penetration). Therefore, the present modelling framework can be readily employed in large parametric and uncertainty quantification studies.

6.5. Conclusions

In this chapter, a computationally efficient model for vibratory pile installation has been presented, that aims to bridge the gap between medium- and high-fidelity approaches. The pile is described by a thin shell theory and the soil is modelled as a linear elastic layered half-space. In particular, a SAFE model is used for the thin cylindrical shell and the Green's functions in the frequency-space domain are computed for the layered soil medium via the TLM coupled with PMLs. The pile-soil interaction is described by a history-dependent frictional interface, based on loading cycles accumulation and a visco-elasto-plastic tip reaction model, both characterized by SCPT measurements. For the solution of the coupled problem, a sequential HBM has been developed, that was motivated by the quasi-periodic character of the response. The latter approach comprises a remarkably efficient scheme for this problem and a potential candidate for a wider class of systems with quasi-periodic response due to slow amplitude modulation of the involved harmonics. The present modelling framework was employed to study the case of a vibro-driven pile from the GDP field campaign. Conclusively, the numerical results were compared with field data and the major points are listed as follows:

(i) vibratory pile installation comprises a quasi-periodic process, i.e. amplitude modulation of the involved harmonics is induced by the continuous - yet slow compared to the excitation time scale - change of the non-linear soil reaction and the input excitation.

(ii) the normalized distance from the pile tip is widely used as control parameter for friction reduction in impact piling, jacking and axial capacity purposes. In this study, the

distance-based mechanism is proved to be inadequate - both qualitatively and quantitatively - to provide accurate drivability predictions for vibratory pile installation.

(iii) a memory mechanism that accounts for friction reduction at the pile-soil interface is proposed and implemented, based on the number of accumulated loading cycles. Comparison between model predictions and field data showcases the potential of the proposed shaft reaction model in the analysis of vibratory pile installation.

(iv) the shaft friction is identified as the main mechanism of soil reaction to driving in the present case, while the pile penetration is found insensitive to variation of the plastic tip resistance. This finding is strongly dependent on the pile dimensions and for offshore monopiles it is expected to be even more apparent, given the large embedment depths required.

(v) the average penetration rate was found to be a monotonic function of the driving frequency, based on a numerical study conducted by means of the presented model. Field tests that focus on the effect of the driving frequency on both installation and post-installation performances are necessary to define what may constitute the optimal driving frequency.

7

The mechanics of the Gentle Driving of Piles

The main findings of the experimental campaign (see Chapter 5) showcased the potential of the GDP method and encouraged its further development. The proof of concept of the GDP method has been successful and the hypothesis that it can enhance installation performance was experimentally confirmed. Numerical modelling is the following necessary step in order to further analyse and interpret the field observations. To achieve that aim, the development of a numerical framework for the analysis of the GDP method is one of the foremost objectives in this research line.

In Chapter 6, a new vibratory pile installation model has been presented, that significantly advances the capabilities of engineering-oriented models, while retaining applicability and computational efficiency. Based on the physical similarity of the two processes (i.e. GDP and axial vibro-driving), the developed vibratory model is utilized in this chapter as the basis for the GDP modelling framework. By means of this development, the main novel contribution of the present chapter is realized, namely deciphering the mechanics of the GDP method and the beneficial effect of torsion on pile-soil interaction. The redirection of the friction force vector emerges as the major driving mechanism of GDP, as it enhances installation performance by greatly reducing the soil reaction along the penetration axis. Conclusively, a case study is performed to compare the performance of axial vibratory technique with GDP, on the basis of the respective benchmarked numerical models.

7.1. A numerical model for pile installation via the GDP method

A modelling framework to analyse pile installation by the GDP method is presented in the ensuing sections. The numerical model of vibratory pile driving (see Chapter 6) forms the basis of this development and is expanded accordingly to address the pile and soil circumferential motions. Some repetition of mathematical expressions is inescapable in

Parts of this chapter have been submitted for publication in Tsetas et al. [342].

order to render this chapter self-contained. A schematic of the GDP model is depicted in Fig. 7.1.

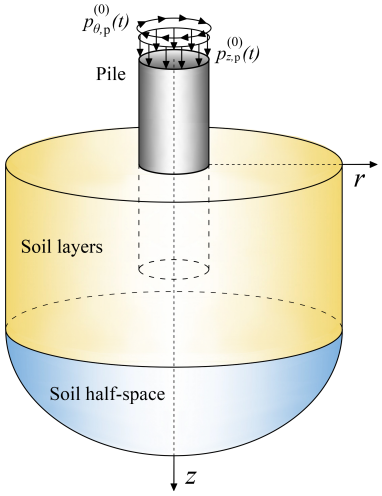

Figure 7.1: A tubular pile installed in a layered soil medium via vertical and torsional excitations at the pile head.

7.1.1. A SAFE cylindrical shell model of a tubular pile

A tubular pile is considered with wall thickness h_p, length L_p and mid-surface radius R_p. The pile material is linear elastic and isotropic with Young's modulus E_p, Poisson's ratio ν_p and mass density ρ_p. Similarly to the vibratory installation model, the GDP model is also axisymmetric ($n = 0$). However, the application of axial and circumferential loads (from the GDP shaker) at the pile top requires the consideration of both the symmetric (axial-radial) and the anti-symmetric (circumferential) modes for $n = 0$. Accordingly, the equations of motion for a thin cylindrical shell based on the SAFE method read:

$$\mathbf{I}^{\mathrm{s}}_{\mathrm{p,o}} \frac{\mathrm{d}^2 \mathbf{u}^{\mathrm{s}}_{\mathrm{p,o}}}{\mathrm{d}t^2} + \mathbf{L}^{\mathrm{s}}_{\mathrm{p,o}} \mathbf{u}^{\mathrm{s}}_{\mathrm{p,o}} = \mathbf{p}^{\mathrm{s}}_{\mathrm{p,o}} \tag{7.1a}$$

$$\mathbf{I}^{\mathrm{a}}_{\mathrm{p,o}} \frac{\mathrm{d}^2 \mathbf{u}^{\mathrm{a}}_{\mathrm{p,o}}}{\mathrm{d}t^2} + \mathbf{L}^{\mathrm{a}}_{\mathrm{p,o}} \mathbf{u}^{\mathrm{a}}_{\mathrm{p,o}} = \mathbf{p}^{\mathrm{a}}_{\mathrm{p,o}} \tag{7.1b}$$

where $\mathbf{I}^{\mathrm{s}}_{\mathrm{p,o}}$, $\mathbf{I}^{\mathrm{a}}_{\mathrm{p,o}}$ are the shell mass matrices, $\mathbf{L}^{\mathrm{s}}_{\mathrm{p,o}}$, $\mathbf{L}^{\mathrm{a}}_{\mathrm{p,o}}$ are the shell stiffness matrices, $\mathbf{u}^{\mathrm{s}}_{\mathrm{p,o}}$, $\mathbf{u}^{\mathrm{a}}_{\mathrm{p,o}}$ are the displacement/rotation vectors at the nodal rings, and $\mathbf{p}^{\mathrm{s}}_{\mathrm{p,o}}$, $\mathbf{p}^{\mathrm{a}}_{\mathrm{p,o}}$ are the vectors of consistent forces/moments at the nodal rings. Specifically, the displacements/rotations vectors read:

$$\mathbf{u}^{\mathrm{s}}_{\mathrm{p,o}} = \begin{bmatrix} \mathbf{u}^{\mathrm{s}}_{0} \\ \mathbf{w}^{\mathrm{s}}_{0} \\ \boldsymbol{\beta}^{\mathrm{s}}_{z,0} \end{bmatrix}, \quad \mathbf{u}^{\mathrm{a}}_{\mathrm{p,o}} = \mathbf{v}^{\mathrm{a}}_{0} \tag{7.2}$$

and similarly the consistent forces/moments vectors may be expressed as follows:

$$\mathbf{p}^{\mathrm{s}}_{\mathrm{p},o} = \begin{bmatrix} \mathbf{p}^{\mathrm{s}}_{zo,\mathrm{p}} \\ \mathbf{p}^{\mathrm{s}}_{ro,\mathrm{p}} \\ \mathbf{m}^{\mathrm{s}}_{zzo,\mathrm{p}} \end{bmatrix} \quad \mathbf{p}^{\mathrm{a}}_{\mathrm{p},o} = \mathbf{p}^{\mathrm{a}}_{\theta o,\mathrm{p}} \tag{7.3}$$

To further improve the computational aspects of the problem, the shell response is decomposed in terms of normal modes *in vacuo*:

$$\mathbf{u}^{\mathrm{s}}_{\mathrm{p},o} = \mathbf{\Phi}^{\mathrm{s}}_{\mathrm{p},o}\mathbf{q}^{\mathrm{s}}_{o} \tag{7.4a}$$

$$\mathbf{u}^{\mathrm{a}}_{\mathrm{p},0} = \mathbf{\Phi}^{\mathrm{a}}_{\mathrm{p},o}\mathbf{q}^{\mathrm{a}}_{o} \tag{7.4b}$$

where $\mathbf{\Phi}^{\mathrm{s}}_{\mathrm{p},o}$, $\mathbf{\Phi}^{\mathrm{a}}_{\mathrm{p},o}$ are the modal matrices for the symmetric and antisymmetric forms of $n = 0$, respectively, and $\mathbf{q}^{\mathrm{s}}_{o}(t)$, $\mathbf{q}^{\mathrm{a}}_{o}(t)$ denote the respective generalized coordinates. In particular, the modal matrices read:

$$\mathbf{\Phi}^{\mathrm{s}}_{\mathrm{p},o} = \begin{bmatrix} \mathbf{U}^{\mathrm{s}}_{o} \\ \mathbf{W}^{\mathrm{s}}_{o} \\ \mathbf{B}^{\mathrm{s}}_{o} \end{bmatrix}, \quad \mathbf{\Phi}^{\mathrm{a}}_{\mathrm{p},o} = \mathbf{V}^{\mathrm{a}}_{o} \tag{7.5}$$

where the modal sub-matrices $\mathbf{U}^{\mathrm{s}}_{o}$, $\mathbf{W}^{\mathrm{s}}_{0}$, $\mathbf{B}^{\mathrm{s}}_{o}$ and $\mathbf{V}^{\mathrm{a}}_{o}$ are defined as follows:

$$\mathbf{U}^{\mathrm{s}}_{o} = \begin{bmatrix} \mathbf{u}^{\mathrm{s}}_{o,1} & \mathbf{u}^{\mathrm{s}}_{o,2} & \cdots \end{bmatrix} \tag{7.6a}$$

$$\mathbf{W}^{\mathrm{s}}_{o} = \begin{bmatrix} \mathbf{w}^{\mathrm{s}}_{o,1} & \mathbf{w}^{\mathrm{s}}_{o,2} & \cdots \end{bmatrix} \tag{7.6b}$$

$$\mathbf{B}^{\mathrm{s}}_{o} = \begin{bmatrix} \boldsymbol{\beta}^{\mathrm{s}}_{o,1} & \boldsymbol{\beta}^{\mathrm{s}}_{o,2} & \cdots \end{bmatrix} \tag{7.6c}$$

$$\mathbf{V}^{\mathrm{a}}_{o} = \begin{bmatrix} \mathbf{v}^{\mathrm{a}}_{o,1} & \mathbf{v}^{\mathrm{a}}_{0,2} & \cdots \end{bmatrix} \tag{7.6d}$$

As can be seen in Eq. (7.5), the modal sub-matrices $\mathbf{V}^{\mathrm{s}}_{o}$, $\mathbf{U}^{\mathrm{a}}_{o}$, $\mathbf{W}^{\mathrm{a}}_{0}$ and $\mathbf{B}^{\mathrm{a}}_{o}$ are erased for convenience, since they are equal to zero. Therefore, the system of ordinary differential equations that governs the shell response is transformed to the space of generalized coordinates:

$$\left(\mathbf{\Phi}^{\mathrm{s}}_{\mathrm{p},o}\right)^{\mathrm{T}}\mathbf{I}^{\mathrm{s}}_{\mathrm{p},o}\mathbf{\Phi}^{\mathrm{s}}_{\mathrm{p},o}\frac{\mathrm{d}^2\mathbf{q}^{\mathrm{s}}_{o}}{\mathrm{d}t^2} + \left(\mathbf{\Phi}^{\mathrm{s}}_{\mathrm{p},o}\right)^{\mathrm{T}}\mathbf{L}^{\mathrm{s}}_{\mathrm{p},o}\mathbf{\Phi}^{\mathrm{s}}_{\mathrm{p},o}\mathbf{q}^{\mathrm{s}}_{o} = \left(\mathbf{\Phi}^{\mathrm{s}}_{\mathrm{p},o}\right)^{\mathrm{T}}\mathbf{p}^{\mathrm{s}}_{\mathrm{p},o} \tag{7.7}$$

$$\left(\mathbf{\Phi}^{\mathrm{a}}_{\mathrm{p},o}\right)^{\mathrm{T}}\mathbf{I}^{\mathrm{a}}_{\mathrm{p},o}\mathbf{\Phi}^{\mathrm{a}}_{\mathrm{p},o}\frac{\mathrm{d}^2\mathbf{q}^{\mathrm{a}}_{o}}{\mathrm{d}t^2} + \left(\mathbf{\Phi}^{\mathrm{a}}_{\mathrm{p},o}\right)^{\mathrm{T}}\mathbf{L}^{\mathrm{a}}_{\mathrm{p},o}\mathbf{\Phi}^{\mathrm{a}}_{\mathrm{p},o}\mathbf{q}^{\mathrm{a}}_{o} = \left(\mathbf{\Phi}^{\mathrm{a}}_{\mathrm{p},o}\right)^{\mathrm{T}}\mathbf{p}^{\mathrm{a}}_{\mathrm{p},o} \tag{7.8}$$

Finally, the pile displacements/rotation vector $\mathbf{u}_{\mathrm{p}}$ and the line load vector $\mathbf{p}_{\mathrm{p}}$, based on the premise of axisymmetric response, may be expressed as follows:

$$\mathbf{u}_{\mathrm{p}} = \begin{bmatrix} \mathbf{u}^{\mathrm{s}}_{o} \\ \mathbf{v}^{\mathrm{a}}_{o} \\ \mathbf{w}^{\mathrm{s}}_{o} \\ \boldsymbol{\beta}^{\mathrm{s}}_{z,o} \end{bmatrix}, \quad \mathbf{p}_{\mathrm{p}} = \frac{1}{2\pi R_{\mathrm{p}}}\begin{bmatrix} \mathbf{p}^{\mathrm{s}}_{zo,\mathrm{p}} \\ \mathbf{p}^{\mathrm{a}}_{\theta o,\mathrm{p}} \\ \mathbf{p}^{\mathrm{s}}_{ro,\mathrm{p}} \\ \mathbf{m}^{\mathrm{s}}_{zzo,\mathrm{p}} \end{bmatrix} \tag{7.9}$$

7.1.2. Green's functions of a layered soil half-space via the TLM+PMLs

During pile installation by the GDP method, all three motion components are present in both pile and soil. Therefore, the elicited wave motion in the soil medium will include both generalized Rayleigh (SV-P) and Love (SH) wave modes. Briefly, the generalized eigenvalue problem for the SV-P waves may be written as:

$$\left(k^2\bar{\mathbf{A}}+\bar{\mathbf{C}}\right)\begin{bmatrix}\boldsymbol{\Phi}_r\\ k\boldsymbol{\Phi}_z\end{bmatrix}=\begin{bmatrix}\mathbf{0}\\ \mathbf{0}\end{bmatrix} \tag{7.10}$$

and the generalized eigenvalue problem for the SH waves reads:

$$\left(k^2\mathbf{A}_\theta+\mathbf{C}_\theta\right)\boldsymbol{\Phi}_\theta=\mathbf{0} \tag{7.11}$$

where $\mathbf{C}_\theta=\mathbf{G}_\theta-\omega^2\mathbf{M}_\theta$, k is the radial wavenumber variable, and $\boldsymbol{\Phi}_r$, $\boldsymbol{\Phi}_\theta$ and $\boldsymbol{\Phi}_z$ denote the radial, circumferential and vertical modal displacements at the layer interfaces, respectively. Furthermore, the TLM matrices $\bar{\mathbf{A}}$ and $\bar{\mathbf{C}}$ are defined as:

$$\bar{\mathbf{A}}=\begin{bmatrix}\mathbf{A}_r & \mathbf{0}\\ \mathbf{B}_{zr} & \mathbf{A}_z\end{bmatrix} \tag{7.12a}$$

$$\bar{\mathbf{C}}=\begin{bmatrix}\mathbf{G}_r-\omega^2\mathbf{M}_r & \mathbf{B}_{rz}\\ \mathbf{0} & \mathbf{G}_z-\omega^2\mathbf{M}_z\end{bmatrix} \tag{7.12b}$$

It is noted that the TLM sub-matrices $\mathbf{A}_r$, $\mathbf{A}_\theta$, $\mathbf{A}_z$, $\mathbf{G}_r$, $\mathbf{G}_z$, $\mathbf{M}_r$ and $\mathbf{M}_z$ are associated with the soil domain as modelled by the coupled TLM+PMLs, i.e. including thin layers with complex-valued stretched thickness[266, 267]; the sub-matrices $\mathbf{B}_{zr}$, $\mathbf{B}_{rz}$ remain unaffected by the complex-valued coordinate stretching.

We proceed to utilize the Green's functions of a linear elastic layered half-space in the non-linear coupled formulation of our problem. For that purpose, the explicit matrix expressions of the Green's functions in the frequency-(radial-azimuthal)-wavenumber domain have been derived in Section 4.4 and read as follows:

$$\hat{\mathbf{u}}_{\mathrm{s},n}=\begin{bmatrix}\hat{\mathbf{u}}_{r,n}\\ \hat{\mathbf{u}}_{\theta,n}\\ \hat{\mathbf{u}}_{z,n}\end{bmatrix}=\begin{bmatrix}\boldsymbol{\Phi}_r\mathbf{D}_\mathrm{R}\boldsymbol{\Phi}_r^\mathrm{T} & \mathbf{0} & k\boldsymbol{\Phi}_r\mathbf{K}_\mathrm{R}^{-1}\mathbf{D}_\mathrm{R}\boldsymbol{\Phi}_z^\mathrm{T}\\ \mathbf{0} & \boldsymbol{\Phi}_\theta\mathbf{D}_\mathrm{L}\boldsymbol{\Phi}_\theta^\mathrm{T} & \mathbf{0}\\ \frac{1}{k}\boldsymbol{\Phi}_z\mathbf{D}_\mathrm{R}\mathbf{K}_\mathrm{R}\boldsymbol{\Phi}_r^\mathrm{T} & \mathbf{0} & \boldsymbol{\Phi}_z\mathbf{D}_\mathrm{R}\boldsymbol{\Phi}_z^\mathrm{T}\end{bmatrix}\begin{bmatrix}\hat{\mathbf{p}}_{r,n}\\ \hat{\mathbf{p}}_{\theta,n}\\ \hat{\mathbf{p}}_{z,n}\end{bmatrix} \tag{7.13}$$

where $\hat{\mathbf{u}}_{r,n}$, $\hat{\mathbf{u}}_{\theta,n}$ and $\hat{\mathbf{u}}_{z,n}$ are the soil displacements and $\hat{\mathbf{p}}_{r,n}$, $\hat{\mathbf{p}}_{\theta,n}$ and $\hat{\mathbf{p}}_{z,n}$ are the applied loads, both expressed in the frequency-(radial-azimuthal)-wavenumber domain. The diagonal matrices $\mathbf{K}_\mathrm{R}$, $\mathbf{K}_\mathrm{L}$, $\mathbf{D}_\mathrm{R}$ and $\mathbf{D}_\mathrm{L}$ are defined as:

$$\mathbf{K}_\mathrm{R}=\mathrm{diag}\left\{k_{\mathrm{R},1}\ \ k_{\mathrm{R},2}\ \ \cdots\right\} \tag{7.14a}$$

$$\mathbf{K}_\mathrm{L}=\mathrm{diag}\left\{k_{\mathrm{L},1}\ \ k_{\mathrm{L},2}\ \ \cdots\right\} \tag{7.14b}$$

$$\mathbf{D}_\mathrm{R}=\left(k^2\mathbf{I}-\mathbf{K}_\mathrm{R}^2\right)^{-1} \tag{7.14c}$$

$$\mathbf{D}_\mathrm{L}=\left(k^2\mathbf{I}-\mathbf{K}_\mathrm{L}^2\right)^{-1} \tag{7.14d}$$

where $k_{\mathrm{R},m}$ and $k_{\mathrm{L},m}$ denote the radial wavenumbers related to the generalized Rayleigh (SV-P) and generalized Love (SH) wave modes, respectively. Finally, the modal matrices $\mathbf{\Phi}_r$, $\mathbf{\Phi}_\theta$ and $\mathbf{\Phi}_z$ are defined as:

$$\mathbf{\Phi}_r = \begin{bmatrix} \boldsymbol{\phi}_{r,1} & \boldsymbol{\phi}_{r,2} & \cdots \end{bmatrix} \tag{7.15a}$$

$$\mathbf{\Phi}_\theta = \begin{bmatrix} \boldsymbol{\phi}_{\theta,1} & \boldsymbol{\phi}_{\theta,2} & \cdots \end{bmatrix} \tag{7.15b}$$

$$\mathbf{\Phi}_z = \begin{bmatrix} \boldsymbol{\phi}_{z,1} & \boldsymbol{\phi}_{z,2} & \cdots \end{bmatrix} \tag{7.15c}$$

Specifically, the Green's functions that need to be evaluated in this problem are associated with: (i) unit radial ring sources at $r = R_\mathrm{p}$, (ii) unit circumferential ring sources at $r = R_\mathrm{p}$ and (iii) unit vertical ring sources at $r = R_\mathrm{p}$. Finally, the vectors of soil displacements $\widetilde{\mathbf{u}}_r$, $\widetilde{\mathbf{u}}_\theta$ and $\widetilde{\mathbf{u}}_z$ may be readily expressed in terms of the ring loads $\widetilde{\mathbf{p}}_{r,\mathrm{s}}$, $\widetilde{\mathbf{p}}_{\theta,\mathrm{s}}$ and $\widetilde{\mathbf{p}}_{z,\mathrm{s}}$ in the frequency-space domain by virtue of the dynamic flexibility matrix $\widetilde{\mathbf{F}}_\mathrm{s}$ as follows:

$$\widetilde{\mathbf{u}}_\mathrm{s} = \begin{bmatrix} \widetilde{\mathbf{u}}_{r,\mathrm{s}} \\ \widetilde{\mathbf{u}}_{\theta,\mathrm{s}} \\ \widetilde{\mathbf{u}}_{z,\mathrm{s}} \end{bmatrix} = \begin{bmatrix} \widetilde{\mathbf{F}}_{rr} & \mathbf{0} & \widetilde{\mathbf{F}}_{rz} \\ \mathbf{0} & \widetilde{\mathbf{F}}_{\theta\theta} & \mathbf{0} \\ \widetilde{\mathbf{F}}_{zr} & \mathbf{0} & \widetilde{\mathbf{F}}_{zz} \end{bmatrix} \begin{bmatrix} \widetilde{\mathbf{p}}_{r,\mathrm{s}} \\ \widetilde{\mathbf{p}}_{\theta,\mathrm{s}} \\ \widetilde{\mathbf{p}}_{z,\mathrm{s}} \end{bmatrix} \tag{7.16}$$

It is noted that the ring loads $\widetilde{\mathbf{p}}_{r,\mathrm{s}}$, $\widetilde{\mathbf{p}}_{\theta,\mathrm{s}}$ and $\widetilde{\mathbf{p}}_{z,\mathrm{s}}$ correspond to the pile-soil interaction loads from both pile shaft and tip, and their formulation as external loads is owed to the solution method to be employed in the following sections.

7.1.3. Pile-soil compatibility conditions during installation via the GDP method

As described in Section 6.2.3, the pile-soil system is considered at discrete depths where the elevations of the pile nodal rings and the soil (thin) layer interfaces coincide along the contact surface. In particular, the nodal rings and layer interfaces corresponding to the region of pile-soil contact are defined by the superscripts c and the remaining rings and interfaces (out-of-contact) are defined by the superscript nc. The compatibility conditions that hold in pile installation via the GDP method are identical with the ones valid for axial vibratory driving, with the addition of the compatibility of circumferential tractions. Therefore, the following compatibility conditions are considered:
(i) continuity of radial displacements at the pile-soil interface:

$$\mathbf{w}^\mathrm{c} = \mathbf{u}_r^\mathrm{c}\Big|_{r=R_\mathrm{p}} \tag{7.17}$$

(ii) compatibility of vertical tractions applied at the pile-soil interface and the pile tip:

$$\mathbf{p}_{z,\mathrm{s}}^\mathrm{c} = -\mathbf{p}_{z,\mathrm{p}}^\mathrm{c}, \quad p_{z,\mathrm{s}}^{(\mathrm{t})} = -p_{z,\mathrm{p}}^{(\mathrm{t})} \tag{7.18}$$

in which the superscript (t) denotes the tip related component.
(iii) compatibility of radial tractions applied at the pile-soil interface:

$$\mathbf{p}_{r,\mathrm{s}}^\mathrm{c} = -\mathbf{p}_{r,\mathrm{p}}^\mathrm{c} \tag{7.19}$$

(iv) compatibility of circumferential tractions applied at the pile-soil interface:

$$\mathbf{p}^{\mathrm{c}}_{\theta,\mathrm{s}} = -\mathbf{p}^{\mathrm{c}}_{\theta,\mathrm{p}} \tag{7.20}$$

The soil reaction to driving is based on the same mechanisms that were formulated for the case of axial vibratory driving, i.e. a history-dependent frictional interface based on Coulomb friction and a visco-elasto-plastic tip reaction. The frictional interface is identical, albeit the presence of circumferential motion - in both pile and soil - results in both vertical and circumferential friction forces. In particular, each pile material point slides (with respect to the soil) along a 2-D cylindrical surface during GDP, instead of sliding along a vertical line as in axial vibro-driving. Therefore, the friction force along the pile shaft is decomposed into:

$$p^{(i)}_{z,\mathrm{s}} = \frac{f^{(i)}_{\mathrm{s,ult}} l^{(i)} \dfrac{\partial u^{(i)}_{\mathrm{rel}}}{\partial t}}{\sqrt{\left(\dfrac{\partial u^{(i)}_{\mathrm{rel}}}{\partial t}\right)^2 + \left(\dfrac{\partial v^{(i)}_{\mathrm{rel}}}{\partial t}\right)^2}} \tanh\left(\frac{1}{v_{\mathrm{tol}}}\sqrt{\left(\frac{\partial u^{(i)}_{\mathrm{rel}}}{\partial t}\right)^2 + \left(\frac{\partial v^{(i)}_{\mathrm{rel}}}{\partial t}\right)^2}\right) \tag{7.21}$$

$$p^{(i)}_{\theta,\mathrm{s}} = \frac{f^{(i)}_{\mathrm{s,ult}} l^{(i)} \dfrac{\partial v^{(i)}_{\mathrm{rel}}}{\partial t}}{\sqrt{\left(\dfrac{\partial u^{(i)}_{\mathrm{rel}}}{\partial t}\right)^2 + \left(\dfrac{\partial v^{(i)}_{\mathrm{rel}}}{\partial t}\right)^2}} \tanh\left(\frac{1}{v_{\mathrm{tol}}}\sqrt{\left(\frac{\partial u^{(i)}_{\mathrm{rel}}}{\partial t}\right)^2 + \left(\frac{\partial v^{(i)}_{\mathrm{rel}}}{\partial t}\right)^2}\right) \tag{7.22}$$

where v_{tol} is a velocity tolerance parameter, $l^{(i)}$ is the length of influence derived from the FE projection and $f^{(i)}_{\mathrm{s,ult}}$ defines the amplitude of static (and kinetic) friction. Finally, the relative velocity is decomposed into a vertical and a circumferential component, i.e. $\dfrac{\partial u^{(i)}_{\mathrm{rel}}}{\partial t}$ and $\dfrac{\partial v^{(i)}_{\mathrm{rel}}}{\partial t}$, respectively, which are defined as follows:

$$\frac{\partial u^{(i)}_{\mathrm{rel}}}{\partial t} = \frac{\partial u^{(i)}_{\mathrm{p}}}{\partial t} - \frac{\partial u^{(i)}_{z,\mathrm{s}}}{\partial t}\bigg|_{r=R_{\mathrm{p}}} \tag{7.23}$$

$$\frac{\partial v^{(i)}_{\mathrm{rel}}}{\partial t} = \frac{\partial v^{(i)}_{\mathrm{p}}}{\partial t} - \frac{\partial u^{(i)}_{\theta,\mathrm{s}}}{\partial t}\bigg|_{r=R_{\mathrm{p}}} \tag{7.24}$$

The formulation of the friction interface is concluded with the hereditary law that governs the friction reduction mechanism and reads:

$$f^{(i)}_{\mathrm{s,ult}} = f^{(i)}_{\mathrm{s},0}\left(\beta_\infty + (1-\beta_\infty)\mathrm{e}^{-c_N N^{(i)}_{\mathrm{cycl}}}\right) \tag{7.25}$$

where β_∞ is the ratio of the ultimately degraded friction amplitude to the initial one ($f^{(i)}_{\mathrm{s},0}$), c_N is a memory parameter that controls the rate of friction degradation and $N^{(i)}_{\mathrm{cycl}}$ is the number of loading cycles accumulated at the soil interface (i) during driving. In the case of GDP, it is postulated that loading cycles corresponding to vertical and circumferential friction

forces are considered equivalent, irrespectively of the dissimilar stress state induced in the surrounding soil and their frequency content; more details on these aspects are discussed in subsequent sections.

Finally, the tip reaction follows a visco-elasto-plastic formulation that reads:

$$p_{z,\mathrm{s}}^{(\mathrm{t})} = -p_{z,\mathrm{p}}^{(\mathrm{t})} = \begin{cases} k_{\mathrm{t}}(u_{\mathrm{p}}^{(\mathrm{t})} - u_{\mathrm{pl}}) + c_{\mathrm{t}}\dfrac{\partial u_{\mathrm{p}}^{(\mathrm{t})}}{\partial t}, & |k_{\mathrm{t}}(u_{\mathrm{p}}^{(\mathrm{t})} - u_{\mathrm{pl}})| < f_{\mathrm{t,ult}} h_{\mathrm{p}} \\ f_{\mathrm{t,ult}} h_{\mathrm{p}} \mathrm{sgn}\left(\dfrac{\partial u_{\mathrm{p}}^{(\mathrm{t})}}{\partial t}\right) + c_{\mathrm{t}}\dfrac{\partial u_{\mathrm{p}}^{(\mathrm{t})}}{\partial t}, & |k_{\mathrm{t}}(u_{\mathrm{p}}^{(\mathrm{t})} - u_{\mathrm{pl}})| = f_{\mathrm{t,ult}} h_{\mathrm{p}} \end{cases} \tag{7.26}$$

where u_{pl} is the plastic tip displacement, $f_{\mathrm{t,ult}}$ is the plastic tip resistance and the stiffness and damping coefficients are defined as k_{t} and c_{t}, respectively. As can be seen, the tip reaction is based solely on the axial pile tip response without any effects due to the circumferential motion. This choice will be elaborated further in the discussion of the numerical results and the comparison against the field data.

7.2. A solution to the coupled problem via the Adjusted Harmonic Balance Method

In Section 6.3, we presented a time-frequency method for the problem of vibratory pile installation, based on sequential application of the HBM. The latter was enabled by postulating that the pile-soil response is virtually periodic "microscopically", i.e. for a small time interval around a certain state of the system. Therefore, assemblage of these solutions via linear interpolation of the response Fourier coefficients in time leads to a quasi-periodic response due to slow amplitude modulation of the involved harmonic components. The preceding approach was validated numerically and was successfully applied to vibratory pile installation in Chapter 6.

During pile installation via the GDP method, a low-frequency (Ω_{a}) axial and a high-frequency (Ω_{t}) torsional excitation are applied simultaneously at the pile top. Most likely the torsional driving frequency will not be an integer multiple of the axial one, due to the impracticality of imposing a true integer ratio $\Omega_{\mathrm{t}}/\Omega_{\mathrm{a}}$ or even by choice, e.g. to avoid potential interaction that may lead to shaker damage. Hence, the premise of periodic pile-soil response (for a single state) with the axial driving frequency as the fundamental one is invalidated. In this case, the response of the system around a single state may even be quasi-periodic in its classical sense, i.e. characterized by a discrete frequency spectrum with at least two incommensurable fundamental frequencies. Therefore, this development requires a generalization of the classical HBM to render our framework applicable in the case of the GDP method.

A HB scheme has been developed for systems exhibiting at least two incommensurable base frequencies, commonly referred to as the generalized or multi-dimensional HBM (MHBM) [343–347, 330, 348]. The MHBM is based on the expansion of the response quantities in terms of multi-dimensional Fourier series and the introduction of the so-called hyper-time concept [344, 330]. For a problem with two fundamental frequencies Ω_1 and Ω_2, the two-dimensional Fourier series of a function $f(t)$ may be expressed in the bi-dimensional time (τ_1, τ_2) (hyper-time) as follows:

$$f(\tau_1,\tau_2) = \sum_{j_1=-h_1}^{h_1} \sum_{j_2=-h_2}^{h_2} \left(c_{j_1,j_2} \cos(j_1\tau_1 + j_2\tau_2) + s_{j_1,j_2} \sin(j_1\tau_1 + j_2\tau_2) \right) \tag{7.27}$$

where $\tau_1 = \Omega_1 t$, $\tau_2 = \Omega_2 t$ are the hyper-time variables and c_{j_1,j_2}, s_{j_1,j_2} are the Fourier coefficients. To further elucidate the preceding ideas, a quasi-periodic velocity signal and the associated friction force are displayed both in time and hyper-time domain (see Fig. 7.2). The time series in Figs. 7.2a and 7.2c are uniquely mapped to their representations in the hyper-time plane shown in Figs. 7.2b and 7.2d, respectively, by tracking the trajectory of the real time variable t on the (τ_1,τ_2)-plane.

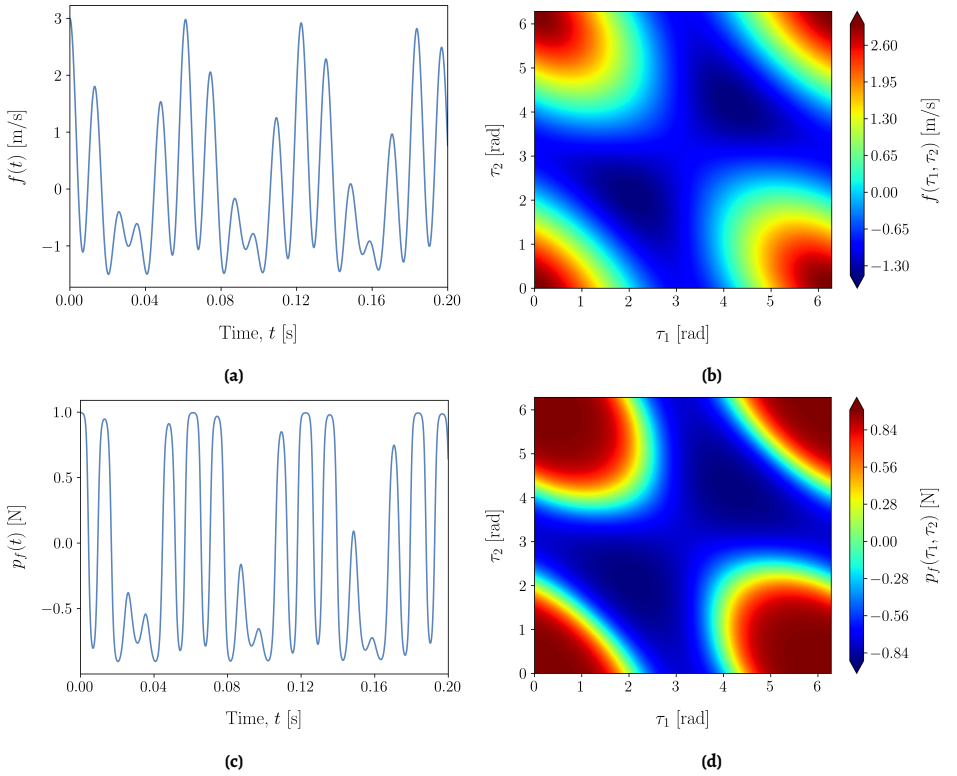

Figure 7.2: A quasi-periodic velocity signal $f(t) = \cos(100t) + \cos(100\sqrt{17}t) + \cos(100t + 100\sqrt{17}t)$ and the associated friction force $p_f = \tanh(f(t))$ in time (a,c) and hyper-time (b,d) domain representations, respectively.

The preceding outline of the multi-dimensional HBM indicates that the formulation of the pile-soil problem at hand may become highly cumbersome, with a laborious numerical implementation. An efficient alternative for quasi-periodic problems has been proposed by Guskov and Thouverez [347], based on a mono-harmonic approximation of the multiple fundamental frequencies leading to the so-called adjusted HBM (AHBM). The latter method is identical to the classical HBM, albeit based on a new fundamental frequency Ω_0 that is the greatest common divisor of $\overline{\Omega}_2$ and $\overline{\Omega}_1$:

$$\Omega_{\circ} = \frac{\bar{\Omega}_2}{p_2} = \frac{\bar{\Omega}_1}{p_1} \tag{7.28}$$

where p_1, p_2 are appropriate integers to approximate the original frequency ratio $\eta_\Omega = \Omega_2/\Omega_1$ up to the desired precision and the approximate frequencies $\bar{\Omega}_2$, $\bar{\Omega}_1$ are obtained as follows:

$$\eta_\Omega = \frac{\Omega_2}{\Omega_1} \approx \bar{\eta}_\Omega = \frac{\bar{\Omega}_2}{\bar{\Omega}_1} = \frac{p_2}{p_1} \tag{7.29}$$

where the rational number $\bar{\eta}_\Omega$ is the new approximate frequency ratio. Accordingly, in the AHBM a response quantity $f(t)$ may be assumed to possess the following form:

$$f(t) = \sum_{j \in S_0} \left(c_j \cos(j\Omega_{\circ} t) + s_j \sin(j\Omega_{\circ} t) \right) \tag{7.30}$$

where the set S_0 is defined as follows:

$$S_0 = \left\{ j_1 p_1 + j_2 p_2 \;\middle|\; j_1 \in [-h_1, h_1],\ j_2 \in [-h_2, h_2] \right\} \tag{7.31}$$

where j_1, j_2 can obtain integer values from the designated intervals and h_1, h_2 are positive integers that denote the truncation limits of the super-harmonics to be included.

The targeted harmonics in the AHBM encompass the two distinct sets of super-harmonic components associated with the two fundamental frequencies, as well as the harmonics that may emerge from the interaction of the previous two sets. It is noted that certain values of j may be generated by more than one pair of (j_1, j_2), so only one term is retained in these scant cases, and the number of terms can be further reduced by virtue of the symmetries of the Fourier series. As regards the accuracy of the AHBM, the discrepancy between the discrete frequency spectra of the AHBM and the MHBM is the decisive factor. As can be seen in Fig. 7.3, the use of $\bar{\eta}_\Omega$ that is approximated in the second decimal place is in great agreement with the frequency spectrum of the MHBM.

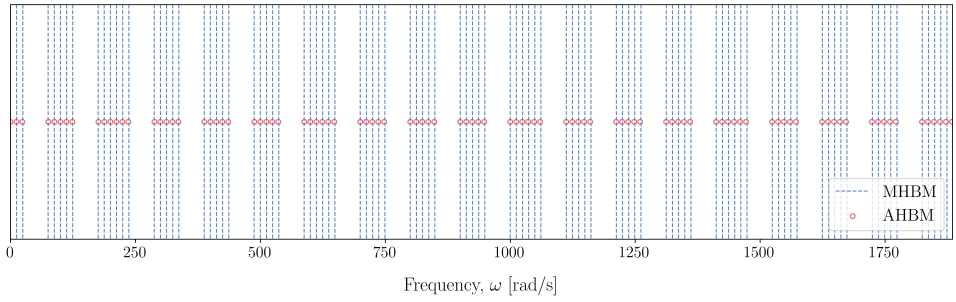

Figure 7.3: Comparison of the frequency components in the discrete spectra of MHBM and AHBM for an example case with $\Omega_1 = 100$ rad/s, $\Omega_2 = 100\sqrt{17}$ rad/s, $h_1 = h_2 = 10$, $\eta_\Omega = 4.123105...$ and $\bar{\eta}_\Omega = 4.12$.

Finally, it is remarked that imposing a predefined irrational ratio of fundamental frequencies in pile driving is infeasible from an engineering point of view; similar to imposing

an integer frequency ratio (as stated above). In all likelihood the driving frequencies cannot be set in practice with such precision to achieve an irrational frequency ratio (even if desired). Therefore, the AHBM may be considered not solely an efficient alternative to MHBM, but also the rational engineering approach to this problem.

Based on the preceding developments, the assumed solutions that were employed in Section 6.3 are identical to the ones to be employed for the case of the GDP method, simply with a new base frequency, i.e. Ω_0 as defined above. The pile generalized coordinates are defined as follows:

$$q^{\mathrm{s}}_{\mathrm{o},m} = \begin{cases} c^{\mathrm{s}}_{\mathrm{o},\mathrm{o}}\, t + \sum\limits_{j\in S_0} \left(c^{\mathrm{s}}_{\mathrm{o},j} \cos(j\Omega_{\mathrm{o}} t) + s^{\mathrm{s}}_{\mathrm{o},j} \sin(j\Omega_{\mathrm{o}} t) \right), & m = 0 \\ c^{\mathrm{s}}_{m,\mathrm{o}} + \sum\limits_{j\in S_0} \left(c^{\mathrm{s}}_{m,j} \cos(j\Omega_{\mathrm{o}} t) + s^{\mathrm{s}}_{m,j} \sin(j\Omega_{\mathrm{o}} t) \right), & m > 0 \end{cases} \tag{7.32}$$

$$q^{\mathrm{a}}_{\mathrm{o},m} = c^{\mathrm{a}}_{m,\mathrm{o}} + \sum_{j\in S_0} \left(c^{\mathrm{a}}_{m,j} \cos(j\Omega_{\mathrm{o}} t) + s^{\mathrm{a}}_{m,j} \sin(j\Omega_{\mathrm{o}} t) \right), \quad m \geq 0 \tag{7.33}$$

where $\mathbf{c}^{\mathrm{s}}_m = \begin{bmatrix} c^{\mathrm{s}}_{m,\mathrm{o}} & c^{\mathrm{s}}_{m,1} & \cdots \end{bmatrix}^{\mathrm{T}}$ and $\mathbf{s}^{\mathrm{s}}_m = \begin{bmatrix} s^{\mathrm{s}}_{m,1} & s^{\mathrm{s}}_{m,2} & \cdots \end{bmatrix}^{\mathrm{T}}$ denote the vectors of Fourier coefficients associated with the m-th axial-radial mode; similarly, the Fourier coefficients of the m-th torsional mode are arranged in the vectors $\mathbf{c}^{\mathrm{a}}_m = \begin{bmatrix} c^{\mathrm{a}}_{m,\mathrm{o}} & c^{\mathrm{a}}_{m,1} & \cdots \end{bmatrix}^{\mathrm{T}}$ and $\mathbf{s}^{\mathrm{a}}_m = \begin{bmatrix} s^{\mathrm{a}}_{m,1} & s^{\mathrm{a}}_{m,2} & \cdots \end{bmatrix}^{\mathrm{T}}$. Furthermore, the vertical and circumferential friction forces along the pile-soil interface may be expressed as:

$$\mathbf{p}^{\mathrm{c}}_{\mathrm{s},z} = \boldsymbol{\Psi}_z \left(\boldsymbol{\alpha}_{z\mathrm{o}} + \sum_{j\in S_0} \left(\boldsymbol{\alpha}_{zj} \cos(j\Omega_{\mathrm{o}} t) + \boldsymbol{\beta}_{zj} \sin(j\Omega_{\mathrm{o}} t) \right) \right) \tag{7.34}$$

$$\mathbf{p}^{\mathrm{c}}_{\mathrm{s},\theta} = \boldsymbol{\Psi}_\theta \left(\boldsymbol{\alpha}_{\theta\mathrm{o}} + \sum_{j\in S_0} \left(\boldsymbol{\alpha}_{\theta j} \cos(j\Omega_{\mathrm{o}} t) + \boldsymbol{\beta}_{\theta j} \sin(j\Omega_{\mathrm{o}} t) \right) \right) \tag{7.35}$$

in which $\boldsymbol{\alpha}_{zj} = \begin{bmatrix} \alpha_{zj,0} & \alpha_{zj,1} & \cdots \end{bmatrix}^{\mathrm{T}}$, $\boldsymbol{\beta}_{zj} = \begin{bmatrix} \beta_{zj,1} & \beta_{zj,2} & \cdots \end{bmatrix}^{\mathrm{T}}$ are the vectors of Fourier coefficients related to the j-th cosine and sine terms and $\boldsymbol{\Psi}_z$ is the matrix encapsulating the basis vectors for the vertical friction forces. Correspondingly, the vectors of Fourier coefficients for the circumferential friction forces are denoted as $\boldsymbol{\alpha}_{\theta j} = \begin{bmatrix} \alpha_{\theta j,0} & \alpha_{\theta j,1} & \cdots \end{bmatrix}^{\mathrm{T}}$, $\boldsymbol{\beta}_{\theta j} = \begin{bmatrix} \beta_{\theta j,1} & \beta_{\theta j,2} & \cdots \end{bmatrix}^{\mathrm{T}}$ and $\boldsymbol{\Psi}_\theta$ is the matrix containing the basis vectors for spatial approximation. Finally, the axial tip reaction is also assumed to be periodic:

$$p^{(\mathrm{t})}_{\mathrm{s},z} = \alpha_{\mathrm{t},\mathrm{o}} + \sum_{j\in S_0} \left(\alpha_{\mathrm{t},j} \cos(j\Omega_{\mathrm{o}} t) + \beta_{\mathrm{t},j} \sin(j\Omega_{\mathrm{o}} t) \right) \tag{7.36}$$

where $\boldsymbol{\alpha}_{\mathrm{t}} = \begin{bmatrix} \alpha_{\mathrm{t},0} & \alpha_{\mathrm{t},1} & \cdots \end{bmatrix}^{\mathrm{T}}$ and $\boldsymbol{\beta}_{\mathrm{t}} = \begin{bmatrix} \beta_{\mathrm{t},1} & \beta_{\mathrm{t},2} & \cdots \end{bmatrix}^{\mathrm{T}}$ denote the vectors encapsulating the Fourier coefficients of the tip reaction.

By substituting the assumed solutions into the dynamic equilibria of pile and soil and the compatibility conditions, the following residuals are obtained:

$$\mathbf{r}_{\mathrm{c},z} = \boldsymbol{\Psi}_z^{\mathrm{T}} \left(\mathbf{p}_{z,\mathrm{s}}^{\mathrm{c}} + \mathbf{p}_{z,\mathrm{p}}^{\mathrm{c}} \right) \tag{7.37a}$$

$$\mathbf{r}_{\mathrm{c},\theta} = \boldsymbol{\Psi}_\theta^{\mathrm{T}} \left(\mathbf{p}_{\theta,\mathrm{s}}^{\mathrm{c}} + \mathbf{p}_{\theta,\mathrm{p}}^{\mathrm{c}} \right) \tag{7.37b}$$

$$r_{\mathrm{t}} = p_{z,\mathrm{s}}^{(\mathrm{t})} + p_{z,\mathrm{p}}^{(\mathrm{t})} \tag{7.37c}$$

$$\mathbf{r}_{q,\mathrm{s}} = \left(\boldsymbol{\Phi}_{\mathrm{p,o}}^{\mathrm{s}} \right)^{\mathrm{T}} \left(\mathbf{I}_{\mathrm{p,o}}^{\mathrm{s}} \boldsymbol{\Phi}_{\mathrm{p,o}}^{\mathrm{s}} \frac{\mathrm{d}^2 \mathbf{q}_{\mathrm{o}}^{\mathrm{s}}}{\mathrm{d}t^2} + \mathbf{L}_{\mathrm{p,o}}^{\mathrm{s}} \boldsymbol{\Phi}_{\mathrm{p,o}}^{\mathrm{s}} \mathbf{q}_{\mathrm{o}}^{\mathrm{s}} - \mathbf{p}_{\mathrm{p,o}}^{\mathrm{s}} \right) \tag{7.37d}$$

$$\mathbf{r}_{q,\mathrm{a}} = \left(\boldsymbol{\Phi}_{\mathrm{p,o}}^{\mathrm{a}} \right)^{\mathrm{T}} \left(\mathbf{I}_{\mathrm{p,o}}^{\mathrm{a}} \boldsymbol{\Phi}_{\mathrm{p,o}}^{\mathrm{a}} \frac{\mathrm{d}^2 \mathbf{q}_{\mathrm{o}}^{\mathrm{a}}}{\mathrm{d}t^2} + \mathbf{L}_{\mathrm{p,o}}^{\mathrm{a}} \boldsymbol{\Phi}_{\mathrm{p,o}}^{\mathrm{a}} \mathbf{q}_{\mathrm{o}}^{\mathrm{a}} - \mathbf{p}_{\mathrm{p,o}}^{\mathrm{a}} \right) \tag{7.37e}$$

which can be arranged in the following residual vector:

$$\mathbf{r} = \begin{bmatrix} \mathbf{r}_{\mathrm{c},z} \\ \mathbf{r}_{\mathrm{c},\theta} \\ r_{\mathrm{t}} \\ \mathbf{r}_{q,\mathrm{s}} \\ \mathbf{r}_{q,\mathrm{a}} \end{bmatrix} \tag{7.38}$$

Based on the AHBM, the Fourier coefficients of the residual vector $\mathbf{r}$ are obtained via a Fourier-Galerkin projection and are required to vanish:

$$\mathbf{R}_{\mathrm{F}} = \frac{1}{T_{\mathrm{o}}} \int_0^{T_{\mathrm{o}}} \mathbf{r}\mathbf{h} \, \mathrm{d}t \tag{7.39}$$

where $\mathbf{R}_{\mathrm{F}}$ is the Fourier coefficients matrix of the residuals, T_{o} is the period corresponding to the base frequency of the AHBM (Ω_{o}) and the row vector $\mathbf{h}$ encapsulates the test functions (i.e. Fourier harmonics) $h_j(t)$ defined as:

$$h_j(t) = \frac{1}{2} \left[\left(1 + (-1)^j \right) \cos\left(\frac{j\Omega_{\mathrm{o}} t}{2} \right) + \left(1 + (-1)^{j+1} \right) \sin\left(\frac{j+1}{2} \Omega_{\mathrm{o}} t \right) \right] \tag{7.40}$$

7.3. Numerical results and comparison with field data

The preceding modelling aspects conclude the numerical developments of this thesis by presenting a complete computational framework for the analysis of pile installation via axial vibratory and GDP techniques. In the ensuing, the characterization of the GDP model parameters is presented on the basis of *in-situ* tests from the GDP field campaign [51]. Numerical results are compared against field data showcasing the model potential and further investigation into the GDP method uncovers the mechanisms that lead to its remarkable installation performance. Finally, a comparison study between axial vibratory and GDP techniques is performed, with a view to the induced wave motion in the soil medium.

7.3.1. Model predictions and installation measurements

The installation process is studied for an embedment interval from 3 m to 8 m, with the aid of field data from two piles driven via the GDP method (i.e. GDP_1 and GDP_2). Similarly to the case of axial vibratory driving (see Chapter 6), the dynamic input excitation - both axial and circumferential - is inferred from strain measurements at the pile top, which were monitored by means of fiber Bragg grating (FBG) sensors. Furthermore, the properties of the GDP piles and the specifications of the GDP shaker used in the field campaign can be found in Tables 7.1 and 7.2, respectively. As regards the characterization of the soil medium, Seismic Cone Penetration Tests with pore water pressure measurements (SCPTu's) were performed and the depth of the water table was found at 4.5 m (see Fig. 7.4). It is noted that material dissipation is introduced in the form of frequency-independent hysteretic damping for pile and soil with ratios $\xi_p = 0.001$ and $\xi_s = 0.025$ (identical for P- and S-waves), respectively.

ρ_p [kg/m^3]	E_p [Pa]	ν_p [-]	L_p [m]	R_p [m]	h_p [m]
7850	$210{\cdot}10^9$	0.3	10	0.373	0.0159

Table 7.1: Properties of the piles driven in the GDP field campaign.

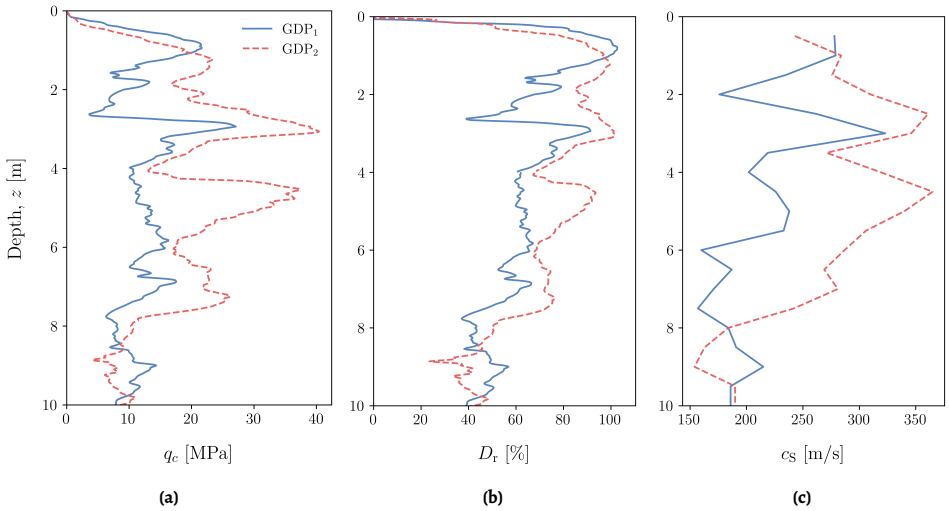

Figure 7.4: Profiles of (a) cone tip resistance (q_c), (b) relative density (D_r), and (c) shear wave velocity (c_S) obtained from the SCPTu tests.

As remarked in the preceding sections, the present modelling framework is aimed to be applicable for the analysis of both axial vibratory and GDP techniques. It is evident that the pile and soil modelling approaches - as a cylindrical shell and a layered half-space, respectively - are common to both installation techniques. With a view to proposing a unified modelling framework, the frictional interface and tip reaction formulations of the axial vibratory model are employed and adjusted to a minimal degree to accommodate the

	GDP shaker	
	Axial shaker	Torsional shaker
Total mass [kg]	5150	
Eccentric moment me [kg m]	15	4
Rotational speed [rpm]	1400	4800
Operational power [kW]	72	188

Table 7.2: Technical specifications of the GDP shaker.

additional requirements for the GDP method. The motivation to retain the formulation of the two models as common as possible lies in the similarity of the installation process (in terms of physics) between the two methods; to put it simply, a physically sound model for GDP should be capable to capture axial vibratory driving as well.

As regards the frictional interface, the generic dependence of friction on relative velocity directly encompasses the case of GDP; however, the question about the parameter calibration for the memory mechanism may be raised. We proceed to retain the expression $f_{\mathrm{s},0}^{(i)} = 0.012 q_c(z_i)$ and the value $\beta_\infty = 0.2$, due to the common soil type encountered in the GDP test site. Subsequently, for the degradation rate parameter c_N an admissible range of values (i.e. $c_N = 0.0003 - 0.0005$) is considered, as proposed in Chapter 6. Furthermore, the tip reaction brings about the complication of the additional circumferential component and its coupling with the axial one. Due to the lack of a dataset that may facilitate the distinction of such effects, the following choices are made: (i) the torsional reaction at the tip is discarded and (ii) the effect of torsion is accounted by modifying the axial tip reaction. Effectively, this approach retains the parameters k_t and c_t as defined in the axial vibratory model and the value of the plastic tip resistance $f_{\mathrm{t,ult}}$ is to be modified. These considerations allow to circumvent the introduction of additional parameters, which would be inescapable if axial-torsional reaction coupling and/or torsional reaction were to be considered.

In Fig. 7.5, the GDP model predictions are compared with the pile penetration records from the GDP field campaign. Specifically, two penetration records are considered, as measured by the potentiometer transducer (PM) and the driving logging (DL) system. The former measurement has a high sampling rate ($f = 1000$ Hz) and is considered more reliable than the latter, which is a sparse measurement (recorded per 25 cm of penetration). It is remarked that PM data are not available for pile GDP_2, due to failure of the sensor during driving. To achieve a first proper validation of the drivability model, the calibrated parameters for GDP_1 and GDP_2 were aimed to be identical. This validation process was successful and resulted in: (i) adoption of $c_N = 0.0003$ for the shaft reaction and (ii) elimination of the viscous damping term and setting $f_{\mathrm{t,ult}} = 0.15 q_c$ for the tip reaction. The value of the degradation parameter falls in the range proposed for the axial vibratory model, while the modification of tip reaction is considered to be a result of the axial-torsional coupling at the pile tip. The latter is clearly an efficient manner to address a presumably more complicated mechanism, which may be better identified by means of additional experiments. As can be seen in Fig. 7.5, these two calibration options led to a great agreement between the GDP model predictions and the penetration records for both GDP_1 and GDP_2. Naturally, further refinement of the calibration process is of utmost importance at this early stage of development; yet the degree of agreement with field data achieved through a single calibration approach for two

different piles is considered more than satisfactory.

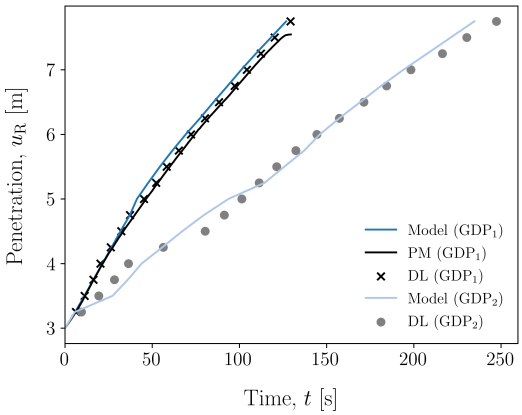

Figure 7.5: Comparison of GDP model predictions with field data for piles GDP_1 and GDP_2; penetration profiles as recorded both by the potentiometer (PM) and the vibratory device logging system (DL) are shown.

A supplementary comparison between numerical results and field data can be provided by studying the dynamic pile response. To that end, the short-time Fourier transform (STFT) is employed for the time-frequency analysis of the axial acceleration at the pile head. The amplitudes of the STFTs for the model output and the acceleration measurement are presented in Figs. 7.6 to 7.9. As regards the axial spectra (see Figs. 7.6 and 7.7), both model output and field data indicate responses with frequency content rich in super-harmonics of appreciable amplitude. However, for both GDP piles it is discernible that the model slightly overestimates the amplitude with ascending frequency compared to the field data. The latter has been observed in the case of axial vibratory driving as well (see Chapter 6) and is considered an indication of a smoother soil reaction than the one adopted in the present models. On the other hand, the circumferential STFT of the model output possesses significant amplitude in the torsional driving frequency and its first super-harmonic, while the STFT of the accelerometer record showcases an appreciable drop in amplitude already from the first super-harmonic. Furthermore, components of minor amplitude are present in many more frequencies related to the axial excitation, as well as its combinations with torsional super-harmonics. The latter are not present in the model output and this discrepancy - along with the previous observations - suggest that that soil reaction can be better identified. For drivability purposes, it is apparent that the present model is more than suitable, thus these observations are to be assessed in the light of further numerical and experimental investigations.

7.3.2. Redirection of the friction force vector: the major driving mechanism of GDP

The preceding discussion focused on the comparison between model output and field data, showcasing the predictive potential of the present GDP model. However, the mechanism that leads to the remarkable performance of the GDP method is yet to be deciphered. As postulated in Chapter 5, the introduction of torsion will mobilize friction in the circumferential

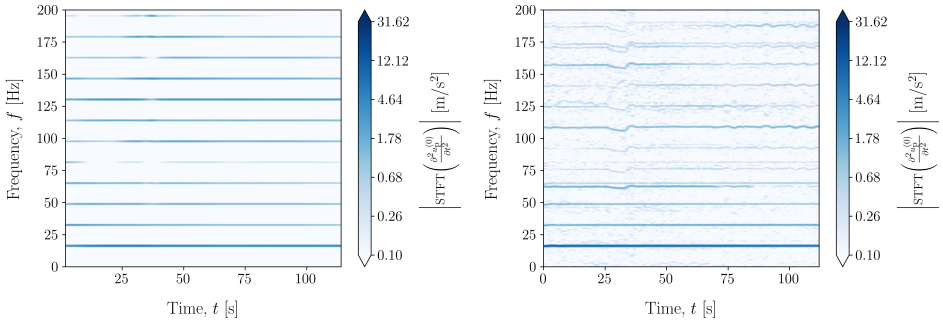

Figure 7.6: Amplitude of the axial acceleration STFT of (a) the model output and (b) the accelerometer record during installation of pile GDP_1.

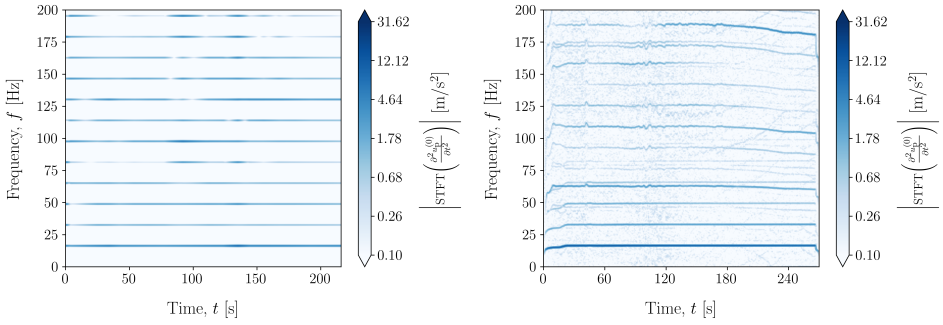

Figure 7.7: Amplitude of the axial acceleration STFT of (a) the model output and (b) the accelerometer record during installation of pile GDP_2.

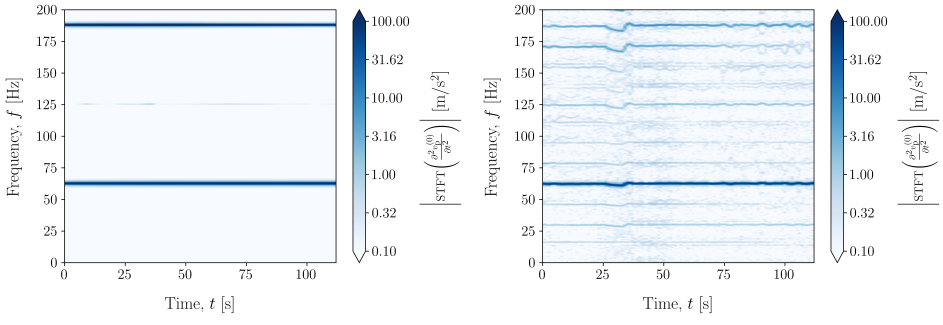

Figure 7.8: Amplitude of the circumferential acceleration STFT of (a) the model output and (b) the accelerometer record during installation of pile GDP_1.

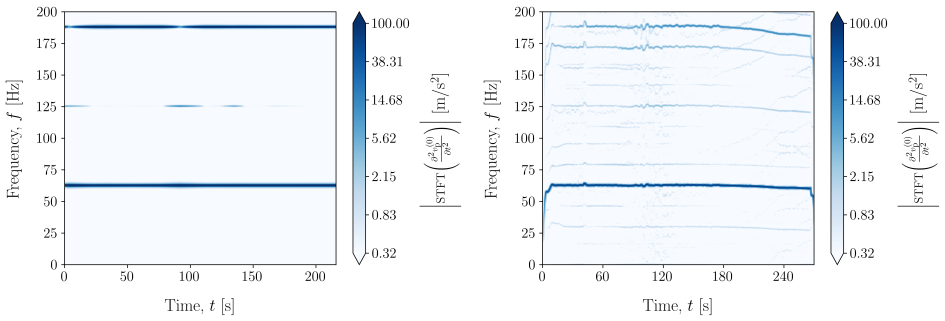

Figure 7.9: Amplitude of the circumferential acceleration STFT of (a) the model output and (b) the accelerometer record during installation of pile GDP_2.

direction, thus the vertical soil reaction along the shaft will be reduced. This hypothesis is confirmed by the friction forces developed at the pile shaft, based on the numerical results of the present model. Specifically, the vertical and circumferential (line) friction forces at an elevation of 3 m below the ground surface are displayed in Figs. 7.10 and 7.11; two distinct time windows are chosen occurring when the pile reaches the penetration depths of 5.5 m and 7.5 m. As can be seen, both friction force components have a common pattern, irrespective of the pile (GDP_1 or GDP_2) and the penetration depth. In Figs. 7.10 and 7.11, it is demonstrated that friction is predominantly expended in the circumferential direction resisting the torsional motion and is accompanied by a substantially lower friction force along the vertical direction. Therefore, the redirection of the friction force vector emerges as the major driving mechanism of GDP, by virtue of major reduction of the soil reaction along the penetration axis.

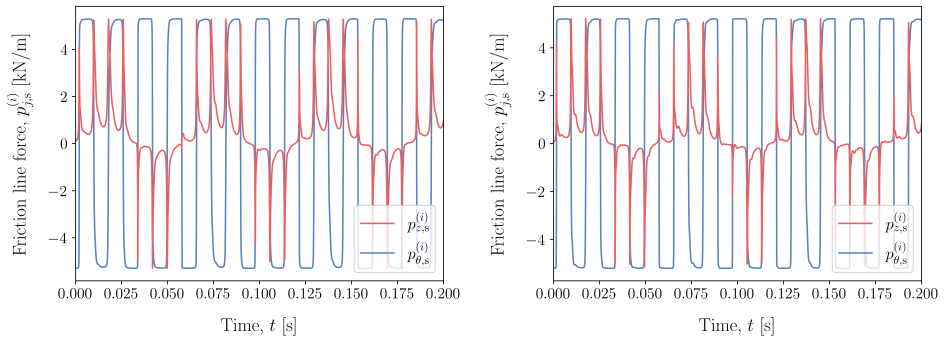

Figure 7.10: Friction force components ($p_{z,s}^{(i)}$, $p_{\theta,s}^{(i)}$) at $z_i = 3.0$ m and $u_R = 5.5$ m

Another visualization of the friction force vector during the studied time intervals is presented in Figs. 7.12 and 7.13. Specifically, the trajectories of the friction force vectors

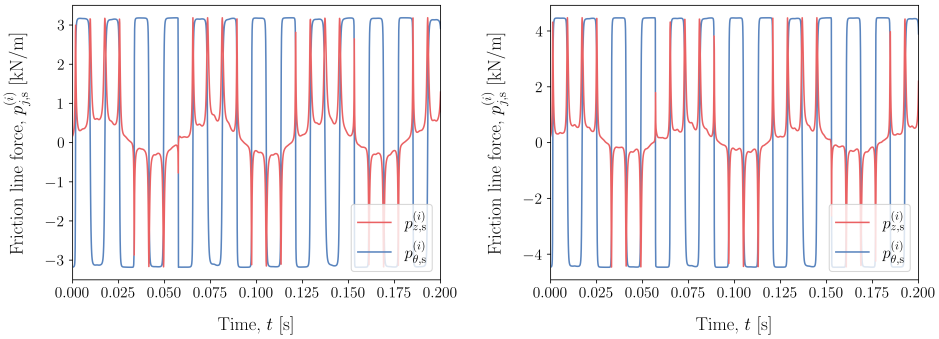

(a) GDP$_1$ **(b)** GDP$_2$

Figure 7.11: Friction force components ($p_{z,\mathrm{s}}^{(i)}$, $p_{\theta,\mathrm{s}}^{(i)}$) at $z_i = 3.0$ m and $u_\mathrm{R} = 7.5$ m

are shown for all the cases discussed in Figs. 7.10 and 7.11. Two loci may be distinguished, which correspond to two horizontal lines that the majority of the points approach. In particular, these two lines (loci) correspond to the cases of zero vertical friction and the extrema of circumferential friction force. This is an additional testament to the mechanism of friction redirection, as the majority of points approach these loci and the extrema of vertical friction are scarcely present. It is noted that a fixed time step of $\Delta t = 0.0001$ s is used for the evaluation of the friction force vectors in the previous plots.

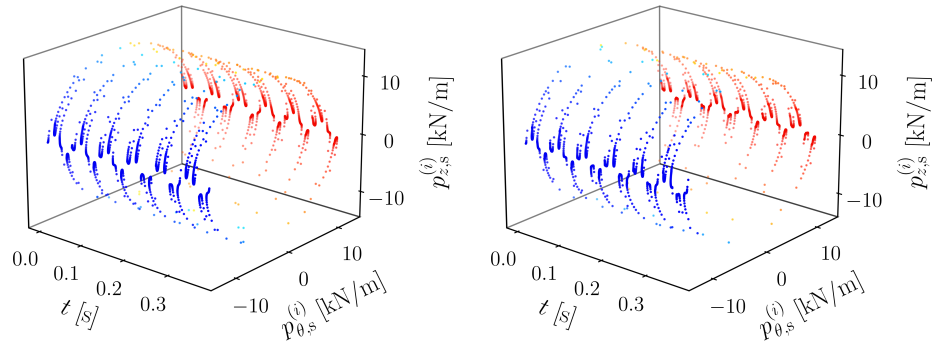

(a) GDP$_1$ **(b)** GDP$_2$

Figure 7.12: Friction force trajectories at $z_i = 3.0$ m and $u_\mathrm{R} = 5.5$ m; the color of the markers is based on the ratio of circumferential to total friction force, i.e. ranging from -1 (blue) to 1 (red).

The identification of the friction redirection mechanism inescapably leads to new research questions regarding the nature of this mechanism and its implications. It becomes evident that successful pile installation via the GDP method requires a set of axial and torsional excitation parameters (amplitudes and frequencies) suitable to achieve the desired result, i.e. redirection of the friction force vector. The latter depends both on the shaker

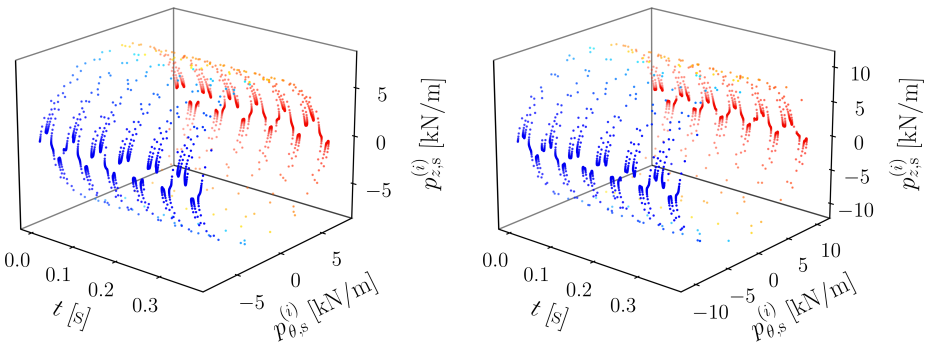

(a) GDP_1 **(b)** GDP_2

Figure 7.13: Friction force trajectories at $z_i = 3.0$ m and $u_R = 7.5$ m; the color of the markers is based on the ratio of circumferential to total friction force, i.e. ranging from -1 (blue) to 1 (red).

specifications, as well as on the soil profile at the driving location, thus special attention is needed for each pile installation and this GDP aspect requires further investigation. Finally, it is recognized that other mechanisms may be present, even though not considered herein; however, friction redirection is solely based on the mechanics of the process - thus requires no further complicating assumptions - and suffices to explain the GDP method both qualitatively and quantitatively.

From the preceding investigations, it became apparent that the bulk of friction is expended in the circumferential direction. Accordingly, the ratio of circumferential to total friction force is an interesting metric that may provide further insight into the mechanics of GDP. In Figs. 7.14 and 7.15, the aforementioned ratio is mapped along the soil depth (in contact with the pile) and during the installation time windows described above. It is apparent that high friction ratios are present along the whole interaction surface for the majority of the installation time. By comparing Figs. 7.14 and 7.15, the friction ratio appears to slightly decrease overall with penetration depth; the region with the lowest friction ratio is consistently found to be close to the pile tip. This outcome is rational (based on the CPT profile), as the soil reaction closer to the tip is the least degraded due to the small number of accumulated loading cycles (i.e. friction fatigue).

Another interesting aspect of GDP is the power redistribution that follows from the introduction of torsion. Specifically, the quantity of interest is the dissipated power due to friction along the pile-soil interface. It is apparent that in the case of axial vibratory driving, power is dissipated solely due to the friction along the vertical axis and the tip reaction. In Figs. 7.16 and 7.17, a comparison in terms of dissipated power is presented due to: (i) the vertical friction forces, (ii) circumferential friction forces and (iii) vertical tip reaction. It is remarked that for the power dissipated at the shaft, the power sum along the shaft in contact with the soil is considered. Evidently, the preponderance of dissipated power corresponds to circumferential friction, whereas vertical friction forces and tip reaction have approximately similar contributions (yet marginal overall). Conclusively, the

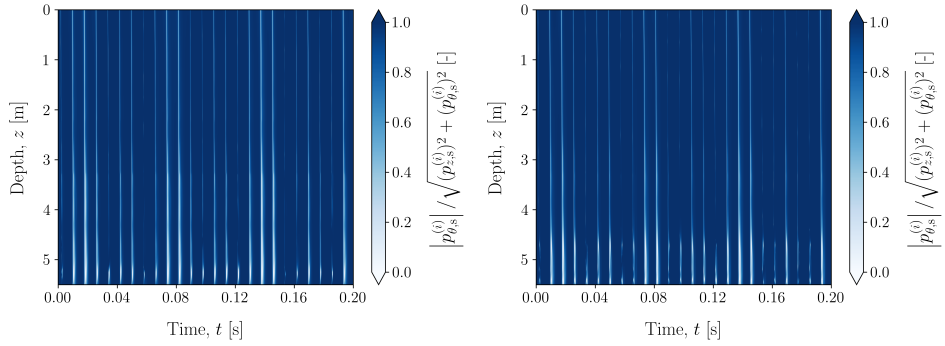

(a) GDP_1 **(b)** GDP_2

Figure 7.14: Ratio of circumferential to total friction force $\left|p_{\theta,s}^{(i)}\right| / \sqrt{(p_{z,s}^{(i)})^2 + (p_{\theta,s}^{(i)})^2}$ at $u_R = 5.5$ m.

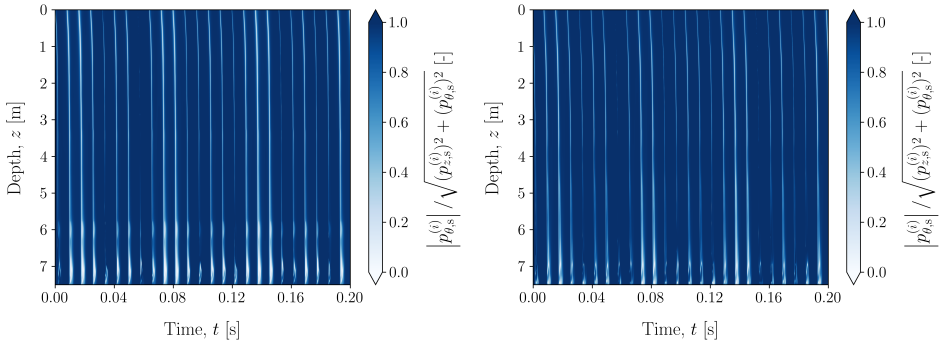

(a) GDP_1 **(b)** GDP_2

Figure 7.15: Ratio of circumferential to total friction force $\left|p_{\theta,s}^{(i)}\right| / \sqrt{(p_{z,s}^{(i)})^2 + (p_{\theta,s}^{(i)})^2}$ at $u_R = 7.5$ m.

friction redirection mechanism irrefutably benefits the installation process in terms of performance, yet it implies that the driving-induced soil motion is dissimilar from axial vibratory driving. Section 7.3.4 is focused on this aspect, i.e. the investigation of the soil response characteristics in the case of axial vibro-driving and GDP.

7.3.3. Friction amplitude reduction in GDP due to memory effects - friction fatigue

In Fig. 7.18, the distribution of friction force amplitude $f_{s,ult}^{(i)}$ along depth z is shown for both GDP piles at different driving instances, i.e. every 0.5 m of pile penetration. As stated in Section 7.1.3, the number of loading cycles experienced at a soil material point is the direct sum of cycles due to vertical and circumferential friction forces. Therefore, no differentiation exists between the contribution of the two components in the memory mechanism. A rational modification would be to differentiate the value of c_N for vertical

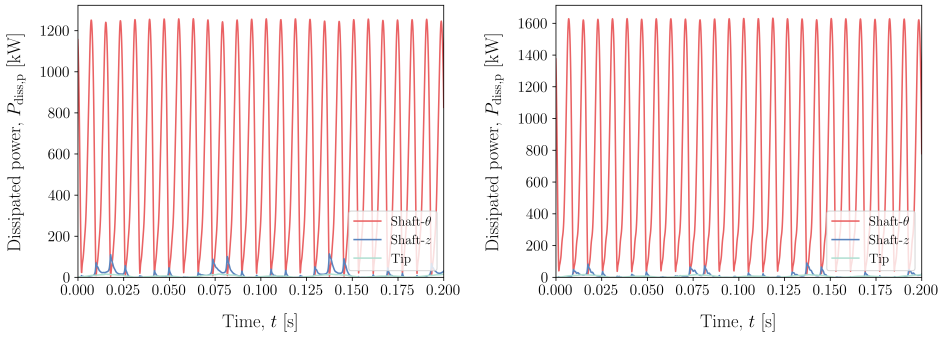

(a) GDP$_1$ **(b)** GDP$_2$

Figure 7.16: Comparison of power dissipated by (i) circumferential shaft reaction, (ii) vertical shaft reaction and (iii) tip reaction at $u_{\mathrm{R}} = 5.5$ m.

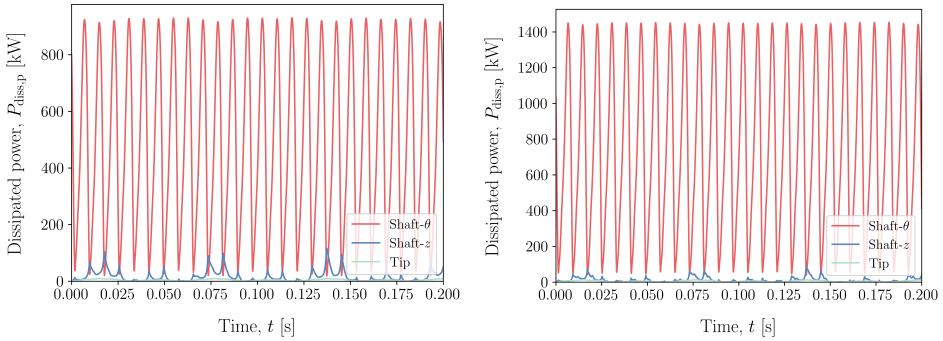

(a) GDP$_1$ **(b)** GDP$_2$

Figure 7.17: Comparison of power dissipated by (i) circumferential shaft reaction, (ii) vertical shaft reaction and (iii) tip reaction at $u_{\mathrm{R}} = 7.5$ m.

and circumferential loading cycles, as their contribution to friction reduction cannot be claimed *a priori* to be equivalent. Presumably, the different type and magnitude of induced stresses in the soil medium at different frequencies support the view that dissimilar values of degradation rate parameter c_N may be adopted for vertical and circumferential friction. However, this approach is practically hindered in this study, given the lack of an extensive data set that may facilitate that distinction. The preceding considerations may be supported by the fact that the degradation rate for GDP was $c_N = 0.0003$ (optimal prediction), whereas the corresponding value in axial vibratory driving was $c_N = 0.0004$ (optimal prediction), i.e. a smaller value was found in GDP due to the lumping of vertical and circumferential loading cycles. Naturally, a more thorough investigation along with additional experimental data is necessary to better understand this mechanism and implement it in the numerical model for GDP.

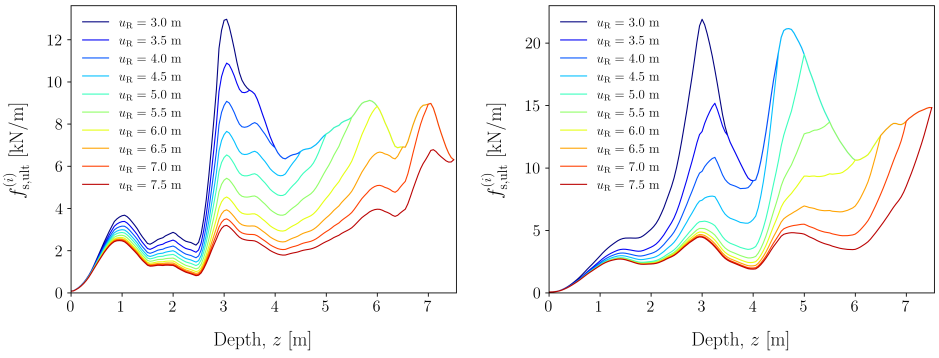

(a) GDP_1 **(b)** GDP_2

Figure 7.18: Friction amplitude distribution along soil depth z for different embedment depths (per 0.5 m), showcasing the memory effect leading to shaft friction reduction.

7.3.4. A comparison of induced ground motion between axial vibratory and GDP methods

In this section, a case study is carried out, focusing on the comparison between the axial vibratory and the GDP methods in terms of the induced ground motion. To facilitate this comparison, the respective benchmarked models are employed to analyse installation cases of piles identical to the GDP piles. To eliminate the influence of dissimilar soil conditions, installations of vibro-driven piles are considered at the locations of the GDP piles, i.e. GDP_1 and GDP_2; hereafter vibro-driven piles in the locations GDP_1 and GDP_2 will be denoted as VH_1 and VH_2, respectively. The installation settings from the GDP field tests are used as a benchmark for GDP_1 and GDP_2, whereas for VH_1 and VH_2 adjustments to the original VH settings are made for comparison purposes. In particular, the driving frequency is considered constant at 24.8 Hz (similar to VH pile), whereas the vibratory device mass is taken equal to the mass of the GDP shaker to erase the bias of increased static load in the GDP cases.

To assess whether the introduction of torsion in GDP enhances certain aspects of the pile installation process (apart from the installation performance), we focus on the induced disturbance in the vicinity of the pile. Specifically, a trial-and-error process is performed with the aim of achieving a fairly similar penetration profile between VH and GDP piles. In the aforementioned process, the dynamic input load of the vibratory device results from adjustment during the installation in order to meet the required penetration of the GDP piles. As shown in Fig. 7.19, the trial-and-error process led to satisfactory penetration profiles for VH_1 and VH_2, so we can proceed to the comparison of the induced soil disturbance between the two methods.

In Fig. 7.20a, the amplitudes of the dynamic input loads of piles VH_1 and VH_2 - required to achieve the penetration profiles in Fig. 7.19 - are shown as functions of the penetration depth. The corresponding amplitudes for GDP_1 and GDP_2 as extracted by the FBG strain measurements are presented in Fig. 7.20b for completeness. It already becomes apparent that the introduction of torsion leads to a substantially lower vertical load compared to axial vibratory driving (even one order of magnitude lower). This observation already confirms

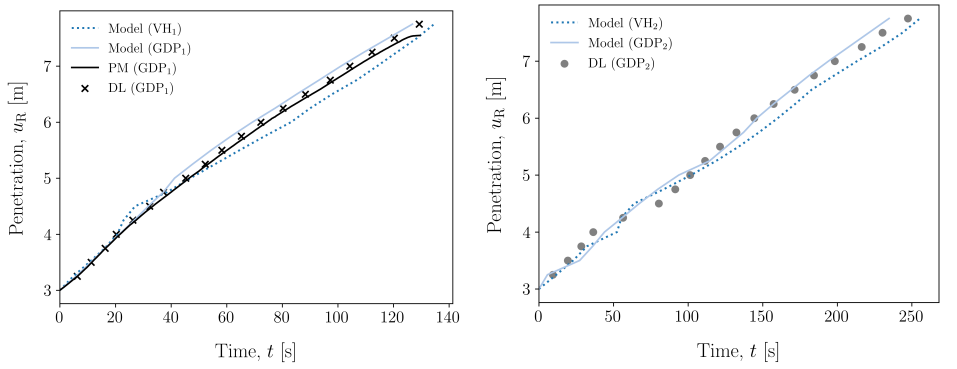

(a) GDP_1 location **(b)** GDP_2 location

Figure 7.19: Comparison of pile penetration predictions from vibratory and GDP models for the GDP_1 and GDP_2 locations; the data recorded by the potentiometer (PM) and the vibratory device logging system (DL) are also shown.

one of the main hypothesis of the GDP method, i.e. the reduction of the vertical driving loads due to the introduction of torsion. Furthermore, the merit of increasing the driving frequency is also evident, as it leads to a higher penetration rate - based on the results presented in Sec. 6.4.4 for constant amplitude - and increased amplitude of dynamic input load; thus increase of driving frequency leads to higher installation performance in essentially two manners. In the following case study, the driving frequency from the VH pile is retained, as it is fairly similar to the commonly used driving frequency of 23 Hz. It is remarked that the significant increase of the input load in Fig. 7.20a after the depth of 4.5 m is due to pile penetration into water-saturated layers, which are characterized by high (linear part of) tip reaction. In particular, for VH_2 this transition also coincides with encountering the stiffest layers of the respective soil profile (approximately at 5 m depth) leading to a substantial input load necessary to match the penetration profile of pile GDP_2 (see Fig. 7.4).

For all the subsequent comparisons, the time windows employed are common with the ones from the previous results (i.e. $u_R = 5.5$ m and $u_R = 7.5$ m). The intensity of ground motion in the immediate vicinity of construction activities (e.g. pile driving) is customarily assessed by means of the peak particle velocity (PPV) [349, 308, 350]. In the ensuing, the so-called true vector sum (TVS) form of PPV is employed [349]. The first and most pivotal comparison of the induced ground motion between the two methods in terms of PPVs at the ground surface is presented in Figs. 7.21 and 7.22. It becomes apparent that GDP leads to substantially reduced PPVs for both penetration depths studied and for any receiver radius (shown up to $r \approx 25D_p$). In particular, the two methods present almost one order of magnitude difference in PPV values, while the soil response is found to be larger at $u_R = 5.5$ m for vibratory driving. The latter is better understood in view of the penetration into water-saturated layers - tip reaction increased significantly leading to high load amplitude (see Fig. 7.20a) - and the high shaft reaction due to the encounter of stiff soil layers (see Figs. 7.4 and 7.18). It is noted that this quantitative disparity between the resulting ground

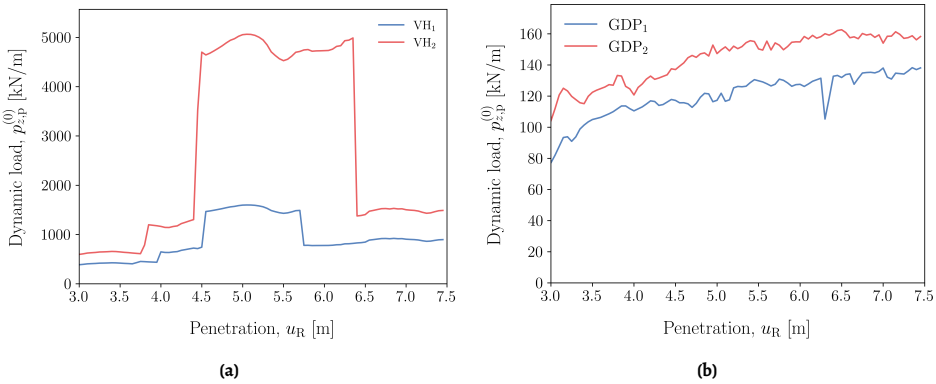

Figure 7.20: Amplitude of the dynamic axial line load at the pile top for (a) the piles VH_1 and VH_2 and (b) the piles GDP_1 and GDP_2.

motions corresponds to significantly different vibration perception levels. In particular, the reported PPVs for GDP pertain to the levels of disturbing up to slightly perceptible (with increasing receiver distance), whereas ground motion from vibratory driving ranges from very disturbing to disturbing throughout the examined region [349].

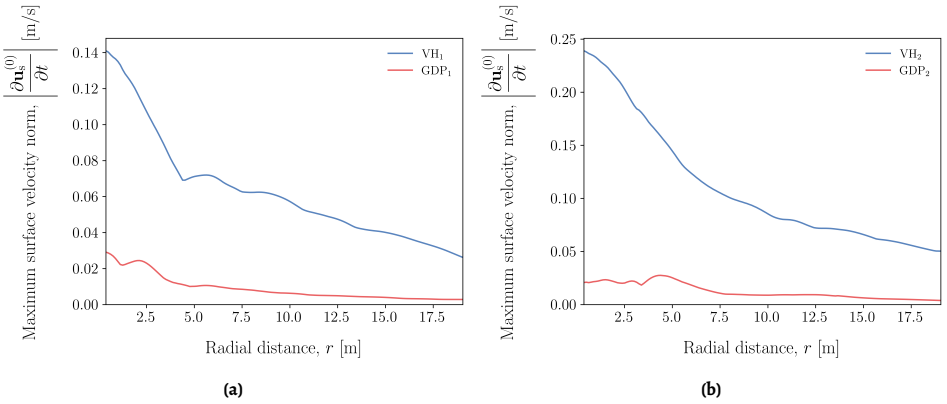

Figure 7.21: PPV at the ground surface for $u_\mathrm{R} = 5.5$ m.

It is evident that the application of GDP in onshore construction projects appears promising, even though the initial motivation of the method has been the installation of monopile foundations for offshore wind turbines. In the case of the latter, the induced SV-P wavefield ($\mathbf{u}_{r,\mathrm{s}}$, $\mathbf{u}_{z,\mathrm{s}}$) - as well as the axial-radial pile motion - are of utmost interest, since they are directly related to the generation of underwater noise. In view of this remark, we proceed to analyse the PPV profiles shown in Figs. 7.21 and 7.22 in terms of the individual components. In Figs. 7.23 and 7.24, the maxima of the surface velocity norms for vertical, radial and circumferential components are shown for the GDP piles. As can be seen, for GDP_1 the circumferential velocity is either larger or equal to the vertical one close to the pile and with

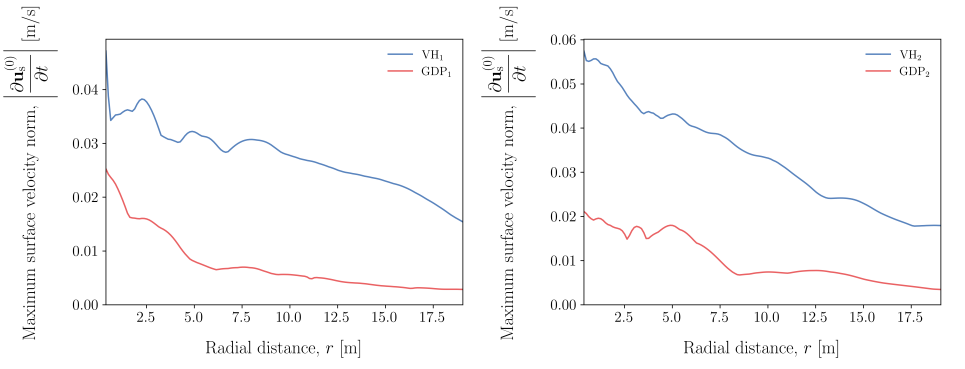

Figure 7.22: PPV at the ground surface for $u_R = 7.5$ m.

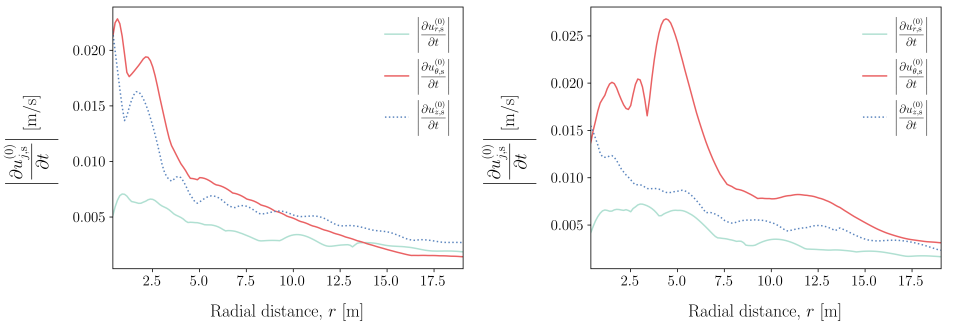

Figure 7.23: PPV at the ground surface per component (r, θ, z) for $u_R = 5.5$ m.

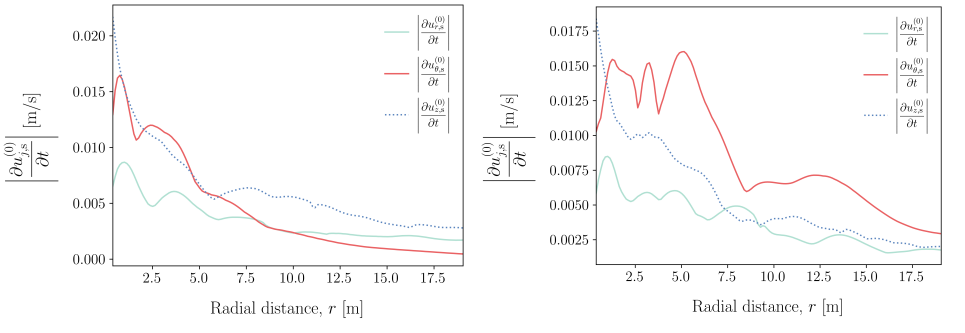

Figure 7.24: PPV at the ground surface per component (r, θ, z) for $u_R = 7.5$ m.

increasing receiver distance drops to even lower levels than the radial component. On the other hand, for GDP_2 the circumferential component is clearly dominant close to the pile and attenuates rapidly with radius, approaching the vertical and radial velocities. In both cases, the reduced ground motion observed for GDP in Figs. 7.21 and 7.22 is characterized by a torsion-induced SH wavefield of either higher or similar intensity with the SV-P wavefield throughout the examined region.

The results shown in Figs. 7.21 to 7.24 are of great significance, as they facilitate a first direct comparison between the two methods in terms of induced soil motion. Specifically, PPVs at the ground surface are pivotal disturbance metrics and of direct interest for onshore applications. To further comprehend the dissimilar response of the soil medium during pile installation, a global view of the resulting response may be of great value. For that reason, in Figs. 7.25 and 7.26 the PPV of each material point in the soil is shown as a contour in the $r-z$ plane. It is noted that the displayed contour patterns do not resemble the wavefield at any instant, as they are not snapshots of the response; they are simply a collection of the PPVs for each soil material point attained during the studied time window (sufficient for stationary response). Furthermore, the colormaps are common for vibro-driven and GDP piles, in order to facilitate the comparison of the resulting fields.

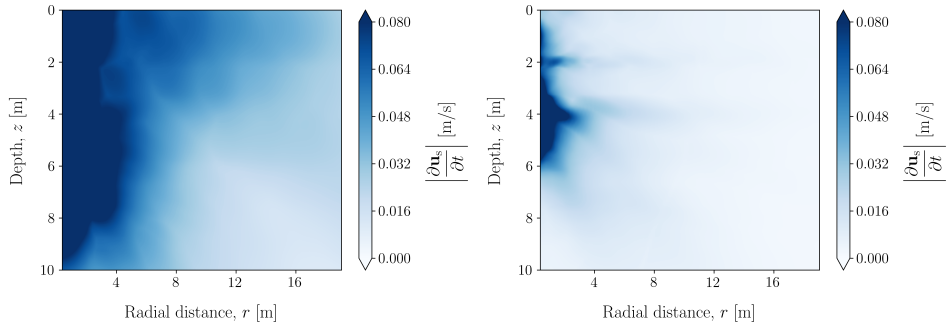

(a) VH_1 **(b)** GDP_1

Figure 7.25: PPVs (surface and interior soil domain) at GDP_1 location for $u_R = 5.5$ m.

As can be seen, the first major observation corresponds to significantly lower velocities in the interior of the soil medium for GDP compared to axial vibratory driving. Furthermore, the disturbance induced by GDP is strongly localized in the pile vicinity, which results from the high-frequency friction forces induced by torsion. The latter observation is in line with one of the main hypotheses of the GDP method, i.e. that the induced disturbance in the surrounding medium will be reduced (compared to axial vibratory driving) due to the high-frequencies that will lead to the preceding localization. It is remarked that for both methods and locations, the PPVs close to the tip present large magnitudes, as is anticipated due to the combined effect of tip reaction and least shaft reaction degradation in the tip vicinity. In general, the preceding observations (both for the surface and the interior soil domain) can be understood as the result of (i) the reduction of vertical loads and (ii) the introduction of torsion-induced circumferential loads. The former reduction led to a large decrease in the amplitude of the SV-P wavefield ($u_{r,s}$, $u_{z,s}$) (compared to vibro-driving) and particularly

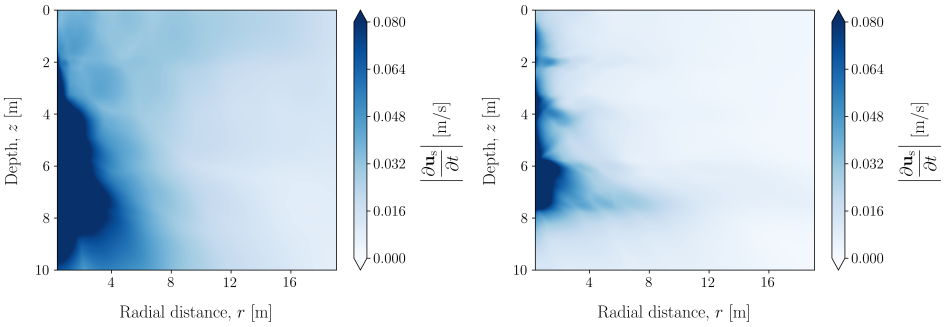

(a) VH_1 **(b)** GDP_1

Figure 7.26: PPVs (surface and interior soil domain) at GDP_1 location for $u_R = 7.5$ m.

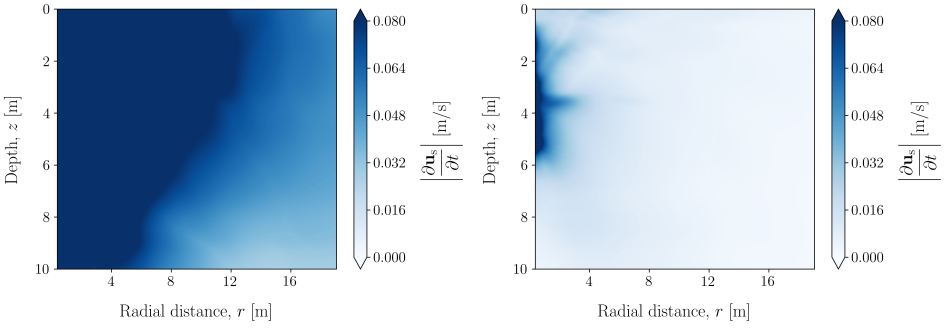

(a) VH_2 **(b)** GDP_2

Figure 7.27: PPVs (surface and interior soil domain) at GDP_2 location for $u_R = 5.5$ m.

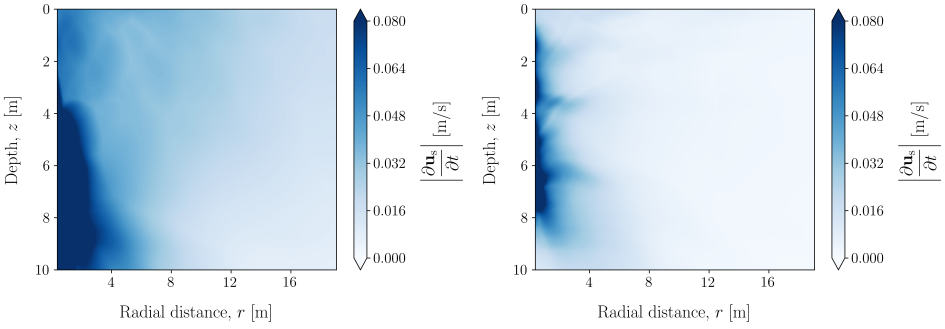

(a) VH_2 **(b)** GDP_2

Figure 7.28: PPVs (surface and interior soil domain) at GDP_2 location for $u_R = 7.5$ m.

of Rayleigh waves that dominate the surface response with increasing receiver distance. On the other hand, the introduction of torsion elicits SH waves - of appreciable magnitude -

that decay rapidly away from the pile by virtue of the high-frequencies excited, whereas Love waves are not visible presumably due to the mild stratification of the shallow soil layers.

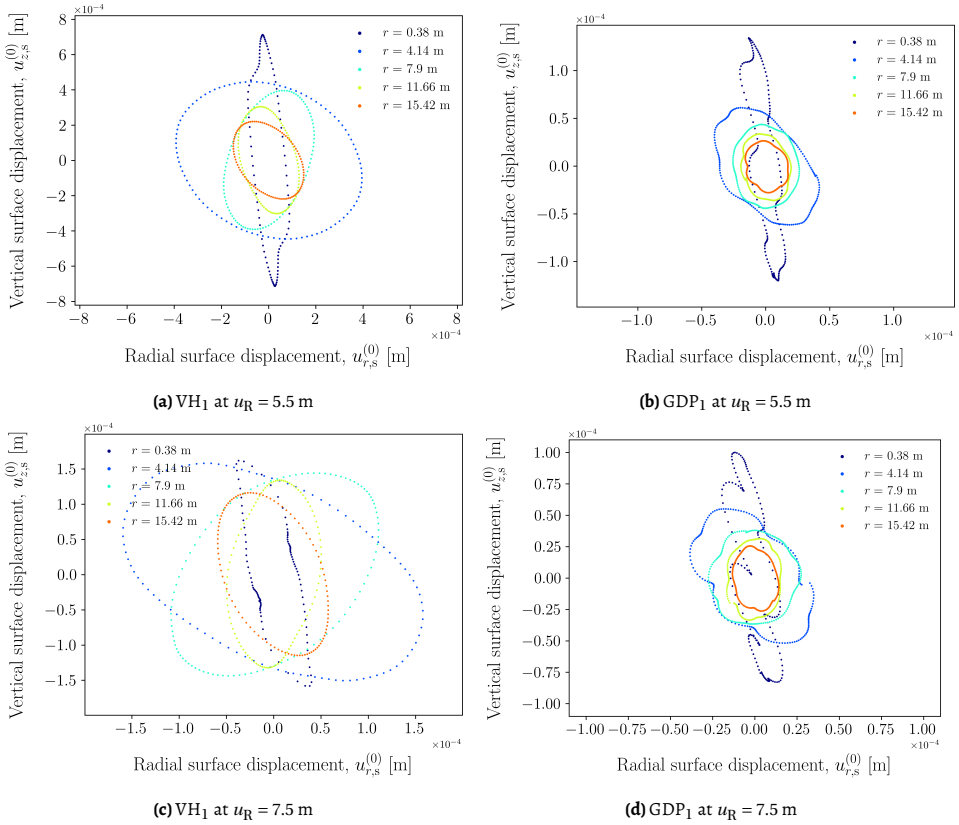

(a) VH_1 at $u_R = 5.5$ m

(b) GDP_1 at $u_R = 5.5$ m

(c) VH_1 at $u_R = 7.5$ m

(d) GDP_1 at $u_R = 7.5$ m

Figure 7.29: Trajectory of particle motion $(u_{r,s}^{(o)}, u_{z,s}^{(o)})$ at the ground surface for GDP_1 location.

To further complement the preceding considerations, we conclude the study of the driving-induced soil motion with the particle trajectories at the ground surface. In Figs. 7.29 and 7.30, the particle trajectories at the ground surface for multiple receiver radii are depicted. It is remarked that the axes are not common for VH and GDP piles, due to the large difference in magnitude. The latter has been previously discussed to a large extent and will not be repeated; yet it is interesting to assess the distinctive behavior of the two driving methods. For vibro-driven piles, the motion is predominantly vertical for small radii, whereas with increasing distance from the source the trajectories transition from vertically-polarized orbits to retrograde elliptical orbits (typical of Rayleigh waves) [218]. This observation is also the case for GDP, with the discrepancy that the frequency content is much richer for GDP as testified by the respective orbits. Naturally, these components decay quickly with radius and at larger receiver distances the characteristic trajectories of Rayleigh waves dominated by lower frequencies also emerge in GDP. It is interesting to note that the particle trajectories appear to shrink at a higher rate with radius for GDP; this stronger

decay is due to the high-frequency components present in the Rayleigh waves elicited in GDP cases. Conclusively, the ground motion results showcased that indeed GDP can lead to lower disturbance in the surrounding medium, following from the same mechanism that enhanced the installation performance, namely the torsion-induced friction redirection.

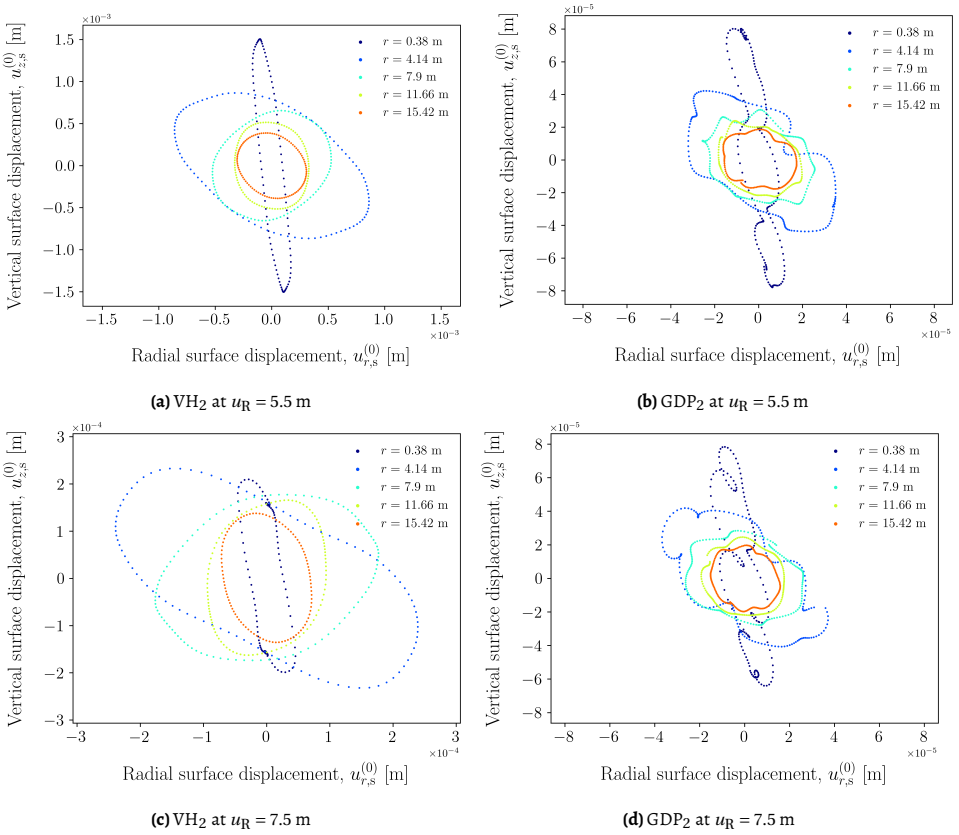

(a) VH_2 at $u_R = 5.5$ m

(b) GDP_2 at $u_R = 5.5$ m

(c) VH_2 at $u_R = 7.5$ m

(d) GDP_2 at $u_R = 7.5$ m

Figure 7.30: Trajectory of particle motion $(u_{r,s}^{(o)}, u_{z,s}^{(o)})$ at the ground surface for GDP_2 location.

7.4. Conclusions

In this chapter, a pile installation model for GDP was presented and utilized to decipher the driving mechanisms of the method, as well as to compare GDP with axial vibratory driving in terms of the induced soil motion. The GDP model is based on the numerical framework developed for vibratory driving (see Chapter 6), with main discrepancies the increase of the degrees-of-freedom (DoFs) (due to the addition of circumferential motion) and the application of the AHBM (due to the relation of driving frequencies). As regards the soil reaction, the (S)CPT-based formulation from vibratory driving was employed as an initial basis. Upon modification of the tip reaction, the adopted set of parameters led to GDP model predictions that compared favourably with field data from the GDP campaign.

Therefore, a unified modelling framework that is suitable to analyse pile installation via axial vibratory and GDP methods has been realized. Conclusively, the main observations and findings pertaining to the developments of this chapter are summarized as follows:

(i) the friction force at the pile-soil interface was predominantly expended in the circumferential direction, thus torsion was leading the driving process. This redirection of the friction force vector emerges as the main GDP driving mechanism that leads to enhanced installation performance.

(ii) the vertical friction forces possessed appreciable amplitude in super-harmonics of axial, torsional driving frequency and their combinations, leading to a vibration pattern that spread widely in the frequency spectrum.

(iii) the proper estimation of axial and torsional excitations - both in terms of amplitudes and driving frequencies - becomes highly important in GDP, since the successful application of the method relies on the realization of friction redirection.

(iv) a comparison study between axial vibratory and GDP techniques by means of the benchmarked installation models was performed with a view to assess the associated soil motion. GDP consistently led to significantly lower PPVs for all receiver depths and radii examined in this study.

(v) a reduction of SV-P waves was achieved in GDP via (i) the reduction of axial driving loads that are necessary for pile penetration and (ii) the introduction of SH waves (via friction redirection) that decay rapidly away from the pile by virtue of the high frequencies involved.

(vi) the coupling of vertical-circumferential friction forces in GDP leads to SV-P waves with a wide frequency spectrum, accompanied by fast attenuation of these high-frequency components and thus large amplitude reduction with increasing distance from the pile even for the SV-P wavefield.

(vii) GDP did not solely reduce the amplitude of the wavefield overall, but also localized the high-amplitude soil motion in the pile vicinity.

8

Conclusions and recommendations

Offshore wind demand soars at a remarkable pace in recent years, continuously posing technical challenges on various fronts. Engineering advancement and innovation are vital to tackle these challenges and accommodate the rapid growth of the offshore wind sector. The foundation installation for offshore wind turbines constitutes one of the most crucial, challenging and costly operations during the construction of an offshore wind farm. At present, monopiles comprise the vast majority of offshore wind foundations and the foremost monopile installation method is impact hammering. However, this technique has raised alarming environmental concerns, leading to intensified investigation and development of sustainable methods for monopile installation. In this thesis, a numerical modelling framework for pile installation is presented, that encompasses the mathematical formulation, the parameter calibration based on in-situ measurements and the implementation of a performant numerical scheme for engineering purposes. The present methodology focuses on two propitious and environmentally friendly installation methods, namely the axial vibratory driving and the Gentle Driving of Piles (GDP).

8.1. Conclusions

As a point of departure, the vibrations of thin-walled cylindrical structures are studied in Chapter 2, with a view to tubular (mono)piles. For that purpose, thin shell theory is presented as the optimal modelling option in terms of physical soundness and computational efficiency. The propagation of harmonic waves and the free vibrations of thin cylindrical shells are both treated briefly, focusing on the dynamic behaviour of such cylindrical waveguides. To facilitate the integration of shell theories in numerical frameworks, a Semi-analytical Finite Element (SAFE) model is developed and validated. The contribution of the preceding framework can be readily realized via its direct incorporation into existing 1-D Finite Element (FE) approaches by mere substitution of tabulated FE matrices.

For drivability purposes, the pile is commonly treated either as a 1-D thin rod or as a rigid body (mostly in vibratory driving). The preceding choices may be invalidated, depending on the pile geometry and the excitation spectrum. Furthermore, pile-soil interaction is

customarily taken into account via local and frequency-independent analogues, mainly due to simplicity and ease of numerical implementation. To investigate the effects of elastic wave dispersion and non-local soil reaction, a case study focusing on impact piling is presented in Chapter 3. Specifically, a standard 1-D impact piling model is compared against its 3-D axisymmetric counterpart, i.e. modified to treat the pile as a thin cylindrical shell under axisymmetric conditions and to include spatially non-local soil reaction.

The significance of elastic wave dispersion in drivability was ascertained for all pile geometries, albeit its effect was amplified with increasing pile diameter. This occurrence is associated with the excitation of motions in the vicinity of the shell ring frequency and is characterized by predominantly radial displacement components. It is remarked that wave dispersion is intrinsic to the dynamic response of monopiles and its oversight may be falsely attributed to other mechanisms, e.g. soil non-linear behaviour. As regards the soil reaction, a flexible approach was employed to generate a spatially non-local model by means of convolving its local counterpart with a spatial kernel (e.g. Gaussian function). However, the previous treatment introduces additional complexity, as a calibration process is necessary in order to reproduce the spatial behaviour of the 3-D soil continuum. Furthermore, non-locality in space and time is coupled in a continuum via its dispersion relation, thus the overall undertaking becomes rather arduous.

To overcome these limitations, the problem of the 3-D soil continuum is addressed directly, towards a rigorous non-local approach (in space and time). Chapter 4 treats the propagation of mechanical waves in a vertically inhomogeneous solid, comprised by arbitrarily thick homogeneous horizontal layers of dissimilar material properties. For drivability analysis purposes, numerical modelling of arbitrarily layered soil media is indispensable. To that end, a semi-discrete approach is employed to analyze layered media in a versatile manner, namely the Thin-Layer Method (TLM). The formulation of the TLM is first outlined, followed by the derivation of the generalized eigenvalue problem of cylindrical waves and the respective normal modes. Furthermore, the incorporation of Perfectly Matched Layers (PMLs) into the TLM is addressed via complex-valued stretching of the vertical coordinate, leading to a superbly efficient approach for half-space approximation in the context of the TLM. By means of these numerical developments, we proceed to derive explicit matrix expressions for the Green's functions in the frequency-space domain based on normal modes. The preceding formulation is valid both in the original, i.e. soil layers resting on rigid bedrock, and in the PMLs-augmented TLM cases. Finally, a set of numerical examples is presented to validate the numerical framework, implemented in the ensuing pile-soil interaction models.

In Chapter 5, the Gentle Driving of Piles (GDP) is presented as a propitious technology, motivated by the growing demand for sustainable methods of offshore monopile installation. Specifically, the proposed technique is characterized by the simultaneous application of low-frequency axial and high-frequency torsional vibrations, aiming to enhance both installation and vibro-acoustic performances. To achieve a first demonstration of this method, a GDP shaker was built and a medium-scale field campaign was executed at the Maasvlakte II site in Rotterdam. Next to the proof of concept, a primary objective of the field tests was the comparison of GDP with two conventional techniques, namely impact hammering and axial vibratory driving. The successful proof of concept accommodated a multitude of objectives encompassed in the research line of GDP, focused on installation and post-installation

performances.

The main highlight of the experimental campaign was the successful installation of two instrumented GDP piles (GDP_1 and GDP_2). These installation tests showcased the remarkable potential of GDP, as it led to a higher penetration rate compared to axial vibro-driving (VH) even though the former piles were installed in significantly stiffer soil. It is noted that the energy consumption between VH and GDP_1 was comparable, suggesting that GDP can also be advantageous in terms of energy efficiency. However, the required power was appreciably higher for GDP - as an outcome of the high-frequency torsion - pointing towards amplitude-frequency decoupling as further advancement of the GDP shaker design. The time-frequency analyses of the pile response revealed that installation is a quasi-periodic process, characterized by slow amplitude modulation of the involved harmonic components. As regards the soil response, excess pore water pressures were measured in the pile vicinity and rapidly dissipated in the permeable soil at hand, accompanied by relaxation of total radial stresses. Furthermore, *in-situ* Cross-hole Sonic Logging (CSL) tests recorded an overall increase in the P-wave velocity profile in the soil medium, which may be linked with increased soil stiffness due to the installation-induced densification. In summary, the described field campaign provided a preliminarily demonstration of the GDP technology, showcasing its potential in terms of both installation and post-installation performances. Towards future development, further experimental studies and quantitative tools are indispensable both for axial vibratory driving and GDP.

By integrating the numerical developments of the preceding chapters, a computationally efficient model for vibratory pile installation is presented in Chapter 6. This numerical framework aims to bridge the gap between medium- and high-fidelity approaches, by alleviating the physical drawbacks of the former, while overcoming the practical limitations of the latter. Specifically, the SAFE cylindrical shell model (Chapter 2) is coupled to a layered soil half-space modelled via the TLM+PMLs (Chapter 4). The non-linear pile-soil coupling is realized through a history-dependent frictional interface and a visco-elasto-plastic tip reaction model, both characterized on the basis of (S)CPT measurements. To retain computational efficiency, a performant scheme based on the sequential application of the Alternating Frequency-Time (AFT) Harmonic Balance Method (HBM) is developed, by postulating that the system response is virtually periodic 'microscopically'. Therefore, the total response is obtained by transitioning between the computed non-linear states via linear interpolation in the time-frequency plane. As a result, a quasi-periodic response is formed due to slow amplitude modulation of the involved harmonics. The present method is applicable to a broad class of non-linear dynamical systems that possess quasi-periodicity of this type. Finally, model predictions are compared with field data from the GDP campaign, showcasing the prediction potential of the vibratory driving model.

On the basis of the previous model, further aspects of vibratory pile installation have been investigated. The identification of the shaft reaction as the main soil reaction mechanism constitutes one of the major findings of this chapter. It is noted that this result strongly depends on the test scale, yet it is anticipated that this trend will be further reinforced for offshore monopiles. A memory mechanism is proposed and implemented to capture the occurrence of shaft friction reduction during driving - commonly termed as friction fatigue - based on the accumulation of loading cycles at each soil material point. Friction fatigue is vastly reported and highly relevant for impact piling, jacking and static axial capacity of

piles. However, the normalized distance of a soil point from the pile tip is mainly considered as the control variable of friction fatigue in the previous cases. In this study, the cyclic and distance-based memory mechanisms have been compared with the field data, leading to accurate predictions for the former, whereas the latter is found inadequate in both qualitative and quantitative terms. Conclusively, a numerical investigation is presented pertaining to the effect of driving frequency on penetration rate, that indicates a monotonically increasing relationship between the two variables. Field tests that focus on such effects are vital to identify what may constitute the optimal driving frequency in terms of installation and post-installation performances.

In Chapter 7, the previous modelling framework is utilized and expanded further, with a view to analyse pile installation via GDP. The circumferential motion is introduced into both pile and soil components, while the frictional interface is retained in view of the inherent physical similarity between the two methods (i.e. axial vibro-driving and GDP). From a computational perspective, the basis of the HB-based scheme (Chapter 6) is modified to utilize the adjusted HBM (AHBM), i.e. an approximate scheme to treat a problem with two different driving (base) frequencies. As regards the soil reaction parameters, the original SCPT-based formulation is employed as the initial basis, leading to favourable comparison of model predictions with field data. The mechanics of the GDP method are deciphered and the advantageous effect of torsion in pile installation is showcased. In particular, the redirection of the friction force vector emerges as the major driving mechanism of GDP. To elaborate further, shaft friction is predominantly expended in the circumferential direction and is greatly reduced along the penetration axis, hence enhancing the installation performance. The dynamic pile response indicates that axial-radial and circumferential motions are coupled through friction (and potentially through the excitation) leading to a vibration pattern with wide spread in the frequency spectrum. As a consequence of the previous findings, the reliable selection of installation settings - both in terms of amplitudes and driving frequencies - is of utmost significance for GDP, as the successful application of the method relies on the realization of friction redirection.

The study of the GDP method is concluded with a comparison between axial vibratory driving and GDP, on the basis of the respective benchmarked numerical models. A trial and error process (in terms of input) was performed to reproduce axial vibro-driving cases with identical penetration profiles to the GDP piles in common soil locations. In that manner, the associated soil motion by the two techniques can be assessed on a fair basis. The numerical results indicate that GDP leads to consistently lower peak particle velocities (PPVs) both on the surface and the interior soil domain for all receiver depths and radii. Furthermore, an overall reduction of the SV-P wavefield (compared to axial vibro-driving) is achieved in GDP due to (i) decrease of required axial loads for pile penetration and (ii) elicitation of SH waves by torsion-induced circumferential friction, which decay rapidly with distance due to their high-frequency content. It is noted that the reduced SV-P wavefield in GDP also attenuates rapidly with distance, as the frictional coupling redistributes energy to higher frequencies and results in a localized region of high-amplitude soil motion in the pile vicinity. Evidently, GDP is found to be an advantageous installation technology in terms of installation performance and induced environmental disturbance, based on the numerical studies performed in Chapter 7.

8.2. Recommendations for future research

In view of the findings presented in this thesis, a set of recommendations is outlined herein, pertaining to numerical modelling and engineering aspects of pile driving via vibratory and GDP methods. Focusing on the former objective, the ensuing proposals have broader applicability beyond the scope of pile driving and their potential in various engineering problems should be realized. Particularly, the SAFE approach introduced in Chapter 2 may be applied to shells of revolution (e.g. conical and spherical shells), thus enabling the study of various structural configurations - e.g. assemblage of conical, cylindrical and spherical segments – in a versatile and efficient manner. This potential development holds significant promise beyond pile driving, as it relates to the broader topic of shell vibrations. Furthermore, as was highlighted in Chapter 6, the extension of the classical HBM to a Petrov-Galerkin scheme would greatly benefit the study of non-linear systems characterized by bounded response continuity. It is deemed that such an advancement will be timely, as ongoing research works are attempting to utilize the HBM in large-scale dynamical systems; this synergy would be a major milestone in the study of periodic and quasi-periodic systems. Finally, the presented numerical framework can be extended by incorporating the Green's functions of an acousto-elastic layered half-space, thus encompassing the presence of seawater fluid. As a result, a coupled approach may be formulated, which would enable the simultaneous prediction of pile drivability and underwater noise emissions during pile installation via vibratory and GDP methods.

With a view to monopile installation, extensive research works are currently ongoing, focusing on diverse engineering aspects. Towards future development, it is essential to undertake comprehensive field campaigns that encompass the major installation aspects, namely drivability, underwater acoustics and response to lateral loading. Adopting a holistic approach is crucial, as progress in these topics independently may not necessarily yield the most effective outcomes. Through such research endeavours, the numerical findings presented in this thesis can be validated through field experiments, reinforcing important observations such as the positive influence of driving frequency on penetration rate - without necessitating higher vibratory amplitudes - as well as the abatement of environmental disturbance induced by GDP compared to axial vibro-driving. Furthermore, experimental validation of relevant findings will contribute significantly towards the formulation of a multi-objective framework for optimizing driving settings in both axial vibratory and GDP techniques. Specifically, for GDP, the field observations of the GDP campaign, combined with the numerical results from this thesis, suggest the potential for further advancements in GDP technology through amplitude-frequency decoupling. Finally, it is worth noting that both axial vibro-driving and GDP methods will encounter unprecedented challenges from a dynamics perspective, as sub- and super-harmonic resonances may come into play in the installation of large-diameter monopiles.

Conclusively, this thesis has presented a unified modelling framework for the analysis of pile installation via axial vibratory driving and GDP. The role of pile installation cannot be overemphasized in offshore wind farm construction, as the installation process itself has also major effects on vibro-acoustic and post-installation behaviours. Therefore, the present framework significantly advances the state of engineering-oriented approaches for drivability prediction and simultaneously initiates a new path towards foundation design, that enables the integration of the previous installation aspects. With a view to vibratory

monopile installation, the non-linear dynamics of the driving process are deemed focal in the forthcoming challenges. As regards GDP, its potential lies in breaking away from the simplicity of the single-variable setting that is common in standard vibro-driving. The versatility of multiple installation parameters, accompanied by the benefits of high-frequency torsion, engenders complexity and harnessing the latter is key to GDP future development.

Bibliography

[1] United Nations. Report of the United Nations Conference on Environment and Development. Technical report, New York, USA, 1993.

[2] United Nations. United Nations Framework Convention on Climate Change. https://unfccc.int/resource/docs/convkp/conveng.pdf, 1992.

[3] United Nations. Kyoto Protocol to the United Nations Framework Convention on Climate Change. https://unfccc.int/sites/default/files/resource/docs/cop3/l07a01.pdf, 1997.

[4] United Nations. Paris Agreement. https://unfccc.int/sites/default/files/english_paris_agreement.pdf, 2015.

[5] United Nations. Transforming our World: The 2030 Agenda for Sustainable Development. https://sdgs.un.org/sites/default/files/publications/21252030%20Agenda%20for%20Sustainable%20Development%20web.pdf, 2015.

[6] E. De Cian and I. Sue Wing. Global energy consumption in a warming climate. *Environmental and resource economics*, 72(2):365–410, 2019.

[7] E. Papadis and G. Tsatsaronis. Challenges in the decarbonization of the energy sector. *Energy*, 205:118025, 2020.

[8] International Energy Agency. World Energy Outlook 2021. Technical report, Paris, France, 2021.

[9] D. Gielen, F. Boshell, D. Saygin, M. D. Bazilian, N. Wagner, and R. Gorini. The role of renewable energy in the global energy transformation. *Energy Strategy Reviews*, 24:38–50, 2019.

[10] T. Ahmad and D. Zhang. A critical review of comparative global historical energy consumption and future demand: The story told so far. *Energy Reports*, 6:1973–1991, 2020.

[11] European Commission. European Green Deal. https://ec.europa.eu/info/strategy/priorities-2019-2024/european-green-deal_en, 2019.

[12] M. Fay, S. Hallegatte, A. Vogt-Schilb, J. Rozenberg, U. Narloch, and T. Kerr. *Decarbonizing development: Three steps to a zero-carbon future*. World Bank Publications, 2015.

[13] J. Rockström, O. Gaffney, J. Rogelj, M. Meinshausen, N. Nakicenovic, and H. J. Schellnhuber. A roadmap for rapid decarbonization. *Science*, 355(6331):1269–1271, 2017.

[14] S. Bilgen. Structure and environmental impact of global energy consumption. *Renewable and Sustainable Energy Reviews*, 38:890–902, 2014.

[15] R. Poudineh, C. Brown, and B. Foley. *Economics of Offshore Wind Power: Challenges and Policy Considerations*. Springer, 2017.

[16] P. Sadorsky. Wind energy for sustainable development: Driving factors and future outlook. *Journal of Cleaner Production*, 289:125779, 2021.

[17] F. Olsen and K. Dyre. Vindeby off-shore wind farm - construction and operation. *Wind Engineering*, pages 120–128, 1993.

[18] K. Sunday and F. Brennan. A review of offshore wind monopiles structural design achievements and challenges. *Ocean Engineering*, 235:109409, 2021.

[19] M. Bilgili, A. Yasar, and E. Simsek. Offshore wind power development in europe and its comparison with onshore counterpart. *Renewable and Sustainable Energy Reviews*, 15(2):905–915, 2011.

[20] J. K. Kaldellis, D. Apostolou, M. Kapsali, and E. Kondili. Environmental and social footprint of offshore wind energy. comparison with onshore counterpart. *Renewable Energy*, 92:543–556, 2016.

[21] International Energy Agency. World Energy Outlook 2016. Technical report, Paris, France, 2016.

[22] International Energy Agency. World Energy Outlook 2019. Technical report, Paris, France, 2019.

[23] A. Smith, T. Stehly, and W. Musial. 2014-2015 Offshore wind technologies market report. Technical report, National Renewable Energy Lab.(NREL), Golden, CO (United States), 2015.

[24] T. J. Stehly and P. C. Beiter. 2018 cost of wind energy review. Technical report, National Renewable Energy Lab.(NREL), Golden, CO (United States), 2020.

[25] L. Ramírez, D. Fraile, and G. Brindley. Offshore wind in europe: Key trends and statistics 2019. Technical report, WindEurope, Brussels, Belgium, 2020.

[26] L. Ramírez, D. Fraile, and G. Brindley. Offshore wind in europe: Key trends and statistics 2020. *WindEurope*, 2021.

[27] D. Kallehave, B. W. Byrne, C. LeBlanc Thilsted, and K. K. Mikkelsen. Optimization of monopiles for offshore wind turbines. *Philosophical Transactions of the Royal Society A: Mathematical, Physical and Engineering Sciences*, 373(2035):20140100, 2015.

[28] M. Asgarpour. Assembly, transportation, installation and commissioning of offshore wind farms. In *Offshore Wind Farms*, pages 527–541. Elsevier, 2016.

[29] M. Bilgili, H. Alphan, and A. Ilhan. Potential visibility, growth, and technological innovation in offshore wind turbines installed in europe. *Environmental Science and Pollution Research*, pages 1–19, 2022.

[30] B. C. Gerwick Jr. *Construction of marine and offshore structures*. CRC press, 2007.

[31] Z. Jiang. Installation of offshore wind turbines: A technical review. *Renewable and Sustainable Energy Reviews*, 139:110576, 2021.

[32] P. G. Reinhall and P. H. Dahl. Underwater Mach wave radiation from impact pile driving: Theory and observation. *The Journal of the Acoustical Society of America*, 130(3):1209–1216, 2011.

[33] G. Hastie, N. D. Merchant, T. Götz, D. J. Russell, P. Thompson, and V. M. Janik. Effects of impulsive noise on marine mammals: investigating range-dependent risk. *Ecological Applications*, 29(5):e01906, 2019.

[34] M. A. Ainslie, M. B. Halvorsen, R. A. Müller, and T. Lippert. Application of damped cylindrical spreading to assess range to injury threshold for fishes from impact pile driving. *The Journal of the Acoustical Society of America*, 148(1):108–121, 2020.

[35] A. Tsouvalas. Underwater noise emission due to offshore pile installation: A review. *Energies*, 13(12):3037, 2020.

[36] A. Tsouvalas and A. Metrikine. Noise reduction by the application of an air-bubble curtain in offshore pile driving. *Journal of Sound and Vibration*, 371:150–170, 2016.

[37] B. Würsig, C. Greene Jr, and T. Jefferson. Development of an air bubble curtain to reduce underwater noise of percussive piling. *Marine environmental research*, 49(1):79–93, 2000.

[38] Y. Peng, A. Tsouvalas, T. Stampoultzoglou, and A. Metrikine. Study of the sound escape with the use of an air bubble curtain in offshore pile driving. *Journal of Marine Science and Engineering*, 9(2):232, 2021.

[39] H. Jansen, C. de Jong, and B. Jung. Experimental assessment of the insertion loss of an underwater noise mitigation screen for marine pile driving. In *Proceedings of the 11th European Conference on Underwater Acoustics, Edinburgh, UK, 2–6 July 2012*, 2012.

[40] Y. Peng, A. Tsouvalas, A. Metrikine, and E. Belderbos. Modelling and development of a resonator-based noise mitigation system for offshore pile driving. In *Proceedings of the 25th International Congress on Sound and Vibration*, 2018.

[41] N. D. Merchant. Underwater noise abatement: economic factors and policy options. *Environmental Science & Policy*, 92:116–123, 2019.

[42] I. Anusic, G. R. Eiksund, S. Meissl, and M. A. Liingaard. Study of a new installation technique for large diameter monopiles. In *Proceedings of the 19th International Conference on Soil Mechanics and Geotechnical Engineering*, pages 2261–2264, 2017.

[43] W. Dirks, J. Kappen, R. Scheltens, J. Winkes, and M. Wochner. Sustainable offshore wind energy: Faster and larger at lower cost and less environmental impact. In *Offshore Technology Conference*. OnePetro, 2018.

[44] A. Rodger and G. Littlejohn. A study of vibratory driving in granular soils. *Géotechnique*, 30(3):269–293, 1980.

[45] D. Barkan. Developments in soil dynamics. In *Proceedings International Symposium on Wave Propagation and Dynamic Properties of Earth Materials, Albuquerque, New Mexico*. University of New Mexico Press, 1967.

[46] R. L. Mosher. Comparison of axial capacity of vibratory-driven piles to impact-driven piles. Technical report, Engineer Research and Development Center (ERDC), 1987.

[47] N. Mazza and A. Holeyman. Frequency-penetration response spectrum on vibratory amplitude matching of monopiles. In *10th International Conference on Stress Wave Theory and Testing Methods for Deep Foundations*. ASTM International, 2019.

[48] M. Achmus, K. A. Schmoor, V. Herwig, and B. Matlock. Lateral bearing behaviour of vibro-and impact-driven large-diameter piles in dense sand. *geotechnik*, 43(3):147–159, 2020.

[49] A. V. Metrikine, A. Tsouvalas, M. L. A. Segeren, A. S. K. Elkadi, F. S. Tehrani, S. S. Gómez, R. Atkinson, F. Pisanò, E. Kementzetzidis, A. Tsetas, T. Molenkamp, K. van Beek, and P. de Vries. Gdp: A new technology for gentle driving of (mono)piles. In *Proceedings of the 4th International Symposium on Frontiers in Offshore Geotechnics, Austin, TX, USA, 16–19 August 2020*, 2020.

[50] A. Tsetas, S. S. Gómez, A. Tsouvalas, K. van Beek, F. S. Tehrani, E. Kementzetzidis, F. Pisanò, A. Elkadi, M. Segeren, T. Molenkamp, and A. V. Metrikine. Experimental identification of the dynamic behaviour of pile-soil system installed by means of three different pile-driving techniques. In *Proceedings of the XI International Conference on Structural Dynamics, EURODYN 2020*, volume II, pages 3005–3015. European Association for Structural Dynamics, 2020.

[51] A. Tsetas, A. Tsouvalas, S. Gómez, F. Pisanò, E. Kementzetzidis, T. Molenkamp, A. Elkadi, and A. Metrikine. Gentle Driving of Piles (GDP) at a sandy site combining axial and torsional vibrations: Part I - installation tests. *Ocean Engineering*, 270:113453, 2023.

[52] S. S. Gómez, A. Tsetas, and A. V. Metrikine. Energy flux analysis for quantification of vibratory pile driving efficiency. *Journal of Sound and Vibration*, 541:117299, 2022.

[53] S. S. Gómez, A. Tsetas, A. Tsouvalas, and A. V. Metrikine. Dynamic pile response during vibratory driving and modal-based strain field mapping. In *International Conference on Wave Mechanics and Vibrations*, pages 1125–1134. Springer, 2023.

[54] E. Kementzetzidis, F. Pisanò, A. Elkadi, A. Tsouvalas, and A. Metrikine. Gentle Driving of Piles (GDP) at a sandy site combining axial and torsional vibrations: Part II - cyclic/dynamic lateral loading tests. *Ocean Engineering*, 270:113452, 2023.

[55] E. Smith. Pile-driving analysis by the wave equation. *Journal of the soil mechanics and foundations division*, 86(4):35–61, 1960.

[56] P. W. Forehand and J. L. Reese Jr. Prediction of pile capacity by the wave equation. *Journal of the Soil Mechanics and Foundations Division*, 90(2):1–25, 1964.

[57] G. C. Gibson and H. M. Coyle. Soil damping constants related to common soil properties in sands and clays. Technical report, Texas Transportation Institute, 1968.

[58] H. M. Coyle and G. C. Gibson. Empirical damping constants for sands and clays. *Journal of the Soil Mechanics and Foundations Division*, 96(3):949–965, 1970.

[59] U. Dayal and J. H. Allen. The effect of penetration rate on the strength of remolded clay and sand samples. *Canadian Geotechnical Journal*, 12(3):336–348, 1975.

[60] S. Litkouthi and T. Poskitt. Damping constants for pile driveability calculations. *Geotechnique*, 30(1):77–86, 1980.

[61] K. Egorov. Calculation of bed for foundation with ring footing. In *Proc. 6th International Conference of Soil Mechanics and Foundation Engineering*, volume 2, pages 41–45, 1965.

[62] J. Lysmer and F. Richart Jr. Dynamic response of footings to vertical loading. *Journal of the Soil Mechanics and Foundations Division*, 92(1):65–91, 1966.

[63] J. Lysmer and R. L. Kuhlemeyer. Finite dynamic model for infinite media. *Journal of the Engineering Mechanics Division*, 95(4):859–877, 1969.

[64] M. Novak. Dynamic stiffness and damping of piles. *Canadian Geotechnical Journal*, 11(4):574–598, 1974.

[65] T. Nogami and M. Novák. Soil-pile interaction in vertical vibration. *Earthquake Engineering & Structural Dynamics*, 4(3):277–293, 1976.

[66] M. Novak. Vertical vibration of floating piles. *Journal of the Engineering Mechanics Division*, 103(1):153–168, 1977.

[67] M. Novak, F. Aboul-Ella, and T. Nogami. Dynamic soil reactions for plane strain case. *Journal of the Engineering Mechanics Division*, 104(4):953–959, 1978.

[68] T. Akiyoshi. Soil-pile interaction in vertical vibration induced through a frictional interface. *Earthquake Engineering & Structural Dynamics*, 10(1):135–148, 1982.

[69] M. Novak and B. El Sharnouby. Stiffness constants of single piles. *Journal of Geotechnical Engineering*, 109(7):961–974, 1983.

[70] T. Nogami and K. Konagai. Time domain axial response of dynamically loaded single piles. *Journal of Engineering Mechanics*, 112(11):1241–1252, 1986.

[71] T. Nogami and K. Konagai. Dynamic response of vertically loaded nonlinear pile foundations. *American Society of Civil Engineers. Journal of Geotechnical Engineering*, 113(2):147–162, 1987.

[72] G. Gazetas. Analysis of machine foundation vibrations: state of the art. *International Journal of soil dynamics and earthquake engineering*, 2(1):2–42, 1983.

[73] G. Gazetas and R. Dobry. Simple radiation damping model for piles and footings. *Journal of Engineering Mechanics*, 110(6):937–956, 1984.

[74] G. Gazetas. Seismic response of end-bearing single piles. *International Journal of Soil Dynamics and Earthquake Engineering*, 3(2):82–93, 1984.

[75] E. Kausel. *Forced vibrations of circular foundations on layered media*. PhD thesis, Massachusetts Institute of Technology, 1974.

[76] E. Kausel and J. M. Roesset. Dynamic stiffness of circular foundations. *Journal of the Engineering Mechanics Division*, 101(6):771–785, 1975.

[77] E. Kausel, G. Waas, and J. M. Roësset. Dynamic analysis of footings on layered media. *Journal of the engineering mechanics division*, 101(5):679–693, 1975.

[78] E. Kausel. An explicit solution for the green functions for dynamic loads in layered media. Technical Report R81-13, Publication No. 699, Department of Civil Engineering, Massachusetts Institute of Technology, 1981.

[79] V. Baranov. On the calculation of an embedded foundation. *Vorposy Dinamiki i Prognosti*, 14:195–209, 1967.

[80] M. F. Randolph and H. A. Simons. An improved soil model for one-dimensional pile driving analysis. In *In Proceedings of the 3rd International Conference on Numerical Methods in Offshore Piling, Nantes, France*, pages 1–17, 1986.

[81] S. Lee, Y. Chow, G. Karunaratne, and K. Wong. Rational wave equation model for pile-driving analysis. *Journal of Geotechnical Engineering*, 114(3):306–325, 1988.

[82] T. Nguyen, B. Berggren, and S. Hansbo. A new soil model for pile driving and driveability analysis. In *Proceedings, Third International Conference on Application of Stress-Wave Theory to Piles*, pages 353–367, 1988.

[83] M. Randolph. IMPACT - Dynamic analysis of pile driving, 2008.

[84] R. Buckley, S. Kontoe, R. Jardine, M. Maron, F. Schroeder, and P. Barbosa. Common pitfalls of pile driving resistance analysis–a case study of the wikinger offshore windfarm. In *Proc. 8th Intl. Conf. Offshore Site Investigation and Geotechnics*, pages 1246–1253, 2017.

[85] A. Deeks and M. Randolph. Analytical modelling of hammer impact for pile driving. *International Journal for Numerical and Analytical Methods in Geomechanics*, 17(5):279–302, 1993.

[86] W. Take, A. Valsangkar, and M. Randolph. Analytical solution for pile hammer impact. *Computers and Geotechnics*, 25(2):57–74, 1999.

[87] R. Salgado, D. Loukidis, G. Abou-Jaoude, and Y. Zhang. The role of soil stiffness non-linearity in 1d pile driving simulations. *Géotechnique*, 65(3):169–187, 2015.

[88] F. Toolan, D. Fox, and BP. Geotechnical planning of piled foundations for offshore platforms. *Proceedings of the Institution of Civil Engineers*, 62(2):221–244, 1977.

[89] R. M. Semple and J. P. Gemeinhardt. Stress history approach to analysis of soil resistance to pile driving. In *Offshore Technology Conference*. OnePetro, 1981.

[90] R. S. Stevens, E. A. Wiltsie, and T. H. Turton. Evaluating drivability for hard clay, very dense sand, and rock. In *Offshore Technology Conference*. OnePetro, 1982.

[91] T. Alm and L. Hamre. Soil model for pile driveability predictions based on cpt interpretations. In *International Conference on soil mechanics and geotechnical engineering*, pages 1297–1302, 2001.

[92] B. Lehane, J. Schneider, and X. Xu. The uwa-05 method for prediction of axial capacity of driven piles in sand. *Frontiers in offshore geotechnics: ISFOG*, pages 683–689, 2005.

[93] R. Jardine, F. Chow, R. Overy, and J. Standing. *ICP design methods for driven piles in sands and clays*, volume 112. Thomas Telford London, 2005.

[94] T. Byrne, P. Doherty, K. Gavin, R. Overy, et al. Comparison of pile driveability methods in north sea sand. In *Offshore Site Investigation and Geotechnics: Integrated Technologies-Present and Future*. Society of Underwater Technology, 2012.

[95] T. Byrne, K. Gavin, L. Prendergast, P. Cachim, P. Doherty, and S. C. Pulukul. Performance of CPT-based methods to assess monopile driveability in North Sea sands. *Ocean Engineering*, 166:76–91, 2018.

[96] K. Chua, S. Gardner, and L. Lowery. Wave equation analysis of a vibratory hammer-driven pile. In *Offshore Technology Conference*. OnePetro, 1987.

[97] S. Gardner. Analysis of vibratory driven pile. Technical report, Naval Civil Engineering Lab, Port Hueneme, California, 1987.

[98] T. J. Hirsch, L. Carr, and L. L. Lowery. Pile driving analysis: Wave equation user's manual, tti program. Technical report, 1976.

[99] R. Moulai-Khatir, M. W. O'Neill, and C. Vipulanandan. Program vpda wave equation analysis for vibratory driving of piles. *Report to the US Army Corps of Engineerings Waterways Experiments Station., Dept of Civil and Environmental Engineering, UHCE*, pages 94–1, 1994.

[100] Allnamics. Allwave-vdp user's reference manual, 2015.

[101] G. Jonker. Vibratory pile driving hammers for pile installations and soil improvement projects. In *Offshore Technology Conference*. OnePetro, 1987.

[102] D. Wong, M. W. O'Neill, and C. Vipulanandan. Modelling of vibratory pile driving in sand. *International Journal for numerical and analytical methods in geomechanics*, 16(3):189–210, 1992.

[103] A. Holeyman. An analytical model-based computer program to evaluate the penetration speed of vibratory driven sheet piles. Technical report, Belgian Building Research Institute, 1993.

[104] A. Holeyman and C. Legrand. A method to predict the drivability of vibratory driven piles. In *Proceedings of the 5th International Conference on the Application of Stress-Wave Theory to Piles*, 1996.

[105] V. Whenham and A. Holeyman. Load transfers during vibratory driving. *Geotechnical and Geological Engineering*, 30(5):1119–1135, 2012.

[106] A. Holeyman and V. Whenham. Critical review of the hypervib1 model to assess pile vibro-drivability. *Geotechnical and Geological Engineering*, 35(5):1933–1951, 2017.

[107] J. V. Berghe and A. Holeyman. Application of a hypoplastic constitutive law into a vibratory pile driving model. In *Proceedings of the international conference on vibratory pile driving and deep soil compaction, Transvib 2002, Louvain-la-Neuve, Belgium*, pages 61–68, 2002.

[108] A. Holeyman and J.-F. Vanden Berghe. Hypoplastic modeling of vibratory pile driving. In *First Euro Mediterranean in Advances on Geomaterials and Structures*, 2004.

[109] Y. Xiao and Y. Ge. A numerical model of vps for offshore wind turbine monopiles based on hypoplastic theory. *International Journal for Numerical and Analytical Methods in Geomechanics*, 46(4):697–716, 2022.

[110] E. Bauer. Calibration of a comprehensive hypoplastic model for granular materials. *Soils and foundations*, 36(1):13–26, 1996.

[111] G. Gudehus. A comprehensive constitutive equation for granular materials. *Soils and foundations*, 36(1):1–12, 1996.

[112] I. Smith and Y. Chow. Three-dimensional analysis of pile drivability. In *Proc. 2nd Int. Conf. on Numerical Methods in Offshore Piling, Austin, Texas*, pages 1–19, 1982.

[113] M. E. Mabsout and J. L. Tassoulas. A finite element model for the simulation of pile driving. *International Journal for numerical methods in Engineering*, 37(2):257–278, 1994.

[114] M. E. Mabsout, L. C. Reese, and J. L. Tassoulas. Study of pile driving by finite-element method. *Journal of geotechnical engineering*, 121(7):535–543, 1995.

[115] Y. F. Dafalias. Bounding surface plasticity. I: Mathematical foundation and hypoplasticity. *Journal of engineering mechanics*, 112(9):966–987, 1986.

[116] Y. F. Dafalias and L. R. Herrmann. Bounding surface plasticity. II: Application to isotropic cohesive soils. *Journal of Engineering Mechanics*, 112(12):1263–1291, 1986.

[117] D. Sheng, K. D. Eigenbrod, and P. Wriggers. Finite element analysis of pile installation using large-slip frictional contact. *Computers and Geotechnics*, 32(1):17–26, 2005.

[118] D. Sheng, P. Wriggers, and S. W. Sloan. Improved numerical algorithms for frictional contact in pile penetration analysis. *Computers and Geotechnics*, 33(6-7):341–354, 2006.

[119] P. Wriggers. *Computational contact mechanics*, volume 2. Springer, 2006.

[120] N. Phuong, A. Van Tol, A. Elkadi, and A. Rohe. Numerical investigation of pile installation effects in sand using material point method. *Computers and Geotechnics*, 73:58–71, 2016.

[121] N. Phuong, A. van Tol, A. Elkadi, and A. Rohe. Modelling of pile installation using the material point method (mpm). *Numerical methods in Geotechnical engineering*, 271:276, 2014.

[122] N. T. V. Phuong. *Numerical Modelling Of Pile Installation Using Material Point Method*. PhD thesis, Delft University of Technology, 2019.

[123] M. W. Evans, F. H. Harlow, and E. Bromberg. The particle-in-cell method for hydrodynamic calculations. Technical report, Los Alamos National Lab, 1957.

[124] F. H. Harlow. The particle-in-cell method for numerical solution of problems in fluid dynamics. Technical report, Los Alamos National Lab, 1962.

[125] F. H. Harlow. The particle-in-cell computing method for fluid dynamics. *Methods Comput. Phys.*, 3:319–343, 1964.

[126] M. Martinelli and V. Galavi. Investigation of the material point method in the simulation of cone penetration tests in dry sand. *Computers and Geotechnics*, 130:103923, 2021.

[127] J. Machaček, P. Staubach, M. Tafili, H. Zachert, and T. Wichtmann. Investigation of three sophisticated constitutive soil models: From numerical formulations to element tests and the analysis of vibratory pile driving tests. *Computers and Geotechnics*, 138:104276, 2021.

[128] P.-A. Von Wolffersdorff. A hypoplastic relation for granular materials with a predefined limit state surface. *Mechanics of Cohesive-frictional Materials: An International Journal on Experiments, Modelling and Computation of Materials and Structures*, 1(3):251–271, 1996.

[129] A. Niemunis and I. Herle. Hypoplastic model for cohesionless soils with elastic strain range. *Mechanics of Cohesive-frictional Materials: An International Journal on Experiments, Modelling and Computation of Materials and Structures*, 2(4):279–299, 1997.

[130] Y. F. Dafalias and M. T. Manzari. Simple plasticity sand model accounting for fabric change effects. *Journal of Engineering mechanics*, 130(6):622–634, 2004.

[131] H. Liu, A. Diambra, J. A. Abell, and F. Pisanò. Memory-enhanced plasticity modeling of sand behavior under undrained cyclic loading. *Journal of Geotechnical and Geoenvironmental Engineering*, 146(11):04020122, 2020.

[132] H. Liu, E. Kementzetzidis, J. A. Abell, and F. Pisanò. From cyclic sand ratcheting to tilt accumulation of offshore monopiles: 3d fe modelling using sanisand-ms. *Géotechnique*, 72(9):753–768, 2022.

[133] J. Vogelsang, G. Huber, and T. Triantafyllidis. Experimental investigation of vibratory pile driving in saturated sand. In *Holistic Simulation of Geotechnical Installation Processes*, pages 101–123. Springer, 2017.

[134] S. Chrisopoulos and J. Vogelsang. A finite element benchmark study based on experimental modeling of vibratory pile driving in saturated sand. *Soil Dynamics and Earthquake Engineering*, 122:248–260, 2019.

[135] P. Staubach and J. Machaček. Influence of relative acceleration in saturated sand: Analytical approach and simulation of vibratory pile driving tests. *Computers and Geotechnics*, 112:173–184, 2019.

[136] P. Staubach, J. Machaček, J. Skowronek, and T. Wichtmann. Vibratory pile driving in water-saturated sand: Back-analysis of model tests using a hydro-mechanically coupled cel method. *Soils and Foundations*, 61(1):144–159, 2021.

[137] H. Kraus. *Thin elastic shells*. John Wiley & Sons, 1967.

[138] J. E. Greenspon. Vibrations of a thick-walled cylindrical shell—comparison of the exact theory with approximate theories. *The Journal of the Acoustical Society of America*, 32(5):571–578, 1960.

[139] A. W. Leissa. *Vibration of shells*, volume 288. Scientific and Technical Information Office, National Aeronautics and Space Administration, 1973.

[140] A. E. H. Love. *A treatise on the mathematical theory of elasticity*. Dover Publications, 1944.

[141] G. Kirchhoff. Über das gleichgewicht und die bewegung einer elastischen scheibe. *Journal für die Reine und Angewandte Mathematik*, 1850(40):51–88, 1850.

[142] I. Mirsky and G. Herrmann. Nonaxially symmetric motions of cylindrical shells. *The Journal of the Acoustical Society of America*, 29(10):1116–1123, 1957.

[143] I. Mirsky and G. Herrmann. Axially symmetric motions of thick cylindrical shells. *Journal of Applied Mechanics*, 25(1):97–102, 1958.

[144] P. L. Gould. *Analysis of Shells and Plates*. Springer, 1988.

[145] V. Novozhilov. The theory of thin elastic shells. *P. Noordhoff*, 1964.

[146] R. Arnold and G. Warburton. The flexural vibrations of thin cylinders. *Proceedings of the Institution of Mechanical Engineers*, 167(1):62–80, 1953.

[147] D. G. Karczub. Expressions for direct evaluation of wave number in cylindrical shell vibration studies using the flügge equations of motion. *The Journal of the Acoustical Society of America*, 119(6):3553–3557, 2006.

[148] Y. C. Liu, Y. F. Hwang, and J. H. Huang. Modes of wave propagation and dispersion relations in a cylindrical shell. *Journal of vibration and acoustics*, 131(4), 2009.

[149] D. Paliwal, R. K. Pandey, and T. Nath. Free vibrations of circular cylindrical shell on winkler and pasternak foundations. *International Journal of Pressure Vessels and Piping*, 69(1):79–89, 1996.

[150] D. Paliwal and R. K. Pandey. The free vibration of a cylindrical shell on an elastic foundation. *Journal of vibration and acoustics*, 120(1):63–71, 1998.

[151] M. Torkaman-Asadi and R. Firouz-Abadi. Free vibration analysis of cylindrical shells partially resting on an elastic foundation. *Meccanica*, 51(5):1113–1125, 2016.

[152] M. C. Junger. Vibrations of elastic shells in a fluid medium and the associated radiation of sound. *Journal of Applied Mechanics*, 19(4):439–445, 1952.

[153] G. Warburton. Vibration of a cylindrical shell in an acoustic medium. *Journal of Mechanical Engineering Science*, 3(1):69–79, 1961.

[154] M. K. Kwak. Free vibration analysis of a finite circular cylindrical shell in contact with unbounded external fluid. *Journal of Fluids and Structures*, 26(3):377–392, 2010.

[155] L. H. Donnell. Stability of thin-walled tubes under torsion. Technical Report NACA-TR-479, National Advisory Committee for Aeronautics, 1933.

[156] L. H. Donnell. A discussion of thin shell theory. In *Proceedings of the 5th International Congress of Applied Mechanics*, pages 66–70, 1938.

[157] K. M. Mushtari. On the stability of cylindrical shells subjected to torsion. *Trudy Kazanskego aviatsionnugo inatituta*, 2, 1938.

[158] A. E. H. Love. XVI. The small free vibrations and deformation of a thin elastic shell. *Philosophical Transactions of the Royal Society of London. (A.)*, 179:491–546, 1888.

[159] S. P. Timoshenko and S. Woinowsky-Krieger. *Theory of plates and shells*. McGraw-hill, 1959.

[160] G. Warburton. Vibration of thin cylindrical shells. *Journal of Mechanical Engineering Science*, 7(4):399–407, 1965.

[161] J. Achenbach. *Wave propagation in elastic solids*. North-Holland Publishing Company, 1973.

[162] A. W. Leissa. *Vibration of plates*, volume 160. Scientific and Technical Information Division, National Aeronautics and Space Administration, 1969.

[163] J. Miklowitz. *The theory of elastic waves and waveguides*. Elsevier, 1978.

[164] J. W. S. B. Rayleigh. *The theory of sound*, volume 1. Macmillan & Company, 1894.

[165] R. Bishop. Longitudinal waves in beams. *Aeronautical Quarterly*, 3(4):280–293, 1952.

[166] P. Meijers, A. Tsouvalas, and A. Metrikine. A non-collocated method to quantify plastic deformation caused by impact pile driving. *International Journal of Mechanical Sciences*, 148:1–8, 2018.

[167] D. C. Gazis. Three-dimensional investigation of the propagation of waves in hollow circular cylinders. i. analytical foundation. *The journal of the Acoustical Society of America*, 31(5):568–573, 1959.

[168] D. C. Gazis. Three-dimensional investigation of the propagation of waves in hollow circular cylinders. ii. numerical results. *The Journal of the Acoustical Society of America*, 31(5):573–578, 1959.

[169] J. E. Greenspon. Flexural vibrations of a thick-walled circular cylinder according to the exact theory of elasticity. *Journal of the Aerospace Sciences*, 27(1):37–40, 1960.

[170] A. E. Armenàkas, D. C. Gazis, and G. Herrmann. *Free vibrations of circular cylindrical shells*. Pergamon Press, 1969.

[171] K. C. Le. *Vibrations of shells and rods*. Springer Science & Business Media, 2012.

[172] C. Loy, K. Lam, and C. Shu. Analysis of cylindrical shells using generalized differential quadrature. *Shock and vibration*, 4(3):193–198, 1997.

[173] L. Zhang, Y. Xiang, and G. Wei. Local adaptive differential quadrature for free vibration analysis of cylindrical shells with various boundary conditions. *International Journal of Mechanical Sciences*, 48(10):1126–1138, 2006.

[174] K. Lam and C. Loy. Effects of boundary conditions on frequencies of a multi-layered cylindrical shell. *Journal of Sound and vibration*, 188(3):363–384, 1995.

[175] X. Zhang, G. Liu, and K. Lam. Vibration analysis of thin cylindrical shells using wave propagation approach. *Journal of sound and vibration*, 239(3):397–403, 2001.

[176] C. Wang and J. Lai. Prediction of natural frequencies of finite length circular cylindrical shells. *Applied acoustics*, 59(4):385–400, 2000.

[177] H. Lee and M. K. Kwak. Free vibration analysis of a circular cylindrical shell using the rayleigh–ritz method and comparison of different shell theories. *Journal of Sound and Vibration*, 353:344–377, 2015.

[178] W. Flügge. *Statik und Dynamik der Schalen*. Springer, 1934.

[179] K. Forsberg. Influence of boundary conditions on the modal characteristics of thin cylindrical shells. *AIAA journal*, 2(12):2150–2157, 1964.

[180] K. Forsberg. Axisymmetric and beam-type vibrations of thin cylindrical shells. *AIAA Journal*, 7(2):221–227, 1969.

[181] W. Flügge. *Stresses in shells*. Springer, 1973.

[182] F. Bogner and R. Archer. On the orthogonality condition of axisymmetric vibration modes for shells of revolution. *Journal of Applied Mechanics*, 32(2):447–448, 1965.

[183] H. Reismann. On the forced motion of elastic solids. *Applied Scientific Research*, 18(1):156–165, 1968.

[184] J. Callahan and H. Baruh. A closed-form solution procedure for circular cylindrical shell vibrations. *International Journal of Solids and Structures*, 36(20):2973–3013, 1999.

[185] D. Chapelle and K.-J. Bathe. *The finite element analysis of shells-fundamentals*. Springer Science & Business Media, 2010.

[186] N. Bandyopadhyay and R. R. Archer. Semi-analytical finite element analysis of end problems for orthotropic cylinders. *International Journal of Solids and Structures*, 15(11):871–883, 1979.

[187] E. Taciroglu, C. Liu, S. Dong, and C. Chun. Analysis of laminated piezoelectric circular cylinders under axisymmetric mechanical and electrical loads with a semi-analytic finite element method. *International Journal of Solids and Structures*, 41(18-19):5185–5208, 2004.

[188] I. Bartoli, A. Marzani, F. L. Di Scalea, and E. Viola. Modeling wave propagation in damped waveguides of arbitrary cross-section. *Journal of sound and vibration*, 295(3-5):685–707, 2006.

[189] A. Marzani, E. Viola, I. Bartoli, F. L. Di Scalea, and P. Rizzo. A semi-analytical finite element formulation for modeling stress wave propagation in axisymmetric damped waveguides. *Journal of Sound and Vibration*, 318(3):488–505, 2008.

[190] W. Soedel. *Vibrations of shells and plates*. CRC Press, 2004.

[191] COMSOL AB. COMSOL multiphysics® v. 5.6. `https://www.comsol.com`, 2022.

[192] L. Meirovitch. *Computational methods in structural dynamics*, volume 5. Springer Science & Business Media, 1980.

[193] A. Tsetas, A. Tsouvalas, and A. V. Metrikine. Installation of large-diameter monopiles: introducing wave dispersion and non-local soil reaction. *Journal of Marine Science and Engineering*, 9(3):313, 2021.

[194] X. Wu, Y. Hu, Y. Li, J. Yang, L. Duan, T. Wang, T. Adcock, Z. Jiang, Z. Gao, Z. Lin, et al. Foundations of offshore wind turbines: A review. *Renewable and Sustainable Energy Reviews*, 104:379–393, 2019.

[195] L. Sa, T. Yinghui, Z. Yangrui, J. Baofan, and W. Jinbiao. Premature refusal of large-diameter, deep-penetration piles on an offshore platform. *Applied Ocean Research*, 42:55–59, 2013.

[196] E. A. Smith. Pile-driving analysis by the wave equation. *American Society of Civil Engineers Transactions*, 1962.

[197] I. Anusic, G. R. Eiksund, and M. A. Liingaard. Comparison of pile driveability methods based on a case study from an offshore wind farm in north sea. *Proceedings of the 17th Nordic Geotechnical Meeting Challenges in Nordic Geotechnic*, 2016.

[198] Q. Deng, W. Jiang, and W. Zhang. Theoretical investigation of the effects of the cushion on reducing underwater noise from offshore pile driving. *The Journal of the Acoustical Society of America*, 140(4):2780–2793, 2016.

[199] P. Meijers, A. Tsouvalas, and A. Metrikine. The effect of stress wave dispersion on the drivability analysis of large-diameter monopiles. *Procedia engineering*, 199:2390–2395, 2017.

[200] A. De Nicola and M. F. Randolph. Tensile and compressive shaft capacity of piles in sand. *Journal of Geotechnical Engineering*, 119(12):1952–1973, 1993.

[201] A. J. Deeks and M. F. Randolph. Axisymmetric time-domain transmitting boundaries. *Journal of Engineering Mechanics*, 120(1):25–42, 1994.

[202] D. Liyanapathirana, A. Deeks, and M. Randolph. Numerical analysis of soil plug behaviour inside open-ended piles during driving. *International journal for numerical and analytical methods in geomechanics*, 22(4):303–322, 1998.

[203] H. G. Poulos and E. H. Davis. *Pile foundation analysis and design*. Number Monograph. 1980.

[204] J. Kumar and M. Chakraborty. Bearing capacity factors for ring foundations. *Journal of Geotechnical and Geoenvironmental Engineering*, 141(10):06015007, 2015.

[205] A. Tsouvalas and A. Metrikine. A semi-analytical model for the prediction of underwater noise from offshore pile driving. *Journal of Sound and Vibration*, 332(13):3232–3257, 2013.

[206] H. Reismann and J. Padlog. Forced, axi-symmetric motions of cylindrical shells. *Journal of the Franklin Institute*, 284(5):308–319, 1967.

[207] M. I. Friswell, S. Adhikari, and Y. Lei. Vibration analysis of beams with non-local foundations using the finite element method. *International Journal for Numerical Methods in Engineering*, 71(11):1365–1386, 2007.

[208] W. Versteijlen, J. de Oliveira Barbosa, K. van Dalen, and A. Metrikine. Dynamic soil stiffness for foundation piles: Capturing 3d continuum effects in an effective, non-local 1d model. *International Journal of Solids and Structures*, 134:272–282, 2018.

[209] Y. Lei, M. I. Friswell, and S. Adhikari. A Galerkin method for distributed systems with non-local damping. *International Journal of Solids and Structures*, 43(11-12):3381–3400, 2006.

[210] W. F. Ames. *Numerical methods for partial differential equations*. Academic press, 2014.

[211] C. A. Fletcher. *Computational Galerkin methods*. Springer, 1984.

[212] R. L. Lowe, S.-T. J. Yu, L. Yang, and S. E. Bechtel. Modal and characteristics-based approaches for modeling elastic waves induced by time-dependent boundary conditions. *Journal of Sound and Vibration*, 333(3):873–886, 2014.

[213] J. R. Dormand and P. J. Prince. A family of embedded Runge-Kutta formulae. *Journal of computational and applied mathematics*, 6(1):19–26, 1980.

[214] K.-J. Bathe. *Finite element procedures*. Prentice Hall, 2014.

[215] M. Géradin and D. J. Rixen. *Mechanical vibrations: theory and application to structural dynamics*. John Wiley & Sons, 2014.

[216] G. Lamé. *Leçons sur la théorie mathématique de l'élasticité des corps solides*. Bachelier, 1852.

[217] P. M. Morse and H. Feshbach. *Methods of theoretical physics*. McGraw-Hill Book Company, Inc., New York, 1953.

[218] K. Aki and P. G. Richards. *Quantitative seismology*. University Science Books, 2002.

[219] E. Kausel. *Fundamental solutions in elastodynamics: a compendium*. Cambridge University Press, 2006.

[220] A. C. Eringen. *Elastodynamics, Linear Theory*, volume 2. Academic press, 1975.

[221] K. Graff. *Wave motion in elastic solids*. Oxford University Press, 1975.

[222] R. Pak. Asymmetric wave propagation in an elastic half-space by a method of potentials. *Journal of applied mechanics*, 54(1):121–126, 1987.

[223] C. Somigliana. *Sulle espressioni analitiche generali dei movimenti oscillatori*. Reale Accademia Lincei Roma, 1892.

[224] E. Kausel. *The thin-layer method in seismology and earthquake engineering*, pages 193–213. WIT Press, 2000.

[225] F. B. Jensen, W. A. Kuperman, M. B. Porter, H. Schmidt, and A. Tolstoy. *Computational ocean acoustics*, volume 794. Springer, 2011.

[226] J. Lysmer. Lumped mass method for rayleigh waves. *Bulletin of the Seismological Society of America*, 60(1):89–104, 1970.

[227] G. Waas. Linear two-dimensional analysis of soil dynamics problems in semi-infinite layer media. *Ph. D. Thesis, University of California*, 1972.

[228] E. Kausel and J. M. Roësset. Semianalytic hyperelement for layered strata. *Journal of the engineering mechanics division*, 103(4):569–588, 1977.

[229] J. L. Tassoulas. *Elements for the numerical analysis of wave motion in layered media*. PhD thesis, Massachusetts Institute of Technology, 1981.

[230] J. L. Tassoulas and E. Kausel. Elements for the numerical analysis of wave motion in layered strata. *International Journal for Numerical Methods in Engineering*, 19(7):1005–1032, 1983.

[231] J. L. Tassoulas and E. Kausel. On the dynamic stiffness of circular ring footings on an elastic stratum. *International journal for numerical and analytical methods in geomechanics*, 8(5):411–426, 1984.

[232] E. Kausel. Thin-layer method: Formulation in the time domain. *International journal for numerical methods in engineering*, 37(6):927–941, 1994.

[233] V. Lotfi, J. M. Roesset, and J. L. Tassoulas. A technique for the analysis of the response of dams to earthquakes. *Earthquake engineering & structural dynamics*, 15(4):463–489, 1987.

[234] S. Bougacha and J. L. Tassoulas. Seismic analysis of gravity dams. i: modeling of sediments. *Journal of Engineering Mechanics*, 117(8):1826–1837, 1991.

[235] S. Bougacha and J. L. Tassoulas. Seismic response of gravity dams. ii: Effects of sediments. *Journal of engineering mechanics*, 117(8):1839–1850, 1991.

[236] S. Bougacha, J. L. Tassoulas, and J. M. Roësset. Analysis of foundations on fluid-filled poroelastic stratum. *Journal of engineering mechanics*, 119(8):1632–1648, 1993.

[237] S. Bougacha, J. M. Roësset, and J. L. Tassoulas. Dynamic stiffness of foundations on fluid-filled poroelastic stratum. *Journal of engineering mechanics*, 119(8):1649–1662, 1993.

[238] E. Kausel. Wave propagation in anisotropic layered media. *International Journal for Numerical Methods in Engineering*, 23(8):1567–1578, 1986.

[239] M. Schevenels, G. Lombaert, G. Degrande, D. Degrauwe, and B. Schoors. The green's functions of a vertically inhomogeneous soil with a random dynamic shear modulus. *Probabilistic Engineering Mechanics*, 22(1):100–111, 2007.

[240] J. Lee, J. Kim, and J. Tassoulas. A stochastic thin-layer method for an inhomogeneous half-space in antiplane shear. In *Proceedings of the Eighth International Conference on Engineering Computational Technology*, 2012.

[241] J. H. Lee, J. K. Kim, and J. L. Tassoulas. Stochastic dynamic analysis of a layered half-space. *Soil Dynamics and Earthquake Engineering*, 48:220–233, 2013.

[242] J. Bielak, K. Loukakis, Y. Hisada, and C. Yoshimura. Domain reduction method for three-dimensional earthquake modeling in localized regions, part i: Theory. *Bulletin of the seismological Society of America*, 93(2):817–824, 2003.

[243] C. Yoshimura, J. Bielak, Y. Hisada, and A. Fernández. Domain reduction method for three-dimensional earthquake modeling in localized regions, part ii: Verification and applications. *Bulletin of the seismological Society of America*, 93(2):825–841, 2003.

[244] K. T. Nguyen, D. S. Kusanovic, and D. Asimaki. Three-dimensional nonlinear soil–structure interaction for rayleigh wave incidence in layered soils. *Earthquake Engineering & Structural Dynamics*, 51(11):2752–2770, 2022.

[245] D. Afolabi. Linearization of the quadratic eigenvalue problem. *Computers & structures*, 26(6):1039–1040, 1987.

[246] F. Tisseur and K. Meerbergen. The quadratic eigenvalue problem. *SIAM review*, 43(2):235–286, 2001.

[247] D. Givoli. *Numerical methods for problems in infinite domains*. Elsevier, 1992.

[248] S. V. Tsynkov. Numerical solution of problems on unbounded domains. a review. *Applied Numerical Mathematics*, 27(4):465–532, 1998.

[249] D. E. Beskos. Boundary element methods in dynamic analysis. *Applied Mechanics Reviews*, 40(1-6):1, 1987.

[250] J. Dominguez. *Boundary elements in dynamics*. Wit Press, 1993.

[251] E. Kausel. Local transmitting boundaries. *Journal of engineering mechanics*, 114(6):1011–1027, 1988.

[252] E. Kausel and J. M. Roësset. Stiffness matrices for layered soils. *Bulletin of the seismological Society of America*, 71(6):1743–1761, 1981.

[253] E. Kausel and R. Peek. Dynamic loads in the interior of a layered stratum: an explicit solution. *Bulletin of the Seismological Society of America*, 72(5):1459–1481, 1982.

[254] S. W. Hull and E. Kausel. Dynamic loads in layered half-spaces. In *Proceedings of the Fifth Engineering Mechanics Division Specialty Conference*, pages 201–204, 1984.

[255] R. Clayton and B. Engquist. Absorbing boundary conditions for acoustic and elastic wave equations. *Bulletin of the seismological society of America*, 67(6):1529–1540, 1977.

[256] S. H. Seale. *Dynamic loads in layered halfspaces*. PhD thesis, Massachusetts Institute of Technology, 1985.

[257] S. H. Seale and E. Kausel. Point loads in cross-anisotropic, layered halfspaces. *Journal of engineering mechanics*, 115(3):509–524, 1989.

[258] J. Park. *Wave motion in finite and infinite media using the thin-layer method*. PhD thesis, Massachusetts Institute of Technology, 2002.

[259] J. M. de Oliveira Barbosa and E. Kausel. The thin-layer method in a cross-anisotropic 3d space. *International journal for numerical methods in engineering*, 89(5):537–560, 2012.

[260] E. Kausel. Physical interpretation and stability of paraxial boundary conditions. *Bulletin of the Seismological Society of America*, 82(2):898–913, 1992.

[261] J.-P. Berenger. A perfectly matched layer for the absorption of electromagnetic waves. *Journal of computational physics*, 114(2):185–200, 1994.

[262] W. Chew and Q. Liu. Perfectly matched layers for elastodynamics: a new absorbing boundary condition. *Journal of computational acoustics*, 4(04):341–359, 1996.

[263] F. Collino and C. Tsogka. Application of the perfectly matched absorbing layer model to the linear elastodynamic problem in anisotropic heterogeneous media. *Geophysics*, 66(1):294–307, 2001.

[264] U. Basu and A. K. Chopra. Perfectly matched layers for time-harmonic elastodynamics of unbounded domains: theory and finite-element implementation. *Computer Methods in Applied Mechanics and Engineering*, 192(11-12):1337–1375, 2003.

[265] J. Park and A. M. Kaynia. Stiffness matrices for fluid and anisotropic soil layers with applications in soil dynamics. *Soil Dynamics and Earthquake Engineering*, 115:169–182, 2018.

[266] E. Kausel and J. M. de Oliveira Barbosa. PMLs: A direct approach. *International journal for numerical methods in engineering*, 90(3):343–352, 2012.

[267] J. M. de Oliveira Barbosa, J. Park, and E. Kausel. Perfectly matched layers in the thin layer method. *Computer Methods in Applied Mechanics and Engineering*, 217:262–274, 2012.

[268] M. Kuzuoglu and R. Mittra. Frequency dependence of the constitutive parameters of causal perfectly matched anisotropic absorbers. *IEEE Microwave and Guided wave letters*, 6(12):447–449, 1996.

[269] J. A. Roden and S. Gedney. An efficient FDTD implementation of the PML with CFS in general media. In *IEEE Antennas and Propagation Society International Symposium. Transmitting Waves of Progress to the Next Millennium. 2000 Digest. Held in conjunction with: USNC/URSI National Radio Science Meeting (C*, volume 3, pages 1362–1365. IEEE, 2000.

[270] D. Komatitsch and R. Martin. An unsplit convolutional perfectly matched layer improved at grazing incidence for the seismic wave equation. *Geophysics*, 72(5):SM155–SM167, 2007.

[271] S. Francois, H. Goh, and L. F. Kallivokas. Non-convolutional second-order complex-frequency-shifted perfectly matched layers for transient elastic wave propagation. *Computer Methods in Applied Mechanics and Engineering*, 377:113704, 2021.

[272] S. Kucukcoban and L. F. Kallivokas. Mixed perfectly-matched-layers for direct transient analysis in 2d elastic heterogeneous media. *Computer Methods in Applied Mechanics and Engineering*, 200(1-4):57–76, 2011.

[273] J. M. de Oliveira Barbosa. *Analysis and mitigation of vibrations induced by the passage of high-speed trains in nearby buildings*. PhD thesis, University of Porto, 2013.

[274] J. Boussinesq. *Application des potentiels à l'étude de l'équilibre et du mouvement des solides élastiques: principalement au calcul des déformations et des pressions que produisent, dans ces solides, des efforts quelconques exercés sur une petite partie de leur surface ou de leur intérieur: mémoire suivi de notes étendues sur divers points de physique, mathematique et d'analyse*, volume 4. Gauthier-Villars, 1885.

[275] H. Lamb. I. on the propagation of tremors over the surface of an elastic solid. *Philosophical Transactions of the Royal Society of London. Series A, Containing papers of a mathematical or physical character*, 203(359-371):1–42, 1904.

[276] R. D. Mindlin. Force at a point in the interior of a semi-infinite solid. *Physics*, 7(5):195–202, 1936.

[277] W. T. Thomson. Transmission of elastic waves through a stratified solid medium. *Journal of applied Physics*, 21(2):89–93, 1950.

[278] N. A. Haskell. The dispersion of surface waves on multilayered media. *Bulletin of the seismological Society of America*, 43(1):17–34, 1953.

[279] W. M. Ewing, W. S. Jardetzky, F. Press, and A. Beiser. Elastic waves in layered media. *Physics Today*, 10(12):27, 1957.

[280] D. G. Harkrider. Surface waves in multilayered elastic media i. rayleigh and love waves from buried sources in a multilayered elastic half-space. *Bulletin of the Seismological Society of America*, 54(2):627–679, 1964.

[281] R. J. Apsel. *Dynamic Green's functions for layered media and applications to boundary-value problems*. PhD thesis, University of California, San Diego, 1979.

[282] J. E. Luco and R. J. Apsel. On the green's functions for a layered half-space. part i. *Bulletin of the Seismological Society of America*, 73(4):909–929, 1983.

[283] R. J. Apsel and J. E. Luco. On the green's functions for a layered half-space. part ii. *Bulletin of the seismological society of America*, 73(4):931–951, 1983.

[284] E. Kausel. Generalized stiffness matrix method for layered soils. *Soil Dynamics and Earthquake Engineering*, 115:663–672, 2018.

[285] E. Kausel. Dynamic point sources in laminated media via the thin-layer method. *International Journal of Solids and Structures*, 36(31-32):4725–4742, 1999.

[286] P. Dineva, G. Manolis, and F. Wuttke. Fundamental solutions in 3d elastodynamics for the bem: A review. *Engineering Analysis with Boundary Elements*, 105:47–69, 2019.

[287] D. R. Bland. *The theory of linear viscoelasticity*. Pergamon Press, 1960.

[288] B. W. Byrne, H. J. Burd, L. Zdravkovic, C. N. Abadie, G. T. Houlsby, R. J. Jardine, C. M. Martin, R. A. McAdam, M. Pacheco Andrade, A. M. Pedro, et al. Pisa design methods for offshore wind turbine monopiles. In *Offshore Technology Conference*. Offshore Technology Conference, 2019.

[289] A. M. Page, K. Norén-Cosgriff, K. S. Skau, and A. M. Kaynia. REDWIN foundation models for integrated dynamic analyses of offshore wind turbines. In *International Conference on Offshore Mechanics and Arctic Engineering*, volume 58899, page V010T09A073. American Society of Mechanical Engineers, 2019.

[290] A. Tsouvalas and A. V. Metrikine. Structure-borne wave radiation by impact and vibratory piling in offshore installations: From sound prediction to auditory damage. *Journal of Marine Science and Engineering*, 4(3):44, 2016.

[291] S. Koschinski and K. Lüdemann. Development of noise mitigation measures in offshore wind farm construction. *Commissioned by the Federal Agency for Nature Conservation*, pages 1–102, 2013.

[292] R. L. Mosher. Axial capacity of vibratory-driven piles versus impact-driven piles. *Transportation Research Record*, (1277), 1990.

[293] I. Anusic, B. Lehane, G. Eiksund, and M. Liingaard. Influence of installation method on static lateral response of displacement piles in sand. *Géotechnique Letters*, 9(3):193–197, 2019.

[294] K. S. Skau, A. M. Page, A. M. Kaynia, F. Løvholt, K. Norén-Cosgriff, H. Sturm, H. Andersen, T. A. Nygaard, H. P. Jostad, G. R. Eiksund, et al. Redwin–reducing cost in offshore wind by integrated structural and geotechnical design. In *IOP Conference Series-Journal of Physics, EERA DeepWind*, 2018.

[295] A. M. Page, R. T. Klinkvort, S. Bayton, Y. Zhang, and H. P. Jostad. A procedure for predicting the permanent rotation of monopiles in sand supporting offshore wind turbines. *Marine Structures*, 75:102813, 2020.

[296] V. Herwig and J. Gattermann. Vibro-project–vergleich der lateralen tragfähigkeit von vibrierten und geschlagenen stahlpfählen in sandigen böden. In *Pfahl-Symposium*, volume 19, page 2015, 2015.

[297] W. Versteijlen, F. Renting, P. Van Der Valk, J. Bongers, K. Van Dalen, and A. Metrikine. Effective soil-stiffness validation: Shaker excitation of an in-situ monopile foundation. *Soil Dynamics and Earthquake Engineering*, 102:241–262, 2017.

[298] F. Pisanò, A. Askarinejad, H. Wang, S. Maghsoodi, K. G. Gavin, M. L. A. Segeren, A. S. K. Elkadi, D. de Lange, and M. Konstadinou. MIDAS: Monopile Improved Design through Advanced cyclic Soil modelling. In *Proceedings of 20th International Conference on Soil Mechanics and Geotechnical Engineering (ICSMGE2022)*. Sydney, Australia, 2022.

[299] IHC IQIP. IHC IQIP TAKES NEXT STEP IN DEVELOPMENT BLUE PILING TECHNOLOGY . `https://www.ihciqip.com/en/news/`

ihc-iqip-takes-next-step-in-development-of-blue-piling-technology, 2020. Accessed: 2021-01-11.

[300] M. Georgiadis and S. Saflekou. Piles under axial and torsional loads. *Computers and Geotechnics*, 9(4):291–305, 1990.

[301] A. E. Holeyman. Soil behavior under vibratory driving. In *Proceedings of the International Conference on Vibratory Pile Driving and Deep Soil Compaction, Transvib 2002*, pages 3–19, 2002.

[302] S. S. Gómez and A. V. Metrikine. Shaker for gentle driving of piles. https://patentscope.wipo.int/search/en/detail.jsf?docId=WO2021040523&tab=PCTBIBLIO, 2021.

[303] OpenStreetMap contributors. Planet dump retrieved from https://planet.osm.org . https://www.openstreetmap.org, 2017.

[304] P. Vos. *Origin of the Dutch coastal landscape: long-term landscape evolution of the Netherlands during the Holocene, described and visualized in national, regional and local palaeogeographical map series*. Barkhuis, 2015.

[305] P. K. Robertson. Soil classification using the cone penetration test. *Canadian Geotechnical Journal*, 27(1):151–158, 1990.

[306] P. K. Robertson. Interpretation of cone penetration tests—a unified approach. *Canadian geotechnical journal*, 46(11):1337–1355, 2009.

[307] M. Jamiolkowski, D. Lo Presti, and M. Manassero. Evaluation of relative density and shear strength of sands from cpt and dmt. In *Soil behavior and soft ground construction*, pages 201–238. 2003.

[308] H. R. Masoumi, S. François, and G. Degrande. A non-linear coupled finite element–boundary element model for the prediction of vibrations due to vibratory and impact pile driving. *International Journal for Numerical and Analytical Methods in Geomechanics*, 33(2):245–274, 2009.

[309] R. M. Buckley, R. A. McAdam, B. W. Byrne, J. P. Doherty, R. J. Jardine, S. Kontoe, and M. F. Randolph. Optimization of impact pile driving using optical fiber bragg-grating measurements. *Journal of Geotechnical and Geoenvironmental Engineering*, 146(9):04020082, 2020.

[310] V. Whenham. *Power transfer and vibrator-pile-soil interactions within the framework of vibratory pile driving*. PhD thesis, Doctoral Thesis, University of Louvain, Belgium, 2011.

[311] G. Rega, F. Benedettini, and A. Salvatori. Periodic and chaotic motions of an unsymmetrical oscillator in nonlinear structural dynamics. *Chaos, Solitons & Fractals*, 1(1):39–54, 1991.

[312] A. Brandt. *Noise and vibration analysis: signal analysis and experimental procedures*. John Wiley & Sons, 2011.

[313] D. Gabor. Theory of communication. part 1: The analysis of information. *Journal of the Institution of Electrical Engineers-Part III: Radio and Communication Engineering*, 93(26):429–441, 1946.

[314] R. Spruit, F. van Tol, W. Broere, E. Slob, and E. Niederleithinger. Detection of anomalies in diaphragm walls with crosshole sonic logging. *Canadian Geotechnical Journal*, 51(4):369–380, 2014.

[315] A. Tsetas, A. Tsouvalas, and A. V. Metrikine. A non-linear three-dimensional pile–soil model for vibratory pile installation in layered media. *International Journal of Solids and Structures*, 269:112202, 2023.

[316] R. Van Dorp, N. Moscoso, M. Bielefeld, and G. Verbeek. Prediction and monitoring of installation of offshore foundation monopiles for windfarms. In *Offshore Technology Conference*. OnePetro, 2019.

[317] C. T. Nguyen and J. L. Tassoulas. Reciprocal absorbing boundary condition with perfectly matched discrete layers for transient analysis of sv-p waves in a layered half-space. *International Journal of Solids and Structures*, 155:89–108, 2018.

[318] T. Cameron and J. H. Griffin. An alternating frequency/time domain method for calculating the steady-state response of nonlinear dynamic systems. *Journal of Applied Mechanics*, 56:149—-154, 1989.

[319] M. Krack and J. Gross. *Harmonic balance for nonlinear vibration problems*, volume 1. Springer, 2019.

[320] F. Marques, P. Flores, J. P. Claro, and H. M. Lankarani. A survey and comparison of several friction force models for dynamic analysis of multibody mechanical systems. *Nonlinear Dynamics*, 86(3):1407–1443, 2016.

[321] P. Wriggers. *Nonlinear finite element methods*. Springer Science & Business Media, 2008.

[322] S. Moriyasu, S. Kobayashi, and T. Matsumoto. Experimental study on friction fatigue of vibratory driven piles by in situ model tests. *Soils and foundations*, 58(4):853–865, 2018.

[323] Z. Juhász and A. Szekrényes. Progressive buckling of a simply supported delaminated orthotropic rectangular composite plate. *International Journal of Solids and Structures*, 69:217–229, 2015.

[324] U. Bhattiprolu, A. K. Bajaj, and P. Davies. Periodic response predictions of beams on nonlinear and viscoelastic unilateral foundations using incremental harmonic balance method. *International Journal of Solids and Structures*, 99:28–39, 2016.

[325] S. Quaegebeur, B. Chouvion, and F. Thouverez. Nonlinear dynamic analysis of three-dimensional bladed-disks with frictional contact interfaces based on cyclic reduction strategies. *International Journal of Solids and Structures*, 236:111277, 2022.

[326] A. Tsetas, A. Tsouvalas, and A. V. Metrikine. An alternating frequency-time harmonic balance method for fast-slow dynamical systems. In *Proceedings of the 28th International Congress on Sound and Vibration*. International Institute of Acoustics and Vibration, IIAV, 2022.

[327] H. Gravenkamp, A. A. Saputra, and S. Duczek. High-order shape functions in the scaled boundary finite element method revisited. *Archives of Computational Methods in Engineering*, 28(2):473–494, 2021.

[328] S. Jones and M. Legrand. Forced vibrations of a turbine blade undergoing regularized unilateral contact conditions through the wavelet balance method. *International Journal for Numerical Methods in Engineering*, 101(5):351–374, 2015.

[329] D. Laxalde and F. Thouverez. Complex non-linear modal analysis for mechanical systems: Application to turbomachinery bladings with friction interfaces. *Journal of sound and vibration*, 322(4-5):1009–1025, 2009.

[330] F. Fontanela, A. Grolet, L. Salles, and N. Hoffmann. Computation of quasi-periodic localised vibrations in nonlinear cyclic and symmetric structures using harmonic balance methods. *Journal of Sound and Vibration*, 438:54–65, 2019.

[331] M. Krack, L. Panning-von Scheidt, and J. Wallaschek. A high-order harmonic balance method for systems with distinct states. *Journal of Sound and Vibration*, 332(21):5476–5488, 2013.

[332] M. J. Powell. A hybrid method for nonlinear equations. *Numerical methods for nonlinear algebraic equations*, 1970.

[333] A. Tsetas, A. Tsouvalas, T. Molenkamp, and A. V. Metrikine. A mode-matching method for the prediction of stick-slip relative motion of two elastic rods in frictional contact. *Acta Mechanica*, 233(2):753–773, 2022.

[334] M. Randolph, R. Dolwin, and R. Beck. Design of driven piles in sand. *Geotechnique*, 44(3):427–448, 1994.

[335] D. White and B. Lehane. Friction fatigue on displacement piles in sand. *Géotechnique*, 54(10):645–658, 2004.

[336] J. A. Schneider, X. Xu, and B. M. Lehane. Database assessment of cpt-based design methods for axial capacity of driven piles in siliceous sands. *Journal of geotechnical and geoenvironmental engineering*, 134(9):1227–1244, 2008.

[337] M. Bielefeld, N. Moscoso, and G. Verbeek. Soil modeling for pile driving simulations using a vibro hammer. In *Offshore Technology Conference*. OnePetro, 2020.

[338] E. P. Heerema. Predicting pile driveability: heather as an illustration of the friction fatigue theory. In *SPE european petroleum conference*. OnePetro, 1978.

[339] A. Bond and R. Jardine. Effects of installing displacement piles in a high ocr clay. *Geotechnique*, 41(3):341–363, 1991.

[340] B. M. Lehane, R. Jardine, A. J. Bond, and R. Frank. Mechanisms of shaft friction in sand from instrumented pile tests. *Journal of Geotechnical Engineering*, 119(1):19–35, 1993.

[341] K. G. Gavin and B. C. O'Kelly. Effect of friction fatigue on pile capacity in dense sand. *Journal of Geotechnical and Geoenvironmental Engineering*, 133(1):63–71, 2007.

[342] A. Tsetas, A. Tsouvalas, and A. V. Metrikine. The mechanics of the Gentle Driving of Piles. *International Journal of Solids and Structures, under review*, 2023.

[343] L. Chua and A. Ushida. Algorithms for computing almost periodic steady-state response of nonlinear systems to multiple input frequencies. *IEEE Transactions on circuits and systems*, 28(10):953–971, 1981.

[344] S. Lau, Y. Cheung, and S.-Y. Wu. Incremental harmonic balance method with multiple time scales for aperiodic vibration of nonlinear systems. *Journal of Applied Mechanics*, 50(4a):871–876, 1983.

[345] R. Pušenjak and M. Oblak. Incremental harmonic balance method with multiple time variables for dynamical systems with cubic non-linearities. *International journal for numerical methods in engineering*, 59(2):255–292, 2004.

[346] *Multi-Dimensional Harmonic Balance Applied to Rotor Dynamics*, volume Volume 1: 21st Biennial Conference on Mechanical Vibration and Noise, Parts A, B, and C of *International Design Engineering Technical Conferences and Computers and Information in Engineering Conference*, 2007.

[347] M. Guskov and F. Thouverez. Harmonic balance-based approach for quasi-periodic motions and stability analysis. *Journal of vibration and acoustics*, 134(3), 2012.

[348] S. Bäuerle, R. Fiedler, and H. Hetzler. An engineering perspective on the numerics of quasi-periodic oscillations. *Nonlinear Dynamics*, 108(4):3927–3950, 2022.

[349] G. Athanasopoulos and P. Pelekis. Ground vibrations from sheetpile driving in urban environment: measurements, analysis and effects on buildings and occupants. *Soil dynamics and earthquake engineering*, 19(5):371–387, 2000.

[350] A. Grizi, A. Athanasopoulos-Zekkos, and R. D. Woods. Ground vibration measurements near impact pile driving. *Journal of Geotechnical and Geoenvironmental Engineering*, 142(8):04016035, 2016.

A

SAFE matrices for a Love-Timoshenko cylindrical shell

The following matrices follow from the Love-Timoshenko shell theory [158, 140, 159]:

$$\mathbf{A}_{\theta,\mathrm{p}} = \begin{bmatrix} 0 & 0 & 0 & 0 \\ 0 & 0 & 0 & 0 \\ 0 & 0 & 0 & 0 \\ 0 & 0 & 0 & 0 \\ 0 & 0 & -\dfrac{1}{R_\mathrm{p}} & 0 \end{bmatrix}, \quad \mathbf{A}_{0,\mathrm{p}} = \begin{bmatrix} 1 & 0 & 0 & 0 \\ 0 & 1 & 0 & 0 \\ 0 & 0 & 1 & 0 \\ 0 & 0 & 0 & 1 \\ 0 & \dfrac{1}{R_\mathrm{p}} & 0 & 0 \end{bmatrix} \tag{A.1}$$

$$\mathscr{L}_{z,\mathrm{p}} = \begin{bmatrix} 1 & 0 & 0 & 0 & 0 & 0 & 0 & 0 & 0 & 0 \\ 0 & 0 & 1 & 0 & 0 & 0 & 0 & 0 & 0 & 0 \\ 0 & 0 & 0 & 0 & 1 & 0 & 0 & 0 & 0 & 0 \\ 0 & 0 & 0 & 0 & 0 & 0 & 1 & 0 & 0 & 0 \\ 0 & 0 & 0 & 0 & 0 & 0 & 0 & 0 & 1 & 0 \end{bmatrix} \tag{A.2}$$

$$\mathscr{L}_{\theta,\mathrm{p}} = \frac{1}{R_\mathrm{p}} \begin{bmatrix} 0 & 0 & 0 & 1 & 0 & 0 & 0 & 0 & 0 & 0 \\ 0 & 1 & 0 & 0 & 0 & 0 & 0 & 0 & 0 & 0 \\ 0 & 0 & 0 & 0 & 0 & 1 & 0 & 0 & 0 & 0 \\ 0 & 0 & 0 & 0 & 0 & 0 & 0 & 0 & 0 & 1 \\ 0 & 0 & 0 & 0 & 0 & 0 & 0 & 1 & 0 & 0 \end{bmatrix} \tag{A.3}$$

$$\mathscr{L}_{0,\mathrm{p}} = \begin{bmatrix} 0 & 0 & 0 & 0 & 0 & 0 & 0 & 0 & 0 & 0 \\ 0 & 0 & 0 & 0 & 0 & \frac{1}{R_\mathrm{p}} & 0 & 0 & 0 & 0 \\ 0 & -\frac{1}{R_\mathrm{p}} & 0 & 0 & 0 & 0 & 0 & 0 & 0 & 0 \\ 0 & 0 & 0 & 0 & -1 & 0 & 0 & 0 & 0 & 0 \\ 0 & 0 & 0 & 0 & 0 & -1 & 0 & 0 & 0 & 0 \end{bmatrix} \tag{A.4}$$

$$\mathscr{I}_\mathrm{p} = \rho_\mathrm{p} h_\mathrm{p} \begin{bmatrix} 1 & 0 & 0 & 0 & 0 \\ 0 & 1 & 0 & 0 & 0 \\ 0 & 0 & 1 & 0 & 0 \\ 0 & 0 & 0 & 0 & 0 \\ 0 & 0 & 0 & 0 & 0 \end{bmatrix} \tag{A.5}$$

$$\mathscr{B}_{\theta,\mathrm{p}} = \begin{bmatrix} 0 & 0 & 0 & 0 & 0 & 0 & 0 & 0 & 0 & 0 \\ 0 & 0 & 0 & 0 & 0 & 0 & 0 & 0 & 0 & 0 \\ 0 & 0 & 0 & 0 & 0 & 0 & 0 & 0 & \frac{1}{R_\mathrm{p}} & 0 \\ 0 & 0 & 0 & 0 & 0 & 0 & 0 & 0 & 0 & 0 \\ 0 & 0 & 0 & 0 & 0 & 0 & 0 & 0 & 0 & 0 \end{bmatrix} \tag{A.6}$$

$$\mathscr{B}_{0,\mathrm{p}} = \begin{bmatrix} 1 & 0 & 0 & 0 & 0 & 0 & 0 & 0 & 0 & 0 \\ 0 & 0 & 1 & 0 & 0 & 0 & 0 & 0 & \frac{1}{R_\mathrm{p}} & 0 \\ 0 & 0 & 0 & 0 & 1 & 0 & 0 & 0 & 0 & 0 \\ 0 & 0 & 0 & 0 & 0 & 0 & 1 & 0 & 0 & 0 \\ 0 & 0 & 0 & 0 & 0 & 0 & 0 & 0 & 0 & 0 \end{bmatrix} \tag{A.7}$$

$$\mathbf{S}_{zz,\mathrm{p}} = \frac{E_\mathrm{p} h_\mathrm{p}}{1-\nu_\mathrm{p}^2} \begin{bmatrix} 0 & 0 & 0 & 0 & 0 & 0 & 0 & 0 & 0 & 0 \\ 0 & 0 & 0 & 0 & 0 & 0 & 0 & 0 & 0 & 0 \\ 0 & 0 & 0 & 0 & 0 & 0 & 0 & 0 & 0 & 0 \\ 0 & 0 & 0 & 0 & k_\mathrm{p} R_\mathrm{p}^2 & 0 & 0 & 0 & 0 & 0 \\ 0 & 0 & 0 & 0 & 0 & (1-\nu_\mathrm{p}) k_\mathrm{p} R_\mathrm{p}^2 & 0 & 0 & 0 & 0 \end{bmatrix}^\mathrm{T} \tag{A.8}$$

$$\mathbf{S}_{\theta\theta,\mathrm{p}} = \frac{E_\mathrm{p} h_\mathrm{p}}{1-\nu_\mathrm{p}^2} \begin{bmatrix} 0 & 0 & 0 & 0 & 0 & 0 & 0 & 0 & 0 & 0 \\ 0 & 0 & 0 & 0 & 0 & 0 & 0 & 0 & 0 & 0 \\ 0 & 0 & 0 & 0 & 0 & 0 & 0 & 0 & 0 & 0 \\ 0 & 0 & 0 & 0 & 0 & 0 & 0 & 0 & 0 & 0 \\ 0 & 0 & 0 & 0 & 0 & k_\mathrm{p} & 0 & 0 & 0 & 0 \end{bmatrix}^\mathrm{T} \tag{A.9}$$

$$\mathbf{S}_{z\theta,\mathrm{p}} = \frac{E_\mathrm{p} h_\mathrm{p}}{1-\nu_\mathrm{p}^2} \begin{bmatrix} 0 & 0 & 0 & 0 & 0 & 0 & 0 & 0 & 0 & 0 \\ 0 & 0 & 0 & 0 & 0 & 0 & 0 & 0 & 0 & 0 \\ 0 & 0 & 0 & 0 & 0 & 0 & 0 & 0 & 0 & 0 \\ 0 & 0 & 0 & 0 & 0 & \nu_\mathrm{p} k_\mathrm{p} R_\mathrm{p} & 0 & 0 & 0 & 0 \\ 0 & 0 & 0 & 0 & k_\mathrm{p} R_\mathrm{p} & 0 & 0 & 0 & 0 & 0 \end{bmatrix}^\mathrm{T} \tag{A.10}$$

$$\mathbf{S}_{z,\mathrm{p}} = \frac{E_\mathrm{p} h_\mathrm{p}}{1-\nu_\mathrm{p}^2} \begin{bmatrix} 1 & \nu_\mathrm{p} & 0 & 0 & 0 & 0 & 0 & 0 & 0 & 0 \\ 0 & 0 & \frac{1-\nu_\mathrm{p}}{2} & \frac{1-\nu_\mathrm{p}}{2} & 0 & 0 & 0 & 0 & 0 & 0 \\ 0 & 0 & 0 & 0 & 0 & 0 & 0 & 0 & 0 & 0 \\ 0 & 0 & 0 & 0 & 0 & 0 & k_\mathrm{p} R_\mathrm{p}^2 & \nu_\mathrm{p} k_\mathrm{p} R_\mathrm{p}^2 & 0 & 0 \\ 0 & 0 & 0 & 0 & 0 & 0 & 0 & 0 & (1-\nu_\mathrm{p}) k_\mathrm{p} R_\mathrm{p}^2 & (1-\nu_\mathrm{p}) k_\mathrm{p} R_\mathrm{p}^2 \end{bmatrix}^\mathrm{T} \tag{A.11}$$

$$\mathbf{S}_{\theta,\mathrm{p}} = \frac{E_\mathrm{p} h_\mathrm{p}}{1-\nu_\mathrm{p}^2} \begin{bmatrix} 0 & 0 & \frac{1-\nu_\mathrm{p}}{2R_\mathrm{p}} & \frac{1-\nu_\mathrm{p}}{2R_\mathrm{p}} & 0 & 0 & 0 & 0 & 0 & 0 \\ \frac{\nu_\mathrm{p}}{R_\mathrm{p}} & \frac{1}{R_\mathrm{p}} & 0 & 0 & 0 & 0 & 0 & 0 & 0 & 0 \\ 0 & 0 & 0 & 0 & 0 & 0 & 0 & 0 & 0 & 0 \\ 0 & 0 & 0 & 0 & 0 & 0 & 0 & 0 & 0 & 0 \\ 0 & 0 & 0 & 0 & 0 & 0 & \nu_\mathrm{p} k_\mathrm{p} R_\mathrm{p} & k_\mathrm{p} R_\mathrm{p} & 0 & 0 \end{bmatrix}^\mathrm{T} \tag{A.12}$$

$$\mathbf{S}_{0,\mathrm{p}} = \frac{E_\mathrm{p} h_\mathrm{p}}{1-\nu_\mathrm{p}^2} \begin{bmatrix} 0 & 0 & 0 & 0 & 0 & 0 & 0 & 0 & 0 & 0 \\ 0 & 0 & 0 & 0 & 0 & 0 & 0 & 0 & 0 & 0 \\ \frac{\nu_\mathrm{p}}{R_\mathrm{p}} & \frac{1}{R_\mathrm{p}} & 0 & 0 & 0 & 0 & 0 & 0 & 0 & 0 \\ 0 & 0 & 0 & 0 & 0 & 0 & 0 & 0 & 0 & 0 \\ 0 & 0 & 0 & 0 & 0 & 0 & 0 & 0 & 0 & 0 \end{bmatrix}^\mathrm{T} \tag{A.13}$$

For $n = 0$, the SAFE mass and stiffness matrices $\mathbf{I}^l_{\mathrm{p},0}$ and $\mathbf{L}^l_{\mathrm{p},0}$ for a cylindrical shell segment l with length d_l read:

$$\mathbf{I}^l_{\mathrm{p},0} = 2\pi R_\mathrm{p} h_\mathrm{p} \rho_\mathrm{p} \begin{bmatrix} \frac{d_l}{3} & 0 & 0 & \frac{d_l}{6} & 0 & 0 \\ 0 & \frac{13d_l}{35} & \frac{11d_l^2}{210} & 0 & \frac{9d_l}{70} & -\frac{13d_l^2}{420} \\ 0 & \frac{11d_l^2}{210} & \frac{d_l^3}{105} & 0 & \frac{13d_l^2}{420} & -\frac{d_l^3}{140} \\ \frac{d_l}{6} & 0 & 0 & \frac{d_l}{3} & 0 & 0 \\ 0 & \frac{9d_l}{70} & \frac{13d_l^2}{420} & 0 & \frac{13d_l}{35} & -\frac{11d_l^2}{210} \\ 0 & -\frac{13d_l^2}{420} & -\frac{d_l^3}{140} & 0 & -\frac{11d_l^2}{210} & \frac{d_l^3}{105} \end{bmatrix} \tag{A.14}$$

$$\mathbf{L}^l_{\mathrm{p},0} = 2\pi R_\mathrm{p} D_\mathrm{p} \begin{bmatrix} \frac{1}{d_l} & -\frac{\nu_\mathrm{p}}{2R_\mathrm{p}} & -\frac{d_l\nu_\mathrm{p}}{12R_\mathrm{p}} & -\frac{1}{d_l} & -\frac{\nu_\mathrm{p}}{2R_\mathrm{p}} & \frac{d_l\nu_\mathrm{p}}{12R_\mathrm{p}} \\ -\frac{\nu_\mathrm{p}}{2R_\mathrm{p}} & \frac{35h_\mathrm{p}^2R_\mathrm{p}^2+13d_l^4}{35d_l^3R_\mathrm{p}^2} & \frac{105h_\mathrm{p}^2R_\mathrm{p}^2+11d_l^4}{210d_l^2R_\mathrm{p}^2} & \frac{\nu_\mathrm{p}}{2R_\mathrm{p}} & \frac{-70h_\mathrm{p}^2R_\mathrm{p}^2+9d_l^4}{70d_l^3R_\mathrm{p}^2} & \frac{210h_\mathrm{p}^2R_\mathrm{p}^2-13d_l^4}{420d_l^2R_\mathrm{p}^2} \\ -\frac{d_l\nu_\mathrm{p}}{12R_\mathrm{p}} & \frac{105h_\mathrm{p}^2R_\mathrm{p}^2+11d_l^4}{210d_l^2R_\mathrm{p}^2} & \frac{35h_\mathrm{p}^2R_\mathrm{p}^2+d_l^4}{105d_lR_\mathrm{p}^2} & \frac{d_l\nu_\mathrm{p}}{12R_\mathrm{p}} & \frac{-210h_\mathrm{p}^2R_\mathrm{p}^2+13d_l^4}{420d_l^2R_\mathrm{p}^2} & \frac{70h_\mathrm{p}{}^2R_\mathrm{p}{}^2-3d_l^4}{420d_lR_\mathrm{p}{}^2} \\ -\frac{1}{d_l} & \frac{\nu_\mathrm{p}}{2R_\mathrm{p}} & \frac{d_l\nu_\mathrm{p}}{12R_\mathrm{p}} & \frac{1}{d_l} & \frac{\nu_\mathrm{p}}{2R_\mathrm{p}} & -\frac{d_l\nu_\mathrm{p}}{12R_\mathrm{p}} \\ -\frac{\nu_\mathrm{p}}{2R_\mathrm{p}} & \frac{-70h_\mathrm{p}{}^2R_\mathrm{p}^2+9d_l^4}{70d_l^3R_\mathrm{p}^2} & \frac{-210h_\mathrm{p}^2R_\mathrm{p}^2+13d_l^4}{420d_l^2R_\mathrm{p}^2} & \frac{\nu_\mathrm{p}}{2R_\mathrm{p}} & \frac{35h_\mathrm{p}^2R_\mathrm{p}^2+13d_l^4}{35d_l^3R_\mathrm{p}^2} & \frac{-105h_\mathrm{p}^2R_\mathrm{p}^2-11d_l^4}{210d_l^2R_\mathrm{p}^2} \\ \frac{d_l\nu_\mathrm{p}}{12R_\mathrm{p}} & \frac{210h_\mathrm{p}{}^2R_\mathrm{p}^2-13d_l^4}{420d_l^2R_\mathrm{p}^2} & \frac{70h_\mathrm{p}{}^2R_\mathrm{p}^2-3d_l^4}{420d_lR_\mathrm{p}^2} & -\frac{h_\mathrm{p}\nu_\mathrm{p}}{12R_\mathrm{p}} & \frac{-105h_\mathrm{p}{}^2R_\mathrm{p}^2-11d_l^4}{210d_l^2R_\mathrm{p}^2} & \frac{35h_\mathrm{p}^2R_\mathrm{p}^2+d_l^4}{105d_lR_\mathrm{p}^2} \end{bmatrix} \tag{A.15}$$

where $D_\mathrm{p} = \dfrac{E_\mathrm{p} h_\mathrm{p}}{1-\nu_\mathrm{p}^2}$.

B

Soil constitutive and TLM matrices

The soil constitutive matrices are defined as [219]:

$$\mathbf{D}_{rr} = \begin{bmatrix} \lambda_{\mathrm{s}} + 2G_{\mathrm{s}} & 0 & 0 \\ 0 & G_{\mathrm{s}} & 0 \\ 0 & 0 & G_{\mathrm{s}} \end{bmatrix}, \mathbf{D}_{\theta\theta} = \begin{bmatrix} G_{\mathrm{s}} & 0 & 0 \\ 0 & \lambda_{\mathrm{s}} + 2G_{\mathrm{s}} & 0 \\ 0 & 0 & G_{\mathrm{s}} \end{bmatrix} \tag{B.1}$$

$$\mathbf{D}_{zz} = \begin{bmatrix} G_{\mathrm{s}} & 0 & 0 \\ 0 & G_{\mathrm{s}} & 0 \\ 0 & 0 & \lambda_{\mathrm{s}} + 2G_{\mathrm{s}} \end{bmatrix}, \quad \mathbf{D}_{r\theta} = \mathbf{D}_{\theta r}^{T} = \begin{bmatrix} 0 & \lambda_{\mathrm{s}} & 0 \\ G_{\mathrm{s}} & 0 & 0 \\ 0 & 0 & 0 \end{bmatrix} \tag{B.2}$$

$$\mathbf{D}_{rz} = \mathbf{D}_{zr}^{T} = \begin{bmatrix} 0 & 0 & \lambda_{\mathrm{s}} \\ 0 & 0 & 0 \\ G_{\mathrm{s}} & 0 & 0 \end{bmatrix}, \quad \mathbf{D}_{\theta z} = \mathbf{D}_{z\theta}^{\mathrm{T}} = \begin{bmatrix} 0 & 0 & 0 \\ 0 & 0 & \lambda_{\mathrm{s}} \\ 0 & G_{\mathrm{s}} & 0 \end{bmatrix} \tag{B.3}$$

$$\mathbf{D}_{r1} = \mathbf{D}_{1r} = \begin{bmatrix} \lambda_{\mathrm{s}} & 0 & 0 \\ 0 & -G_{\mathrm{s}} & 0 \\ 0 & 0 & 0 \end{bmatrix}, \quad \mathbf{D}_{\theta 1} = \mathbf{D}_{1\theta}^{\mathrm{T}} = \begin{bmatrix} 0 & -G_{\mathrm{s}} & 0 \\ \lambda_{\mathrm{s}} + 2G_{\mathrm{s}} & 0 & 0 \\ 0 & 0 & 0 \end{bmatrix} \tag{B.4}$$

$$\mathbf{D}_{z1} = \mathbf{D}_{1z}^{T} = \begin{bmatrix} 0 & 0 & 0 \\ 0 & 0 & 0 \\ \lambda_{\mathrm{s}} & 0 & 0 \end{bmatrix}, \quad \mathbf{D}_{11} = \begin{bmatrix} \lambda_{\mathrm{s}} + 2G_{\mathrm{s}} & 0 & 0 \\ 0 & G_{\mathrm{s}} & 0 \\ 0 & 0 & 0 \end{bmatrix} \tag{B.5}$$

B

For the case of linear Lagrange polynomials used as interpolation functions, the TLM matrices read:

$$\mathbf{A}^l = \frac{h_l}{6}\begin{bmatrix} 2(\lambda_s+2G_s) & 0 & 0 & \lambda_s+2G_s & 0 & 0 \\ 0 & 2G_s & 0 & 0 & G_s & 0 \\ 0 & 0 & 2G_s & 0 & 0 & G_s \\ \lambda_s+2G_s & 0 & 0 & 2(\lambda_s+2G_s) & 0 & 0 \\ 0 & G_s & 0 & 0 & 2G_s & 0 \\ 0 & 0 & G_s & 0 & 0 & 2G_s \end{bmatrix} \tag{B.6}$$

$$\mathbf{B}^l = \frac{1}{2}\begin{bmatrix} 0 & 0 & -G_s+\lambda_s & 0 & 0 & -G_s-\lambda_s \\ 0 & 0 & 0 & 0 & 0 & 0 \\ -G_s+\lambda_s & 0 & 0 & G_s+\lambda_s & 0 & 0 \\ 0 & 0 & G_s+\lambda_s & 0 & 0 & G_s-\lambda_s \\ 0 & 0 & 0 & 0 & 0 & 0 \\ -G_s-\lambda_s & 0 & 0 & G_s-\lambda_s & 0 & 0 \end{bmatrix} \tag{B.7}$$

$$\mathbf{G}^l = \frac{1}{h_l}\begin{bmatrix} G_s & 0 & 0 & -G_s & 0 & 0 \\ 0 & G_s & 0 & 0 & -G_s & 0 \\ 0 & 0 & \lambda_s+2G_s & 0 & 0 & -\lambda_s-2G_s \\ -G_s & 0 & 0 & G_s & 0 & 0 \\ 0 & -G_s & 0 & 0 & G_s & 0 \\ 0 & 0 & -\lambda_s-2G_s & 0 & 0 & \lambda_s+2G_s \end{bmatrix} \tag{B.8}$$

$$\mathbf{M}^l = \frac{\rho_s h_l}{6}\begin{bmatrix} 2 & 0 & 0 & 1 & 0 & 0 \\ 0 & 2 & 0 & 0 & 1 & 0 \\ 0 & 0 & 2 & 0 & 0 & 1 \\ 1 & 0 & 0 & 2 & 0 & 0 \\ 0 & 1 & 0 & 0 & 2 & 0 \\ 0 & 0 & 1 & 0 & 0 & 2 \end{bmatrix} \tag{B.9}$$

Similarly, for quadratic Lagrange polynomials, the interpolation matrix and vector of layer interface values read:

$$\mathbf{N}_s = \begin{bmatrix} N_1^q(z)\mathbf{I}_3 & N_2^q(z)\mathbf{I}_3 & N_3^q(z)\mathbf{I}_3 \end{bmatrix}, \quad \mathbf{x}_s = \begin{bmatrix} \mathbf{x}_s^{(i)} \\ \mathbf{x}_s^{(i+1)} \\ \mathbf{x}_s^{(i+2)} \end{bmatrix} \tag{B.10}$$

where the quadratic Lagrange polynomials $N_1^q(z)$, $N_2^q(z)$ and $N_3^q(z)$ are defined as:

$$N_1^q(z) = 1 - \frac{3z}{h_l} + \frac{2z^2}{h_l^2}, \quad N_2^q(z) = \frac{4z}{h_l} - \frac{4z^2}{h_l^2}, \quad N_3^q(z) = \frac{2z^2}{h_l^2} - \frac{z}{h_l} \tag{B.11}$$

The TLM matrices, following from quadratic Lagrange polynomials used as interpolation functions, read:

$$\mathbf{A}^l = \frac{h_l}{30}\begin{bmatrix} 4(\lambda_s+2G_s) & 0 & 0 & 2(\lambda_s+2G_s) & 0 & 0 & -(\lambda_s+2G_s) & 0 & 0 \\ 0 & 4G_s & 0 & 0 & 2G_s & 0 & 0 & -G_s & 0 \\ 0 & 0 & 4G_s & 0 & 0 & 2G_s & 0 & 0 & -G_s \\ 2(\lambda_s+2G_s) & 0 & 0 & 16(\lambda_s+2G_s) & 0 & 0 & 2(\lambda_s+2G_s) & 0 & 0 \\ 0 & 2G_s & 0 & 0 & 16G_s & 0 & 0 & 2G_s & 0 \\ 0 & 0 & 2G_s & 0 & 0 & 16G_s & 0 & 0 & 2G_s \\ -(\lambda_s+2G_s) & 0 & 0 & 2(\lambda_s+2G_s) & 0 & 0 & 4(\lambda_s+2G_s) & 0 & 0 \\ 0 & -G_s & 0 & 0 & 2G_s & 0 & 0 & 4G_s & 0 \\ 0 & 0 & -G_s & 0 & 0 & 2G_s & 0 & 0 & 4G_s \end{bmatrix} \tag{B.12}$$

$$\mathbf{B}^l = \frac{1}{6}\begin{bmatrix} 0 & 0 & 3(\lambda_s-G_s) & 0 & 0 & -4(\lambda_s+) & 0 & 0 & \lambda_s+G_s \\ 0 & 0 & 0 & 0 & 0 & 0 & 0 & 0 & 0 \\ 3(\lambda_s-G_s) & 0 & 0 & 4(\lambda_s+G_s) & 0 & 0 & -(\lambda_s+G_s) & 0 & 0 \\ 0 & 0 & 4(\lambda_s+G_s) & 0 & 0 & 0 & 0 & 0 & -4(\lambda_s+G_s) \\ 0 & 0 & 0 & 0 & 0 & 0 & 0 & 0 & 0 \\ -4(\lambda_s+G_s) & 0 & 0 & 0 & 0 & 0 & 4(\lambda_s+G_s) & 0 & 0 \\ 0 & 0 & -(\lambda_s+G_s) & 0 & 0 & 4(\lambda_s+G_s) & 0 & 0 & -3(\lambda_s-G_s) \\ 0 & 0 & 0 & 0 & 0 & 0 & 0 & 0 & 0 \\ (\lambda_s+G_s) & 0 & 0 & -4(\lambda_s+G_s) & 0 & 0 & -3(\lambda_s-G_s) & 0 & 0 \end{bmatrix} \tag{B.13}$$

$$\mathbf{G}^l = \frac{1}{3h_l}\begin{bmatrix} 7G_s & 0 & 0 & -8G_s & 0 & 0 & G_s & 0 & 0 \\ 0 & 7G_s & 0 & 0 & -8G_s & 0 & 0 & G_s & 0 \\ 0 & 0 & 7(\lambda_s+2G_s) & 0 & 0 & -8(\lambda_s+2G_s) & 0 & 0 & \lambda_s+2G_s \\ -8G_s & 0 & 0 & 16G_s & 0 & 0 & -8G_s & 0 & 0 \\ 0 & -8G_s & 0 & 0 & 16G_s & 0 & 0 & -8G_s & 0 \\ 0 & 0 & -8(\lambda_s+2G_s) & 0 & 0 & 16(\lambda_s+2G_s) & 0 & 0 & -8(\lambda_s+2G_s) \\ G_s & 0 & 0 & -8G_s & 0 & 0 & 7G_s & 0 & 0 \\ 0 & G_s & 0 & 0 & -8G_s & 0 & 0 & 7G_s & 0 \\ 0 & 0 & \lambda_s+2G_s & 0 & 0 & -8(\lambda_s+2G_s) & 0 & 0 & 7(\lambda_s+2G_s) \end{bmatrix} \tag{B.14}$$

$$\mathbf{M}^l = \frac{\rho_s h_l}{30} \begin{bmatrix} 4 & 0 & 0 & 2 & 0 & 0 & -1 & 0 & 0 \\ 0 & 4 & 0 & 0 & 2 & 0 & 0 & -1 & 0 \\ 0 & 0 & 4 & 0 & 0 & 2 & 0 & 0 & -1 \\ 2 & 0 & 0 & 16 & 0 & 0 & 2 & 0 & 0 \\ 0 & 2 & 0 & 0 & 16 & 0 & 0 & 2 & 0 \\ 0 & 0 & 2 & 0 & 0 & 16 & 0 & 0 & 2 \\ -1 & 0 & 0 & 2 & 0 & 0 & 4 & 0 & 0 \\ 0 & -1 & 0 & 0 & 2 & 0 & 0 & 4 & 0 \\ 0 & 0 & -1 & 0 & 0 & 2 & 0 & 0 & 4 \end{bmatrix} \tag{B.15}$$

Curriculum Vitæ

Athanasios Tsetas

13-12-1994 Born in Drama, Greece

Academic experience

2012–2017 Diploma of Civil Engineering
Aristotle University of Thessaloniki, Greece
Thesis: Non-linear dynamic analysis of R/C plane frame structures considering soil-structure interaction.
Supervisors: Dr. V.K. Papanikolaou, Dr. D. Pitilakis

2018–2022 Ph.D. researcher
Delft University of Technology, the Netherlands
Thesis: A unified modelling framework for vibratory pile driving methods
Promotor: Prof. dr. A. V. Metrikine
Copromotor: Dr. ir. A. Tsouvalas

2022– Post-doctoral researcher
Delft University of Technology, the Netherlands

Professional experience

2016 Civil engineer intern
Ydrami Construction Company, Drama, Greece

2017–2018 Engineer
NATO Rapid Deployable Corps (NRDC), Thessaloniki, Greece

Publications

Journal publications

8. Molenkamp, T., **Tsetas, A.**, Tsouvalas, A., & Metrikine, A. V. (2023). Underwater noise prediction model for vibratory pile driving including non-linear frictional pile-soil interaction. *Journal of Sound and Vibration*, under review.
7. **Tsetas, A.**, Tsouvalas, A., & Metrikine, A. V. (2023). The mechanics of the Gentle Driving of Piles. *International Journal of Solids and Structures*, under review.
6. Kementzetzidis, E., Pisanò, F., **Tsetas, A.**, & Metrikine, A. V. (2023). Gentle Driving of Piles (GDP) at a sandy site combining axial and torsional vibrations: quantifying the influence of pile installation method on lateral behaviour. *Journal of Geoenvironmental and Geotechnical Engineering*.
5. **Tsetas, A.**, Tsouvalas, A., & Metrikine, A. V. (2023). A non-linear three-dimensional pile-soil model for vibratory pile installation in layered media. *International Journal of Solids and Structures, 269*, 112202.
4. **Tsetas, A.**, Tsouvalas, A., Gómez, S. S., Pisanò, F., Kementzetzidis, E., Molenkamp, T., Elkadi, A. S. K., & Metrikine, A. V. (2023). Gentle Driving of Piles (GDP) at a sandy site combining axial and torsional vibrations: Part I-installation tests. *Ocean Engineering, 270*, 113453.
3. Gómez, S. S., **Tsetas, A.**, & Metrikine, A. V. (2022). Energy flux analysis for quantification of vibratory pile driving efficiency. *Journal of Sound and Vibration, 541*, 117299.
2. **Tsetas, A.**, Tsouvalas, A., Molenkamp, T., & Metrikine, A. V. (2022). A mode-matching method for the prediction of stick-slip relative motion of two elastic rods in frictional contact. *Acta Mechanica, 233*(2), 753-773.
1. **Tsetas, A.**, Tsouvalas, A., & Metrikine, A. V. (2021). Installation of large-diameter monopiles: introducing wave dispersion and non-local soil reaction. *Journal of Marine Science and Engineering, 9*(3), 313.

Conference publications

8. **Tsetas, A.**, Tsouvalas, A., & Metrikine, A. V. (2023).The effect of high-frequency torsion in vibratory pile installation: the Gentle Driving of Piles method. In *Proceedings of the XII International Conference on Structural Dynamics, EURODYN 2023*. Delft, the Netherlands.
7. Gómez, S. S., **Tsetas, A.**, Middelplaats, L. N. M., & Metrikine, A. V. (2023). Frequency-amplitude decoupling in the Gentle Driving of Piles (GDP) method: shaker design and experiments. In *Proceedings of the XII International Conference on Structural Dynamics, EURODYN 2023*. Delft, the Netherlands.

6. **Tsetas, A.**, Tsouvalas, A., & Metrikine, A. V. (2023). Ground motion reduction in vibratory pile driving via axial and torsional vibrations. In *Proceedings of the 29th International Congress on Sound and Vibration (ICSV29)*. Prague, the Czech Republic.

5. **Tsetas, A.**, Tsouvalas, A., & Metrikine, A. V. (2022). An alternating frequency-time harmonic balance method for fast-slow dynamical systems. In *Proceedings of the 28th International Congress on Sound and Vibration (ICSV28)*. Singapore.

4. Gómez, S. S., **Tsetas, A.**, Tsouvalas, A., & Metrikine, A. V. (2022). Dynamic Pile Response During Vibratory Driving and Modal-Based Strain Field Mapping. In *Recent Trends in Wave Mechanics and Vibrations: Proceedings of WMVC 2022*. Lisbon, Portugal (pp. 1125-1134). Springer.

3. Molenkamp, T., **Tsetas, A.**, Tsouvalas, A., & Metrikine, A. (2020). Dynamic response of two interacting extensible bars in frictional contact. In *Proceedings of the XI International Conference on Structural Dynamics, EURODYN 2020*. Athens, Greece (Vol. 1, pp. 252-264).

2. **Tsetas, A.**, Gómez, S. S., Tsouvalas, A., van Beek, K., Tehrani, F. S., Kementzetzidis, E., Pisanò, F., Elkadi, A., Segeren, M., Molenkamp, T., & Metrikine, A. V. (2020). Experimental identification of the dynamic behaviour of pile-soil system installed by means of three different pile-driving techniques. In *Proceedings of the XI International Conference on Structural Dynamics, EURODYN 2020*. Athens, Greece (Vol. 2, pp. 3005-3015).

1. Metrikine, A. V., Tsouvalas, A., Segeren, M., Elkadi, A. S. K., Tehrani, F., Gómez, S. S., Atkinson, R., Pisanò, F., Kementzetzidis, E., **Tsetas, A.**, Molenkamp, T., van Beek, K., & De Vries, P. (2020). GDP: a new technology for Gentle Driving of (mono)Piles. In *Proceedings of the 4th International Symposium on Frontiers in Offshore Geotechnics (ISFOG)*, Austin, TX, USA (pp. 736–745).